COMPUTATIONAL MOLECULAR DESIGN OF POLYHEDRAL OLIGOMERIC SILSESQUIOXANE BASED ORGANIC-INORGANIC HYBRID SEMICONDUCTORS

by

Feng Qi

A dissertation submitted in partial fulfillment
of the requirements for the degree of
Doctor of Philosophy
(Materials Science and Engineering)
in The University of Michigan
2011

Doctoral Committee:

Professor John Kieffer, Chair
Professor Richard M. Laine
Professor Duncan G. Steel
Assistant Professor Donald J. Siegel

Dedication

To My Mother

Acknowledgements

This would not have been possible without the generosity and assistance of many:

My family, my advisor, my committee, many professors, and friends.

Table of Contents

List of Figures

List of Tables

List of Abriveations

SQ	Silsesquioxane
BZ	Brillouin Zone
CB	Conduction Band
COMPASS	Condensed-phase Optimized Molecular Potentials for Atomistic Simulation Studies
CTR	Charge-transfer Reactive
DACSQ	Diacene-SQ
DASQ	Dianthracene-SQ
DIB	1,4-diiodobenzene
DFT	Density Functional Theory
DOS	Density of States
DPSQ	Dipentacene-SQ
DTSQ	Ditetracene-SQ

EL	Electroluminescence
FTIR	Fourier Transform Infrared Spectroscopy
GGA	Generalized Gradient Approximation
HF	Hartree-Fock
HOMO	Highest Occupied Molecular Orbital
ICSD	International Crystal Structures Database
KS	Kohn-Sham
LAMMPS	Large-scale Atomic/Molecular Massively Parallel Simulator
LDA	Local Density Approximation
LJ	Lennard-Jones
LUMO	Lowest Unoccupied Molecular Orbital
MD	Molecular Dynamics
MPI	Message Passing Interface
ODIPS	Octa(2,5-diiodophenyl)-SQ
OFET	Organic Field-effect Transistor

OLED	Organic Light-Emitting Diode
OPVC	Organic Photovoltaic Cell
POSS	Polyhedral Oligomeric Silsesquioxane
SCF	Self-consistent Field
SIESTA	Spanish Initiative for Electronic Simulations with Thousands of Atoms
STO	Slater-type Orbital
TFT	Thin-Film Transistor
VB	Valance Band

Abstract

Cubic silsesquioxanes (T8 SQs), with the formula of $[RSiO_{1.5}]_8$, enable advanced materials design. In this thesis, a computational materials science framework, including *ab initio* density functional theory (DFT) calculations, molecular dynamics (MD), and Monte Carlo (MC) simulations, was developed to perform computational molecular design and crystal engineering of SQ based diacene-SQ and then octa(halogenphenyl)-SQ molecular systems. The goal of this project was to identify novel molecular architectures, *a priori*, that exhibit targeted self-assembly behaviors and result in materials with improved electronic properties. First, existing force fields, including our in house charge transfer reactive (CTR) force field, and COMPASS, were evaluated for simulating cubic SQ systems. All force fields reproduced the experimental structure of SQ-based crystals very well. However, only the FLX force field reproduced the experimentally observed vibrational properties and thermodynamic behavior. Next, targeting materials performance, such as high electronic mobility, a series of diacene-SQ molecules were designed and their crystal structures predicted by following the computational molecular design recipe that accounts for transport theory, symmetry relationships, polymorph prediction procedures, and solid state

electronic property evaluation methods. Computationally derived diacene-SQ crystals are predicted to exhibit advanced electronic properties, such as very small band gaps and parallel packing of the acene groups in crystal structures, indicating excellent transport properties, as well as improved thermal and mechanical properties. Finally, a series of new small-band gap octa(halogenphenyl)-SQ molecular systems were identified by computationally exploring alternative architectures and functionalization of recently synthesized octa(halogenphenyl)-SQ crystals. These hybrid molecular crystals also feature other unique properties, such as solution processability, cubic molecular symmetry, and the three-dimensional conjugation. The computationally designed octa(2,5-diiodophenyl)-SQ (ODIPS) shows a calculated conduction band structure similar to that of 1,4-diiodobenzene (DIB), whose high hole mobility is known from experiment. Electronic band structure calculations indicate that the SQ cages, which are by themselves insulators, contribute to the electronic transport process in these hybrid molecules, and enhance the intrinsic electronic properties of the organic semiconductor functional groups.

Chapter 1
Introduction

1.1 Polyhedral Oligomeric Silsesquioxane (SQ) Based Materials

1.1.1 SQ molecules as an ideal nano-building block

Silicon, one of the most abundant and easy to get elements on the earth, provides the basis for a number of key materials to human life. The development and application of advanced silicon based science and technology over the last two centuries, mainly as semiconductor materials, greatly and effectively improved the quality of life in many respects. The most common silicon based materials are inorganic solids, that consist of silicon, covalently bonded compounds to other elements, such as carbon, nitrogen, oxygen, etc., in mixed phases that contain group VI, VII, or VIII elements to extents that vary from dopant to alloy concentration levels.

Silicon and oxygen atoms can also form molecular building blocks that assemble into new kinds of molecular solids. An example of such building blocks is silsesquioxanes. Silsesquioxanes are molecules with the formula $(RSiO_{1.5})_n$, where n is an even number (>4) and R can be an atom, a monomer or any

organo-functional group, which can be connected to either the silicon or oxygen atom. Silsesquioxanes can form many structures, e.g., random, bridged, ladder, cage, and partial cage structures.

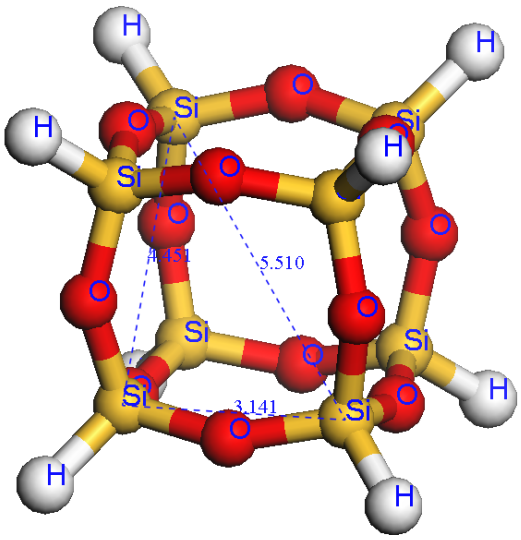

Figure 1-1 Molecular structure of T8 H-SQ (Octahydridosilsesquioxane)

Cage-shaped silsesquioxanes are also called polyhedral oligomeric silsesquioxanes, and are often referred to by the acronym SQ. A basic cage-shaped SQ is T8 H-SQ (octasilsesquioxane $[HSiO_{1.5}]_8$) or cubic SQ. Here each of the eight functional sites on the silicon atoms is terminated with a single hydrogen atom, as shown in Figure 1-1. However, it has been demonstrated that many functional groups can be attached to the SQ cage including alcohols, phenols, alkoxysilanes, aminophenyls, carbohydrates, chlorosilanes, epoxides, esters, fluoroalkyls, halides, isocyanates, methacrylates, acrylates, alkyls, cycloalkyls, nitriles, norbornenyls, olefins, phosphines, silanes, silanols, styrenes, and amphiphiles, etc.[1-10]

The functionalization of the inorganic $(SiO_{1.5})_n$ core with organic groups results in the close juxtaposition of disparate materials and chemical characteristics, which are the hallmark of the relatively novel class of hybrid (inorganic-organic) materials. The impressive variety of functional groups that can be attached to the SQ cage make SQ an excellent candidate as a foundation for hybrid building blocks that are compatible with many polymers materials and biological systems. These SQ based materials are increasingly recognized for their unique properties, which can be attributed to the molecules possessing the hybrid (inorganic-organic) architecture.

In terms of the self-assembly behavior of SQ hybrid building blocks, an outstanding feature is that many of the organic groups attached to the SQ cage can be themselves functionalized, allowing for hybrid building blocks to react with a large variety of polymers to form hybrid (inorganic-organic) macromolecules. Because of the scale of integration and strong covalent bonds between inorganic cores and organic functional groups in these macromolecules, the self-assembled materials possess unique properties that differ substantially from traditional polymer-matrix composites, thus providing an unprecedented number of opportunities to fabricate novel, nano-structured hybrid materials.[1]

The synthesis of SQ based materials has greatly advanced in recent years. For example, several SQ-siloxane monomers and triblocks copolymers were reported in [11,12] Among the synthetic methods reported in the literature, hydrolytic

polycondensation[13], hydrosilation of alkenes with octakis(hydridosilsesquioxane) $(HSiO_{1.5})_8$[14] and polymerization or copolymerization with organic monomers are the most often used.

The synthesized SQ based polymers have four basic architectures [15] as illustrated in Figure 1-2. They are differed by the relative position of the SQ with respect to the polymer chain. The pendant structure features SQ connected to the backbone polymer by a short chain tethered. The AB multiblock 'bead' features the backbone polymer composed by alternating short polymer chaine and SQ cages. The ABA triblocks features two SQ cages connected by a polymer chaine. The star structure features four SQ cages by a pair of crossing polymer chains.

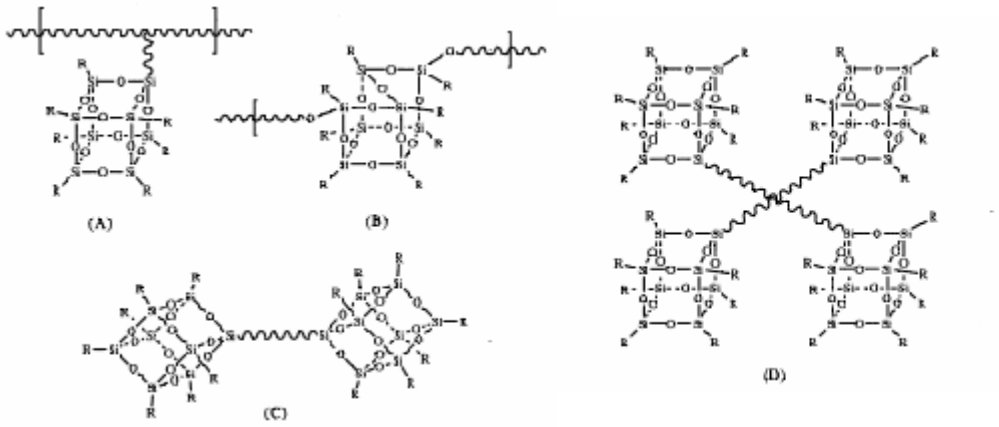

Figure 1-2 Polymer architectures available from SQ monomers: (A) pendant; (B) AB multiblock 'bead', (C) ABA triblock; (D) star.

1.1.2 Crystal packing and self-assembling of cubic SQ

The rigid cubic shape and the long-range interactions resulting from the partial charges localized on Si and O cause the T8 SQ to crystallize with the cubes oriented parallel to each other. This makes SQ an ideal building block for nano self-assembly of molecular systems, because this predictable packing behavior provides a significant degree of control over the assembly of complex molecular semiconductor structures.[65]

The simplest SQ molecular crystal showing parallel packed SQ cubes is the octahydridosilsesquioxane. The crystal structure of octahydridosilasequioxane was first determined by Larsson in 1960[16], then was determined again by Törnroos in 1994[17]. Both reported H-SQ crystals have a trigonal unit cell with space group symmetry of $R\bar{3}$ (no. 148 in the International Tables for Crystallography). The crystal structure is shown in Figure 1-3.

In octamethylsilsequioxane all eight H atoms are replaced by methyl groups. The crystal structure was studied by powder diffraction,[18] and was determined to have the same space group of $R\bar{3}$ as the octahydridosilsesquioxane crystal. The parallel packing of SQ cubes in the crystal unit cell is shown in Figure 1-4. As shown in Figure 1-5, the monotethered SQ molecular crystal structure shows similar parallel packing of SQ cubes, and tethers are aligned as well.[19] The

general crystal packing of T8 SQ is summarized by Waddon *et al.*,[20] as shown in Figure 1-6.

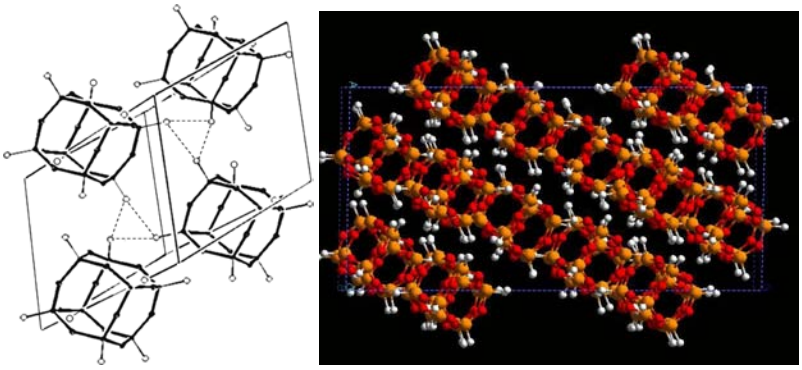

Figure 1-3 Molecular packing of octahydridosilsesquioxane

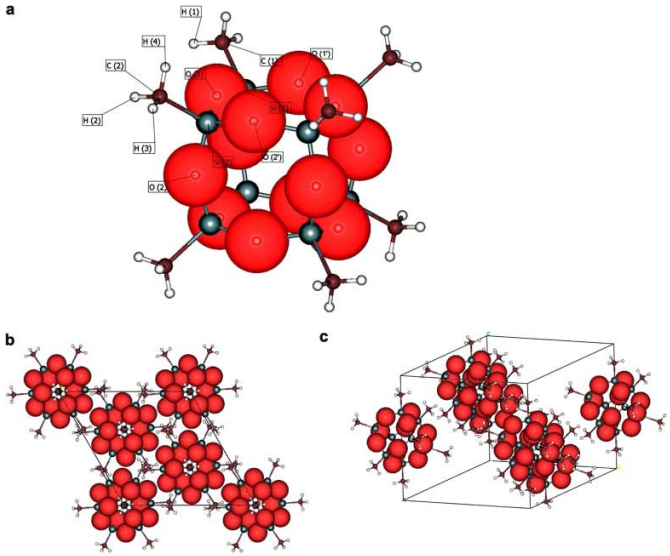

Figure 1-4 Molecular structure and packing of octamethylsilsesquioxane (figure adapted from [18])

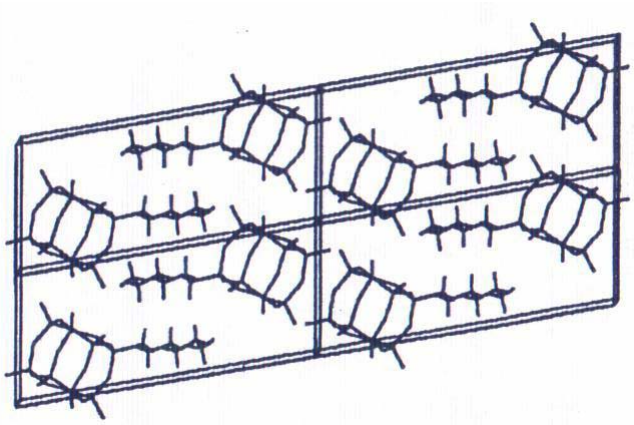

Figure 1-5 Molecular packing of monotethered SQ (figure adapted from [19])

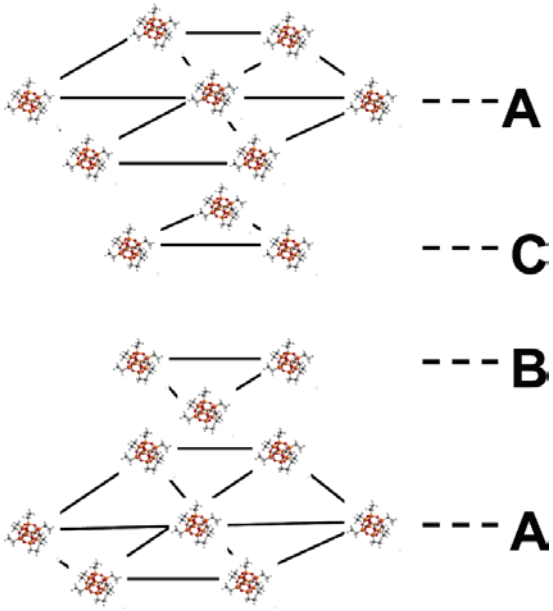

Figure 1-6 General packing behavior of octaarylsilsesquioxane molecular crystals (figure adapted from [20])

If the assembly behavior of SQ-based derivatives is dominated by the parallel positioning of the cubes, then it might be possible to exploit this tendency to coerce the organic groups tethered to the corners of the cube to arrange into specific configurations.

1.1.3 SQ based materials and applications

Due to the great flexibility with regard to chemical functionalization and steric connectivity, SQ can be made into many new materials with a broad range of applications. For example, through reaction between functional groups SQ macromolecules can be readily synthesized into polymeric materials.[21-29] Due to the incorporation of rigid inorganic cores, SQ-based polymers possess many superior properties as compared to ordinary polymers, such as improved thermal and mechanical properties, better abrasion resistance, higher melting temperatures, enhanced fire retardation, radiation resistance, etc.[21-29] Hence, these polymeric systems have been used to create nano-composites for lightweight high-strength materials, biomedical materials, resistant resins on space air craft, packaging materials, elastomers, advanced plastics, composite resins, etc. [21-29] Besides polymers, SQ has also been used to make heterogeneous catalysts and surfactant materials. [30, 31]

SQ is also a very attractive candidate in energy and electronic materials applications. SQ materials have been used in liquid crystal (LC),[32]

electroluminescent (EL) materials,[33] light emitting device (LED) materials,[34] non-linear optics (NLO),[35] Optical Limiting (OL) materials,[36] lasers,[37] lithographic masks, [38] sensors, [39] fuel cells,[40] batteries, [41] and lubricants.[42] SQ based energy and electronic materials have been found to have the following benefits:

- Improved quantum efficiencies
- Greater solubility in many solvents for the whole polymer
- Higher thermal stability
- Brighter color in blue electroluminescent devices [33]
- Compatibility with substrates and metal electrode [41]
- Less color noise due to increased chain spacing in LCDs [32]

Most successful applications of SQ molecules are in the form of polymers. [21-29] Molecular SQs are used mainly as precursors for the synthesis of longer chain or networked polymers.[1] Although possessing unique self-assembling properties, direct applications of small molecule SQ crystals as semiconductors are seldom found.

1.1.4 Computational studies of SQ

Although many experimental studies have been reported for SQ based materials, there have been only a limited number of computational studies. Among existing simulation and calculation works of SQ systems, Xiang *et al* reported

first principles calculations of the structure and electronic properties of $H_8Si_8O_{12}$ (T8 H-SQ).[43] Calzaferri *et al* performed molecular orbital calculations to determine atomic charges for $H_8Si_8O_{12}$ and used these charges in the QCMP067 program package to calculate the normal modes of motion for $H_8Si_8O_{12}$.[44] Pernisz *et al* reported the frequency dependence of linear and nonlinear optical susceptibilities of $H_8Si_8O_{12}$ and other SQ cage molecules using the INDO/CI empirical method.[45]

- Farmer *et al* performed MD simulations of cyclopentyl- and cyclohexyl-SQ as pendent groups in polynorbornene.[46] The calculated volume-temperature behavior and X-ray scattering profiles are in agreement with experiments. The polymer chain dynamics and mechanical property are also studied and compared with experiments of norbornene homopolymer system. Lamm *et al* studied the influence of chain length on the porosity, spatial distribution of SQ cages, and extent of cross-linking during assembly of networked SQ materials by lattice Monte Carlo simulation.[47] The results were compared with the experimental data to test the underlying model of the simulation method. The porosity predicted by the model decreases as tether length increases, which is in agreement with the experimental results.

This thesis is part of a recent collaborative project to conduct a comprehensive computational study of SQ, involving the collaboration between five research groups at three different universities. The respective roles of each group are

illustrated in Figure 1-7. In this effort, Neurock *et al* performed *ab initio* quantum mechanical calculations of the electronic structure and geometric characteristics of T8 H-SQ. As shown in Table 1-1, and Figure 1-8, they determined the HOMO-LUMO optical gap to be 6.77 eV for the T8 H-SQ by a periodic DFT method, which involving using periodic boundary conditions for the constructed unit cell. Interestingly, the LUMO occupies the center of the SQ cage and is highly electrophilic.[48] The iso-electron density contour of the LUMO is predominantly convex and has a highly symmetric shape. As the result of another recent *ab initio* quantum mechanical calculation by Schutte *et al*, based on a hybrid HF-DFT scheme that uses a large 6-311++G basis and B3LYP exchange correlation functional, a HOMO-LUMO energy gap of 8.53 eV was reported. [49] The LUMO is also reported inside the SQ cage as shown in Figure 1-8 on the right.

In collaboration with Laine, Neurock studied stilbeneoctasilsesquioxane and calculated the photophysical properties of the molecule using periodic nonlocal *ab initio* DFT. They found that when functionalizing T8 SQ functionalized with conjugated tethers such as phenyl or stilbene the HOMO and LUMO are localized on the tethered organic groups, and HOMO-LUMO optical gap of the hybrid decreases corresponding with the organic group's HOMO-LUMO energy gap ranges. The smaller energy gap was confirmed by the red shift of the optical UV-vis absorption and PL spectra. [48] Durandurdu *et al* studied the self-assembly of T8 H-SQ cubes by *ab initio* quantum mechanical MD using the Siesta

code with the double zeta polarized (DZP) basis set and the PBE exchange correlation functional.[50] Independent of the starting configuration, which was purposely perturbed, the SQ cubes always rearrange from starting cubic arrangement into a rhombohedral packing very similar to that of the experimental crystal structure (Figure 1-9).

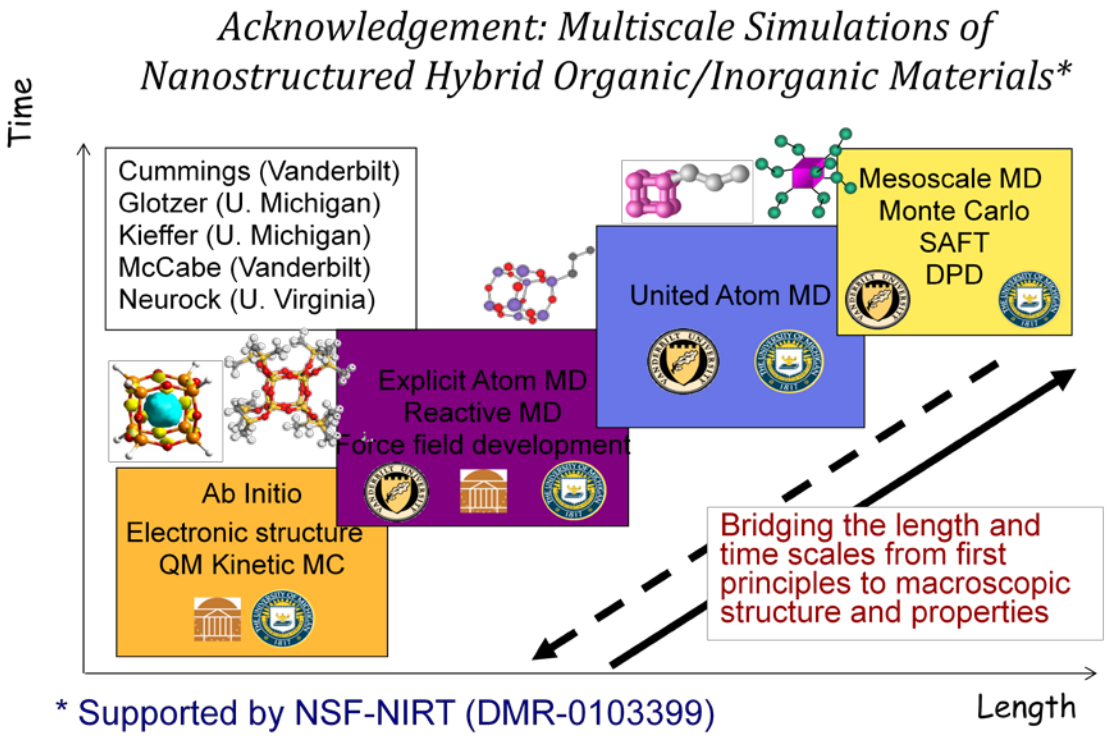

Figure 1-7 Multiscale simulation study of SQ

Table 1-1 calculated bond lengths and angles of T8 H-SQ

	VASP	DMol3	ADF	Experimental
Si-O (Å)	1.631	1.630	1.643	1.626
Si-H (Å)	1.464	1.444	1.474	1.461
∠O-Si-O (°)	109.7	109.7	109.8	109.39
∠Si-O-Si (°)	147.5	147.7	147.7	147.35
Symmetry	T_h	T_h	T_h	T_h

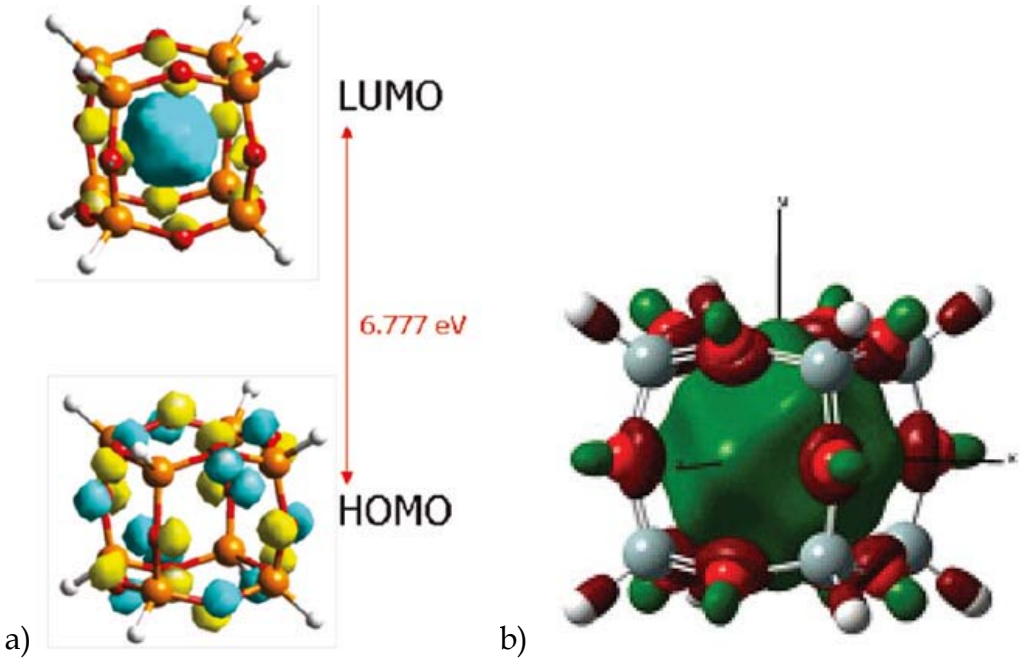

Figure 1-8 a) Optical HOMO and LUMO; and b) Conduction LUMO of T8 H-SQ (Figure adopted from [48, 49])

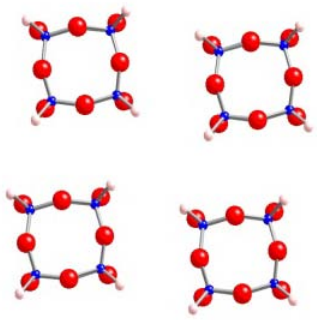

Figure 1-9 Packing structure of four T8 H-SQ cubes upon self-assembly. The four simulated T8 H-SQ molecules are self-assembling from perfect square arrangement into a rhombohedral packing by *ab initio* MD methods.

1.2 Organic Molecular Semiconductors

1.2.1 Chemical bonding and packing structures of molecular semiconductors

Inorganic semiconductors refer to covalently bonded solids such as silicon or germanium, which are the predominant semiconductor materials. Organic semiconductors are relatively new types of materials that are mainly composed of C and H. There are two types of organic semiconductors, molecular organic semiconductors and polymeric organic semiconductors. Molecular organic semiconductors consist of small organic molecules, instead of polymer chains. Some examples of organic semiconducting molecules are shown in Figure 1-10.

The bonding in organic semiconductors is usually very different from inorganic semiconductors. The neighboring C and C-atoms are usually bonded by σ bonds. The whole molecule, especially the aromatic rings, features a conjugated π-electron systems formed by the p_z-orbitals of sp^2-hybridized C-atoms in the molecule, as shown in Figure 1-11. Electrons in the π orbital are delocalized and shared by all C-atoms. Most of these molecules have a planar conformation of aromatic rings with conjugated π orbitals.

Molecular organic semiconductor solids are a collection of ordered (oftentimes crystalline) or randomly packed molecules held together via van der Waals bonding. The intermolecular interactions and bonding between these molecules are much weaker than those in covalently bonded inorganic semiconductors solids. This leads to significant differences in the mechanical and thermal

properties for these molecular solids: usually these materials exhibit low hardness, mechanical strength, and melting points.

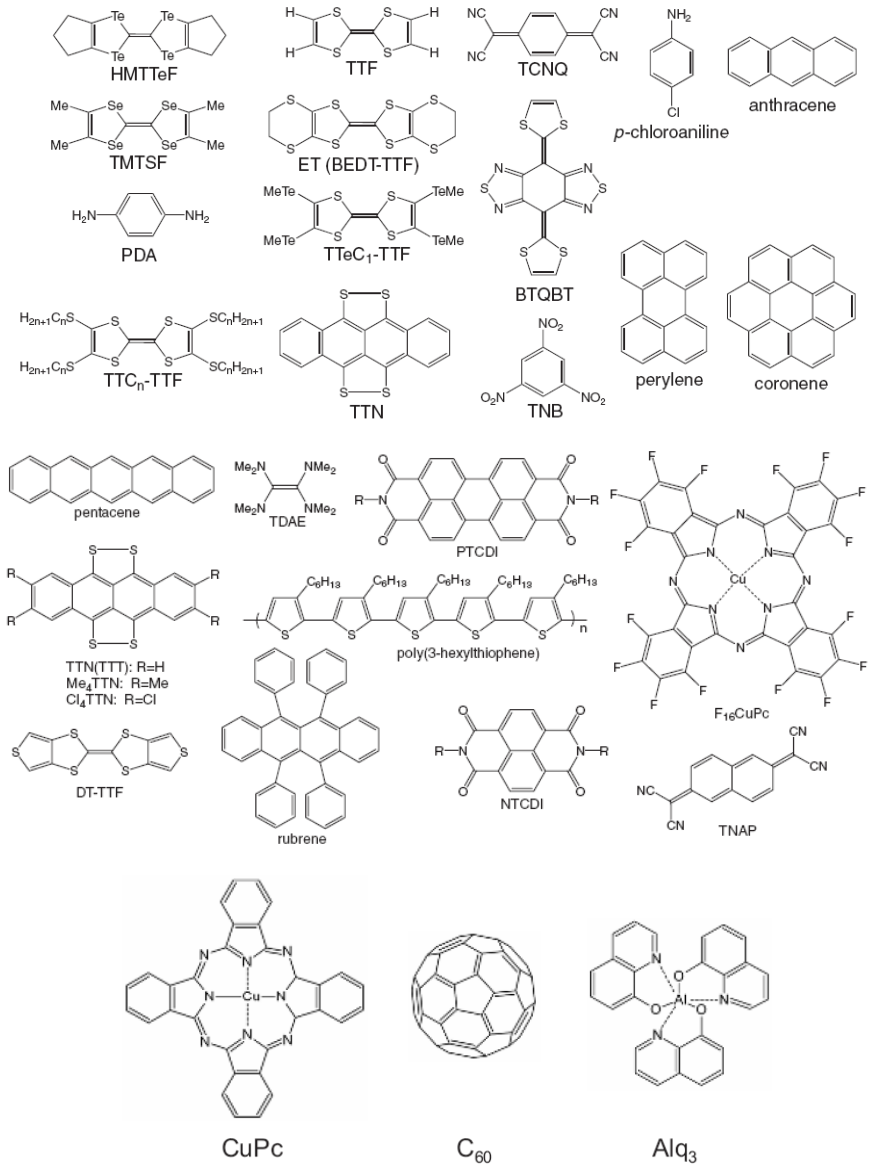

Figure 1-10 Molecular structure of semiconducting organic molecules (Figure adapted from [59, 60]), including HMTTeF (hexamethylenetetratellurafulvalene, TTF (tetrathiafulvalene),TCNQ (tetracyano-p-quinodimethane), TMTSF (tetramethyltetraselenafulvalene), ET (bis(ethylenedithio)-TTF or BEDT-TTF, BTQBT (bis(1,2,5-thiadiazolo)-p-quinobis-(1,3-dithiole)), PDA (p-phenylenediamine), TTeC1-TTF (tetrakis(methyltelluro)-TTF), TTCn-TTF

(tetrakis(alkylthio)-TTF), TTN (tetrathionaphthacene (naphthaceno[5,6-c,d:11,12-c0,d0]bis[1,2]dithiole)), TNB (s-trinitrobenzene), etc.

The weak interaction of molecules in molecular organic semiconductors also means weaker delocalization of electrons between molecules in a molecular solid. This causes unique electronic, optical and charge carrier transport properties of molecular organic semiconductors. Particularly, the long-range transport properties depend directly on the packing of individual molecules in a molecular crystal. It is surmised that the parallel packing of π conjugation systems is highly desired for improved charge carrier transport.[51-58] However, the natural tendency for these molecules to arrange does not always lead to this type of configurations. For example, consider the herringbone structure of pentacene in its innate crystalline state shown in Figure 1-12. This edge-to-face arrangement rather limits the π–π orbital overlap between molecules.

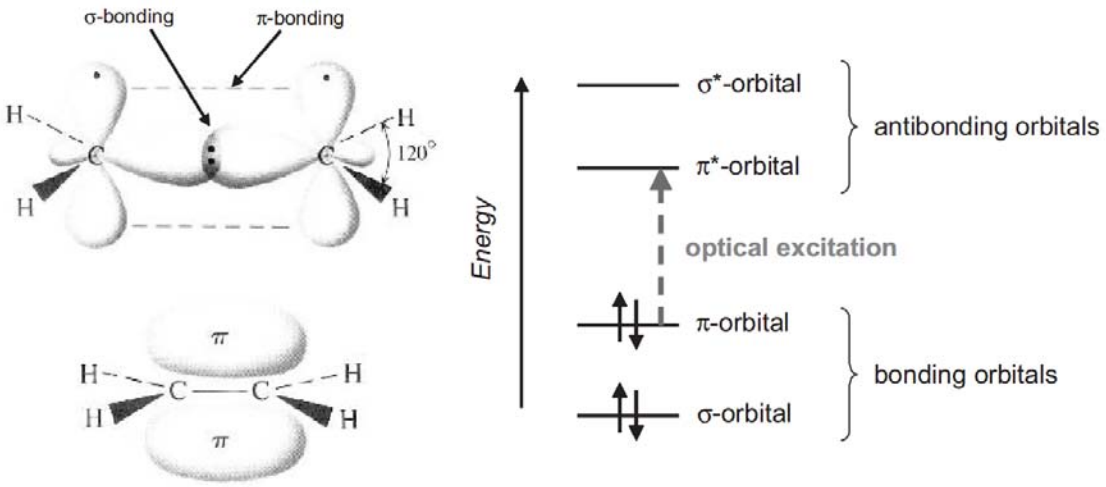

Figure 1-11 Molecular bonding and orbital in an ethene molecule with conjugated π-electron system with orbital energy levels. The lowest electronic excitation is between the bonding π-orbital and the antibonding π*-orbital (adapted from [60]).

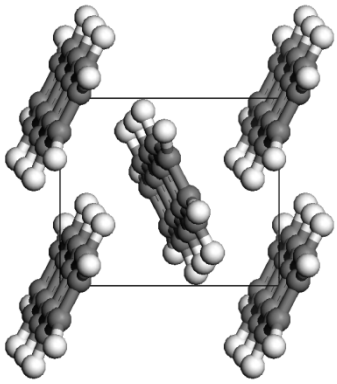

Figure 1-12 Herringbone packing of anthracene molecules in crystal unit cell.[109]

Many efforts have therefore been reported to try to modify the packing behavior of molecular organic semiconductors.[52,61,62] In general, there are two ways to modify the packing behavior of molecules. One way is to control the polymorph of the original molecular crystals, either by changing physical conditions, such as pressure and temperature, or relying on the presence of interfacial forces to control assembly in thin layers. Another way is by introducing additional chemical components to form a new molecule. This latter approach requires molecular design of new molecular organic semiconductor building blocks targeting materials with better properties due to their inherent electronic characteristics as well as controlled self-assembly behavior.

1.2.2 Photonic and electronic properties

1.2.2.1 Electronic structure of an individual molecule

The electronic structure of a molecule determines its photonic and electronic properties. Electrons are distributed in a molecule according to their spatial

probability wavefunctions, and occupy discrete electronic energy levels. Each energy level has a corresponding molecular orbital and maximum of two electrons can be distributed to the same molecular orbitals with opposite spin. Photonic properties of an organic molecule originate from the transition of electrons between these molecular orbitals, and involve the exchange of some form of energy with the environment, e.g., absorption or emission of photons, interaction with a phonon, etc.

Molecular orbital concepts also enter in the description of chemical bonding schemes. A simple molecular orbital bonding scheme, showing a transition between energy levels that could couple to photonic excitations is illustrated in the Figure 1-11 for an ethene molecule.[60] The σ–bond is the most stable molecular orbital. It has the lowest energy in the molecular orbital scheme. The π-bond is significantly weaker than the σ–bonds and has a higher energy level. The next higher energy levels are the anti bonding π^* orbital and then σ^* orbital. The electrons of the molecule occupy these molecular orbitals according to a set of physical principles, such as maximum of two electrons per orbital, lowest energy orbitals must first be occupied, etc. The highest occupied molecular orbital (HOMO) is the orbital that accommodates the last electron of the molecule. In ethene molecule, the HOMO is the π orbital of this molecule. The lowest unoccupied molecular orbital (LUMO) is the empty orbital corresponding to the next higher energy level above the HOMO. In this ethene molecule, it is the

π orbital. Photonic excitation thus can promote the electron from the HOMO to the LUMO, where the necessary energy is gained by absorbing a photon. Upon the reverse transition, the electron in the LUMO releases energy to create photon or a phonon. The energy difference between HOMO and LUMO is called HOMO-LUMO energy gap, and is considered a principal characteristic of an organic semiconductor molecule. Organic semiconductor molecules usually have a low HOMO-LUMO gap between 0.7 to 3 eV.

There are many molecular energy levels for transitions of electrons besides the HOMO and LUMO in a molecule. A more complete energy level scheme of an organic molecule is shown in Figure 1-13. Due to the weak electron delocalization in molecular organic semiconductors, the spin states of a pair of electrons before and after a transition can be either the same or opposite. Depending on the total spin of the two electrons, the electron excitation or exciton can be categorized as a singlet or triplet, illustrated on the left hand and right hand sides of Figure 1-13, respectively. Short bold arrows in the boxes denote the spin states of the electrons. Transitions of electrons are denoted with long arrows pointing between the respective energy levels. Solid line arrows indicate transitions involving release or absorption of photons; broken line arrows indicate transitions in which energy is exchanged with phonons. The photo-physical phenomena of fluorescence and phosphorescence are distinguished based on whether electron transitions involve singlets or triplets.

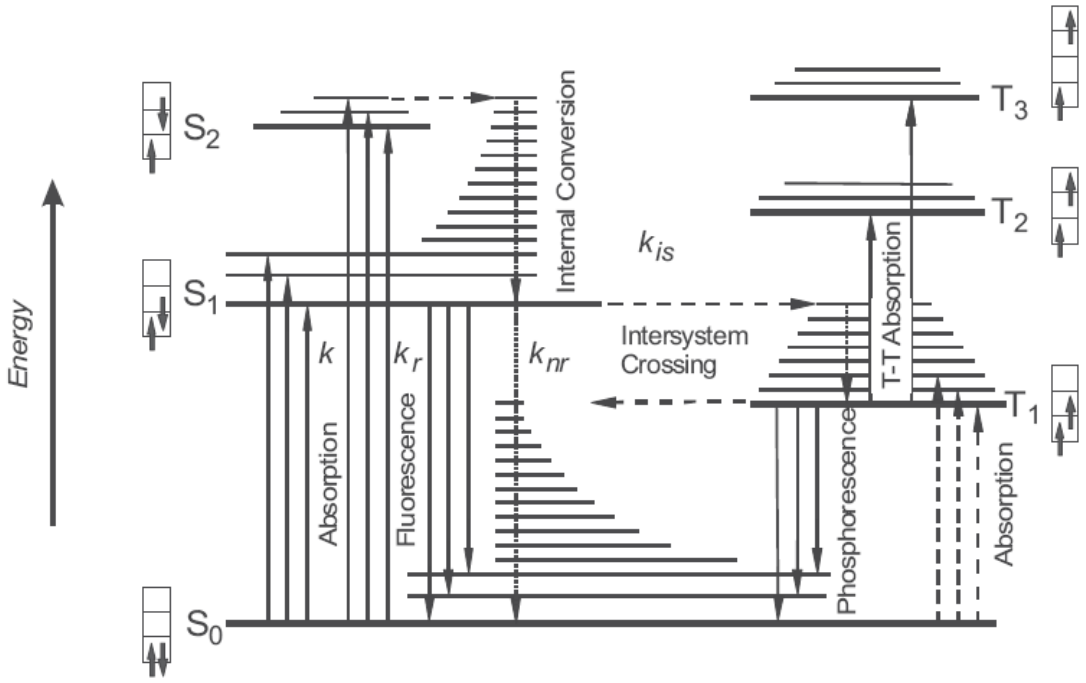

Figure 1-13 Optical properties of an organic molecule (Left part shows singlet and right part shows triplet energy levels) (figure adapted from [60])

1.2.2.2 Photonic and electronic properties of molecular crystals, and amorphous solids

Molecular solids of organic semiconductors are formed by the assembly of individual molecules. In the resulting structures, the intramolecular delocalization of electrons is typically strong, while intermolecular delocalization is weak. Therefore, the photonic and electronic properties of molecular solids, either in a crystalline or amorphous form, retain certain similarities with those of the individual molecules they are derived from. For example, the optical absorption and luminescence energy peak positions in the spectra of molecular organic solids are very close to those in the spectra of individual molecules in the gas or liquid phase, as shown in Figure 1-14.

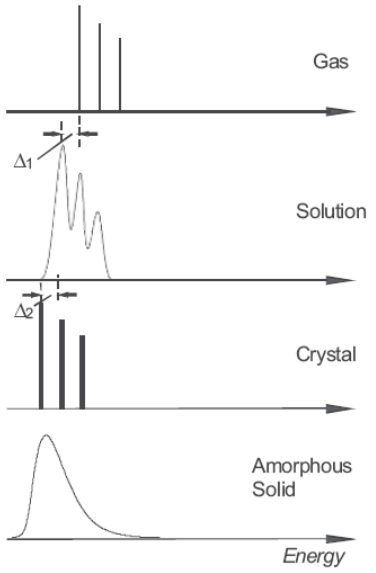

Figure 1-14 General experimental measured optical energy spectra of organic molecules in different phases (Figure adapted from [60])

A closer examination of the orbital energy levels and band structures of organic semiconductors reveals that the peak position for a given transition in the condensed phases (crystalline or amorphous) is shifted towards lower energy compared to the isolated molecule. The shift results from the broadening of the distinct HOMO and LUMO energy levels of an individual molecule into the energy bands of the corresponding molecular crystal, which in turn requires a narrowing of the band gap. The scheme of energy levels of an individual molecule and band structures of its corresponding molecular crystal solid is shown in Figure 1-15. The left part of Figure 1-15 shows the energy level scheme for an individual molecule in the gas phase and the right part shows the energy band structure of a molecular crystal.

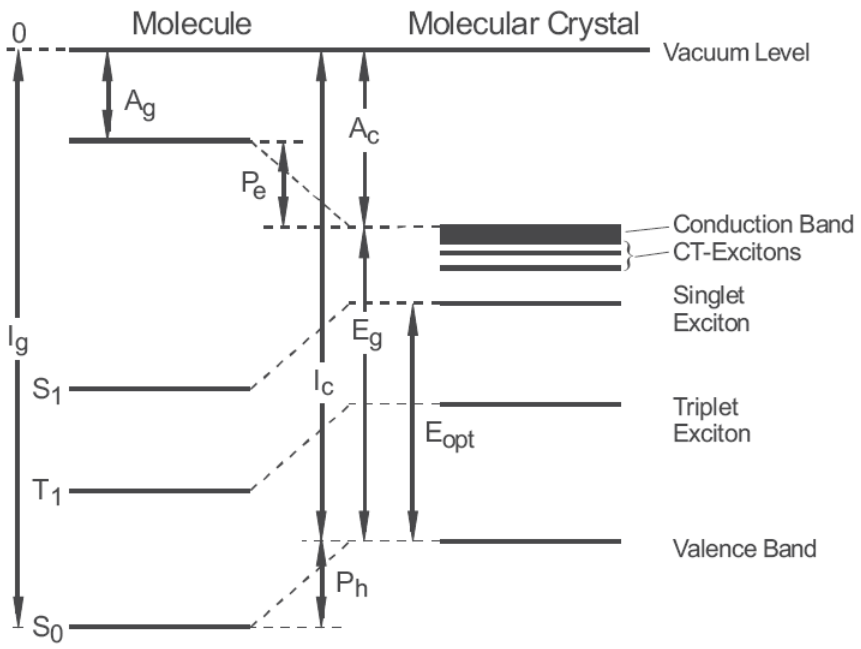

Figure 1-15 Energy levels of an isolated molecule and a corresponding molecular crystal (Figure adapted from [60])

The molecular energy levels can be calculated by solving the Schrödinger equation of the coupled system. Because of the lattice periodicity and symmetry in a molecular crystal, together with the large difference of the speed of electrons and nuclei, the Bloch theorem can be applied to such systems.[63]In this theorem, the periodic potential created by the nuclei can be considered as a perturbation to the general system Schrödinger equation. By introducing Bloch type wavefunctions, the system Schrödinger equation can then be solved with a much lower calculation load. As shown in Figure 1-15, what for the isolated molecule is referred to as ionization energy, I_g, and electron affinity, A_g, translates into I_c and A_c for the molecular crystal. I_g is larger than I_c by P_h, which is the polarization energy of holes. The upper valance band edge of the crystal is

higher than the molecular HOMO, S_0, by P_h. A_c is larger than A_g by P_e, which is the polarization energy of electrons. Therefore, the LUMO of the crystal is lower than the LUMO of the molecule by P_e. [60] The energy level splitting further decreases the lower edge of the conduction band. For all these reasons, the band gap E_g of a molecular crystal at the gamma point is typically smaller than the individual molecule's HOMO-LUMO energy gap. At the Brillouin zone boundaries along any reciprocal lattice vectors, the band gaps can be even smaller. The general energy level structure of a molecule and its crystal is shown in Figure 1-16.

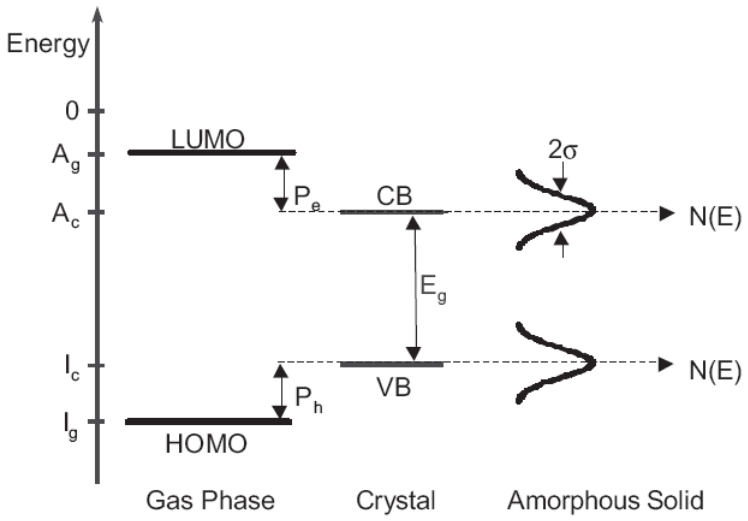

Figure 1-16 Energy levels of an isolated molecule, a molecular crystal and an amorphous solid (Figure adapted from [60])

The optical gap of molecular crystals, E_{opt} , shown in Figure 1-15 can be directly measured in absorption and luminescence experiments. It is smaller than the charge carrier band gap energy E_g, because the electron and hole of an exciton

pair are usually not from the same molecule. Therefore, the optical gap E_{opt} is larger than the singlet energy level difference, $S_1 - S_0$, in the same molecule. The energy of a singlet pair that originates within the same molecule is usually called the Frenkel exciton. The difference of $E_{opt} - (S_1 - S_0)$ is the exciton binding energy of the molecular system, as shown in Figure 1-17. Based on the Coulomb energy of an electron-hole pair with a distance around 10 nm in a molecular crystal and a dielectric constant of 3, the estimated binding energy is around 0.5 eV. [60]

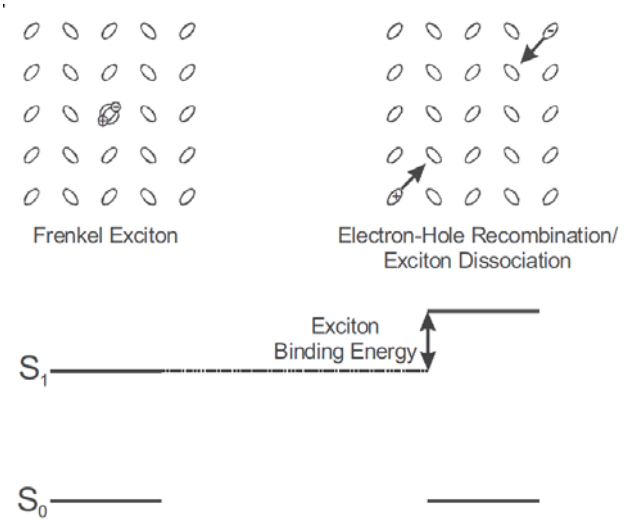

Figure 1-17 The Frenkel exciton and exciton binding energy of uncorrelated negative and positive carriers sitting on different molecules (figure adapted from [60])

1.2.3 Charge carrier transport properties

1.2.3.1 Conductivity and charge carrier mobility

The conductivity of a material can be expressed as

$$\sigma = ne\mu \ , \tag{1.1}$$

where n is the charge carrier density, e the unit electron charge, and μ the charge carrier mobility. The room temperature experimentally measured conductivities of select inorganic and organic materials (left hand side) are shown in Figure 1-18 (right hand side and left hand side, respectively).[59] Accordingly, the conductivity of organic materials can reach the same level of inorganic semiconductors, and some molecular organic semiconductors, such as pentacene and rubrene, reportedly have better performance than amorphous Si.[59,60]

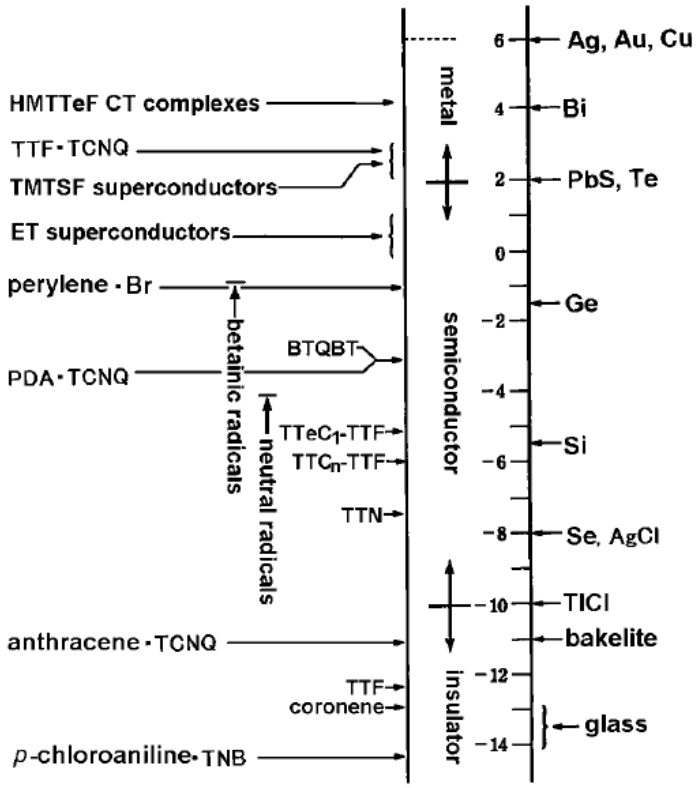

Figure 1-18 Conductivities (in units of $S \cdot cm^{-1}$) of typical organic semiconductors and inorganic semiconductors (Figure adapted from [59])

According to equation 1.1, the conductivity of a material is mainly determined by the charge carrier density and mobility. The charge carrier density is related to the band gap and temperature as

$$n \propto \exp(-\varepsilon_g / 2k_B T) \quad , \tag{1.2}$$

where ε_g is the band gap, T is temperature, and k_B is the Boltzmann constant. As discussed in the previous section, the band gap of a molecular crystal can be expected to be close but always somewhat smaller than the HOMO-LUMO gap of the corresponding isolated molecule. As illustrated in Figure 1-19, for a molecular solid the crystal band gap ε_g and the HOMO-LUMO energy gap ΔE are related as

$$\varepsilon_g = \Delta E - 2(t_1 + t_2) \quad , \tag{1.3}$$

where $4t_1$ and $4t_2$ are the widths of valance band and conduction bands of the crystal.

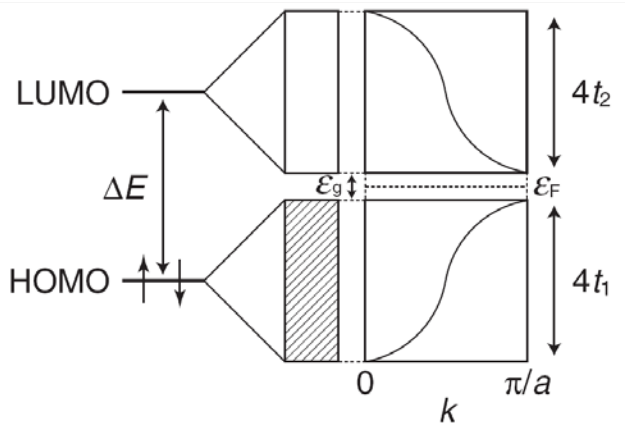

Figure 1-19 HOMO-LUMO gaps of organic molecule (left) and band gaps of molecular crystals (right) (Figure adapted from [59]), ΔE is the HOMO–LUMO gap of the molecule, $4t_1$ and $4t_2$ are the bandwidth of valance band and conduction band of the crystal, k is the wavevector, ε_F is Fermi energy

Based on equations 1.1 to 1.3, high carrier densities can be expected for systems with a small molecular HOMO-LUMO energy gap and large crystal bandwidth. To have higher carrier densities, a small HOMO-LUMO energy gap and large bandwidth are required for the molecular semiconductor. Ultimately, however, the charge carrier mobility in equation 1.1 is a more decisive variable, as it actually contains all the factors that control the transport of carriers. Even though mobility is one of the most studied subjects in molecular organic semiconductor, we expect that computational studies of molecular organic semiconductors can still advance our understanding of charge transport in these materials.

1.2.3.2 1D model of charge carrier mobility

Although the complete understanding of mobility is still an ongoing research topic, there are established models that can be used at this point. Charge carrier mobility can be best estimated using a 1D Holstein molecular model, which is based on the tight binding approximation.[59, 64] Accordingly, the total mobility of a material is given by

$$\mu = 2a^2 e\tau t \cos ka / \hbar^2 \propto \tau t \quad , \tag{1.4}$$

where a is intermolecular distance, τ is the electron relaxation time and t is the intermolecular transfer integral. The relaxation time is related to the electron scattering behavior of the system and depends on electronic density of states at the Fermi level and the square of the scattering potential V_s according to

$$\tau \propto \frac{1}{D(\varepsilon_F)\left|V_s\right|^2} = \frac{2\pi t \sin ka}{N\left|V_s\right|^2} \propto t \quad , \tag{1.5}$$

where N is total number of electrons in the band. τ is proportional to the bandwidth and transfer integral t, defined as

$$t = \left\langle \Psi_i \middle| \hat{\mathrm{H}} \middle| \Psi_j \right\rangle \propto S \quad , \tag{1.6}$$

where H is the system electronic Hamiltonian; Ψ_i and Ψ_j are the unperturbed HOMO or LUMO of the two individual molecules. (The transfer integral is proportional to the overlap integral S).[59] Therefore, to design high mobility

materials, the premium factors considered are low band gap and better overlap. If the constructed single molecule has small HOMO-LUMO energy gap and the predicted crystal structure has low band gap and features parallel packed organic conjugation, it can be expected that the designed molecular crystal will have better electronic properties.

1.2.4 Applications and expected improvements

There are three main applications for organic molecular semiconductors, organic light emitting diodes (OLED), organic photovoltaic cells (OPVC) and organic field-effect transistors (OFET), as shown in Figure 1-20.

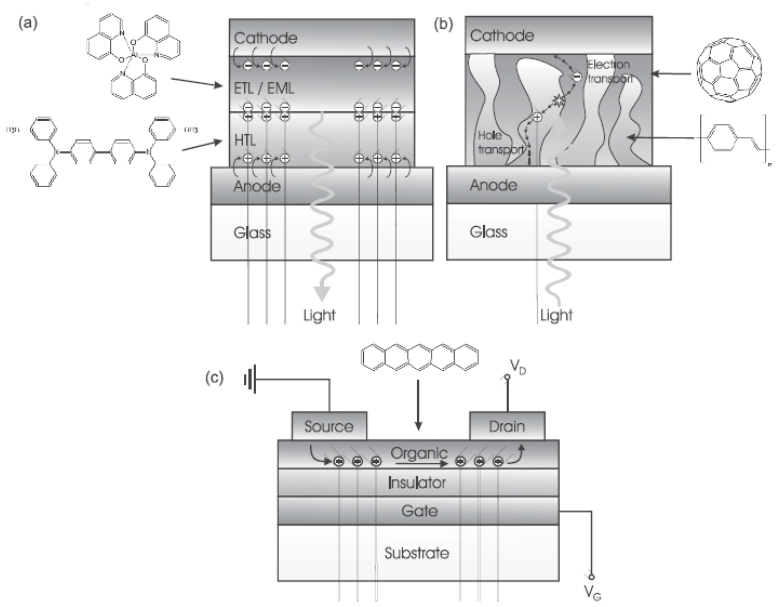

Figure 1-20 Different types of organic semiconductor devices are shown. (a) Organic light emitting diode (OLED), (b) Organic photovoltaic cell (OPVC) (c) Organic field-effect transistor (OFET) (figure adapted from [60])

The major benchmark is the quantum efficiency of the materials used in OLEDs.[110] Another important parameter is the exciton binding energy. These two material properties are also crucial in photovoltaic cells. Since SQ has been shown to increase EQE of incorporated polymers, similar benefit can be expected for other SQ incorporated molecular organic semiconductors. The exciton binding energy optimization, however, seems not related directly to incorporating SQ. As for the OFET, mobility is also a principal property for molecular organic semiconductors in an OFET. Therefore, SQ based new molecular organic-inorganic hybrid semiconductors seem to be potential good candidates with improved charge carrier transport and the quantum efficiency for OLEDs, OPVCs and OFETs.

Conventional fabrication methods for molecular semiconductors are gas phase evaporation and single crystal growing under strict atmospheric conditions.[115] In contrast, polymeric semiconductors can be solution processed, which is much cheaper. Difficult processing methods increase the cost of introducing molecular organic semiconductors into devices. Hence, the solution processablity of SQ molecules seem will offer low cost and advanced properties. Other known limitations of organic molecular semiconductors include, for example, insufficient current densities and light output, insufficient stability, high operating voltage due to the crystal thicknesses, difficulties in crystal growth scale up, and difficulties in making stable and sufficient contacts.[59] Despite

these drawbacks, the design and fabrication of crystalline molecular semiconductors are still a popular subject of ongoing research. This is because single crystal molecular semiconductors allow intrinsic electronic properties to be studied. It can be expected that high performance and low fabrication cost molecular crystalline semiconductors are desired for better applications, for example, flexible OLED displays, printed integrated circuits and low cost solar cells. [111-113]

1.3 Molecular Design for New Organic Semiconductor Materials

1.3.1 Molecular and building-block based crystal engineering

The advancement of synthetic methods and the ability to control processing conditions has allowed engineering the design of molecules and crystals for improved properties, such as molecular packing. In a recent study, naphthalimide was incorporated into the molecule as shown in Figures 1-21 to 1-23.[65] Upon crystallizing, the resulting molecule arranges so that the aromatic rings in the pyrazolyl groups stack parallel to each other, possibly providing for $\pi-\pi$ orbital overlap between them. This would likely result in better intermolecular charge transfer.[63] This is an example demonstrating a successful attempt for targeted molecular design via functionalization to control the self-assembly behavior of the molecular building block. This concept can be applied

broadly to molecular groups. Giving the strong tendency of T8 SQ cubes to assemble parallel to each other, it is interesting to explore SQ as an agent for controlling the self-assembly of organic molecular groups attached to the cube. Moreover, the unique inorganic character of the SQ cage may provide additional benefits as far as the properties of the resulting material are concerned.

Finally, with the continued increase in computer performance, much of the conception and testing tasks in the materials design cycle can be accomplished through computation, and it may be possible to narrow the selection of the molecular building blocks for a material with specific performance requirements to a subset of most promising candidates before synthesis is attempted in the laboratory.

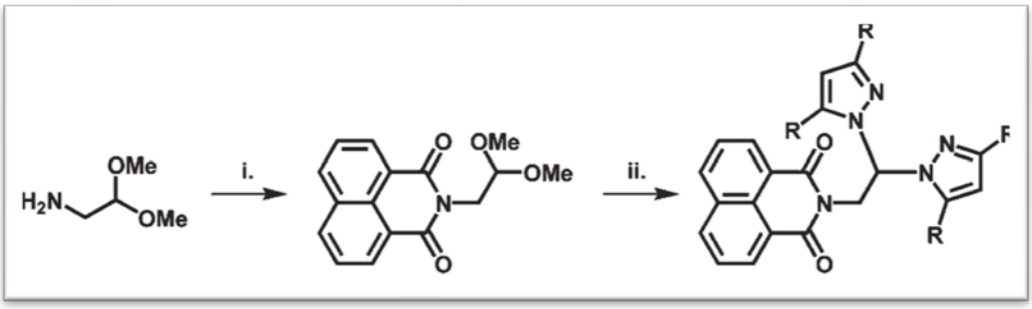

Figure 1-21 Synthetic route to N-[2,2-bis-(3,5-R-pyrazolyl)ethane]-1,8-naphthalimide, when R =H, L1; R = Me, L2 (Figure adapted from[65])

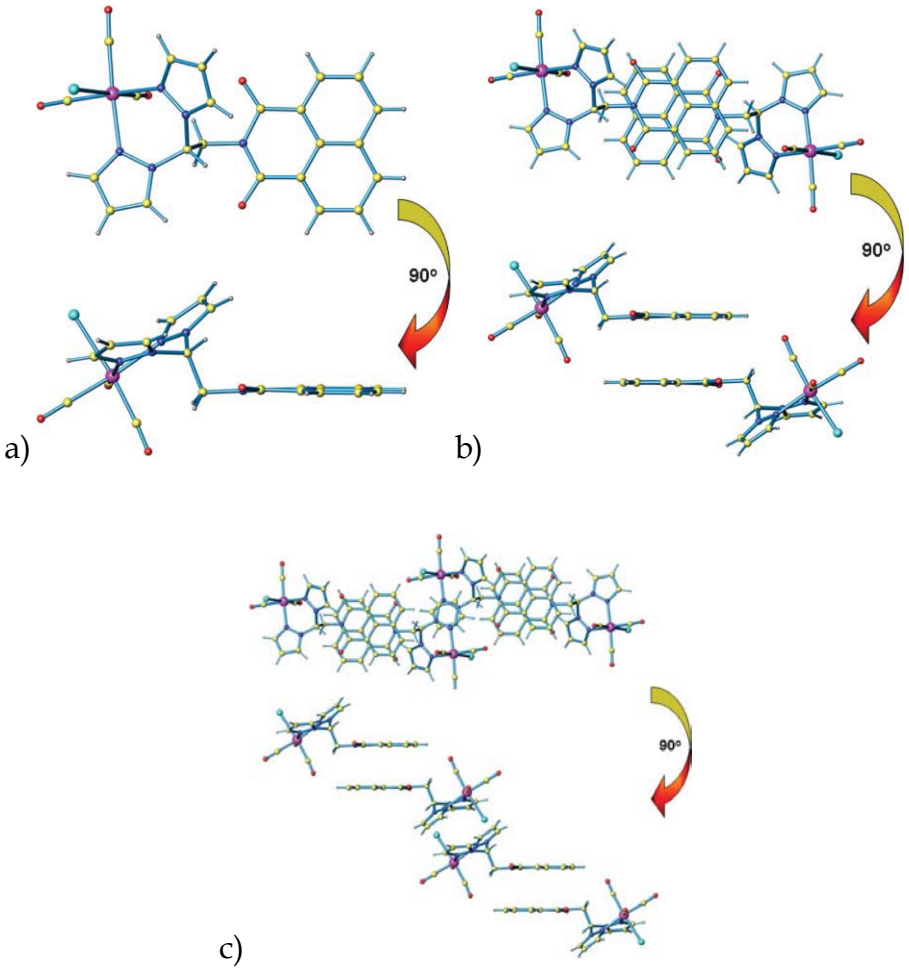

Figure 1-22 a) molecular structure of L1 a); b) π-π stacking for the pyrazolyl embrace in L1; c) crystalline packing of L1 (Figures adapted from [65])

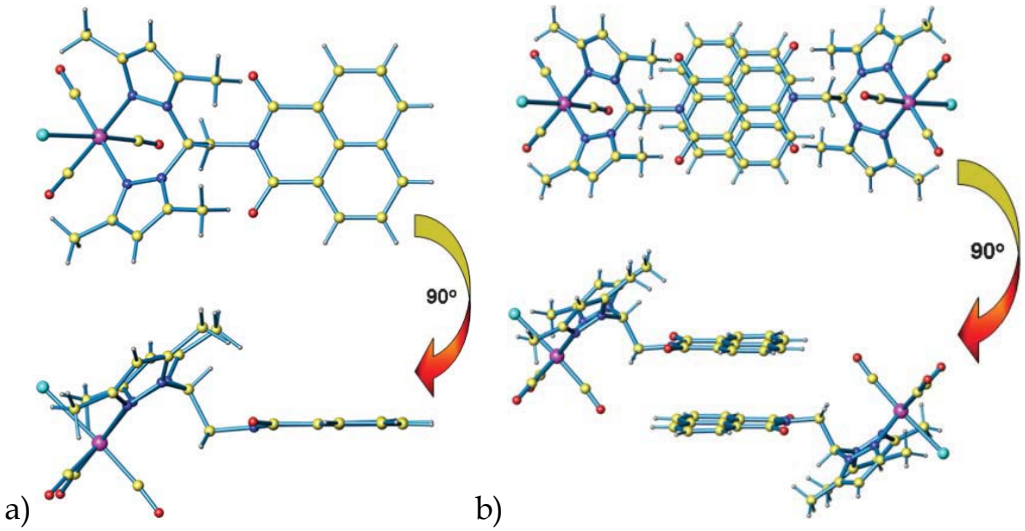

Figure 1-23 a) Molecular structure of L2; b) π-π stacking of L2 in a molecular solid (Figure adapted from [65])

1.3.2 Computational molecular design methods and strategy

With the fast development of science and technology, especially in energy and electronics related fields, a shortage of useful materials with certain performance requirements is now well recognized. Many kinds of new materials must be developed to meet these needs, for example, hydrogen storage nano composite materials, fuel cells, high performance and low fabrication cost organic semiconductors for OPVCs and OLEDs, high performance and low weight batteries for hybrid and electronic vehicles, etc. Almost all of these new applications involve quantum physics in characterizing the material performance and properties. Apparently, in such circumstances, given the high cost and limited ability in probing at the atomic level, a combined experimental and simulation development strategies are the key in developing new materials.

Computational materials design has emerged and developed rapidly as a subject of simulation based materials science in recent years, driven by demand. Among the applied simulation methods, density functional theory (DFT) based computational quantum mechanics framework is the most common method due to its efficiency and level of accuracy in solving the Schrödinger equation for the interested system, as well as the availability of current computing technologies, such as super and parallel computing. Therefore, it has been deployed as the main simulation method by many research groups including us, for example [66-70]

Hafner *et al*[71] suggests that applying DFT successfully to a materials design problem has the following stages: (1) identify the atomistic model that can be used to study an engineering problem, (2) obtain necessary physico-chemical properties from the calculation, and (3) verify the results by comparing to experimental work. In summary, DFT has been applied to help resolve the following questions: crystal structure prediction together with genetic algorithms [72,73]; mechanical properties such as elastic constants[74]; vibrational spectroscopy calculations via direct force-constant methods[75] or a linear response route [76]; surface and interface problems [77]; adsorption processes, reactions and catalysis [78,79]; spectroscopy[80-84]; magnetic properties [85]; electronic transport[86,87]; liquid and glasses[88].

There are several model methods that can be used to transfer results from DFT calculations to larger length and time scale as proven in experimental work. For

example, cluster-expansion methods [89,90] can be used to obtain configurational free energies of extended systems, including substitutional disorder in multicomponent systems. In these methods, representative lattice models are first calculated by DFT, then using the information extracted from these calculations, Monte Carlo simulations are performed to obtain temperature-composition phase diagrams, short-range order of disordered phases, interfacial free energies, and precipitate shapes, etc. The quasi-random structure approach can be used to directly calculate electronic and energetic properties of disordered systems by using small-unit-cell structures that studied from DFT. Both methods have been used successfully to predict structures and verified by experiments. [91] It can be summarized that DFT in these models is first used to obtain reliable pioneer quantities, such as free energies, diffusion constants, and interfacial energies, etc. Then these calculated quantities are applied to certain phase-field expansion models to further simulate microstructural properties in larger length scale. The embedding method is another example of expanding length scale, in which local quantum computations are used to continually tune the parameters of the force field, by which classical part of the problem is simulated.[92]

Recently, a first principle quantum mechanics computation based materials design approach was applied successfully by Siegel *et al* to discover novel hydrogen storage materials. [103] In predicting the crystal structures, database searching using the International Crystal Structures Database (ICSD) and lattice

algebra enumeration methods are used successfully. The presented examples illustrate that this computational approach has the capabilities of : (1) prediction of hybridization enthalpies and free energies across a wide range of hydride materials, (2) prediction of low energy crystal structures for complex hydrides, and (3) prediction of decomposition pathways for $Li_4BN_3H_{10}$ and destabilized systems based on combinations of $LiBH_4$, $Ca(BH_4)_2$ and metal hydrides. [103]

In other work, Ceder *et al* used first-principles quantum mechanics to successfully design Li battery electrode materials.[104] This group is implementing computational property prediction into the Materials Genome Project at the Massachusetts Institute of Technology. A high-throughput computational environment, featured with a coupled database of all known inorganic materials and a large number of novel "designed" materials, is being used to design more energy materials.[104] Goddard *et al* established a Computational Materials Design Facility (CMDF) at Caltech that can be used for complex materials. This facility coupled first principle quantum mechanics, the first principles ReaxFF reactive force field, empirical all atom force fields, and mesoscale or continuum methods.[105]

Computational materials design has been shown applied successfully to identify inorganic materials, such as hydrogen storages materials, Li batteries, etc. The successful computational design of SQ nano building block based molecular

semiconductor materials is a relatively new avenue due to large interest in developing these materials in polymeric forms.

Direct construction of a crystal is one way to develop new materials and is difficult. A practical way is to design the individual molecule first, then predict its crystal structure. One can use symmetry to decrease the number of possibilities given that molecular symmetry will affect the final crystal symmetry. There are two facts that aid. First, there are a limited number of 230 symmetry groups; second, among the 230 space groups, most of molecular organic crystal symmetries are featured with loose packing of small molecules in the unit cell due to symmetry operations, such as mirror planes and rotation axes, that generating large vacancies or gaps. Kitaigorodsky conducted a systematic study of space group symmetries of molecular organic crystals, and concluded that close-packing is possible in only 13 of the 230 space groups. This finding has been proved by the later experimental observation of around 30,000 molecular organic crystals. Mighell, Himes and Rodgers found that of 29059 experimental determined organic compounds crystal structures reported till 1981, 75% are among only five of the following space groups: $P\bar{1}$, $P2_1$, $P2_1/c$, $Pca2_1$, $Pna2_1$ and $P2_12_12_1$. These space groups features symmetry combinations of inversion centers, screw axes and glide planes that allow for close-packing in all three lattice directions. When the molecule has certain symmetry, for example, centrosymmetry, then the most probable crystal symmetry can be further

decreased to only three possibilities which are $P\bar{1}$, $P2_1/c$ and $Pbca$. [106-108] These findings provide us a practical way that successful molecular designs can be done with reasonable efforts.

When the molecular structure is determined, there are mainly two ways to predict its crystal structures:

1) Predict the packing and space group of the targeting molecule based on a polymorph prediction procedure involving Monte Carlo, symmetry operation and MD simulations
2) Modifying the experimental crystal coordination with a MD method

1.4 Objective and Outline

In this thesis, we propose to perform atomistic MD simulations and *ab inito* quantum mechanical calculations based on density functional theory to design and evaluate of novel SQ-based molecular semiconductors, by systematically exploring molecular architectures, including functional group types, sizes, symmetries, etc., and predicting their properties. This computational design is aimed at providing insight into the mechanisms that govern the electronic properties and structures of SQ-based molecules, and thereby provide valuable guiding information for the practical design and synthesis of novel SQ based hybrid materials.

The research approach pursued in this dissertation is to (i) develop and validate force fields for MD simulation of SQ molecules; (ii) use these and existing force fields in large-scale MD and Monte Carlo simulations to predict the most probable structures into which the molecules assemble; (iii) carry out quantum mechanical calculations to determine the thermodynamic stability of novel molecules and predict their inherent single-molecule electronic properties; (iv) verify the stability of predicted crystalline structures and calculate their electronic band structure using DFT calculations.

The major accomplishments include (i) the parameterization of the FLX force field, a reactive three body charge transfer force field, by which the interactions and packing behavior of bare SQ cubes can be studied, and simulations of T8 H-SQ crystals compared with other existing force field simulations, i.e. diacene tethered SQ molecular systems; (ii) molecular design and evaluations of semiconductor acene based SQ systems, which has controllable very small band gaps and parallel packing fashion in their molecular crystals; and (iii) the molecular design and analysis of semiconductor halogen-benzene SQ molecular crystals complementing ongoing experimental work.

This thesis is organized so as to detail the motivations for the research in Chapter1. Chapter 2 provides the theoretical methods, numerical recipes, and computational techniques for simulation-based molecular design. Chapter 3 describes the development and evaluation of force fields for atomistic

simulations of SQ crystals. Chapter 4 contains the details of a molecular design study of acene functionalized SQ. Chapter 5 describes the molecular design of halogen-benzene functionalized SQ systems. Chapter 6 summarizes the above chapters and provides an outlook into future works.

1.5 References

[1] Laine, R. M.; Roll, M. *et al.* Perfect and nearly perfect silsesquioxane (SQs) nanoconstruction sites and Janus SQs. *J. Sol-Gel Sci. Technol.***46,** 335-347 (2008)

[2] Baney, R. H. *et al*. Silsesquioxanes. *Chemical Reviews* **95**(5), 1409-1430 (1995)

[3] Lichtenhan, J. D. *et al*. Polyhedral oligomeric silsesquioxane (POSS)-based polymers. *Appl. Organometal. Chem.* **12**, 707-713 (1998)

[4] Leu, C. *et al*. Synthesis and dielectric properties of polyimide-chain-end tethered polyhedral oligomeric silsesquioxane nanocomposites. *Chem. Mater.* **15**, 2261-2265 (2003)

[5] Carroll, J. B. *et al*. "Plug and play" polymers. Thermal and X-ray characterization of noncovalently silsesquioxane (POSS) – polystyrene nanocomposites. *Marocomolecules* **36**, 6289-6291(2003)

[6] Shea, K. J.; Loy, D. A. Bridged polysilsesquioxanes. Molecular-engineered hybrid organic-inorganic materials. *Chem. Mater*. **13,** 3306-3319 (2001)

[7] Bolln, C.; Tsuchida, A. Thermal properties of the homologous series of 8-fold alkyl-substituted octasilsesquioxane. *Chem. Mater.* **9**, 1475-1479 *(*1997)

[8] Tamaki, R. *et al*. A Polyimide nanocomposite from octa(aminophenyl)silsesquioxane. *Chem. Mater.* **15**, 793-797 (2003)

[9] Abad, M. J. *et al*. Epoxy networks containing large mass fractions of a monofunctional polyhedral oligomeric silsesquioxane (POSS). *Macromolecules* **36**, 3128-3135 (2003)

[10] Lucke, S.; Stoppek-Langner, K. Polyhedral oligosilsesquioxanes (POSS)-building blocks for the development of nano-structured materials. *Applied Surface Science* **144-145**, 713-715 (1999)

[11] Shockey, E. G.; Bolf, A. G. Functionalized polyhedral oligosilsesquioxane (POSS) macromers: new graftable POSS hydride, POSSS α-olefin, POSS epoxy, and POSS chlorosilane macromers and POSS-siloxane triblock. *Appl. Organometal. Chem.* **13**, 311-327 (1999)

[12] Pyun, J., *et al.* ABA triblock copolymers containing polyhedral oligomeric silsesquioxane pendant groups: synthesis and unique properties. *Polymer* **44**, 2739-2750 (2003)

[13] Zhang, C. X. *et al*. Highly porous polyhedral silsesquioxane polymers. Synthesis and characterization. *Journal of the American Chemical Society* **120**, 8380-8391 (1998)

[14] Kim, B. S.; Mather, P.T. Amphiphilic telechelics incorporating polyhedral oligosilsesquioxane: 1 syntheses and characterization. *Macromolecules* **35**, 8378-8384 (2002)

[15] Laine, R. M.; Choi, J.; Lee, I. Organic-inorganic nanocomposites with completely defined interfacial interactions. *Advanced Materials* **13**, (11), 800-803 (2001)

[16] Larsson, K. The crystal structure of Octa-(silsesquioxane) $(HSiO_{1.5})_8$. *Arkiv for kemi band* **16**, nr 17, 205 (1960)

[17] Törnroos, K. W. Octahydridosilasesquioxane determined by neutron diffraction. *Acta Crystallogr*. **C50**, 1646-1648 (1994)

[18] Handke, B.; Jastrzebski, W. *et al.* Structural studies of crystalline octamethylsilsesquioxane $(CH_3)_8Si_8O_{12}$. *Journal of Molecular Structure* **887** 159-164 (2008)

[19] Calzaferri, G.; Imhof, R.; Törnroos, K. W. Structural and vibrational properties of the octanuclear silasesquioxane $C_6H_{13}(H_7Si_8O_{12})$. *Journal of the Chemical Society-Dalton Transactions* **21**, 3123-3128 (1994)

[20] Waddon, A. J.; Coughlin, E. B. Crystal structure of polyhedral oligomeric silsesquioxane (POSS) nano-materials: a study by X-ray diffraction and electron microscopy. *Chem. Mater.* **15**, 4555-4561 (2003)

[21] Ulrich, R.; Chesne, A.D., Nano-objects with controlled shape, size, and composition from block copolymer mesophases. *Advanced Materials* **11**, 141-146 (1999)

[22] Klok, H.; Lecommandoux, S. Supramolecular materials via block copolymer self-assembly. *Advanced Materials,* **13**, 1217-1229 (2001)

[23] Moel,k.; Ekenstein, A. *et al*. Polymeric nanofibers prepared from self-organized supramolecules. *Chem. Mater.* **13**, 4580-4583 (2001)

[24] Zheng, L.; Farris, R. J. *et al*. Synthesis of polyethylene hybrid copolymers containing polyhedral oligomeric silsesquioxane prepared with ring opening metathesis copolymerization. *Journal of Polymer Science Part A: Polymer Chemistry* **39**, 2920-2928 (2001)

[25] Li, G. Z. *et al*. Viscoelastic and mechanical properties of vinyl ester (VE)/multifunctional polyhedral oligomeric silsesquioxane (POSS) nanocomposites and multifunctional POSS-styrene copolymers. *Polymer* **43**, 4167-4176 (2002)

[26] Fu, B. X. *et al*. Physical gelation in ethylene-propylene copolymer melts induced by polyhedral oligomeric silsesquioxane (POSS) molecules. *Polymer* **44**, 1499-1506 (2003)

[27] Lin, W. J.; Chen, W. C. Synthesis and characterization of polyimide/oligomeric methylsilsesquioxane hybrid films. *Polymer International* **53**, 1245-1252 (2004)

[28] Wright, M. E. *et al*. Chemical modification of fluorinated polyimides: New thermally curing hybrid polymers with POSS. *Macromolecules* **39,** 4710-4718 (2006)

[29] Cordes, D. B. *et al*. Recent developments in the chemistry of cubic polyhedral oligosilsesquioxanes. *Chem. Rev.* **110**, 2081-2173 (2010)

[30] Arrais, A. *et al.* The reactions of two new alkoxy-silyl functionalized alkynes with $M_3(CO)_{12}$ {M = Fe, Ru} and $Co_2(CO)_8$. Spectroscopic identification of the products. *Journal of Cluster Science* **18**, 535-548 (2007)

[31] Toh, C. L. *et al.* Packing behaviors of structurally different polyhedral oligomeric silsesquioxane-imidazolium surfactants in clay. *J. Phys. Chem. B* **114**, 207-214 (2010)

[32] Sellinger, A. *et al.* Palladium- and platinum-catalyzed coupling reactions of allyloxy aromatics with hydridosilanes and hydridosiloxanes: novel liquid crystalline/organosilane materials. *Journal of Polymer Science Part A: Polymer Chemistry* **32**, 3069-3089 (1994)

[33] Shin, S. B. *et al.* Properties of polymer light-emitting diodes coated on surface-treated ITO/glass substrates. *Journal of Applied Polymer Science* **110**, 3678-3682 (2008)

[34] Andre, P. *et al.* Hybrid dendritic molecules with confined chromophore architecture to tune fluorescence efficiency. *J. Phys. Chem. B* **112**, 16382-16392 (2008)

[35] Cui, Y. *et al.* Preparation and second-order optical nonlinearity of inorganic organic hybrid films. Journal of Non-crystalline solids **354**, 1211-1215 (2008)

[36] Su, X. *et al.* Controllable preparation and optical limiting properties of poss-based functional hybrid nanocomposites with different molecular architectures. *Macromolecules* **42**, 8969-8976 (2009)

[37] Costela, A. *et al.* Dye-doped POSS solutions: random nanomaterials for laser emission. *Advanced Materials* **21**, 4163-4166 (2009)

[38] Douvas, A. M. *et al.* Partially fluorinated, polyhedral oligomeric silsesquioxane-functionalized (meth)acrylate resists for 193 nm bilayer lithography. *Chem. Mater.* **18**, 4040-4048 (2006)

[39] Hartmann-Thompson, C. *et al.* One- and two-photon fluorescent polyhedral oligosilsesquioxane(POSS) nanosensor arrays for the remote detection of analytes inclouds, in solution, and on surfaces. *Chem. Mater.*, **20**, 2829–2838 (2008)

[40] Hartmann-Thompson1, C. *et al.* Proton-conducting polyhedral oligosilsesquioxane nanoadditives for sulfonated polyphenylsulfone hydrogen fuel cell proton exchange membranes. *Journal of Applied Polymer Science* **110**, 958-974 (2008)

[41] Zhang, H. *et al.* Blends of POSS−PEO$(n=4)_8$ and high molecular weight poly(ethylene oxide) as solid polymer electrolytes for lithium batteries. *J. Phys. Chem. B* **111**, 3583–3590 (2007)

[42] DARE, E. O. Synthesis of some new functionalized octasilsesquioxane hybrid nanoclusters. III. Potential of the octameric clusters as hydraulic lubricating fluids. *Turkish Journal of Chemistry* **30**, 585-593 (2006)

[43] Xiang, K. H.; Pandey, R.; Pernisz, U. C.; Freeman, C. Theoretical study of structural and electronic properties of H-silsesquioxanes. *J. Phys. Chem. B*, **102**, 8704-8711 (1998)

[44] (a) Calzaferri, G. *et al*. Infrared and Raman spectra of octa(hydridosilasesquioxanes). *Spectrochimica Acta* **47A**, (11), 1627-1629 (1991); (b) Calzaferri, G. *et al*. ATR-FTIR experiments with $R_8[Si_8O_{12}]$ on Ge and ZnSe. *Journal of Electron Spectroscopy and Related Phenomena,* **44,** 121-130 (1987); (c) Calzaferri, G. *et al*., Vibrations of $H_8Si_8O_{12}$, $D_8Si_8O_{12}$ and $H_{10}Si_{10}O_{15}$ as determined by INS, IR, and Raman experiments. *J. Phys. Chem. B* **101**, 1171-1179 (1997)

[45] Cheng, W. D.; Xiang, K. H.; Pandey, R.; Pernisz, U. C. Calculations of linear and nonlinear optical properties of h-silsesquioxanes *J. Phys. Chem. B* **104**, 6737-6742 (2000)

[46] Bharadwaj, R.K.; Berry, R. J.; Farmer, B.L. Molecular dynamics simulation study of norbornene-POSS polymers. *Polymer* **41**, (19), 7209-7221 (2000)

[47] Lamm, M. H.; T. Chen; Glotzer, S. C. Simulated assembly of nanostructured organic/inorganic networks. *Nano Letters* **3**, (8), 989-994 (2003)

[48] Laine, R. M.; Sulaiman, S.; Brick, C.; Roll, M. Tamaki, R.; Asuncion, M. Z.; Neurock, M.; Filhol, J.-S.; Lee, C.-Y.; Zhang, J.; Goodson III, T.; Ronchi, M.; Pizzotti, M.; Rand, S. C.; Li, Y. Synthesis and photophysical properties of stilbeneoctasilsesquioxane. Emission behavior coupled with theoretical modeling studies suggest a 3-D excited state involving the silica core. *J. Am. Chem. Soc.* **132**, 3708–3722 (2010)

[49] Schutte, C. J. H.; Pretorius, J. A. Computational study of the molecular and crystal structure and selected physical properties of octahydridosilasequioxane-$(Si_2O_3H_2)_4$ I. Electronic and structural aspects. *Proc. R. Soc. A* **467**, 928-953 (2011)

[50] Durandurdu, M.; Kieffer, J. unpublished results.

[51] Sancho-García, J. C.; Pérez-Jiménez, A. J.; Olivier, Y.; Cornil, J. Molecular packing and charge transport parameters in crystalline organic semiconductors from first-principles calculations. *Phys. Chem. Chem. Phys.* **12**, 9381–9388 (2010)

[52] Anthony, J. E.; Brooks, J. S.; Eaton, D. L.; Parkin, S. R. Functionalized pentacene: improved electronic properties from control of solid-state order. *J. Am. Chem. Soc.* **123**, 9482 - 9483 (2001)

[53] Anthony, J. E. *et al*. Functionalized acenes and heteroacenes for organic electronics. *Chem. Rev. Vol.* **106**, 5028 - 5048 (2006)

[54] Salman, S.; Ruiz-Delgado, M.-C.; Coropceanu, V. ; Bre´das, J.-L. Electronic structure and charge-transport parameters of functionalized tetracene crystals: Impact of partial fluorination and alkyl or alkoxy derivatization. *Chem. Mater.* **21**, 3593-3601 (2009)

[55] Dunitz, J. D.; Gavezzotti, A. Molecular pair analysis: C-H...F interactions in the crystal structure of fluorobenzene and related matters. *Chem. Eur. J.* **12**, 6804 (2006)

[56] Dunitz, J. D.; Gavezzotti, How molecules stick together in organic crystals: weak intermolecular interactions. *Chemical Society Reviews* **38**, 2622-2633 (2009)

[57] Chi, X.; Li, Zhang, D.H. *et al.* 5,6,11,12-Tetrachlorotetracene, a tetracene derivative with pi-stacking structure: The synthesis, crystal structure and transistor properties. *Org. Electron.* **9**, 234-240 (2008)

[58] Deng, W.-Q.; Goddard III, W. A. Predictions of hole mobilities in oligoacene organic semiconductors from quantum mechanical calculations. *J. Phys. Chem. B*, **108**, 8614-8621 (2004)

[59] Saito, G.; Yoshida, Y. Development of conductive organic molecular assemblies: organic metals, superconductors, and exotic functional materials. *Bull. Chem. Soc. Jpn*. **80**, No. 1, 1–137 (2007)

[60] Brütting, W. *Physics of organic semiconductors* WILEY-VCH Verlag GmbH & Co., KGaA, Weinheim (2005)

[61] Li, A.; Deng, W.-Q. *et al.* Synthesis of cyanated tetracenes as the organic semiconductors. *Org. Electron.* **10**, 1054-1059 (2009)

[62] Katsuta, S. *et al*. Synthesis, properties, and ambipolar organic field-effect transistor performances of symmetrically cyanated pentacene and naphthalene as air-stable acene derivatives. *Org. Lett.* **13**, 1454–1457 (2011)

[63] (a) Bloch, F. Über die quantenmechanik der elektronen in kristallgittern. **Z.** Physik. **52**, 555–600 (1928); (b) Kittel, C. *Introduction to Solid State Physics, 7th ed.* Wiley, New York (1996)

[64] (a) Holstein, T. Studies of polaron motion .1. the molecular-crystal model. *Annals of Physics* **8**, 325-342 (1959); (b) Holstein, T. Studies of polaron motion .2. the small polaron. *Annals of Physics* **8**, 343-389 (1959)

[65] Reger, D. L.; Elgin, J.D.; Semeniuc, R. F.; Pellechia, P. J.; Smith, M. D. Directional control of p-stacked building blocks for crystal engineering: the 1,8-naphthalimide synthon. *Chem. Commun*. **2005**, 4068–4070 (2005)

[66] Energy storage and materials simulation lab, University of Michigan, - Ann Arbor, http://www-personal.umich.edu/ ~djsiege/ Energy_ Storage _Lab/ESMS_Lab_Home.html

[67] Computational and experimental design of emerging materials research group (CEDER), Massachusetts Institute of Technology, http://burgaz.mit.edu/

[68] Center for computational materials, the University of Texas, Austin, http://users.ices.utexas.edu/~jrc/

[69] Louie research group, University of California, Berkeley, http://civet.berkeley.edu/louie/

[70] Materials and process simulation center, California Institute of Technology, Pasadena, http://www.wag.caltech.edu/

[71] Hafner, J.; Wolverton, C.; Ceder, G. *et al*. Toward computational materials design: the impact of density functional theory on materials research. *MRS Bulletin* **31,** 659-665 (2006)

[72] Deaven, D. M.; Ho, K. M. Molecular-geometry optimization with a genetic algorithm. *Phys. Rev. Lett.* **75,** 288-291 (1995)

[73] Oganov, A. R.; Glass, C. W.; Ono, S. High-pressure phases of $CaCO_3$: Crystal structure prediction and experiment. *Earth Planet. Sci. Lett.* **241,** 95 (2006)

[74] Le Page, Y. ; Saxe, P. Symmetry-general least-squares extraction of elastic coefficients from *ab initio* total energy calculations. *Phys. Rev. B* **63,** 174103 (2001)

[75] Kresse, G.; Furthmüller, J.; Hafner, J. A*b initio* force constant approach to phonon dispersion relations of diamond and graphite. J. *Europhys. Lett.* **32**, 729-734 (1995)

[76] Giannozzi, P.; de Gironcoli, S.; Pavone, P.; Baroni, S. *ab initio* calculation of phonon dispersions in semiconductors. *Phys. Rev. B* **43**, 7231-7242 (1991)

[77] Kresse, G.; Schmid, M.; Napetschnig, E.; Shishkin, M.; Köhler, L.; Varga, P. Structure of the ultrathin aluminum oxide film on NiAl(110). *Science* **308**, 1440-1442 (2005)

[78] Hammer, B. Special sites at noble and late transition metal catalysts. *Top. Catal.* **37**, 3-16 (2006)

[79] Hafner, J.; Benco, L.; Bucko, Acid-based catalysis in zeolites investigated by density-functional methods. T. *Top. Catal.* **37**, 41-54 (2006)

[80] Gajdos, M.; Hummer, K.; Kresse, G.; Furthmüller, J.; Bechstedt, F. Linear optical properties in the projector-augmented wave methodology. *Phys. Rev. B* **73**, 045112 (2006)

[81] Vanderbilt, D. First-principles theory of polarization and electric fields in ferroelectrics. *Ferroelectrics* **301**, 9-14 (2004)

[82] Hamann, D. R.; Rabe, K. M; Vanderbilt, D. Generalized-gradient-functional treatment of strain in density-functional perturbation theory. *Phys. Rev. B* **72**, 033102 (2005)

[83] Pickard, C. J.; Mauri, F. All-electron magnetic response with pseudopotentials: NMR chemical shifts. *Phys. Rev. B* **63**, 245101 (2001).

[84] Hofer, W. A.; Foster, A. S.; Shluger, A. L. Theories of scanning probe microscopes at the atomic scale. *Rev. Mod. Phys.* **75**, 1287-1331 (2003)

[85] Hobbs, D.; Kresse, G.; Hafner, J. Fully unconstrained noncollinear magnetism within the projector augmented-wave method. *Phys. Rev. B* **62**, 11556-11570 (2000)

[86] Kudrnovsky, J.; Drchal, V.; Blaas, C.; Weinberger, P.; Truek, I.; Bruno, P. *Ab initio* theory of perpendicular magnetotransport in metallic multilayers. *Phys. Rev. B* **62**, 15084-15095 (2000)

[87] Stokbro, K.; Taylor, J.; Brandbyge, M.; Ordejon, P. TranSIESTA - A spice for molecular electronics. *Ann. N.Y. Acad. Sci.* **1006**, 212-226 (2003)

[88] Sheng, H. W.; Luo, W. K.; Alamgir, F. M.; Bai, J. M.; Ma, E. Atomic packing and short-to-medium-range order in metallic glasses. *Nature* **439**, 419-425 (2006)

[89] de Fontaine, D. *Solid State Physics*, **47**, edited by Ehrenreich, H; Turnbull, D. Academic Press, New York, 33, (1994)

[90] Wang, J. W.; Wolverton, C.; Müller, S.; Liu, Z. K.; Chen, L. Q. First-principles growth kinetics and morphological evolution of Cu nanoscale particles in Al. *Acta Mater.* **53**, 2759 (2005)

[91] Ceder, G. Computational materials science - Predicting properties from scratch. *Science* **280**, 1099-1100 (1998)

[92] Csanyi, G.; Albaret, T.; Payne, M. C.; De Vita, A. "Learn on the fly": A hybrid classical and quantum-mechanical molecular dynamics simulation. *Phys. Rev. Lett.* **93**, 175503 (2004)

[93] Hao, S.; Liu, W. K.; Moran, B.; Vernery, F.; Olson, G. B. Multi-scale constitutive model and computational framework for the design of ultra-high strength, high toughness steels. *Computer Methods in Appl. Mechan.Eng.* **193**, 1865-1908 (2004)

[94] Wolverton, C.; Yan, X.-Y.; Vijayaraghavan, R.; Ozolins, V. Incorporating first-principles energetics in computational thermodynamics approaches. *Acta Mater.* **50** 2187 (2002)

[95] Vaithyanathan, V.; Wolverton, C.; Chen, L. Q. Multiscale modeling of theta ' precipitation in Al-Cu binary alloys. *Acta Mater.* **52**, 2973 (2004)

[96] Mokaya, R.; Poliakoff, M. Chemistry - A cleaner way to nylon? *Nature* **437**, 1243-1244 (2005)

[97] Bucko, T.; Hafner, J.; Benco, L. Active sites for the vapor phase Beckmann rearrangement over mordenite: An *ab initio* study. *J. Phys. Chem. A* **108**, 11388-11397 (2004)

[98] Burkert, T.; Nordström, L.; Eriksson, O.; Heinonen, O. Giant magnetic anisotropy in tetragonal FeCo alloys. *Phys. Rev. Lett.* **93**, 27203 (2004)

[99] Andersson, G.; Burkert, T.; Warnicke, P.; Björck, M.; Sanyal, B.; Chacon, C.; Zlotea, C.; Nordström, L.; Nordblad, P.; Eriksson, O. Perpendicular magnetocrystalline anisotropy in tetragonally distorted Fe-Co alloys. *Phys. Rev. Lett.* **96**, 037205 (2006)

[100] Böhringer, M.; Morgenstern, K.; Schneider, W. D.; Berndt, R.; Mauri, F.; De Vita, A.; Car, R. Two-dimensional self-assembly of supramolecular clusters and chains. *Phys. Rev. Lett.* **83**, 324 (1999)

[101] Sugihara, M.; Buss, V.; Entel, P.; Hafner, J. The nature of the complex counterion of the chromophore in rhodopsin. *J. Phys. Chem. B* **108**, 3673 (2004)

[102] Röhrig, U. F.; Guidoni, L.; Röthlisberger, U. Solvent and protein effects on the structure and dynamics of the rhodopsin chromophore. *Chem. Phys. Chem.* **6**, 1836 (2005)

[103] Wolverton, C.; Siegel, D. J.; Akbarzadeh, A. R.; Ozoliņš, V. Discovery of novel hydrogen storage materials: an atomic scale computational approach. *J. Phys.: Condens. Matter* **20,** 064228 (2008)

[104] Ceder, G. Opportunities and challenges for first-principles materials design and applications to Li battery materials. *MRS Bulletin* **35**, 693-701 (2010)

[105] Buehler, M. J.; Dodson,J.; van Duin, A. C. T.; Meulbroek, P.; Goddard III, W. A. The computational materials design facility (CMDF): A powerful framework for multiparadigm multi-scale simulations. *Mat. Res. Soc.*

Proceedings (Combinatorial Methods and Informatics in Materials Science) **894**, LL3.8, (2006)

[106] Simon, J.; Bassoul, P. *Design of Molecular Materials: Supramolecular Engineering* John Wiley&Sons LTD, Chichester (2000)

[107] Chaka, A. M.; Zaniewski, R.; Youngs, W.; Tessier, C.; Klopman, G. Predicting the crystal structure of organic molecular materials. *Acta Cryst.* **B52**, 165-183 (1996)

[108] Leach, A. R. *Molecular modelling : principles and applications, 2nd edition* Prentice Hall: Harlow, England ; New York (2001)

[109] Bragg, W. H. *Proc. Phys. Soc. London* **35**, 167-169 (1923)

[110] Chan, K. L.; Sonar, P; Sellinger, A. Cubic silsesquioxanes for use in solution processable organic light emitting diodes (OLED). *J. Mater. Chem.***19**, 9103–9120 (2009)

[111] Sirringhaus, H. *Advanced Materials* **17**, 2411 (2005)

[112] Sirringhaus, H.; Kawase, T.; Friend, R. H.; Shimoda, T.; Inbasekaran, M.; Wu, W.; Woo, E. P. *Science* **290**, 2123. (2000)

[113] Baldo, M. A.; Thompson, M. E.; Forrest, S. R. *Nature* **403**, 750 (2000)

[114] Sun, Y. R.; Giebink, N. C.; Kanno, H.; Ma, B. W.; Thompson, M. E.; Forrest, S. R. *Nature* **440**, 908 (2006)

[115] Forrest, S. R. The path to ubiquitous and low-cost organic electronic appliances on plastic. *Nature* **428**, 911 (2004)

Chapter 2
Theoretical Methods, Numerical Recipes and Computing Techniques for Computational Molecular Design and Engineering

2.1 Introduction

For the computational molecular design of SQ-based hybrid semiconductors we use mainly *ab initio* quantum mechanical calculations based on the density functional theory (DFT) and explicit-atom molecular dynamics (MD) simulations. Combining these methods we explore and evaluate molecular and crystal structures that exhibit the major desired semiconductor properties, such as small band gaps and spatial molecular orbital overlap in crystal packing, etc. To properly interpret and use the results of such multi-scale and multi-method simulations, it is important to be aware of the capabilities and limitations of these computational techniques. In this chapter we therefore present a brief overview of the numerical procedures, the underlying theoretical frameworks, and the model approximations used in this research.

2.2 A*b initio* Quantum Mechanics for Electronic Structure Calculations

2.2.1 Schrödinger equation

The full quantum description of any atomic, molecular or crystal/solid system can be represented by the following time dependent Schrödinger equation:

$$\mathrm{H}\Psi(r,t) = i\hbar\frac{\partial\Psi(r,t)}{\partial t}, \tag{2.1}$$

where H is the Hamiltonian operator $\mathrm{H} = -\frac{\hbar^2}{2m}\nabla^2 + V$, V is the external potential of the system, Ψ(r,t) is the wavefunction describing the probability density of a particle in a given energy state of the system. In this thesis, only two types of particles, nuclei and electrons are considered. If the external potential V is independent of time, equation 2.1 is reduced (by considering Ψ(r,t) = Ψ(r)T(t)) to the time independent Schrödinger equation

$$\mathrm{H}\Psi(r) = E\Psi(r), \tag{2.2}$$

where E is the energy of the system. Equation 2.2 is a second order differential equation. This time independent Schrödinger equation constitutes an eigenvalue problem that can only be solved exactly for the simplest of systems. The eigenvalues satisfying the equation correspond to the discrete energy levels of the particles (e.g., electrons), and the corresponding eigenfunction is the wavefunction or molecular orbital of the particle. Due to the electron spin, each orbital can accommodate two electrons. The probability of an electron to appear at point **r** in space, or the electron density at this location, is the product of

eigenfunction with its complex conjugate for this value of **r**, i.e., the square of its wavefunction.

2.2.2 Born-Oppenheimer approximation

For complicated many particle system, equation 2.2 usually cannot be solved exactly. To lower the complexity of solving equation 2.2, the Born-Oppenheimer approximation was introduced, which uses the fact that the mass of the electron is far smaller than the nuclei and speed of the electron is much greater than the nuclei, and therefore the electron will always follow the movement of nuclei instantaneously. The total system wavefunction now is approximated by product of the electron and nuclei wavefunctions,

$$\Psi_{system}(n_1, n_2, , , n_N, e_1, e_2, , , e_M) = \Psi(n_1, n_2, , , n_N)\Psi(e_1, e_2, , , e_M) \ , \tag{2.3}$$

where n and e denote nuclei and electrons respectively.

2.2.3 Hamiltonian, atomic orbital and molecular orbital in Hartree-Fock solutions with numerical recipes

The Hamiltonian for the molecular system composed of nuclei and electrons is

$$\mathrm{H} = -\sum_i \frac{\hbar^2}{2m_e}\nabla_{r_i}^2 - \sum_I \frac{\hbar^2}{2m_n}\nabla_{R_I}^2 - \sum_{iI} \frac{Z_I e^2}{4\pi\varepsilon_0 |R_I - r_i|} + \frac{1}{2}\sum_{i\neq j} \frac{e^2}{4\pi\varepsilon_0 |r_i - r_j|} + \frac{1}{2}\sum_{I\neq J} \frac{Z_I Z_J e^2}{4\pi\varepsilon_0 |R_I - R_J|} \ , \tag{2.4}$$

where R and r are the coordinate vectors of nuclei and electrons respectively, Z is number of electrons on the nucleus. Under the Born-Oppenheimer

approximation, the kinetic part for nuclei is zero and interactions between nuclei are a constant. This allows one to consider only electron wavefunctions in the Hamiltonian, which then simplifies to

$$\mathrm{H}^{HF} = -\sum_i \frac{\hbar^2}{2m_e}\nabla_{r_i}^2 - \sum_{iI} \frac{Z_I e^2}{4\pi\varepsilon_0 \left|R_I - r_i\right|} + \frac{1}{2}\sum_{i\neq j} \frac{e^2}{4\pi\varepsilon_0 \left|r_i - r_j\right|} \quad . \tag{2.5}$$

Under the Born-Oppenheimer approximation, the Hartree-Fock method can be used to solve the time-independent Schrödinger equation. The variational theorem provides a convenient numerical approach for the Hartree-Fock method. Instead of solving directly for the eigenfunctions, the Hartree-Fock method starts with a best-guess trial wavefunction and then improves the wavefunction iteratively through a self-consistent field (SCF) method toward the best answer, where the system energy is at a minimum.

The system's electronic wavefuction can be constructed by using a Slater determinant of all one-electron spin orbital wave functions, $\phi_i(r_i)$, which is the product of a space function and a spin function. For a N electrons system this is

$$\Psi = \frac{1}{\sqrt{N!}} \begin{vmatrix} \phi_1(r_1) & \phi_1(r_2) & \cdots & \phi_1(r_N) \\ \phi_2(r_1) & \phi_2(r_2) & \cdots & \phi_2(r_N) \\ \vdots & \vdots & & \vdots \\ \phi_N(r_1) & \phi_N(r_2) & \cdots & \phi_N(r_N) \end{vmatrix} . \tag{2.6}$$

This construction satisfies antisymmetry principle, i.e., exchanging any two rows, or two electrons, in the determinant changes the sign of the wavefunction. One

way to construct atomic orbitals/basis sets is by using multiple Gaussian functions and polarization functions. 6-31G* basis sets usually give enough accuracy for molecular system *ab initio* quantum mechanical calculations.[1] The molecular orbital is then approximated by a liner combination of atomic orbitals (LCAO) strategy.

$$\psi_i = \sum_{u=1}^{K} c_{ui}\phi_u \tag{2.7}$$

The energy of a HF system can be calculated by

$$\begin{aligned}
E &= \langle \Psi | H^{HF} | \Psi \rangle \\
&= \langle \Psi | -\sum_i \frac{\hbar^2}{2m_e}\nabla_{r_i}^2 - \sum_{iI}\frac{Z_I e^2}{4\pi\varepsilon_0 |R_I - r_i|} + \frac{1}{2}\sum_{i\neq j}\frac{e^2}{4\pi\varepsilon_0 |r_i - r_j|} | \Psi \rangle \\
&= \sum_i \langle \phi_i | -\frac{\hbar^2}{2m_e}\nabla_{r_i}^2 - \sum_I \frac{Z_I e^2}{4\pi\varepsilon_0 |R_I - r_i|} | \phi_i \rangle + \frac{e^2}{2}\sum_{i\neq j}\langle \phi_i\phi_j | \frac{1}{4\pi\varepsilon_0 |r_i - r_j|} | \phi_i\phi_j \rangle \\
&- \frac{e^2}{2}\sum_{i\neq j}\langle \phi_i\phi_j | \frac{1}{4\pi\varepsilon_0 |r_i - r_j|} | \phi_j\phi_i \rangle \\
&= E^{core} + E^{Coulomb} + E^{exchange}
\end{aligned} \tag{2.8}$$

In the Hartree-Fork approximation, the system energy has three parts: core energy, Coulomb energy and exchange energy, as shown in equation 2.8. The correlation energy between electrons, which is treated under density functional theory (DFT) method in Kohn-Sham equation, is not considered in HF. This is a major drawback of the HF method. One of the numerical implementations of HF is the Roothaan-Hall equation. By expanding all terms into matrix, the Roothaan-Hall equation is

FC=SCE , (2.9)

where F is the Fock matrix, C is coefficient matrix, S is overlap matrix, and E is the orbital energy matrix. This numerical equation can be solved by an iterative method.

2.2.4 Density functional theory (DFT), Kohn-Sham equation, and the exchange-correlation functional with numerical implementation

Density functional theory (DFT) is based on an idea first introduced in the late 1920s in the Thomas-Fermi model and then confirmed in 1964 by Hohenberg and Kohn that the electron system's ground-state energy and other properties could be defined by the electron density of the system [2]

$$E[\rho(r)] = \int V_{ext}(r)\rho(r)dr + F[\rho(r)] , \quad (2.10)$$

where V_{ext} is the external potential, usually due to the potential energy of a fixed configuration of nuclei, and ρ(r) is the electron density of the system

$$\rho(r) = \sum_i |\psi_i(r)|^2 \quad . \quad (2.11)$$

F[ρ(r)] is a function that contains kinetic energy and interelectronic interaction energy of the electrons. Kohn and Sham further approximated the *F*[ρ(r)] into three terms[3]

$$F[\rho(r)] = E_{KE}[\rho(r)] + E_H[\rho(r)] + E_{XC}[\rho(r)] \tag{2.12}$$

Where $E_{KE}[\rho(r)]$ is the kinetic energy of electrons without interactions,

$$E_{KE}[\rho(r)] = \sum_i \langle \psi_i | -\frac{\nabla^2}{2} | \psi_i \rangle \ , \tag{2.13}$$

$E_H[\rho(r)]$ is the Hartree electrostatic energy,

$$E_H[\rho(r)] = \frac{1}{2} \iint \frac{\rho(r)\rho(r')}{|r - r'|} dr dr' \ , \tag{2.14}$$

and $E_{XC}[\rho(r)]$ is the exchange-correlation energy functional, which includes exchange, correlation, and the difference between the true kinetic energy and $E_{KE}[\rho(r)]$. The Kohn-Sham ground state energy of the system in terms of electron density is then expressed as

$$\begin{aligned} E[\rho(r)] = & -\sum_I \int \frac{Z_I}{|r - R_I|} \rho(r) dr + \sum_i \langle \psi_i | -\frac{\nabla^2}{2} | \psi_i \rangle \\ & + \frac{1}{2} \iint \frac{\rho(r)\rho(r')}{|r - r'|} dr dr' + E_{XC}[\rho(r)] \end{aligned} \ . \tag{2.15}$$

The one-electron Kohn-Sham Hamiltonian can then be written as

$$H^{KS} = -\frac{\nabla^2}{2} - \sum_I \frac{Z_I}{|r_i - R_I|} + \int \frac{\rho(r_j)}{|r_i - r_j|} dr_j + V_{XC}(r_i) \ , \tag{2.16}$$

where $V_{XC}(r) = \frac{\delta E_{XC}[\rho(r)]}{\delta \rho(r)}$, (2.17)

and the one-electron Kohn-Sham equation is

$$H^{KS}\psi_i = \varepsilon_i\psi_i \ . \tag{2.18}$$

One of the advantages of DFT and Kohn-Sham equation is that the contributions from exchange-correlation interactions between electrons are accounted for. Accordingly, the type of approximation to the exchange–correlation functional crucially affects the results obtained when solving the Kohn-Sham equation. A simple exchange-correlation functional is the local density approximation (LDA)

$$E_{XC}^{LDA}[\rho(r)] = \int \rho(r)\varepsilon_{XC}(\rho(r))dr \ , \tag{2.19}$$

where $\varepsilon_{XC}(\rho(r))$ is the per electron exchange-correlation energy in a uniform electron gas with density $\rho(r)$. Then the exchange-correlation energy is equal to the per electron exchange-correlation energy times the number of electrons, which amounts to the integration of the product of the two functions over all space. Although LDA already performs well for the description of many systems, a number of authors have made improvements to the exchange-correlation functional by considering the gradient of the electron density. This series of functionals are called generalized gradient approximations (GGA)

$$E_{XC}^{GGA}[\rho(r)] = \int f(\rho(r), \nabla\rho(r))dr \tag{2.20}$$

For example, a popular GGA was developed by Perdew, Burke and Ernzerhof in 1996.[4-9] Numerical implementation of the one-particle Kohn-Sham equations

allows one to solve this partial differential equations iteratively. The electronic wave functions are constructed by a linear combination of a set of basis functions. There are two types of basis sets for the Kohn-Sham equation: plane-wave basis sets and local basis sets. One of the advantages of the plane-wave potential is that the calculation of forces on the atoms and stress on the unit cell is easy. Hence, it is also convenient to use plane wave basis sets in *ab initio* MD simulations. Local basis sets require computational efforts that scale linearly with the number of atoms in the systems. This approach is therefore used for the treatment of large system and is suitable in molecular, insulating and semiconductor systems.

Numerical basis set is one of the popular local basis sets and can be created by solving the Kohn-Sham equations. Usually more than one basis functions can be used to construct an atomic orbital, just as in the case of Gaussians.[1] For molecular systems, the Kohn-Sham molecular orbitals are usually expressed as a linear combination of atomic basis functions.

$$\psi_i(r) = \sum_v C_{vi}\phi_v \tag{2.21}$$

Expanding the Kohn-Sham equation into matrix form, one then can implement numerical methods to solve this equation with the Roothaan-Hall equation similar to HF method.

HC=SCE, (2.22)

where H is the Kohn-Sham matrix.

2.2.5 DFT applications in the solid state

2.2.5.1 Bloch theorem, band structure, and density of states

For a crystalline solid, the near free electrons can be assumed to move in a periodic potential field. To illustrate, the one-dimensional wavefunction can be expressed as

$$\psi_k(r) = Ae^{ik\cdot r} \ , \tag{2.23}$$

where k is the wavevector and r is the position vector in real space.

As previously mentioned, if we know the Hamiltonian of the system, the system energy can be calculated as a function of wavevector magnitude and direction. The distribution of energy versus k is the electronic band structure of the crystal. The *bandwidth* is the difference of the lowest and highest energy levels in the band. The band structure for a three-dimensional crystal lattice is often plotted along typical high symmetry directions in the k space within the first Brillouin zone (BZ). Conventionally, Roman or Greek capital letters are used to label specific values of k. For example, Gamma point refers to k=0. It is not necessary to sample all the possible k values within the first BZ. Suitable sets of discrete k values can often give enough sampling accuracy in calculating properties such as

charge densities. One of the popular k-sampling methods is proposed by Monkhorst and Pack.[10]

The density of states (DOS) is also a very useful way to illustrate the electronic structure of a crystal solid. It is the number of electronic states, or total number of electron wavefunctions within an energy interval, normalized per unit volume. A definition of DOS is shown in the following equation:

$$N_n(E) = \frac{1}{4\pi^3} \int \delta(E - E_n(k)) dk \ , \tag{2.24}$$

where $E_n(k)$ is the dispersion of the given band and the integral is determined over the Brillouin Zone.

The partial density of states (PDOS) and local density of states (LDOS) are useful semi-quantitative tools for analyzing electronic structure. LDOS is a spatially resolved DOS showing which atoms in the system contribute electronic states to various parts of the DOS. PDOS further qualifies these results by resolving the contributions according to the angular momentum of the DOS. It is often useful to know whether the main peaks in the DOS are of s, p, d or f character. LDOS and PDOS analyses give a qualitative way to describe the nature of electron hybridization in the system. PDOS calculations are based on Mulliken population analysis[11], which allows the contribution from each atomic orbital to a given energy band to be calculated. Summation of these contributions over all bands produces a weighted DOS.

2.2.5.2 Plane waves and pseudopotentials

As previously mentioned, especially in light of the Bloch theorem, plane waves are intuitively the most convenient basis set for calculations pertaining to periodic crystal systems. Every wavefunction can be defined as a linear combination of plane waves as

$$\psi_k(r) = \sum_G \phi_{k+G} e^{i(k+G)\cdot r} \quad , \tag{2.25}$$

where *G* is a reciprocal lattice vector that satisfies the diffraction condition, $\vec{G} = 2\pi n_1 \vec{a}^* + 2\pi n_2 \vec{b}^* + 2\pi n_3 \vec{c}^*$, and *a*, b*, c** are the are the basis vectors of the Wigner-Seitz unit cell. The corresponding Kohn-Sham equation of DFT is then expressed as

$$\sum_{G'} \left\{ \begin{matrix} \frac{\hbar^2}{2m} |k+G| \delta_{GG'} + V_{nuclei}(G-G') + V_{electron}(G-G') + \\ V_{exchange}(G-G') \end{matrix} \right\} \phi_{k+G'} = \varepsilon \phi_{k+G'} \quad , \tag{2.26}$$

where $V_{nuclei}, V_{electron}$ *and* $V_{exchange}$ are the electron-nuclei, electron-electron and exchange-correlation functional, and $\delta_{GG'}$ is a delta function of G and G′

The valence electrons are the most interesting ones in most of the cases, because they are involved in chemical bonding and physical properties that involve the corresponding energy levels, e.g., electronic excitations. Therefore, less attention has to be paid to core electrons, which therefore need not be treated explicitly.

When describing electrons using wavefunctions, such as can be constructed in a plane wave basis set, these wavefunctions show rapid oscillation near the core region. This is because the core wavefunctions and valance electron wavefunctions are orthogonal in this region. The electron and core nuclei wavefunctions overlap and produce these oscillations. These oscillations are associated with large kinetic energies and require many plane waves to describe this region.

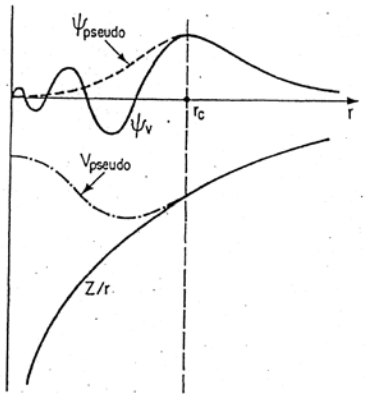

Figure 2-1 Pseudowavefunction and pseudopotential scheme

Describing these oscillations is enormously time consuming and bears little benefit, because the effect of the core electrons on the behavior of the valence electrons is largely overshadowed by the strong electrostatic interactions between electrons and the nuclei. It has therefore become common practice to lump the core-valence electron interactions into a pseudopotential between nucleus and valence electrons, as illustrated in Figure 2-1. Pseudopotentials are derived to have a smooth wavefunction at close to the core region and replace the oscillating wavefunction. This reduces the number of terms in equation 2.38

and hence reduces computational loads and improves the efficiency of the calculation. Most pseudopotential function can be derived from all-electron model calculations. However, the choice of pseudopotential is crucial, as it will significantly affect the outcome of DFT calculations. The pseudopotential developed by Troullier and Martins [49] is very popular. It is a wave function norm conserving pseudopotential and is good for most of the simulations performed here. Another popular pseudopotential is the ultrasoft pseudopotentials developed by Vanderbilt. [50, 51] It allows for calculating *d*- and *f*-electron metals at an acceptable computation cost.

2.3 Explicit-atom molecular dynamics (MD) simulations

2.3.1 Molecular Dynamics (MD) simulation methods

MD simulations consist of solving Newton's equations of motion for a system of particles that interact with each other as described by an atomic interaction model. The force acting on a particle is defined by the negative derivative of potential energy with respect to a length coordinate, i.e.,

$$\mathrm{F}_i = -\frac{\partial U(r_1, r_{2,} \ldots r_N)}{\partial r_i} \,, \tag{2.27}$$

where U is the total potential energy and r is the particle's position vector. This force causes the particle to accelerate in the direction of the applied force, as described by Newton's law

$$a_i = \frac{F_i}{m_i} = \frac{d\upsilon_i}{dt} = \frac{d^2 r_i}{dt^2} \ , \tag{2.28}$$

where t is time, m is the mass. There is one such equation per particle in the system, and solving this set of equations simultaneously in an iterative fashion yields the trajectories of all the atoms. From these trajectories one can derive the systems properties using the formalisms of statistical thermodynamics. Algorithms for integrating Newton's equations of motion for atomistic systems are described briefly in the following. They involve the extrapolation to new atomic positions and momenta based on current and past values of these variables and the repeated evaluation of the instantaneous forces. Because differentials are replaced with finite differences, an error may be accumulated upon integration over time, and the art of developing the appropriate numerical procedure lies in minimizing this error. One of the most popular methods is the Verlet algorithm.[18] In the Verlet algorithm, the atomic coordinates are calculated as

$$\mathrm{r_i}(t + \Delta t) = 2r_i(t) - r_i(t - \Delta t) + \frac{F_i(t)}{m_i}\Delta t^2 \ , \tag{2.29}$$

and velocities is defined as

$$\upsilon_i(t) = \frac{r_i(t+\Delta t) - r_i(t-\Delta t)}{2\Delta t} \ . \tag{2.30}$$

An improved algorithm is the Leap-Frog algorithm, [19] in which the equation of motion is defined by:

$$r^i(t+\Delta t) = r^i(t) + \Delta t \upsilon^i_{t+\frac{\Delta t}{2}} \ , \tag{2.31}$$

$$\upsilon^i_{t+\frac{\Delta t}{2}} = \upsilon^i_{t-\frac{\Delta t}{2}} + \Delta t \frac{F^i(t)}{m^i} \ . \tag{2.32}$$

Compared to Verlet algorithm, the Leap-Frog algorithm has two main improvements. One is that velocity is explicitly included in the calculation and the other is that it does not need to calculate large number differences. The next improvement is Beeman's algorithm,[20] which generates Verlet like particle trajectories, and has an improved estimation of the particle velocities. In Beeman's algorithm, the velocities are defined as

$$\upsilon_i(t+\Delta t) = \upsilon_i(t) + \frac{2F_i(t+\Delta t) + 5F_i(t) - F_i(t-\Delta t)}{6m_i}\Delta t^2 \ , \tag{2.33}$$

and positions are defined as

$$\upsilon_i(t+\Delta t) = \upsilon_i(t) + \frac{2F_i(t+\Delta t) + 5F_i(t) - F_i(t-\Delta t)}{6m_i}\Delta t \quad . \tag{2.34}$$

In Beeman's formulation, velocity is more accurately computed, and the total energy conservation condition is better treated. Beyond Beeman, Gear *et al*

formulated the predictor-corrector integration method.[21] Most contemporary high level MD code uses this method of integration. The concept in these methods is to use the difference between predicted and calculated accelerations to modify particle positions and velocities, etc.:

$$\Delta a(t+\delta t) = a^c(t+\delta t) - a(t+\delta t) \ , \tag{2.35}$$

Then

$$r^c(t+\delta t) = r(t+\delta t) + c_0 \Delta a(t+\delta t) \ , \tag{2.36}$$

$$v^c(t+\delta t) = v(t+\delta t) + c_1 \Delta a(t+\delta t) \ , \tag{2.37}$$

$$a^c(t+\delta t)/2 = a(t+\delta t)/2 + c_2 \Delta a(t+\delta t) \ , \tag{2.38}$$

$$b^c(t+\delta t)/6 = b(t+\delta t)/6 + c_3 \Delta a(t+\delta t) \ , \tag{2.39}$$

where c_0, c_1, c_2… depend on the order of Taylor expansion.

The actual integration process usually takes very small time steps. Typical values are one or several femtoseconds for most atomic systems.

2.3.2 Simulation ensembles

Running an MD simulation of a system usually requires one to maintain control over certain system parameters. For example, one may choose to maintain the system energy, temperature, or pressure constant during the course of an MD

simulation. These conditions correspond to different thermodynamic ensembles, and thus allow evaluation of different statistical measures. They also mimic different experimental conditions. In order to optimize the crystal unit cell, constant temperature and constant pressure ensembles are often used.

If the number of particles, total system volume and total system energy during the simulation are conserved and kept a constant, the corresponding simulation ensemble is called a microcanonical (NVE) ensemble. Constant NVT and NPT ensembles can also be used. [22] While keeping N, the total number of particles, and V, the system volume, as constants is straightforward, constant temperature and pressure are treated indirectly. The temperature of a system is defined by the time average of the kinetic energy of the unconstrained system with the following equation:

$$\langle \mathrm{K} \rangle_{NVT} = \frac{3}{2} N k_B T \ . \tag{2.40}$$

Algorithms that can generate rigorous canonical ensembles are the stochastic collision method by Anderson[23] and extended system method by Nose and Hoover[24-27]. The constant pressure ensemble algorithm usually involves scaling of the system volume or connects the system to a pressure pool, so that the pressure change can be defined by:

$$\frac{dP(t)}{dt} = \frac{1}{\tau}(P_{pool} - P(t)) \tag{2.41}$$

The constant temperature and constant pressure, NPT, MD simulations are typically performed using a Parrinello-Rahman method[28], which allows for unit cell parameters such as basis vector lengths and angles between them to vary with evolving system dynamics under constant pressure and temperature. A detailed discussion is given in reference [28].

2.4 Crystal Polymorph Prediction Method

2.4.1 Introduction

In order to calculate the crystal properties, such as the band gap and molecular packing behavior, it is crucial to be able to predict the crystal structure based on the designed molecule. According to a study of 30,000 molecular crystals conducted by Mighell *et al*[29], as shown in Figure 2-2, 36% of these studied crystals have symmetries belong to $P2_1/c$, 14% belong to $P\bar{1}$, and 12% belong to $P2_12_12_1$. Most organic crystals crystallize in only a few space groups. For example, 88.6% of the organic molecular crystal structures published between 1929 and 1975 belonged to one of the following nine space groups: $P2_1/c$, $P2_12_12_1$, $P1$, $P2_1$, $C2/c$, $Pbca$, $Pna2_1$, $Pnma$, $Pbcn$ [30, 31]. A connection exists between the symmetry of the molecules and the possible space groups of the crystals they form [32, 33].

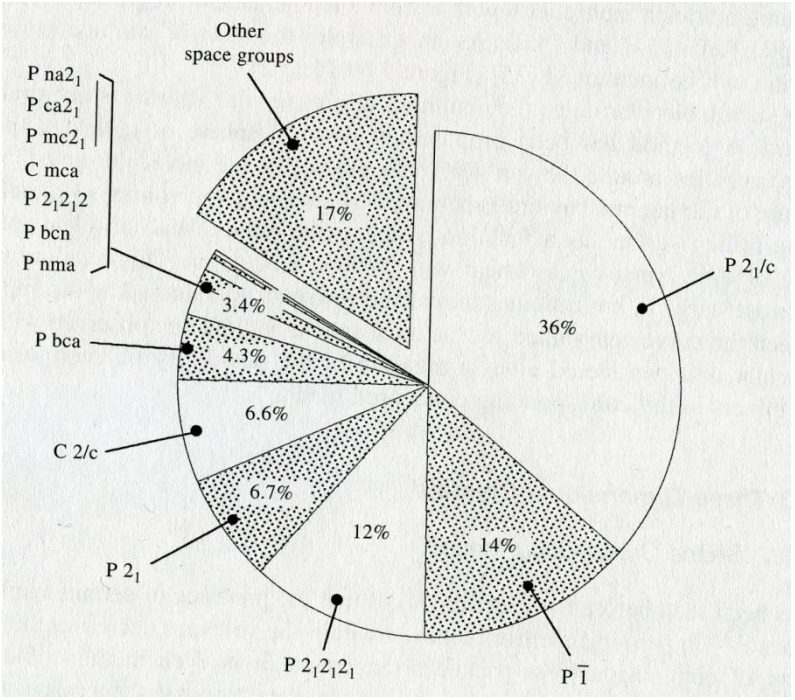

Figure 2-2 Three-dimensional space groups observed statistically by examining 30000 organic crystals [29]

The most probable space group symmetry as a function of molecular site symmetry was studied, as shown in Table 2-1. The molecular symmetry seems limit to crystal packing symmetry to a sub-set of possibilities. These possible crystal structures are called the polymorphs of a molecular crystal.

Table 2-1 The most probable crystal space group symmetries as a function of the molecular site symmetry with the number of molecules per unit cell Z.[29]

Molecular site symmetry							
1 (C1)		$\bar{1}$ (C_i)		2 (C2)		M (Cs)	
	Z		Z		Z		Z
$P\bar{1}$	2,4	$P\bar{1}$	1,2	$C2/c$		$Pmc2_1$	4
$P2_1$	2,4	$P2_1/c$	2,4	$P2_12_12_1$		$Cmca$	4
$P2_1/c$	4	$C2/c$	4	$Pbcn$		$Pnma$	4
$Pca2_1$	4	$Pbca$	4				
$Pna2_1$	4						
$P2_12_12_1$	4						

To find the most probable crystal structures, it may at first appear that all possible space groups (230 in total) must be searched with a variable number of molecules in the unit cell — a very time-consuming process. However, the search can be dramatically reduced in scope because of the observed facts described in section 1.3.2.

Consequently, one can obtain highly probable molecular crystal structures by determining the most stable structures in just a few space groups and by comparing their energies and structures. Therefore, the general idea for a polymorph search is to generate possible packing configurations by mapping the internal molecular symmetries onto crystal space groups and then optimizing these structures through energy minimization methods. The structure with the lowest energy is considered the most probable crystal structure. There are successful solutions that for predicting molecular crystal structures. [34] An available tool for predicting molecular crystal structure is the POLYMORPH program by Accelrys [35].

2.4.2 Theory of the POLYMORPH method

2.4.2.1 Predicting polymorphs problem definition

As previously shown, molecular crystals exhibit polymorphism, i.e., they can crystallize in multiple space group symmetries. The actual space group symmetry of a molecular crystal is often determined by the physical conditions, such as temperature and pressure, and by the processing kinetics in which the crystals are obtained, such as vacuum deposition or precipitated from a solution. Different polymorphs of a molecular crystal usually have distinct Gibbs free energies (G). The crystallization process not always yields the polymorph with the lowest value of G. Actually, the relationship between crystallization conditions and the resulting polymorph is still an ongoing research topic, and not very well understood as yet. [35] Within algorithm accuracy and limitations, the crystal polymorph prediction method, such as the POLYMORPH program by Accelrys [35], can predict crystal structures highly possible to be found experimentally.

Expansion of G yields $G = E + PV - TS$, where E is energy, P is pressure, V is volume, T temperature, and S is entropy. Usually, the magnitude of the product PV is very small compared to the total energy and therefore can be disregarded. At finite temperatures, crystal structure entropies should have a significant influence on G. However, calculating entropy of a crystal is more difficult, and in a first approximation, is therefore neglected as well. This approximation,

however, eliminates the well-known effect that entropy has on the stability ranges of crystal polymorphs as a function of temperature. The results of polymorph searches based on the minimization of the system potential energy alone must therefore be considered with caution, and it is clear that polymorphs within a reasonable ($\sim k_B T$) proximity of the lowest-energy structure should not be discarded from consideration as a stable phase at high temperatures.

2.4.2.2 POLYMORPH prediction procedures

For the POLYMORPH program by Accelrys[35] the following procedures are performed during the prediction process:

First, a Monte Carlo simulated annealing process is performed to generate thousands of possible molecular packing structures. During this packing step, the contents of the unit cell are packed into a crystal of a given space group symmetry. The packing algorithm modifies cell parameters and the orientation and position of the fragments in the primitive unit cell to generate thousands of trial packings. A Monte Carlo simulated annealing procedure is applied to select potential packing structures with low energy. The packing step ends with a large number of unoptimized candidate crystal structures.

Second, these candidate crystal structures are clustered into groups according to packing similarity. Duplicate crystal structures are retained or removed according to which one has the lowest energy.

Third, the geometry of every structure is optimized using molecular dynamics energy minimization methods.

Fourth, these optimized structures are clustered again to remove duplicates.

Finally, these optimized structures are sorted according to normalized total system energy. (This will be illustrated in Chapter 4.)

The algorithms and theories used in these steps are detailed in the following.

2.4.2.3 Monte Carlo simulated annealing

POLYMORPH uses a Monte Carlo simulated annealing algorithm to search for the lowest global energy minima of molecular packings. This method works around the search for the global energy minimum problem as a thermodynamic problem. At some non-zero temperature, T, the crystal changes its structure randomly, and its energy fluctuates accordingly. To prevent the simulation from becoming trapped in a local minimum, cooling begins at a relatively high temperature; every crystal structure (within the constraints of the space group and asymmetric unit contents) can then be reached theoretically and therefore ergodicity ensured.

The Monte Carlo simulated annealing process first generates thousands of possible crystal structures based on symmetry space groups. The Metropolis algorithm is used to determine whether generated trial structures are accepted or rejected. The simulation consists of two stages, heating and cooling.

Heating stage — In the heating stage, the temperature for each new trial, T_2, is obtained from the previous trial, T_1, and a user-definable heating factor, T_{heat} by $T_2 = T_1 \times (1.0 + T_{heat})$. Heating stops when a preset maximum temperature is reached or a specified number of consecutive trial moves have been accepted.

Cooling stage — The cooling stage simulates the annealing of a heated structure. It changes the temperature from high values where the algorithm is able to globally sample the phase space of possible packing arrangements to low values, where it samples areas of energetically favorable packings more locally. If a trial is accepted during cooling, the temperature to use for the next trial T_2, is obtained from that used for the previous trial, T_1, using a user-definable cooling factor, T_{cool}, by $T_2 = T_1 \times (1.0 + T_{cool})$. The run stops when either the temperature reaches a preset minimum, or a specified maximum number of trials have been reached.

Trial steps — Each Monte Carlo trial consists of the following steps:

1. Make a random change to the orientation of each asymmetric unit.

2. If more than one asymmetric unit exits, make a random change to the relative orientation of each unit.

3. According to space group symmetry, make a random change to the relative orientation of the unit cell lattice vectors.

4. Expand the asymmetric unit in free space until no van der Waals contacts can be found within the asymmetric unit.

5. Contract the asymmetric unit in free space while maintaining zero van der Waals contacts within the asymmetric unit such that the molecules in the asymmetric unit are brought into close contact..

6. Increase the magnitude of the lattice vectors until there are no van der Waals contacts.

7. Decrease the magnitude of the lattice vectors while maintaining zero van der Waals contacts.

8. Calculate the energy and density of the crystal structure and apply a standard Metropolis acceptance/rejection test.

2.4.2.4 Cluster analysis algorithm

The clustering algorithm finds similarity between two crystal packings with the same asymmetric unit cells. The crystal similarity is determined by a comparison of radial distribution functions (RDF). The calculation of the crystal similarity involves following steps:

First, all atoms in the asymmetric unit cell are divided into groups according to their chemical information. For each pair of atoms, squared interatomic distances are calculated up to a specified cutoff distance.

Second, the radial distribution function (RDF) is then calculated, over a user defined number of bins.

The crystal similarity measure can then be determined by the difference of bin values between the two structures.

2.4.3 Geometry optimization algorithms

The optimization of a molecular structure can be treated in mathematical terms of an optimization in a multidimensional space. There are several standard algorithms that can be applied to such a problem:

- Steepest descents[36]
- Conjugate gradient [37]
- Newton-Raphson methods [38]

2.5 Computing techniques and algorithms for computational materials design

Computational molecular design requires substantial computing power. Solving for interested problems is still limited by available computing techniques and resources. Only with future computing techniques, such as quantum computing advanced to application stage [39-47], can our computational studies have the ability to reach any system size and time scale.

In most of cases, a solvable system size within the Schrödinger equation method frame is typically a few hundred to a few thousand atoms. The time scale for typical *ab initio* molecular dynamics (MD) simulations is several tens of picoseconds. Classical MD can cover longer time scales, but with the sacrifice of accuracy in terms of real physical interactions with the simulated system. For current applications of computational materials design, a popular strategy is to use multiscale simulations techniques to link atomistic DFT simulations to other approximate simulation level, such as atomistic MD simulations, mesoscale simulations and Monte Carlo simulations, to span over enough system size and time scale.

For fast molecular dynamics, many algorithms of better calculating physical quantities are developed. For example, the long-range interactions can be calculated by an efficient Ewald summation method together with linked cell scheme and periodic boundary conditions. Parallel computing techniques, such as message passing interface (MPI), can also naturally be applied to the MD system to speed up the simulations. There are existing highly efficient successful parallel computing MD codes [48], which can implement most of the current MD force field and ensemble algorithms.

2.6 References

[1] Leach, A. R. Molecular modeling: principles and applications. *Harlow: Pearson Education Limited* 26-164 (2001)

[2] Hohenberg, P.; Kohn, W. *Physical Review B* **136**, B864 (1964)

[3] Kohn, W.; Sham, L. J. *Physical Review* **140**, 1133 (1965)

[4] Perdew, J. P. *Physical Review B*, **33**, 8822 (1986);

[5] Becke, A. D. *Physical Review A* **38**, 3098 (1988);

[6] Lee, C. T.; Yang, W. T.; Parr, R. G. *Physical Review B* **37**, 785 (1988);

[7] Perdew, J. P.; Wang, Y. *Physical Review B* **45**, 13244 (1992);

[8] Becke, A. D. *Journal of Chemical Physics* **98**, 1372 (1993);

[9] Becke, A. D. *Journal of Chemical Physics* **98**, 5648 (1993)

[10] Monkhorst, H. J.; Pack, J. D. *Physical Review B* **13**, 5188 (1976)

[11] Mulliken, R. S. *Journal of Chemical Physics* **23**, 1833-1846 (1955)

[12] Sun, H. Macromolecules 1995, 28, 701.

[13] Sun, H.; Rigby, D. Polysiloxanes: *ab initio* force field and structural, conformation and thermophysical properties. *Spectrochimica Acta Part A* **53** 1301 (1997)

[14] Sun, H.; Ren, P.; Fried, J. R. The COMMPASS force field: parameterization and validation for phosphazenes. *Computational and Theoretical Polymer Science* **8**, 229 (1998)

[15] Sun, H. COMPASS: an *ab initio* force field optimized for condensed-phase applications – overview with details on alkane and benzene compounds. *J. Phys. Chem. B* **102**, 7338-7364 (1998)

[16] Kieffer, J.; Anderson, D. C.; Klarsfeld, S. Molecular dynamic simulations of the infrared dielectric response of silica structures. *J. Chem. Phys.* **1**, 8978-8986 (1998)

[17] Bunte, S. W.; Sun, H. *Journal of Physical Chemistry B*, **104**, 2477 (2000)

[18] Verlet, L. *Physical Review* **159**, 98 (1967)

[19] Hockney, R. W.; Eastwood, J. W. *Computer simulation using particles*

McGraw-Hill: New York (1981)

[20] Beeman, D. *Journal of Computational Physics* **20**, 130 (1976)

[21] Gear, C. W. *Numerical Initial Value Problems in Ordinary Differential Equations* Prentice Hall: Englewood Cliffs, NJ (1971)

[22] Frenkel, D.; Smit, B. *Understanding molecular simulation : from algorithms to applications, 2nd ed.* Academic: San Diego, Calif. London (2002)

[23] Anderson, H. C. Molecular dynamics simulations at constant pressure and/or temperature. *J. Chem. Phys* **72**, 2384 (1980)

[24] Hoover, W. G. Canonical dynamics: Equilibrium phase-space distributions. *Physical Review A* **31**, 1695-1697 (1985)

[25] Hoover, W. G.; Ladd, A. J. C.; Moran, B. High strain rate plastic flow studied via nonequilibrium molecular dynamics. *Phys. Rev. Lett.* **48**,1818-1820 (1982)

[26] Nose, S. A molecular dynamics for simulations in canonical ensemble. *Molecular Physics* **52**, 255-268 (1984)

[27] Nose, S. A unified formulation of the constant temperature molecular dynamics methods. *J. Chem. Phy.* **81**, 511 (1984)

[28] (a) Parrinello, M.; Rahman, A. *Physical Review Letters* **45**, 1196 (1980); (b) Car, R.; Parrinello, M. *Physical Review Letters* **55**, 2471 (1985)

[29] Mighell, A. D.; Himes, V. L.; Rodgers, J. R. Acta Cryst. Sect. *A* **39**, 737 (1983)

[30] Baur, W. H.; Kassner, D. *Acta Crystallogr. Sect. B* **48**, 356-369 (1992).

[31] Belsky, V. K.; Zorkii, P. M. *Acta Crystallogr. Sect. A* **33** 1004 (1977).

[32] Hahn, T. *International Tables for Crystallography*, *3rd Edition* **A**, Riedel: Dordrecht (1983)

[33] Kitaigorodsky, A. I. *Organic Chemical Crystallography*, Consultants Bureau: New York (1961)

[34] Chaka, A. M.; Zaniewski, R.; Youngs, W.; Tessier, C.; Klopman, G. Predicting the crystal structure of organic molecular materials. *Acta Cryst. B* **52**, 165-183 (1996)

[35] Inc., A. S. http://www.accelrys.com/mstudio/ms_modeling/index.html

[36] Debye, P. J. W. Näherungsformeln für die zylinderfunktionen für große werte des arguments und unbeschränkt veränderliche werte des index. *Mathematische Annalen* 67, (4), 535–558 (1954)

[37] Hestenes, M. R.; Stiefel, E. Methods of conjugate gradients for solving linear systems. *Journal of Research of the National Bureau of Standards* **49**, (6), 409-436 (1952)

[38] Press, W. H.; Flannery, B. P.; Teukolsky, S. A.; Vetterling, W. T. *Numerical recipes in c: the art of scientific computing* Cambridge University Press (1992)

[39] Xu, X. D.; Sun, B.; Berman, P. R.; Steel, D. G.; Bracker, A. S.; Gammon, D.; Sham, L. J. Coherent optical spectroscopy of a strongly driven quantum dot. *Science* **317**, 929, (2007)

[40] Xu, X. D; Sun, B.; Berman, P. R.; Steel, D. G.; Bracker, A. S.; Gammon, D; Sham, D. L. Coherent population trapping of an electron spin in a single negatively charged quantum dot. *Nature Physics* **4**, 692-695 (2008)

[41] Xu, X. D.; Yao, W.; Sun, B.; Steel, D. G.; Bracker, A. S.; Gammon, D.; Sham, L. J. Optically controlled locking of the nuclear field via coherent dark-state spectroscopy. *Nature* **459**, 1105 – 1109, (2009)

[42] Li, X.; Wu, Y. W.; Steel, D. G.; Gammon, D.; Stievater, T. H.; Katzer, D. S.; Park, D.; Piermarocchi, C.; Sham, L. J. An all-optical quantum gate in a semiconductor quantum dot. *Science* **301**, 809-11 (2003)

[43] Guest, J. R.; Stievater, T. H.; Chen, G; Tabak, E. A.; Orr, B. G.; Steel, D. G.; Gammon, D.; Katzer, D. S. Near field coherent spectroscopy and microscopy of a quantum dot system. *Science* **293**, 2224-2227 (2001)

[44] Chen, G.; Bonadeo, N. H.; Steel, D. G.; Gammon, D.; Katzer, D. S.; Park, D.; Sham, L. J. Optically induced entanglement of excitons in a single quantum dot. *Science* **289**, 1906-1909 (2000)

[45] Bonadeo, N. H.; Erland, J.; Gammon, D.; Katzer, D. S.; Park, D.; Steel, D. G. Coherent optical control of the quantum state of a single quantum dot. *Science* **282**, 1473-1475 (1998)

[46] Kima, E. D.; Truexa, K.; Xu, X. D.; Sun, B.; Steel, D. G. *et al.* Fast optically driven spin qubit gates in an inas quantum dot. *Advances in Photonics of Quantum Computing, Memory, and Communication III. Proceedings of SPIE-The International Society for Optical Engineering* 7611 (2010)

[47] DiVincenzo, D. P. The physical implementation of quantum computation. *Fortschr. Phys.* **48**, 771 (2000)

[48] http://www.cs.sandia.gov/~sjplimp/lammps.html

[49] Troullier, N.; Martins, J. L. *Phys. Rev. B* **43**,1993 (1991)

[50] Vanderbilt, D. *Phys. Rev. B* **41**, 7892 (1990)

[51] Kresse, G.; Hafner, J. *J. Phys.: Condens. Matter* **6**, 8245 (1994)

Chapter 3
Force Field Development and Evaluation for Molecular Dynamics Simulations of Polyhedral Oligomeric Silsesquioxanes

3.1 Introduction

In molecular crystal solids the intermolecular interactions are weak compared to intramolecular interactions. Therefore, conventional DFT calculation methods will not be able to accurately describe the crystal structure. While reliable and successful incorporation of van der Waals functions into *ab initio* DFT codes is currently underway, it was not available at the outset of this project and we therefore had to rely on empirical force fields that could be used in MD simulations for the investigation of the self-assembly of organic molecular systems. The structures predicted by MD can still be verified using *ab initio* DFT calculations.

The first step in our MD simulation approach was to identify a suitable force field for SQ-based building blocks and, if necessary, parameterize it. In this chapter, we describe a newly parameterized reactive MD force field for the

simulation of T8 SQ molecular systems and compare the results it produces to those achieved using an existing force fields T8 SQ.

Figure 1-1 shows the molecular structure of the simplest cubic octasilsesquioxane, with the chemical formula $H_8Si_8O_{12}$ with the eight reactive silicon sites occupied by hydrogen atoms. Larsson *et al* were among the earliest experimentalists to study T8 H-SQ and a variety of alkyl and aryl functionalized T8 SQ molecular crystals by X-ray diffractometry methods.[1-3] The crystal structures of other octasubstituted silsesquioxanes $R_8Si_8O_{12}$, with R = $-C_2H_3$ [4], $-CH_3$ [5], -Cl [6], $-nC_3H_6I$[7] were solved in a series of investigations. More recently, Waddon *et al* reported the crystal structure of $(cyclopentyl)_7(norbornyl)(Si_8O_{12})$ [8, 9], which has been used as monomer in SQ composite applications. All these studies indicate that in the crystal structures formed by alkyl-substituted octasilsesquioxane molecules, the SQ cages are packing parallel to each other in approximately rhombohedral arrangements.

To properly understand and predict the packing and crystallization behavior in T8 SQ based molecular materials, it is necessary to have a force field that can correctly describe molecular level interactions between SQ units, so as to facilitate MD simulations of these systems.

To accomplish this, the in house charge-transfer reactive (CTR) force field FLX[10] was parameterized by a trial and error method. With this force field, the crystal

structures and selected thermal properties of T8 H-SQ were investigated via MD simulations. The performance of our force field was benchmarked against that of other force fields described in the literature, including the Condensed-phase Optimized Molecular Potentials for Atomistic Simulation Studies force field (COMPASS), a simplified version of COMPASS [11, 12], and the Universal Force Field (UFF) [13]

3.2 FLX Force Field

The FLX force field, includes a Coulomb term, a Born-Huggins-Mayer repulsive term, a three-body term, and a charge transfer term. It was initially conceived to study phase transformations in silica, which led to a number of new insights and discoveries.[14] Given the mixed covalent ionic bonding between silicon and oxygen, the partial charges localized on these atoms and the resulting long-range Coulomb interactions likely play an important role in the self-assembly behavior of SQ. The various force field terms are described in the following. The total energy per atom is

$$E_{total} = E_{coulomb} + E_{BMH} + E_{Threebody} + E_{\xi_6} \quad , \tag{3.1}$$

where $E_{coulomb}$ is the non-bonding long-range Coulomb interaction term

$$E_{coulomb} = \frac{1}{4\pi\varepsilon_0} \sum_{j \neq i}^{N} \frac{q_i q_j}{r_{ij}} \tag{3.2}$$

q_i is a variable point charge localized on atom i that is defined as

$$q_i = -2\sum_{k=1}^{NN} \delta_{ik}\zeta_{ik} \quad , \tag{3.3}$$

where δ_{ik} is the transferable charge between atom i and its nearest bonded neighbor k, and ζ_{ik} is the charge transfer function.

$$\zeta_{ik} = (e^{(r_{ik}-a)b} + 1)^{-1} \quad , \tag{3.4}$$

where r_{ik} is the distance between atom i and its nearest neighbor k, and a and b are empirical parameters. $E_{\xi 6}$ describes the attractive interaction between two oscillating dipoles,

$$E_{\xi_6} = -\sum_{j\neq i}^{N} \frac{C_{ij}}{r_{ij}^6} \quad , \tag{3.5}$$

where, C_{ij} is also an empirical parameter. E_{BMH} is a Born-Mayer-Huggins repulsive term

$$E_{BMH} = \sum_{j\neq i}^{N} A_{ij}\left(1 + \frac{z_i}{n_i} + \frac{z_j}{n_j}\right)e^{(\sigma_i + \sigma_j - r_{ij})\cdot\rho_{ij}} \quad , \tag{3.6}$$

where A_{ij} is the pre-exponential factor ρ_{ij} is the hardness parameter, z_i is the valence electron number, n_i is number of outer shell electrons, amd σ_i is a parameter indicative of size of the atom. $E_{Threebody}$ describes the directional character of covalent bonds by constraining the angle between pairs of bonds. In

this term, angular constraints are coupled with a covalent attractive interaction, i.e., one does not exist without the other, which is unlike most other threebody interaction potentials described in the literature. This coupling prevents artificial channeling of particle trajectories, which along with the charge transfer are a major hallmark of the potential that allows for the simulation of reactions and changes in bonding patterns.

$$E_{Threebody} = \sum_{j=1}^{NC-1} \sum_{k=j+1}^{NC} (E_{ij} + E_{jk}) e^{-\gamma_{ijk}(\theta_{ijk}-\theta_0)^2} , \quad (3.7)$$

where, θ is the angle formed by bonds i-j and i-k, θ_0 is the equilibrium angle, and γ_{ijk} is an angular spring constant.

3.3 FLX Force Field Parameterization

3.3.1 Potential parameterization tool and methods

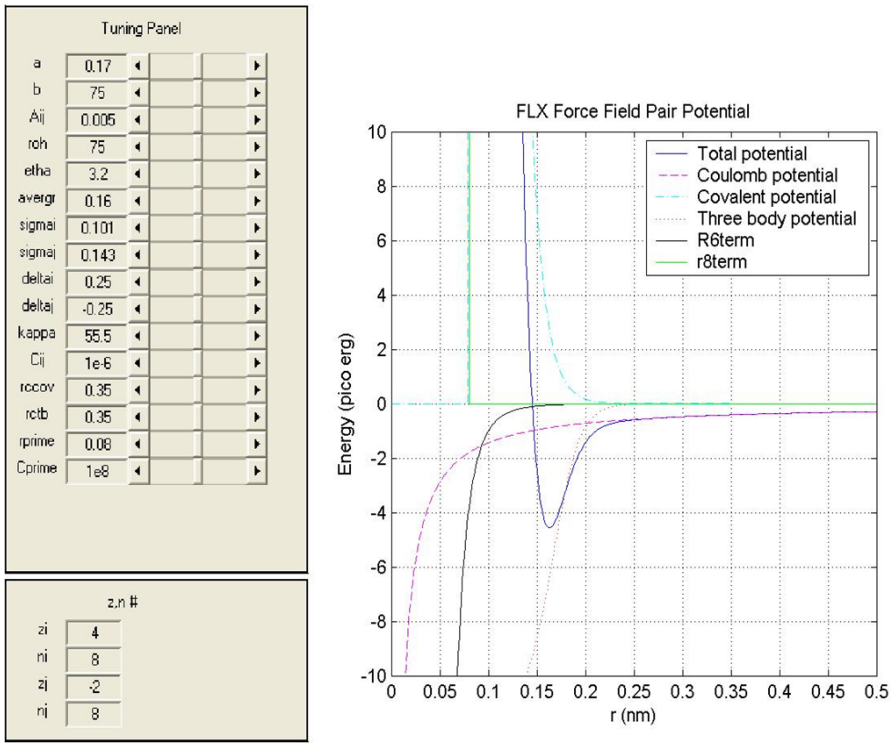

Figure 3-1 A pair potential tuning and plotting tool by GUI programming in Matlab

Since the FLX force field contains a non-linear three body term, a numerical method to parameterize the force field usually is not derived easily. The main method to parameterization is therefore by trial and errors. To assist in this potential parameter optimization, a Matlab program was developed that has a graphical user interface to visualize the interaction potential function and to assist in tuning the potential shape via adjustment of interaction parameters. An example screen shot is shown in Figure 3-1[14]. In this tool, initial guesses for parameters can be entered in a text box and then adjusted by dragging the slide bar while the graphical display of the pair potential curve on the screen is

refreshed in response. The effect is that the changes in atomic interactions become apparent in real time, i.e., as fast as it takes for the potential energy curves to be redrawn.

Although FLX potential parameters for silica were established in earlier work, we found that these parameters are not correct for describing the SQ molecule. This is not a surprising result. There is apparently a significant difference between covalent bonding in glassy or crystalline compounds and molecular T8 SQ molecules. The cohesive strength and elastic properties of molecular crystals is governed long-range electrostatic and van der Waals interactions, while in a glassy or crystalline inorganic solid these properties can be attributed to ionic and covalent bonding. Therefore, a complete new set of parameters had to be developed. The initial parameters values are derived by reproducing the pair chemical bond energies obtained from reference books. These values were used as initial criteria to select training parameters. With each set of trial parameters, a number of simulations and analysis were run to examine the performance of these parameters.

The benchmark of the parameterization work was based on reproducing existing experimental data or/and quantum mechanical calculation results, which include crystal density, bond lengths and angles, and vibrational properties, i.e., infrared spectra, and structural characteristics, i.e., X-ray diffraction patterns, etc.

After examination of simulation results, parameters are further optimized until a satisfactory parameter set is found. This tool noticeably expedites the parameterization of the FLX force field, which requires optimization of 48 parameters in total, to simulate T8 H-SQ, and thus, greatly reduces the time and effort to parameterize the force field. However, even with this tool, the parameterization work for the FLX force field via trial and error for T8 H-SQ is still not trivial. There are 48 parameters to be tuned at the same time. Some simulated properties are very sensitive to the parameter values. When confronted with more complex multi-component chemical systems, higher-level parameterization methods are needed for faster FLX potential parameterization. In this work, a significant effort was made to develop fine FLX parameter sets for the T8 SQ system. Eventually, an ideal parameter set was found, as reported in the Table 3-1.

Table 3-1 Optimized parameters for FLX force fields

Element	σ (Å)	Z					
Si	0.101	4					
O	0.143	2					
H	0.065	1					
Pair	A_{ij} (10^{-19} J)	ρ_{ij} (nm^{-6})	λ_{ij} (nm)	η_{ij} (nm)	κ_{ij} (nm^{-1})	r_{ij} (nm)	C_{ij} (Jm^{-1})
Si-Si	0.10	34.50	0	0	34.50	0	0
Si-O	0.05	45.12	0	3.2	45.12	0.1600	0
Si-H	0.10	56.20	0	3.0	56.20	0.1515	0
O-O	0.10	30.50	0	0	30.50	0	0
O-H	0.48	80.50	0	3.0	80.50	0	0
H-H	0.10	34.50	0	0	34.50	0	0
Charge Transfer	δ_{ij} (e)	a (nm)	b (nm^{-1})				
Si-O	-0.1940	0.20	57				
Si-H	-0.0230	0.19	75				
Triplet	γ_{ijk}(rad^{-2})	θ(rad)					
O-Si-O	0.21	1.911					
O-Si-H	0.49	1.911					
Si-O-Si	40.19	2.591					

3.3.2 Bond lengths and angles validation

A first test of the quality of the parameters we developed consisted of determining the geometric characteristics of the crystalline configuration of T8 H-SQ at 300K, simulated in the NPT ensemble. The calculated bond lengths and angles are in good agreement with experimental findings[1-3], with quantum mechanical calculations by VASP with plane wave basis sets, with results from DMOL calculations based on atomic orbital numerical basis sets, and with Gaussian, as well as with calculations using other force fields, including COMPASS implemented in Cerius2, UFF, and EA/CII implemented in DL_POLY. The results of this comparison are summarized in Table 3-2.

Table 3-2 Bond lengths and angles by FLX and other methods

	Exp. [a]	Plane Wave (VASP)	Atomic Orbital (DMOL)	RHF (Gaussian 98)	J. Kieffer FLX	Cerius2 COMPASS	DL_POLY (EA/CII)	DL_POLY (UFF)
Si-O (Å)	1.619	1.630	1.654	1.650	1.620	1.624	1.643	1.593
Si-H (Å)	1.476	1.463	1.481	1.462	1.470	1.473	1.484	1.473
Si-O-Si (°)	147.5	146.7	145.9	148.7	146.1	146.9	145.6	147.0
O-Si-O (°)	109.6	109.6	109.6	109.1	109.6	110.2	109.8	109.3

a) Reference [1-3]

3.3.3 Infrared spectrum calculation by FLX

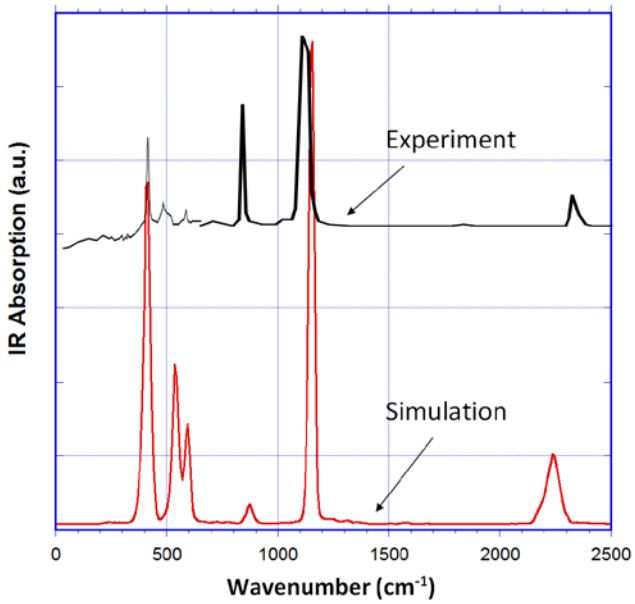

Figure 3-2 Comparison of calculated infrared spectrum with experiment

The ability of the FLX force field, using the parameter set we derived, to reproduce vibrational properties was evaluated by calculating the infrared spectrum of crystalline T8 H-SQ from the Fourier transform of the dipole current-dipole moment time correlation function according to

$$I(\omega) = \frac{\hbar}{4\pi^2(1-e^{-\hbar\omega/k_BT})}\,\mathrm{Im}\left(\int_{-\infty}^{\infty}\langle\dot{\mu}(0)\mu(t)\rangle e^{-i\omega t}dt\right), \qquad (3.8)$$

where μ is the total electrostatic dipole moment of the simulated configuration; the frequency dependent absorption coefficient for electromagnetic radiation is then obtained as the imaginary part of the Fourier transform of the dipole current-dipole moment time correlation function, $\langle \dot{\mu}(0)\mu(t) \rangle$. [10] To evaluate equation 3.10, the force field needs to account for the fluctuations in the charge distribution in the simulated structure. The infrared spectrum generated using FLX agrees very well with the experimental results [15, 16], as illustrated in Figure 3-3. The peak positions in the simulated spectrum agree with experimental data to within less than 50 cm^{-1}, and the relative intensities also match those of the experimental spectrum well. We find that peak positions and relative intensities depend very sensitively on potential parameters. Changing the spacing between two spectral peaks invariably requires the adjustment of more than one potential parameter, and vice versa, changing a single potential parameter affects the position and intensity of more than one spectral feature. This is why it is difficult to design interaction potentials that accurately reproduce vibrational spectra. In our experience, the agreement between simulated and experimental spectra shown in Figure 3-2 can be considered to be very good. In fact, vibrational properties such as IR spectra are not often reported in the literature. Moreover, on the basis of a simulated spectrum, it is straightforward to assign the vibrational modes of motion that correspond to the various spectral peaks. This can be done by Fourier filtering the underlying atomic trajectories.[10]

Accordingly, we were able to confirm that the 2280 cm^{-1} peak corresponds to the Si-H stretching mode, the 1150 cm^{-1} peak to the asymmetric Si-O-Si stretching mode, the 890 cm^{-1} peak to rattling of Si in its tetrahedral coordination shell, and the three low-frequency peaks to various Si-O-Si rocking modes. We also note that, except for the highest-frequency mode, there is a strong similarity between this spectrum and that for cristobalite silica.[14]

3.3.4 Crystal symmetry

After equilibration for 100 picoseconds, a production simulation run of a T8 H-SQ crystal in the NPT ensemble was performed for about 10 picoseconds at 300K, using the Parrinello-Rahman method in FLX with the above parameter set. Initial coordinates were constructed based on experimental X-ray diffraction data in a hexagonal unit cell with the $R\bar{3}$ space group symmetry [1].

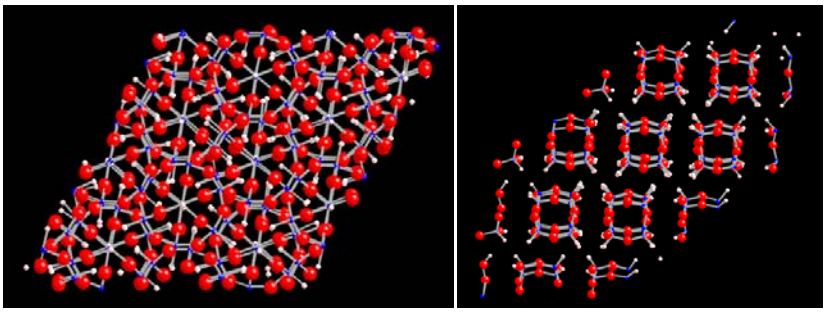

Figure 3- 3 Simulated crystal structure

The crystal with these average coordinates was found to be very stable at temperatures below 600 K. Hence, the atomistic scale simulations successfully reproduced the experimental determined crystal structure of T8 H-SQ. Above

600 K, the crystal starts to melt. This melting temperature is in good agreement with the experimental value of 523 K[1] differing by ~15%. The crystal structures are shown in Figure 3-3. The pair correlation functions, g(r), which describes how the atomic density varies as a function of the distance from one particular atom, and is defined by:

$$g(r) = \frac{V}{4\pi r^2 N^2}\left\langle \sum_i \sum_{j \neq i} \delta(r - r_{ij}) \right\rangle \quad , \tag{3.9}$$

are shown in Figure 3-4 (Figure is adapted from [17]). In the same figure, our pair correlation functions are also compared with those resulting from simulations using other force fields. These calculated pair correlation functions showed very similar atom pair distance through the simulated structures.

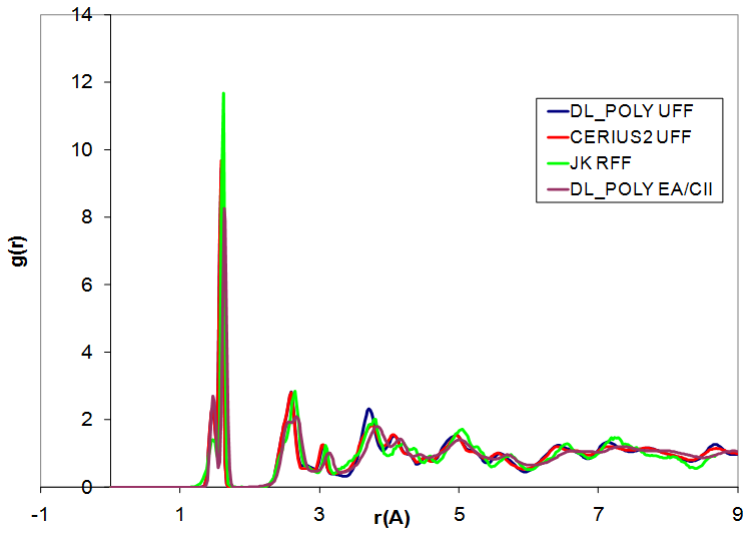

Figure 3-4 Total pair correlation functions for the $H_8Si_8O_{12}$ system obtained from the UFF, COMPASS, hybrid COMPASS (HC w/o) and CTR force fields

3.3.5 T8 H-SQ packing behavior

When T8 H-SQ cubes crystallize, the preferred packing pattern is always so that neighboring SQ cages are parallel to each other but shifted in (0 0 1) direction by half the cubic cage edge. Eight of these closed SQ cubes form a rhombohedral primitive unit cell, with $R\bar{3}$ crystal symmetry. This preferred packing behavior has been confirmed by *ab initio* calculations and experimental data [1-9,18]. It is interesting to note that almost all the known octa-functionalized SQ molecules, with all functional groups being the same, have a rhombohedral unit cell when crystallizing. [1-3, 29-31]

In order to test whether the parameterized FLX force field can reliably reproduce this preferred rhombohedral packing behavior, eight face to face packed SQ cubes were placed in a simulation box with cubic symmetry under periodic

boundary conditions. A simulation in the NPT ensemble with the Parrinello-Rahman method and a small negative pressure (i.e., tensile stress) of -0.2M Pa using the parameterized FLX force field was performed. The results showed the eight cubic packed SQ cubes transformed from a cubic configuration to a rhombohedral unit cell. The starting and ending configurations of this transformation are shown in the Figure 3-5.

a) 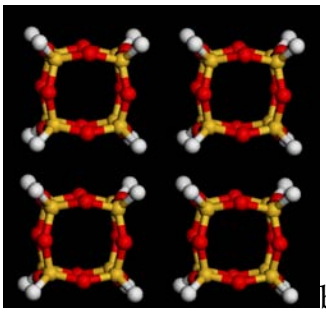 b) 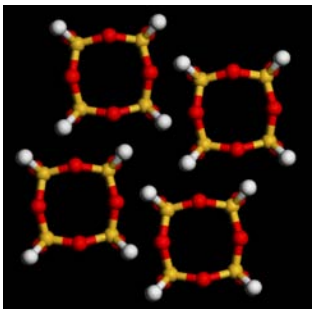

Figure 3-5 a) Simple cubic SQ unit cell; b) transforming to a rhombohedral one

3.4 Force Fields Evaluation

3.4.1 COMPASS force field

The performance of FLX for the simulation of crystalline T8 SQ was compared to that of other force fields, including UFF and COMPASS. Among these force fields, the Condensed-phase Optimized Molecular Potentials for Atomistic Simulation Studies force field (COMPASS) was able to describe the T8 SQ geometric and assembly behavior very well. Since UFF and simplified COMPASS are both subsets of COMPASS, only the latter is described here. The total potential energy per particle is

$$E = E_b + E_\theta + E_\phi + E_\chi + E_{bb'} + E_{b\theta} + E_{b\phi} + E_{\theta\phi} + E_{b\theta\phi} + E_{coul} + E_{vdw} \quad (3.10)$$

The terms on the right hand side of equation 3.10 can be divided into the following types: (i) Valence terms, which include (a) bond stretching (E_b), angle bending (E_θ), torsion (E_Φ), out-of-plane angle ($E\chi$); (ii) coupling terms, which include bond-bond ($E_{bb'}$), bond-angle ($E_{b\theta}$), bond-torsion ($E_{b\Phi}$), bond-angle-torsion ($E_{b\theta\Phi}$) interactions,, and (iii) non-bonded interaction terms, which include the Coulomb potential (E_{coul}) and the LJ 9-6 function (E_{vdw}) describing van der Waals interactions.

The bond stretching term E_b is defined by a quartic function:

$$E_b = k_2(b - b_0)^2 + k_3(b - b_0)^3 + k_4(b - b_0)^4 \ , \quad (3.11)$$

where b_0 is the equilibrium bond length, b is the actual bond length value, k_2, k_3 and k_4 are constants. The angle bending term E_θ is defined as

$$E_\theta = H_2(\theta - \theta_0)^2 + H_3(\theta - \theta_0)^3 + H_4(\theta - \theta_0)^4 \ , \quad (3.12)$$

where θ_0 is the equilibrium angle, θ is the actual angle, and H_2, H_3 and H_4 are empirical parameters. The torsion term E_Φ is defined as

$$E_\Phi = V_1(1 - \cos(\Phi)) + V_2(1 - \cos(2\Phi)) + V_3(1 - \cos(3\Phi)) \ , \quad (3.13)$$

where Φ is the dihedral angle, and V_1, V_2 and V_3 are constants. The electrostatic interactions are described by the Coulomb function

$$E_{coul} = \sum_{i,j} \frac{q_i q_j}{r_{ij}} \ , \tag{3.14}$$

where q_i and q_j are the partial point charges of atoms i and j, and r_{ij} is the distance between atoms i and j. The partial charges are computed using the method of bond increments (3.15), as implemented in COMPASS by Sun[11,12]. For atom i, the partial charge is given by the sum of all bond charge increments δ_{ij} by

$$q_i = \sum_j \delta_{ij} \ , \tag{3.15}$$

where j represents all atoms that are covalently bonded to atom i. The van der Waals interactions are described by the Lennard Jones 9-6 potential

$$E_{vdw} = \varepsilon_0 \left\{ 2\left[\frac{r_0}{r_{ij}}\right]^9 - 3\left[\frac{r_0}{r_{ij}}\right]^6 \right\} \ , \tag{3.16}$$

where ε_0 represents the depth of the potential well, r_0 is the distance between the atoms where $E_{vdw} = -\varepsilon_0$ and r_{ij} is the actual distance between the atom pair. The van der Waals potential is calculated for every atom pair within a certain cutoff radius, usually 10 Å, except for atoms separated by only two or less bonds on the same chain. The Lennard Jones parameters ε_0 and r_0 are given for similar atom pairs. Otherwise, a 6th order combining rule is used to calculate the parameters (3.17) and (3.18).

$$r_{IJ} = \left(\frac{r_I^6 + r_J^6}{2} \right)^{1/6} \tag{3.17}$$

$$\varepsilon_{IJ} = \left(\frac{2 r_I^3 r_J^3 \sqrt{\varepsilon_I \varepsilon_J}}{r_I^6 + r_J^6} \right), \tag{3.18}$$

where r_I, r_J, ε_I, ε_J represent the atomic interaction parameters.

3.4.2 MD simulation details

MD simulations using COMPASS were done by our collaborators Ionescu *et al* using the public domain DL_POLY 2 code [19] and Materials Studio[20]. The FLX force field simulation is carried out using our in house FLX MD code. The simulation details are as follows: The $H_8Si_8O_{12}$ crystal system in our simulations has a 2 by 2 by 2 supercell, which contains a total of 24 SQ molecules or 672 atoms. Initial configurations were set up according to the experimental crystal structure [1]. Periodic boundary conditions were used in all simulations. A time step of 1 fs was used. The Nose-Hoover constant temperature algorithms, together with the general form of the Parrinello-Rahman constant pressure algorithm were used in the NPT ensemble simulations. During the MD simulation, the infrared spectra of the crystal were computed from the Fourier transform of the instantaneous total dipole current-dipole moment autocorrelation function.

3.4.3 Results

The intra-molecular structure was predicted using FLX and the other force fields and characterized based on the average bond lengths and angles for various temperatures. Comparisons were then made with experimental data from the literature and *ab initio* calculation results obtained by our collaborators. Table 3-3 presents selected structural parameters for polyhedral octahydridosilsesquioxane ($H_8Si_8O_{12}$). FLX and all the other potential models give very good predictions of bond lengths and angles compared to the experimental values and *ab initio* calculation results.

Table 3-3 Selected structural parameters of octahydridosilsesquioxane

	CTR	UFF	COMPASS	HC	HCw/o	Expt. [a)]
Si-O(Å)	1.620	1.590	1.624	1.670	1.638	1.619
Si-H(Å)	1.476	1.464	1.473	1.482	1.476	1.481
Si-O-Si(°)	146.8	147.0	147.0	146.7	146.9	147.5
O-Si-O(°)	109.7	109.9	110.2	110.3	110.1	109.6

a)Reference [1-3]

Our results demonstrate that FLX force fields satisfactorily reproduce available experimental data for the conformation of SQ monomers. We also evaluated molecular packing by comparing densities, unit cell parameters, and X-ray diffraction patterns of the simulation results using different force fields and experimental data. The average densities and unit cell parameters are listed in Table 3-4. The simulation carried by FLX uses a simulation box containing

3X3X2 unit cells. The structures were allowed to equilibrate for 100 ps at 100K for $H_8Si_8O_{12}$ and then data were collected from 10 ps simulations.

Table 3-4 Densities and unit cell parameters of octahydridosilsesquioxane

	$H_8Si_8O_{12}$ 100K			$H_8Si_8O_{12}$ 300K		
	ρ(g/cc)	a(Å)	c(Å)	ρ(g/cc)	a(Å)	c(Å)
UFF	2.164	8.67	15.02	2.131	8.70	15.12
HC	1.998	8.88	15.48	1.950	8.95	15.60
HC w/o	2.041	8.84	15.29	1.988	8.91	15.46
CTR	2.0683	8.74	15.55	2.044	8.76	14.49
Experimental	1.97[a)]	9.04[a)]	15.16[a)]	1.91[b)]	9.13[b)]	15.35[b)]

a) Reference [22]

b) Reference [1]

Figure 3-6 is a simulation snapshot for the $H_8Si_8O_{12}$ crystal at 100K. The initial hexagonal unit cell, which is in agreement with experimental data, was preserved during the simulation [1, 22]. The predicted crystal structure parameters for crystalline $H_8Si_8O_{12}$ at 100K and 300K are shown in Table 3-4, along with experimental data. The results show that FLX overestimates the experimental crystal density by approximately 10% in all cases considered. The prediction of the density and unit cell dimensions by a Hybrid COMPASS force field including electrostatic interactions is the most accurate.

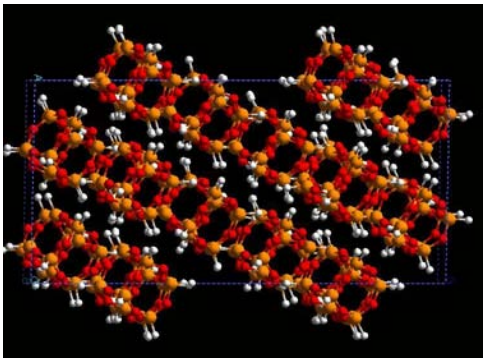

Figure 3-6 Snapshot of T8 H- SQ crystal.

The structure of the simulated crystal was also compared to experiment by calculating the powder X-ray diffraction patterns, using an algorithm we developed based on classical diffraction theory. Supercell crystal coordinates for the simulated structures after equilibration at different temperatures were used for the diffraction pattern calculations, as well as experimental coordinates were obtained from [1-3]. Comparison of the diffraction patterns are shown in Figures 3-7.[17] The X-ray diffraction patterns for simulated crystals and experiment is satisfactory. The UFF force field yields the least accurate pattern. The crystal structures predicted by Hybrid COMPASS (HC), with or without electrostatic interactions (HC w/o), are better in reproducing the experimental results.

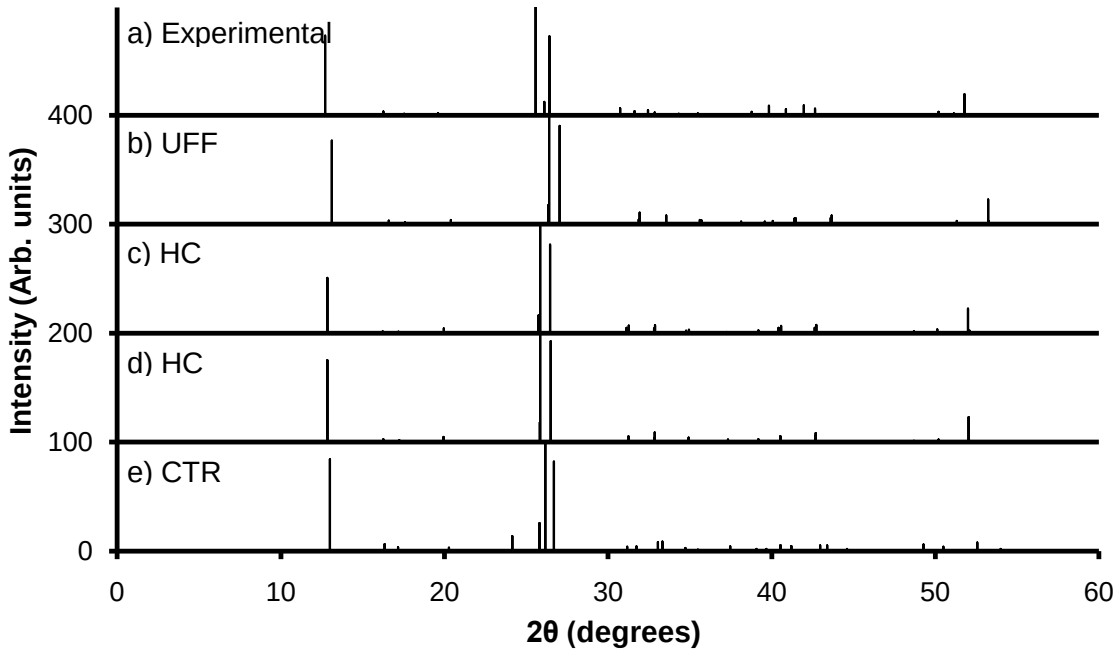

Figure 3-7 The X-ray pattern for simulated crystal compared with experiment.

The melting properties were also studied to evaluate the force fields. Melting property provides a measure of how well the bond energies are reproduced. Simulations were carried out using the Parrinello-Rahman algorithm [23] in the NPT ensemble. The crystal structures were equilibrated for 100 ps at 100K for $H_8Si_8O_{12}$. Data were collected from 100 ps for each simulation. After 100 ps, the system temperature was raised by 100K and crystal structures were equilibrated for 100 ps and densities were collected again from a 100 ps simulation. This process was repeated until the simulated structures melted. The result is shown in Figure 3-8 (figure adapted from [17]).

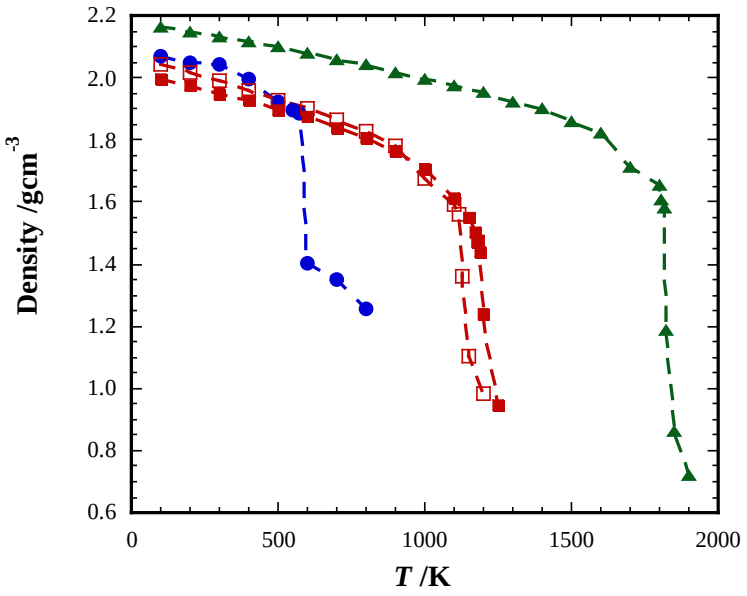

Figure 3-8 The melting properties based on different force fields. Density as a function of temperature for the $H_8Si_8O_{12}$ crystal obtained from the FLX (●), Hybrid-COMPASS (□), HC w/o (■) and UFF (▲).

Since the crystal-liquid phase transition is of the first order, thermodynamic and transport properties of the system, such as density, and enthalpy, as well as self diffusion coefficients show discontinuous behavior. Thus, the melting point T_{mp} can be determined as the temperature at which these thermodynamic quantities and rate coefficients change abruptly. In addition, the translational order parameter ρ(k) [24] for the configuration has also been computed to determine the melting transition. The order parameter is given by

$$\rho(\mathbf{k}) = \frac{1}{N}\sqrt{\left(\sum_{1}^{N}\cos(\mathbf{k}\cdot\mathbf{r}_i)\right)^2 + \left(\sum_{1}^{N}\sin(\mathbf{k}\cdot\mathbf{r}_i)\right)^2}\ , \tag{3.19}$$

where, N is the number of molecules in the system, k is the reciprocal lattice vector and r_i are the position vectors pointing to the centers of mass of the SQ

molecules. The translational order parameter ρ(k) is a measurement of the order of a system. It reaches 1 for a perfectly ordered crystal, and 0 for a totally disordered liquid. The result for T8 SQ is shown in Figure 3-9[17].

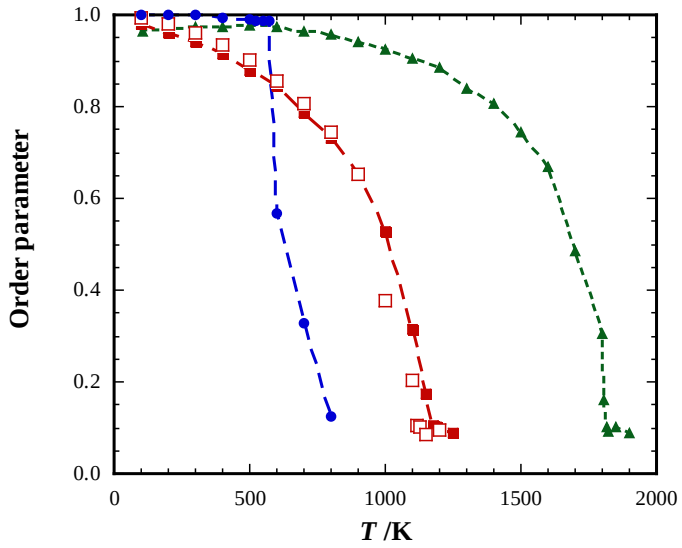

Figure 3-9 Translational order parameter as a function of temperature for the $H_8Si_8O_{12}$ crystal obtained from the FLX (●), Hybrid-COMPASS (■), HC w/o (□) and UFF (▲).

The transport properties of T8 SQ simulated using FLX and other force fields was also evaluated. The self diffusion coefficients were computed using the Einstein diffusion equation: [24]

$$D = \lim_{t\to\infty} \frac{1}{6}\frac{d}{dt}\left\langle \left|\mathbf{r}_i(t) - \mathbf{r}_i(0)\right|^2 \right\rangle \quad , \tag{3.20}$$

where D is the self diffusion coefficient determined for the SQ, $r_i(0)$ is the position of the centers of mass at the time 0, and $r_i(t)$ the one at time t. The self-diffusion coefficient is of the order of 10^{-13} m^2/s or smaller for a solid and 10^{-9}

m^2/s for a liquid. The diffusion coefficient magnitudes for SQ simulated using the various force fields are shown in Figure 3-10 as a function of temperature.[17] The melting point can be identified as the temperature at which the diffusion coefficient begins to ascend steeply on the scale shown in figure 3-10.

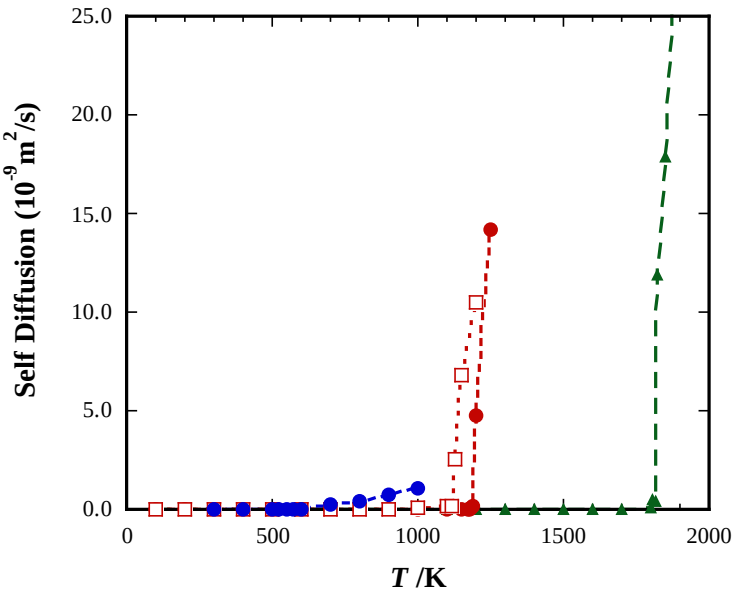

Figure 3-10 The self diffusion coefficient as a function of temperature for the $H_8Si_8O_{12}$ crystal obtained from the FLX (●) on the left side , Hybrid-COMPASS (●) on the right side, HC w/o (□), and UFF (▲).

Note that all methods used to identify the melting temperature of the $H_8Si_8O_{12}$ yield results in agreement with each other, and all methods give melting temperatures far beyond the experimental value of 523 K, except for FLX.

Determining melt transitions using molecular simulation is not a trivial task [22]. Using perfect, defect free crystals leads to higher melting temperatures than real crystals that include defects and surfaces, which have been shown to initiate

melting [25]. For this reason MD simulations typically overestimate the melting temperature by 20-30% [22]. There have been reports of other refined methods to determine the melting transition, such as finding the melting temperature as a function of number of defects in the crystal [25], finding the melting temperature as a function of increasing size of nano crystal size, by extrapolating to infinite size [26], introducing a solid-liquid interface in the system,[27] or by calculating the Gibbs free energies of the system [28]. In this work, attempts were made to apply the first two methods, without any conclusive results. There is one experimental report though that mentions a clear melting temperature of 523K[1]. Thus, all potential models used in this work seem to overestimate the melting temperature by at least a factor of two, except for FLX, which estimates the melting temperature at about 600 K.

3.5 Summary

The charge-transfer reactive (CTR) force field FLX for $H_8Si_8O_{12}$SQ molecule was parameterized by using a graphical parameter tuning tool that we developed for this purpose. The simulations of T8 H-SQ molecule with this force field and other force fields described in the literature, including COMPASS and UFF shows that they all successfully reproduce the experimentally crystalline structure of T8-SQ. The performance of COMPASS is slightly better in reproducing experimental x-ray diffraction patterns than other potentials. However, as far as vibrational, kinetic, and thermodynamic properties are

concerned, the FLX force field yields the most accurate results. These results suggest that when simulating SQ using the MD method, the packing behavior can be accurately predicted with both the FLX and COMPASS force fields. The melting temperature will be more difficult to predict using COMPASS than FLX force field.

3.6 Reference

[1] Larsson, K. *Arkiv for Kemi* **16**, 215 (1960)

[2] Larsson, K. *Arkiv for Kemi* **16**, 203 (1960)

[3] Larsson, K. *Arkiv for Kemi* **16**, 209 (1960)

[4] Baidina, I. A.; Podberezskaya, N. V.; Alekseev, V. I.; Martynova, T. N.; Borisov, S. V.; Kanev, A. N. *Journal of Structural Chemistry* **20**, 550 (1979)

[5] Koellner, G.; Muller, U. *Acta Crystallographica Section C-Crystal Structure Communications* **45**, 1106 (1989)

[6] Tornroos, K. W.; Calzaferri, G.; Imhof, R. *Acta Crystallographica Section C-Crystal Structure Communications* **51**, 1732 (1995)

[7] Dittmar, U.; Hendan, B. J.; Florke, U.; Marsmann, H. C. *Journal of Organometallic Chemistry* **489**, 185 (1995)

[8] Waddon, A. J.; Coughlin, E. B. *Chemistry of Materials* **15**, 4555 (2003)

[9] Waddon, A. J.; Zheng, L.; Farris, R. J.; Coughlin, E. B. *Nano Letters* **2**, 1149 (2002)

[10] Anderson, D. C.; Kieffer, J.; Klarsfeld, S. *Journal of Chemical Physics* **98**, 8978 (1993)

[11] Sun, H. *Macromolecules* **28**, 701 (1995)

[12] Sun, H. *Journal of Physical Chemistry B* **102**, 7338 (1998)

[13] Rappe, A. K.; Casewit, C. J.; Colwell, K. S.; Goddard, W. A.; Skiff, W. M. *Journal of the American Chemical Society* **114**, 10024 (1992)

[14] Huang, L.; Kieffer, J. *Physical Review B* **69**, 224204 (2004)

[15] Bartsch, M.; Bornhauser, P.; Burgy, H.; Calzaferri, G. *Spectrochimica Acta Part A-Molecular And Biomolecular Spectroscopy* **47**, 1627 (1991)

[16] Beer, R.; Burgy, H.; Calzaferri, G.; Kamber, I. Journal Of Electron Spectroscopy And Related Phenomena 1987, 44, 121.

[17] Ionescu, T. C.; Qi, F.; McCabe, C.; Striolo, A.; Kieffer, J.; Cummings, P. T. Evaluation of forcefields for molecular simulation of polyhedral oligomeric silsesquioxanes. *Journal of Physical Chemistry B* **110**, 2502 (2006)

[18] Durandurdu, M.; Kieffer, J. unpublished results.

[19] Smith, W.; Forester, T. R. *Journal of Molecular Graphics* **14**, 136 (1996)

[20] Inc., A. S. http://www.accelrys.com/mstudio/ms_modeling/index.html

[21] Auf der Heyde, T. P. E.; Burgi, H. B.; Burgy, H.; Tornroos, K. W. *Chimia* **45**, 38 (1991)

[22] Velardez, G. F.; Alavi, S.; Thompson, D. L. *Journal of Chemical Physics* **119**, 6698 (2003)

[23] Parrinello, M.; Rahman, A. *Physical Review Letters* **45**, 1196 (1980)

[24] Allen, M. P.; Tildesley, D. J. *Computer Simulation of Liquids* Oxford University Press: Oxford (1987)

[25] Agrawal, P. M.; Rice, B. M.; Thompson, D. L. *J. Chem. Phys.* **118**, 9680 (2003)

[26] Briant, C. L.; Burton, J. J. *J. Chem. Phys.* **63**, 2045 (1975)

[27] Morris, J. R.; Song, X. Y. *J. Chem. Phys.*, **116**, 9352 (2002)

[28] Leach, A. R. *Molecular modelling : principles and applications, 2nd edition* Prentice Hall: Harlow, England ; New York (2001)

[29] Handke, B.; Jastrzebski, W. *et al.* Structural studies of crystalline octamethylsilsesquioxane $(CH_3)_8Si_8O_{12}$. *Journal of Molecular Structure* **887** 159-164 (2008)

[30] Calzaferri, G.; Imhof, R.; Törnroos, K. W. Structural and vibrational properties of the octanuclear silasesquioxane $C_6H_{13}(H_7Si_8O_{12})$. *Journal of the Chemical Society-Dalton Transactions* **21**, 3123-3128 (1994)

[31] Waddon, A. J.; Coughlin, E. B. Crystal structure of polyhedral oligomeric silsesquioxane (POSS) nano-materials: a study by X-ray diffraction and electron microscopy. *Chem. Mater.* **15**, 4555-4561 (2003)

Chapter 4
Computational Molecular Design of Organic-Inorganic Hybrid Semiconductors Using Polyhedral Oligomeric Silsesquioxane and Acene

4.1 Introduction

With the advancement of synthesis techniques, the ability to generate novel SQ building blocks continues to evolve [1-6]. Of the multitude of molecular architectures that can be conceived, only a subset may be optimally suited for a particular application. In this context, simulation-based predictive design of molecular building blocks can be used to accelerate materials development. In this chapter we describe the example of the molecular design of SQ based organic-inorganic hybrid semiconductors, based on the combination of SQ and various members of the acene family of molecules. According to our predictions, this combination can result in targeted semiconducting molecules with structural adaptations and property improvements.

Acenes constitute a group of molecules that possess semiconductor properties. They consist of benzene rings joined together so that two adjacent rings share

one carbon-carbon bond. Joining two, three, four, or five rings in linear progression produces naphthalene, anthracene, tetracene, and pentacene, respectively, as shown in Figure 4-1. The stable configuration of these molecules is flat, i.e., all rings lie in the same plane. With increasing number of rings in the molecule the HOMO-LUMO gap decreases, and, with an energy gap of about 1 eV, pentacene is of particular interest for semiconductor applications. In crystalline form, pentacene stack in a herringbone fashion, which places the edge of one molecule next to the face of its neighbor, as shown in Figure 4-2.

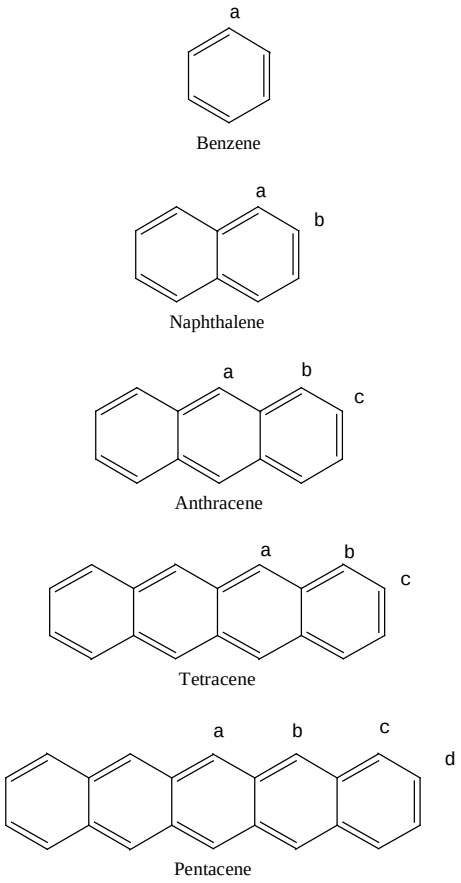

Figure 4-1 Acene molecules and labeled carbon atoms with unique symmetric positions on the molecule

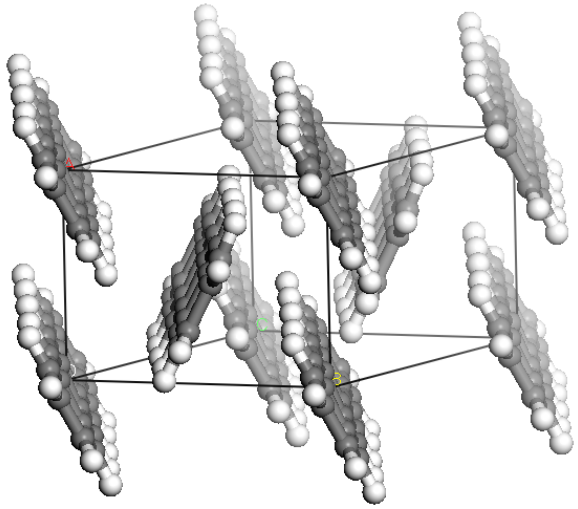

Figure 4-2 Pentacene unit cell structure showing herringbone packing fashion (Crystal unit cell reconstructed from [32])

This results in poor π - π orbital overlap between molecules and impedes electron transport. To remedy this situation, modification to acene molecules, mainly by adding side groups, have been attempted and were found to be successful in modifying the packing behavior and conductivity of the acenes [7,8]. In the crystalline structures of cube-shaped SQ molecules, i.e., octasilsesquioxane ($R_8Si_8O_{12}$) units, or T8 SQ, either terminated with hydrogen (R = H) or functionalized with small hydrocarbons, such as methyl (R = CH_3) or propyl (R = C_3H_7) groups, the peculiar slightly offset face-to-face stacking of the SQ cubes is prevalent. It appears that the long-range Coulomb interactions between the core constituents dominate the crystalline arrangements, even when the size of the organic functional groups begins to exceed that of the inorganic core. [9, 10] This observation prompted us to attempt combining SQ with acene groups with the objective to improve the stacking of the latter. Using this simulation-based

design procedure to combine SQ hybrid molecular building block configurations and acene molecules provided a potential way to design a series of new molecules that have desired crystallization behavior, as well as exhibit better electronic, mechanical, and thermal properties.

4.2 Molecular Design and Simulations

The purpose of this design approach is to find a SQ-acene hybrid molecule that exhibits improved physical properties compared to pure acene. In order to do this, we start with pentacene, which by itself is known for its good semiconductor properties as a molecular solid. The design procedure involves four steps: (i) conception of a candidate molecule and assessment of its thermodynamic stability and inherent electronic properties using DFT calculations; (ii) prediction of the structural assembly and lowest-energy crystalline configuration using Polymorph method to identify good molecular designs that associate with high density and featured parallel packing of acene groups in the crystal structures; (iii) calculation and evaluation of electronic properties for the predicted crystalline configurations using *ab initio* DFT method; and (iv) computation of mechanical and thermal properties of these structures with classical MD methods. Accordingly, by using classical force field based molecular modeling tool,[11-14] we designed a number of candidate molecules. This is done essentially by connecting two acene groups, i.e., via bonding to the labeled carbon atoms on the acenes shown in Figure 4-1, to the body diagonal

corners (two silicon atoms) of a SQ cube to maintain its molecular central symmetry so that it falls in the most probable space groups for polymorph prediction, and by choosing acenes containing between two and five rings, i.e., naphthalene, anthracene, tetracene and pentacene. For pentacene, new molecular structures constructed by bonding the pentacene to SQ cube via carbon atom a, b, c and d respectively are all studied. The molecular structure with the pentacene bonding to SQ cube through the number 4 carbon atom is found to be able to generate high density closed packing polymorphs with feature of parallel packed pentacene groups. This bonding pattern is applied to the Naphthalene, Anthracene and Tetracene directly to construct dinaphthalene-SQ, dianthracene-SQ and ditetracene-SQ molecules, as shown in Figure 4-3. Benzene was also chosen to examine the influence of number of acenes on the SQ cube to the HOMO-LUMO gap changes. Among these diacene-SQ (DACSQ) molecules, each molecule was constructed using initial coordinates that were consistent with the anticipated bonding pattern, but otherwise without any preconception concerning the steric orientation of the functional groups relative to each other or the SQ cube. The actual ground state configurations of individual DACSQ were then determined by relaxing these initial structures using *ab initio* DFT total energy minimization procedures.

From the ground state configurations of each single molecule, the crystal structures were predicted by using the Polymorph method.[11] The current

Polymorph grogram covered 10 of the 13 most frequently observed close packing space groups, including *C*2, *C*2/c, *C*c, $P\bar{1}$, $P2_1/c$, $P2_1$, $P2_12_12_1$, $Pna2_1$, *P*bca, and *P*bcn. These space groups were all included in our study. The polymorph study yields with a series of energy-minimized crystal structures of the DACSQ systems. These predicted crystals were compared to identify which molecular structure design is the most interesting one, i.e., which has best closed packing (higher density) and features parallel overlapping of acene groups. A snap shot of dipentacene-SQ molecular design is shown in Scheme 4-1.

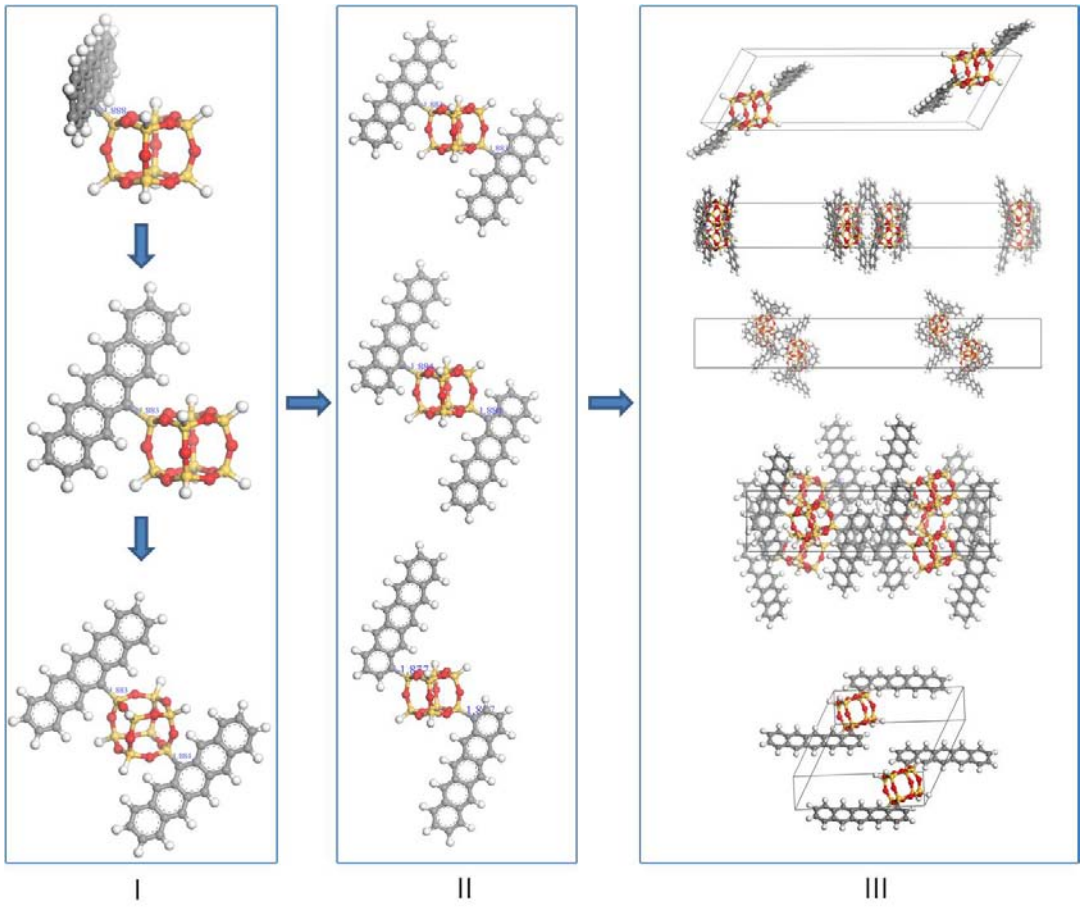

Scheme 4-1 Dipentacene-SQ molecule construction and packing evaluation process. In stage I, molecular modelling tool is used to construct the DPSQs. In stage II, DFT method is used to relax these constructed molecules. In stage III, Polymorph prediction method is used to derive the crystal structures of these DPSQs. Among the predicted crystal structures, a-DPSQ, and b-DPSQ were found to have low density polymorphs for all the 10 space groups. High density packing was found in both c-DPSQ and d-DPSQ, with d-DPSQ has overall the highest packing density. Parallel pentacene group packings were found only in $P\bar{1}$ for c-DPSQ. d-DPSQ has six polymorphs, which include $P\bar{1}$, $P2_1/c$, $C2$, $C2/c$, $P2_1$, and $Pbca$, showing parallel packing of pentacene groups the molecular design as shown in Figure 4-3 and Figur 4-8 a).

For every space group, there were a number of predicted polymorphs for the same molecule, typically from several to a few hundred. Crystal structures with the lowest total energy are considered as the final stable crystal structure in that

space group. Then total energies of these crystal structures are compared again to determine which space group is the most stable polymorph for the corresponding molecule. The space group with the lowest total energy is considered as the final crystalline state.

After the final crystalline states were identified, Dmol3 and then SIESTA are used again to further relax these crystal structures towards their ground state configurations before calculating their electronic band structure. The band structure and density of states (DOS) of these predicted DACSQ crystals are calculated by using SIESTA and Dmol3. A *k*-point grid of four by four by four is used for the Brillouin zone integration in both methods. The mechanical and thermal properties of the fully optimized crystals then were calculated by performing MD simulations using Parrinello-Rahman and other ensemble algorithms. [29, 30]

After the dipentacene-SQ (DPSQ), using the same procedure and methods, other diacene-SQ (DACSQ) molecules, namely ditetracene-SQ (DTSQ), dianthracene-SQ (DASQ) and dinaphthalene-SQ (DNSQ), were designed and studied. The procedures and methods worked very well in those prediction and evaluations. Detailed procedures and results are discussed in the following.

4.2.1 Molecular dynamics simulation and *ab initio* DFT calculations of isolated diacene-SQ molecules

Single molecule geometry optimizations were carried out using classical force field energy minimization and *ab initio* DFT methods. The molecular dynamics were carried out using COMPASS force field. [12-14] A*b initio* DFT calculations were carried by using SIESTA [15-21] and Dmol3 [22-24]. A smart geometry optimization method, which is a combination of available methods including the steepest descent method, conjugate gradient method and Newton-Raphson method, was used to relax the dipentacene-SQ molecular structure in the MD simulations. The MD optimized structure coordinates were used as input for *ab initio* DFT calculations to further optimize the structure. Additional relaxation using DFT methods yielded only very slight changes compared to the MD optimized structure, showing that the two methods agree very well in modeling this series of molecules. A comparison between the geometric measures characterizing the structures of the molecules obtained with either method is shown in Figure 4-3. Select bond lengths and angles are summarized in Table 4-1. All these measures were reproduced by the COMPASS force field with less than 3% error.

Table 4-1 Selected bond lengths and angles from MD and DFT calculation

	DNSQ		DASQ		DTSQ		DPSQ	
	DFT	MD	DFT	MD	DFT	MD	DFT	MD
Si-O(Å)	1.641-1.650	1.622-1.628	1.641-1.650	1.621-1.628	1.642-1.649	1.621-1.628	1.641-1.650	1.631-1.645
Si-H(Å)	1.467-1.468	1.470-1.472	1.467-1.468	1.468-1.470	1.467-1.468	1.469-1.472	1.467	1.455-1.457
Si-C(Å)	1.852-1.852	1.874-1.874	1.851-1.851	1.874-1.874	1.852-1.852	1.874-1.874	1.851-1.851	1.821-1.821
C-H(Å)	1.091-1.093	1.097-1.101	1.094-1.096	1.098-1.101	1.094-1.096	1.098-1.101	1.094-1.096	1.091-1.093
C-C(Å)	1.379-1.436	1.375-1.445	1.374-1.448	1.375-1.448	1.370-1.455	1.374-1.449	1.370-1.458	1.380-1.468
∠Si-O-Si(°)	145.4-150.3	144.0-151.5	144.6-150.5	143.8-151.6	145.1-150.1	143.6-151.6	144.7-150.1	143.5-151.6
∠O-Si-O(°)	108.2-110.4	107.8-110.6	108.0-110.5	107.7-110.9	108.1-110.2	107.6-111.0	108.2-110.2	107.6-111.0
∠C-Si-O(°)	108.9-111.3	110.5-111.5	109.3-110.4	110.4-112.0	109.1-110.5	110.4-112.2	109.2-110.5	110.3-112.3
∠C-C-Si(°)	120.6-120.7	119.8-122.4	119.8-121.5	119.4-122.7	120.6-120.7	119.2-122.9	120.3-120.9	119.1-123.1

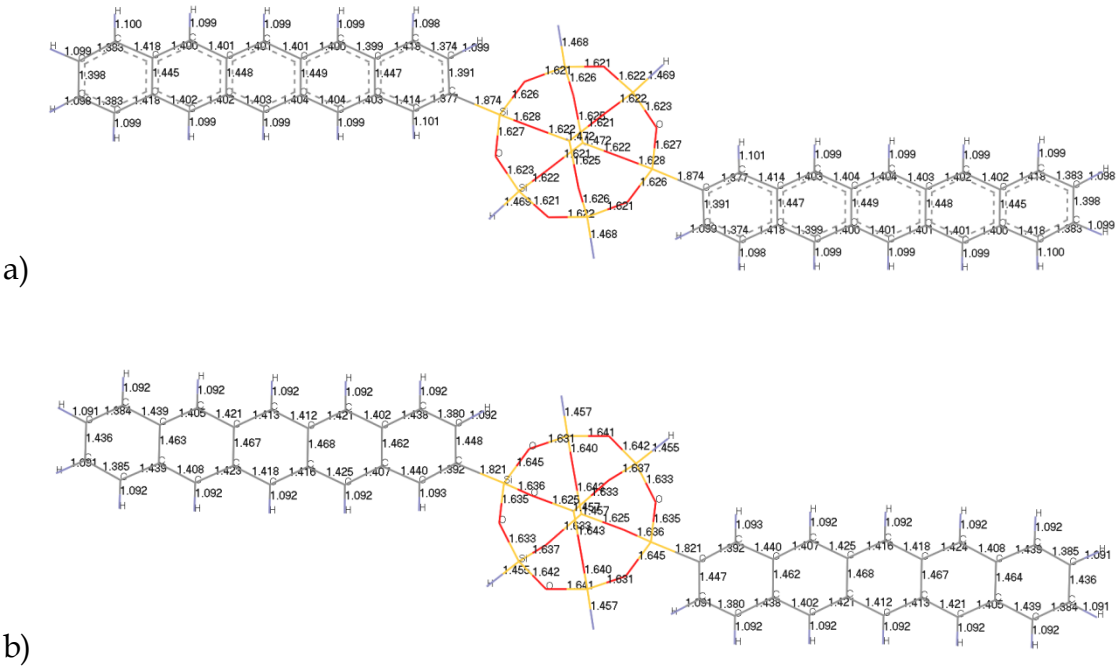

a)

b)

Figure 4-3 a) MD relaxed and b) DFT relaxed dipentacene-SQ molecules by SIESTA

Higher level geometry optimization to the molecular structure was carried out by the *ab initio* quantum mechanical calculation within the density-functional formalism [26, 27]. The choice of SIESTA and DMol3 as the *ab initio* DFT code is based on 1) the performance consideration, and 2) the ability to compare with existing calculations described in Chapter 1 by Durandurdu and Neurock *et al*. Both codes now have parallel versions that implement the message passing interface (MPI) communication protocol and are available on our multi-CPU node Linux cluster. All SIESTA calculations used a linear combination of atomic orbitals (LCAO) of the basis set for the molecular orbitals and norm-conserving Troullier-Martins pseudopotential for the electron-nuclei interaction in the core region. The split-valence double-zeta basis set was tested and employed in all calculations. The exchange correlation functional is treated under GGA with Perdew-Becke- Ernzerhof formalism.[28] . For individual molecule calculation, molecules were place in a large unit cell to exclude intermolecular interactions. All Dmol3 calculations used high performance double numerical polarized (DNP) basis set with PBE exchanged-correlation functional under GGA and DFT Semi-core pseudopotential for core electrons. HOMO and LUMO structures were visualized using graphics routines available in the DMol3 package.

4.2.2 Polymorph prediction method

The identification of the most probable crystal structures for the various candidate building blocks was accomplished using molecular modeling software from Accelrys' Materials Studio suite of programs. [11] These structure optimization simulations were based on the COMPASS force field, which provided the expediency required for sampling large numbers of trial structures and was reported by our previous study to be able to handle the SQ molecule. The Polymorph prediction program uses MD and Monte Carlo simulated annealing methods to predict multiple space groups for a given single molecule conformation. The typical Polymorph control parameters are show in Table 4-2. It first generates a large number of low-density crystal packing structures during the packing stage.

Table 4-2 Polymorph control parameters

Maximum number of steps	Steps to accept before cooling	Minimum move factor	Heating factor	Maximum temperature (K)	Minimum temperature (K)
2000	8	1×10^{-5}	0.025	3×10^{4}	300
4000	10	1×10^{-7}	0.025	6×10^{4}	300
7000	12	1×10^{-9}	0.025	1×10^{5}	300
10000	14	1×10^{-10}	0.025	1.5×10^{5}	300

During the clustering step, it filters out duplicate packing structures and to reduce the total number of structures based on Monte Carlo and MD relaxation energy. Then a geometry optimization is performed after the structures using the smart energy minimization method. In a second clustering step duplicate

structures, if there are any, are removed and potential crystal packing structures are sorted according to total system energy. As a final step, the stability of this structure is verified using Dmol3 and SIESTA. A Parrinello-Rahman algorithm was used to control the size and shape of the simulation box at finite temperatures.

4.3 Results and Discussion

4.3.1 Conformational and electronic properties calculations of individual molecules

Among the four optimized dipentacene-SQs shown in Scheme 4-1, i.e., di(a-pentacene)-SQ (a-DPSQ), di(b-pentacene)-SQ (b-DPSQ), di(c-pentacene)-SQ (c-DPSQ), and di(d-pentacene)-SQ (d-DPSQ), only c-DPSQ and d-DPSQ are associated with predicted high density polymorphs, as shown in Table 4-3. Considering potential benefits from packing arrangements and molecular symmetry, we decided the d-DPSQ with two acene molecules head to head bonded with one SQ cube corner at body diagonal position to be the best candidates, as shown in Table 4-3 and Figure 4-4. We also constructed molecular structures beyond the two identical molecules functionalized at SQ body diagonal position. Among all the tested molecular structures, the body diagonal functionalized diacene-SQ molecules with the two acene along their long axis show most interesting packing and electronic properties. The results are summarized in Table 4-4.

Table 4-3 Polymorphs with highest density and corresponding total energy of DPSQs

	a-DPSQ		b-DPSQ		c-DPSQ		d-DPSQ	
Space Group	Total Energy*	Density (g/cm3)	Total Energy*	Density (g/cm3)	Total Energy*	Density (g/cm3)	Total Energy*	Density (g/cm3)
$P\bar{1}$	-9.71	0.975	-13.63	1.004	-38.83	1.600	-34.35	1.653
$P2_1$	-13.43	1.068	-25.68	1.042	-39.30	1.601	-26.82	1.618
$C2$	-13.56	1.100	-21.13	1.103	-33.50	1.584	-17.80	1.574
Cc	-8.83	1.038	-17.79	0.941	-37.89	1.570	-30.56	1.646
$P2_1/c$	-18.40	0.904	-12.02	0.962	-35.78	1.570	-30.91	1.635
$C2/c$	-22.48	0.890	-22.08	1.070	-36.72	1.587	-24.37	1.605
$P2_12_12_1$	-8.31	0.952	-15.47	0.968	-35.96	1.598	-23.96	1.612
$Pna2_1$	-2.29	0.964	-16.59	0.986	-29.47	1.546	-18.23	1.572
$Pbca$	-11.82	1.002	-15.05	1.009	-33.55	1.574	-20.33	1.579
$Pbcn$	-6.33	0.882	-11.61	0.843	-28.96	1.533	-21.63	1.550

*Energy Unit: $Kcal^{-1}mol^{-1}$asymmetry $cell^{-1}$

Table 4-4 Selected molecular design with acene and T8 H-SQ

# of Acenes	Function Site on the SQ	Acene direction	Center Symmetry	Tuned HUMO-LUMO Gap	Parallel packing in Crystal	Electronic Property
2	Body Diagonal	Along long axis	Yes	Yes	A+	A+
2	Body Diagonal	Along short axis	Yes	Yes	A	A
2	Face Diagonal	Along long axis	No	Yes	B	B
1	Corner	Along long axis	No	Yes	B	B
8	All corners	Along long axis	Yes	Yes	C	A

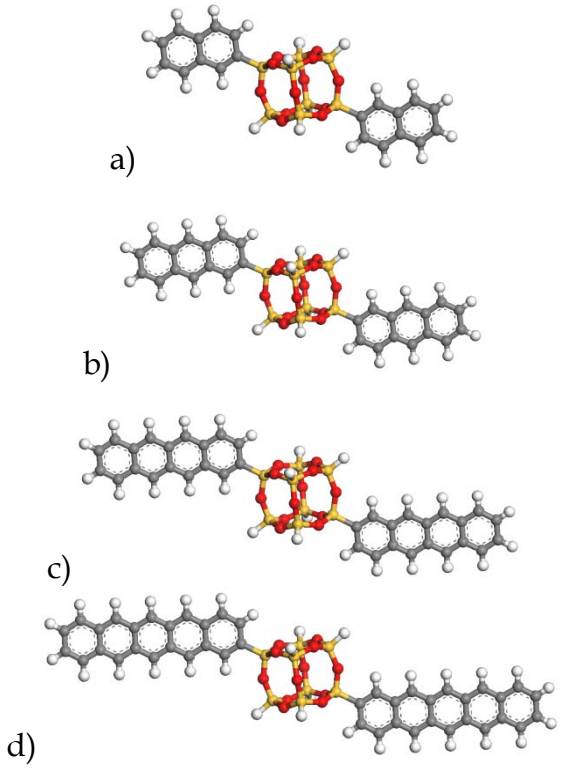

Figure 4-4 Optimized molecular conformation of acene molecules head to head attached along the body diagonal position of T8 SQ. a) Dinaphthalene-SQ; b) Dianthracene-SQ; c) Ditetracene-SQ and d) Dipentacene-SQ.

Attaching SQ with acene groups affects the electronic structure of both molecules. For example, the calculated HOMO-LUMO gap of SQ is 8.4 eV and that of benzene is 5.17 eV. When combining the two molecules, new electronic states develop and reduce the energy gap to 4.84 eV. This is illustrated in Figure 4-5, which shows the electronic density of states of a series of hybrid molecules in which an increasing number of benzene groups, ranging from one to eight, occupy the corners of the SQ cage. By attaching more benzene molecules to SQ further decreases the HOMO-LUMO gap of the molecule, but only by a very small amount.

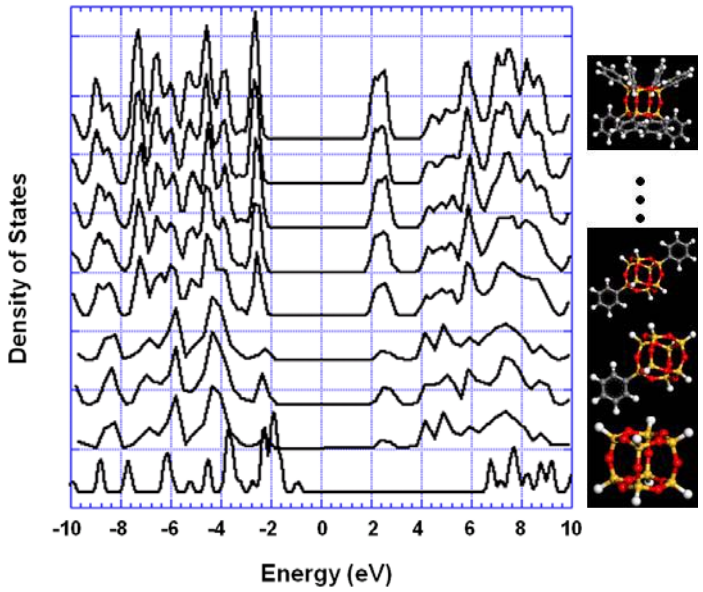

Figure 4-5 Total density of states plot for the T8 H-SQ cages functionalized with benzene molecules, the lowest curve is the T8 H-SQ, then goes from 1 benzene to 8 benzene molecules, with a sequence from bottom to top

Figure 4-6 shows electronic density of states plot for the T8 H-SQ cages functionalized at the two corners of the cube on the opposite ends of the body diagonal with naphthalene, anthracene, tetracene and pentacene, respectively. In general, by bonding two acene molecules to SQ cube, the energy gap of the former is reduced. However, as can be seen in Figure 4-5, the number of benzene groups bonded to a single SQ cube has little or nearly no effect on the magnitude of the energy gap. We expect that this trend also applies to other acene molecules with SQ considering the similarity of bonding pattern among the attached acene groups and SQ cube. Furthermore, the relative change in the energy gap magnitude lessens the smaller the acene group, i.e., the wider the energy gap of the pure acene molecule is to begin with, except for the case of

benzene. To illustrate this, in Table 4-5 the HOMO-LUMO gaps for a series of DACSQ hybrid molecules are compared to those of the corresponding pure acene molecules. The hybrids consist of a T8 H-SQ functionalized with two acene groups on two diagonally opposed corners. In the sequence of T8 H-SQ, benzene, naphthalene, anthracene, tetracene, and pentacene, the energy gap decreases monotonously. Compared to pure acenes, the DACSQs have lower HOMO-LUMO gaps.

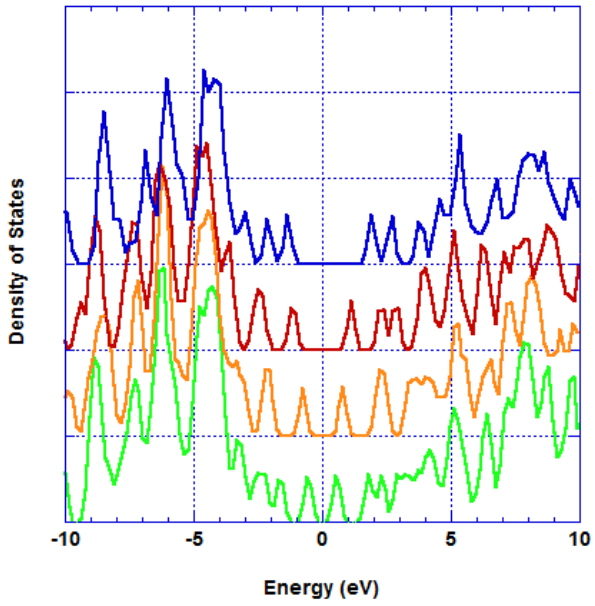

Figure 4-6 Total density of states plot for the T8 SQ cages functionalized at the two body diagonal position with naphthalene, anthracene, tetracene and pentacene at each corner respectively. The lowest curve is the dipentacene-SQ, then goes from ditetracene-SQ to dinaphthalene-SQ.

In this study we constructed a series of different hybrid configurations, by changing the size of acene groups bonded to SQ cube, as well as the connecting points on the acene molecules, thereby changing extents and symmetry of the

resulting hybrids, as shown in Scheme 4-1. Of all the structural variations we examined, most interesting is the configuration described above, i.e., with two acene groups bonded end-on to the diagonally opposed corners of the cube via a Si-C bond.

Table 4-5 Calculated HOMO-LUMO energy gaps and band gaps of diacene-SQ, acene and T8 SQ

Hybrids	Energy Gap (eV)	Acene Gap (eV)	ΔE (eV)	Band Gap (eV)	Acene Band Gap (eV)	ΔE (eV)	DACSQ Space Group
DPSQ	1.14	1.16	-0.20	0.69	1.01	-0.32	$P\bar{1}$
DTSQ	1.62	1.64	-0.02	0.94	1.41	-0.47	$P\bar{1}$
DASQ	2.31	2.35	-0.04	1.69	2.10	-0.41	$P\bar{1}$
DNSQ	3.35	3.43	-0.08	2.60	3.07	-0.47	$P\bar{1}$
OPS	4.84	5.17	-0.33	4.36	-	-	$P4/n$
T8 SQ	8.40	-	-	6.48	-	-	$R\bar{3}$

Figure 4-3 and Figure 4-4 shows this series of molecules after they have been fully relaxed using *ab initio* DFT methods. Notably, in each of these configurations the two acene molecules are not only parallel to each other, but lie in the same plane, which also contains the body diagonal of the SQ cube. All molecules have C1 symmetry. This arrangement promotes efficient packing in crystalline configurations, as explained below. Figure 4-7 and Figure 4-8 show the Frontier orbitals of geometry optimized DACSQ molecules corresponding to the HOMO and LUMO states at an iso-value level of 10^{-4}.

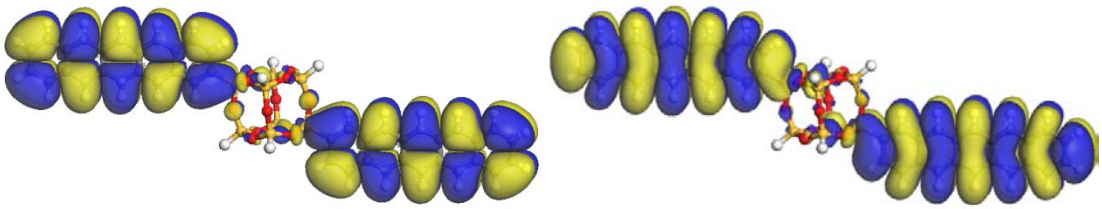

a) HOMO(left) and LUMO(right) of DPSQ

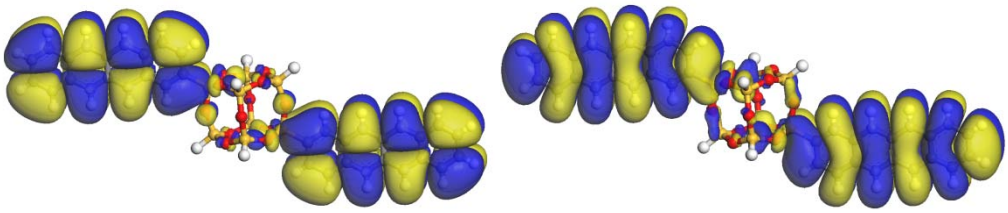

b) HOMO (left) and LUMO (right) of DTSQ

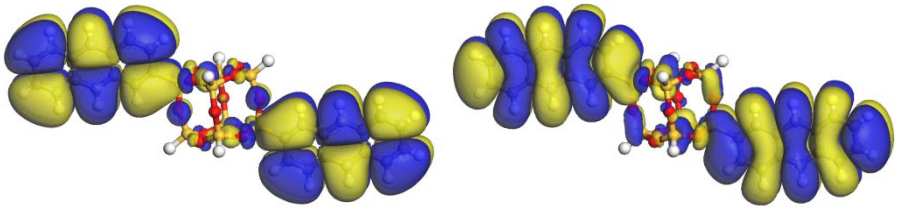

c) HOMO (left) and LUMO (right) of DASQ

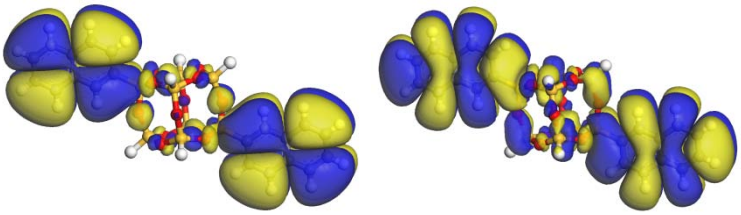

d) HOMO (left) and LUMO (right) of DNSQ

Figure 4-7 DFT optimized DACSQ molecules with HOMO and LUMO displayed at an iso value of 10^{-4} from a) to d)

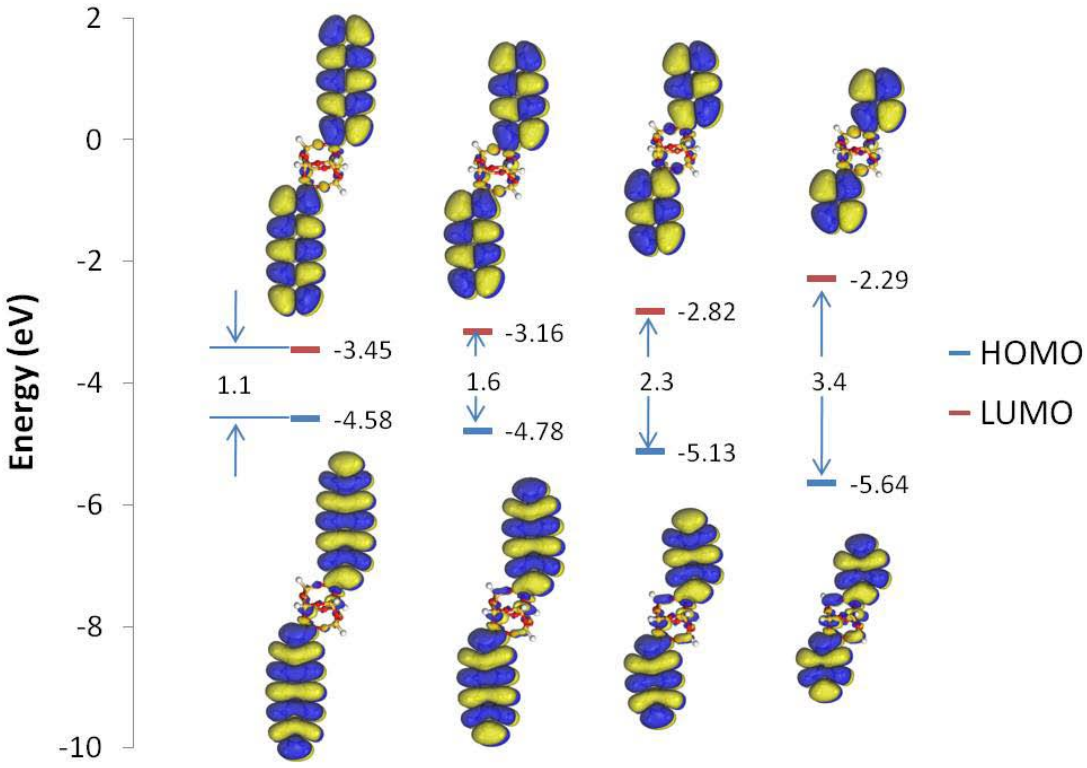

Figure 4-8 HOMO, LUMO and HOMO-LUMO gaps of DACSQs.

4.3.2 Polymorph prediction of the crystal structures

Once we identified stable molecules with promising single-molecule properties, we explored the most probable crystalline structures that these building blocks would assemble into by searching for the stacking configurations characterized by the lowest energies. A recent study [31] shows that among the 230 possible space groups, a centrosymmetric molecule will crystallize in the most possible three space groups of $P\bar{1}$, $P21/c$ and $Pbca$. Since we constructed DACSQ molecules with $C1$ symmetries, the structures predicted by the search algorithm included these three symmetry groups together with the other seven space

groups as possible polymorphs for the DACSQ building blocks. The lowest total energy and crystal density of DPSQ, DTSQ, DASQ and DNSQ are shown in Table 4-6. Since $P\bar{1}$ space group has the lowest energy for all the four DACSQs, we consider the corresponding crystal structures are the most stable polymorph of these DACSQs.

Table 4-6 Total energy and crystal densities for predicted polymorphs of DACSQs.

	DPSQ		DTSQ		DASQ		DNSQ	
Space Group	Total Energy*	Density (g/cm^3)	Total Energy*	Density (g/cm^3)	Total Energy*	Density (g/cm^3)	Total Energy*	Density (g/cm^3)
$P\bar{1}$	-34.35	1.653	-223.35	1.667	-412.41	1.686	-601.50	1.711
$P2_1$	-26.82	1.618	-220.58	1.646	-409.91	1.666	-600.90	1.709
$C2$	-17.80	1.574	-220.68	1.660	-410.04	1.675	-595.80	1.613
Cc	-30.56	1.646	-220.68	1.660	-407.51	1.652	-598.52	1.674
$P2_1/c$	-30.91	1.635	-220.20	1.637	-410.71	1.671	-599.86	1.682
$C2/c$	-24.37	1.605	-216.00	1.642	-406.49	1.621	-598.44	1.680
$P2_12_12_1$	-23.96	1.612	-215.24	1.629	-406.59	1.638	-599.83	1.687
$Pna2_1$	-18.23	1.572	-215.55	1.614	-406.04	1.617	-598.58	1.671
$Pbca$	-20.33	1.579	-215.55	1.614	-405.43	1.578	-597.16	1.686
$Pbcn$	-21.63	1.550	-213.25	1.594	-403.86	1.595	-595.79	1.620

*Energy Unit: $Kcal^{-1}mol^{-1}$asymmetry $cell^{-1}$

Figure 4-9 shows the crystal unit cells of all the four DACSQs predicted to have the lowest energy. The crystal unit cell information was summarized in Table 4-7.

Table 4-7 Predicted stable crystal structures of DACSQs

Molecule	DPSQ	DTSQ	DASQ	DNSQ
Space group	$P\bar{1}$	$P\bar{1}$	$P\bar{1}$	$P\bar{1}$
a(Å)	15.88	18.35	16.49	16.96
b(Å)	20.56	15.92	15.58	7.34
c(Å)	7.34	7.35	7.36	12.87
α(°)	78.12	64.89	69.28	84.16
β(°)	114.94	75.19	60.90	55.77
γ(°)	115.29	64.49	73.82	82.90

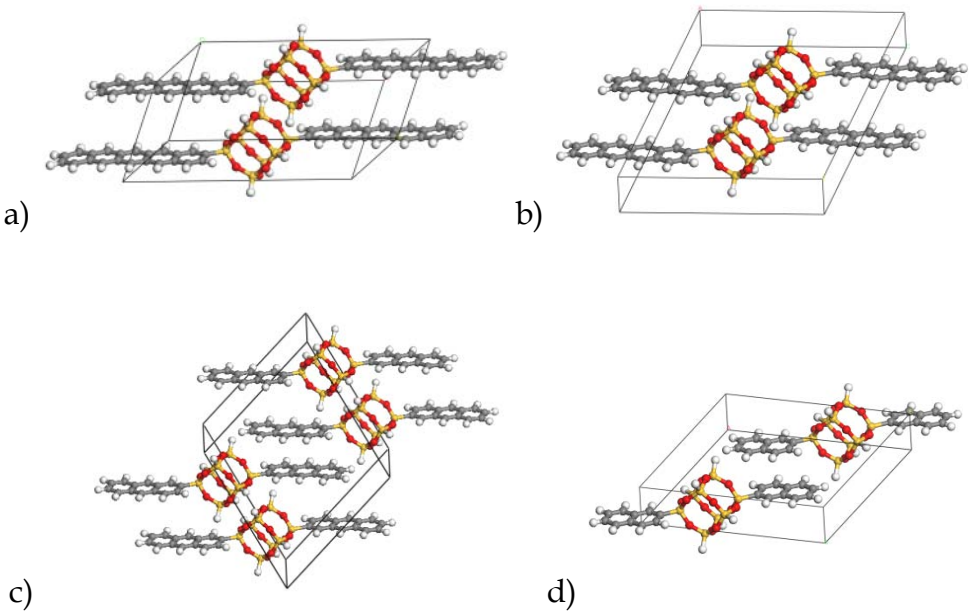

Figure 4-9 Predicted crystal unit cell of a) dipentacene-SQ; b) ditetracene-SQ; c) dianthracene-SQ; d) dinaphthalene-SQ

For DPSQ, the lowest energy and highest density configuration was found for the crystal structure with $P\bar{1}$ symmetry. The polymorph procedure found total of 358 crystal structures of DPSQ for all the 10 space groups. Ranking the 358 crystal structures with respect to the normalized total energy, as shown in Table 4-8, the first five lowest energy crystal structures all belong to the $P\bar{1}$ space group. For the five lowest energy $P\bar{1}$ crystal structures, the differences in total energy

with respect to the lowest one in the ranking list are less than 0.02%; the differences in density are less than 0.03%. This indicates the five structures are all possible candidates of the final crystal structure for the DPSQ, with the first structure is slightly more stable than the other four. All the five above mentioned structures feature with parallel packing of both the pentacene groups and the SQ cubes in the crystal unit cell, and the two pentacene groups lie in the same plane as the body diagonal split plane for the SQ cube, as shown in Figure 4-9 a) and Figure 4-10. The crystal structures with the 6th and 7th lowest total energy belong to the $P2_1/c$ space group. Compared to the lowest total energy of the crystal structure with the $P\bar{1}$ space group, the total energy for the two $P2_1/c$ space group structures increased 7.1% and 10.0% respectively; the density decreased 1.8% and 1.1% respectively. The No. 6th structure features with roughly but not perfect parallel packing of pentacene groups and alternating parallel packing of SQ cubes, as shown in Figure 4-14 a) and b). The two pentacene molecules are still nearly located within the same plane as the body diagonal of the SQ cube. The No.7th structure features with even more close to perfect parallel packing of the pentacene groups and alternating parallel packing of SQ cubes. It can be seen that by adapting to the $P2_1/c$ space group symmetry, the packing and geometry of the DPSQ changed to higher energy states, and therefore increased the total system energy. Therefore, within the accuracy associated with the polymorph prediction method, it can be concluded that the *P*

$\bar{1}$ space group is more favorable for the DPSQ than the $P2_1/c$ space group in crystalline states. The structure with *P*bca symmetry has a higher energy, ranked 49th among all the predicted polymorphs, indicating that it may not be as stable as those with $P\bar{1}$ or $P2_1/c$ symmetry. Similar structures and relative stabilities were found for ditetracene-SQ, dianthracene-SQ, and dinaphthalene-SQ crystal. Evidently, these simulation-based predictions do not yield the unit cell parameters and atomic positions with absolute certainty. Due to procedural inaccuracies in the calculations, small discrepancies between predicted and experimental structures may be expected. However, we do expect that the actual experimental structures will be close to ones listed in Table 4-7. Figure 4-10 to Figure 4-22 show a sampling of all the tested polymorph structures for the DACSQs. The total energy and density are listed from Table 4-8 to Table 4-11.

Table 4-8 Total energy and densities of predicted crystal structure polymorphs for DPSQ.

#	Frame #	Space group	Density (g/cm^3)	Total Energy (Ha)	ΔE_{tot} (Ha)	$\%\Delta\rho$
1	1	$P\bar{1}$	1.653184	-34.35324542	0	0.00
2	2	$P\bar{1}$	1.653358	-34.35268682	0.000559	0.01
3	3	$P\bar{1}$	1.653323	-34.34939075	0.003855	0.01
4	4	$P\bar{1}$	1.652741	-34.34750162	0.005744	-0.03
5	5	$P\bar{1}$	1.653149	-34.34707746	0.006168	-0.002
6	1	$P2_1/c$	1.623292	-31.90201638	2.451229	-1.81
7	2	$P2_1/c$	1.635179	-30.91116223	3.442083	-1.09
8	1	Cc	1.646379	-30.56447253	3.788773	-0.41
9	6	$P\bar{1}$	1.641722	-30.49789314	3.855352	-0.69
10	1	$P\bar{1}$	1.598908	-30.01388163	4.339364	-3.28
11	7	$P\bar{1}$	1.645626	-29.85315546	4.50009	-0.46
12	8	$P\bar{1}$	1.631101	-29.682794	4.670451	-1.34
13	9	$P\bar{1}$	1.631038	-29.68012304	4.673122	-1.34
14	10	$P\bar{1}$	1.595413	-28.84433677	5.508909	-3.49
15	11	$P\bar{1}$	1.621007	-28.43622605	5.917019	-1.95
16	12	$P\bar{1}$	1.621109	-28.4294851	5.92376	-1.94
17	3	$P2_1/c$	1.623311	-27.91298655	6.440259	-1.81
18	4	$P2_1/c$	1.624749	-27.56173236	6.791513	-1.72

Table 4-9 Total energy and densities of predicted crystal polymorphs for DTSQ

#	Frame #	Space group	Density (g/cm^3)	Total energy (Ha)	ΔE_{Tot}	$\%\Delta\rho$
1	1	$P\bar{1}$	1.666899	-223.35	0	0.00
2	2	$P\bar{1}$	1.66657	-223.348	0.002219	-0.02
3	3	$P\bar{1}$	1.666724	-223.316	0.034595	-0.01
4	1	$C2$	1.659833	-220.679	2.671543	-0.42
5	1	Cc	1.660115	-220.677	2.67327	-0.41
6	2	Cc	1.661052	-220.674	2.676038	-0.35
7	1	$P2_1$	1.64573	-220.575	2.77546	-1.27
8	1	$P2_1/c$	1.636761	-220.195	3.155616	-1.81
9	2	$P2_1/c$	1.637106	-220.192	3.158046	-1.79
10	2	$P2_1$	1.631574	-220.099	3.251188	-2.12
11	3	$P2_1$	1.645603	-219.962	3.388478	-1.28
12	4	$P\bar{1}$	1.655948	-219.301	4.049302	-0.66
13	4	$P2_1$	1.604519	-218.942	4.408455	-3.74
14	5	$P2_1$	1.603442	-218.924	4.426603	-3.81
15	5	$P\bar{1}$	1.641893	-218.842	4.508526	-1.50
16	6	$P2_1$	1.640676	-218.81	4.540693	-1.57
17	7	$P2_1$	1.613915	-218.789	4.561398	-3.18
18	8	$P2_1$	1.640099	-218.787	4.563913	-1.61
19	3	$P2_1/c$	1.630898	-218.526	4.824042	-2.16

Table 4-10 Total energy and densities of predicted crystal polymorphs for DASQ

#	Frame #	Space group	Density (g/cm^3)	Total energy (Ha)	ΔE_{Tot}	$\%\Delta\rho$
1	1	$P\bar{1}$	1.685925	-412.4128302	0	0.00
2	2	$P\bar{1}$	1.685821	-412.4070759	0.005754	-0.01
3	1	$P2_1/c$	1.671373	-410.7054388	1.707391	-0.86
4	2	$P2_1/c$	1.670985	-410.7053174	1.707513	-0.88
5	3	$P2_1/c$	1.671567	-410.703089	1.709741	-0.85
6	1	$C2$	1.675206	-410.043551	2.369279	-0.63
7	1	$P2_1$	1.665725	-409.9068219	2.506008	-1.20
8	2	$P2_1$	1.665728	-409.9050566	2.507774	-1.20
9	3	$P2_1$	1.665476	-409.9039906	2.50884	-1.21
10	4	$P2_1$	1.665704	-409.9014881	2.511342	-1.20
11	5	$P2_1$	1.665715	-409.9012303	2.5116	-1.20
12	6	$P2_1$	1.666108	-409.8993671	2.513463	-1.17
13	7	$P2_1$	1.668462	-409.828258	2.584572	-1.03
14	8	$P2_1$	1.669065	-409.8268139	2.586016	-1.00
15	2	$C2$	1.677467	-409.7580401	2.65479	-0.50
16	3	$P\bar{1}$	1.687398	-409.7218145	2.691016	0.09
17	4	$P\bar{1}$	1.687494	-409.7213576	2.691473	0.09
18	5	$P\bar{1}$	1.687573	-409.7170839	2.695746	0.10
19	6	$P\bar{1}$	1.654487	-408.8658544	3.546976	-1.86
20	7	$P\bar{1}$	1.654634	-408.8616497	3.55118	-1.85
21	8	$P\bar{1}$	1.652597	-408.8522045	3.560626	-1.97
22	9	$P2_1$	1.626122	-408.6556016	3.757229	-3.54
23	10	$P2_1$	1.626202	-408.648619	3.764211	-3.53
24	11	$P2_1$	1.625178	-408.6437742	3.769056	-3.60

Table 4-11 Total energy and densities of predicted crystal polymorphs for DNSQ

#	Frame #	Space group	Density (g/cm^3)	Total energy (Ha)	ΔE_{Tot}	$\%\Delta\rho$
1	1	$P\bar{1}$	1.711096	-601.499	0	0
2	2	$P\bar{1}$	1.711021	-601.494	0.004336	-0.00436
3	3	$P\bar{1}$	1.709734	-601.489	0.009533	-0.07962
4	4	$P\bar{1}$	1.711973	-601.485	0.01309	0.051253
5	1	$P2_1$	1.709455	-600.902	0.59619	-0.09587
6	5	$P\bar{1}$	1.699612	-600.799	0.699632	-0.67117
7	6	$P\bar{1}$	1.697144	-600.79	0.708674	-0.81541
8	7	$P\bar{1}$	1.696926	-600.784	0.7146	-0.82814
9	8	$P\bar{1}$	1.697112	-600.774	0.724554	-0.81725
10	9	$P\bar{1}$	1.699899	-600.743	0.755726	-0.6544
11	10	$P\bar{1}$	1.70134	-599.981	1.517272	-0.57016
12	11	$P\bar{1}$	1.699885	-599.977	1.521744	-0.65517
13	1	$P2_1/c$	1.681854	-599.858	1.640423	-1.70897
14	1	$P2_12_12_1$	1.687101	-599.826	1.67261	-1.40229
15	2	$P2_12_12_1$	1.695198	-599.761	1.73735	-0.92911
16	3	$P2_12_12_1$	1.694989	-599.76	1.738922	-0.94135
17	12	$P\bar{1}$	1.716977	-599.724	1.774647	0.343719
18	2	$P2_1/c$	1.688729	-599.591	1.907386	-1.30714
19	13	$P\bar{1}$	1.699724	-599.445	2.053585	-0.6646
20	14	$P\bar{1}$	1.698239	-599.443	2.055691	-0.7514
21	15	$P\bar{1}$	1.700633	-599.441	2.057421	-0.61148
22	2	$P2_1$	1.687022	-599.301	2.197369	-1.40693
23	16	$P\bar{1}$	1.679264	-599.105	2.393934	-1.86034
24	17	$P\bar{1}$	1.680067	-599.1	2.398193	-1.81338
25	3	$P2_1$	1.681469	-598.845	2.653261	-1.73147
26	3	$P2_1/c$	1.708287	-598.586	2.912287	-0.16419
27	4	$P2_1/c$	1.708167	-598.585	2.91387	-0.17115
28	1	$Pna2_1$	1.671239	-598.579	2.919602	-2.32931
29	2	$Pna2_1$	1.672102	-598.577	2.921901	-2.27889
30	1	Cc	1.674221	-598.519	2.979537	-2.15502
31	2	Cc	1.67412	-598.518	2.980264	-2.16094

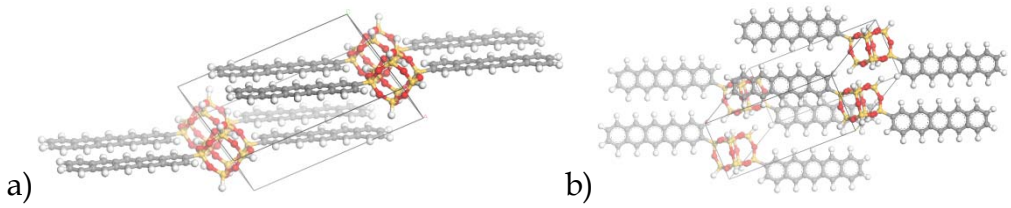

Figure 4-10 The frame #2 polymorph with $P\bar{1}$ space group of DPSQ showing excellent parallel packing of both the pentacenes and the SQs in view a) and b). The pentacenes are alging themselves in the same plane of the body diagonal of the SQ cage.

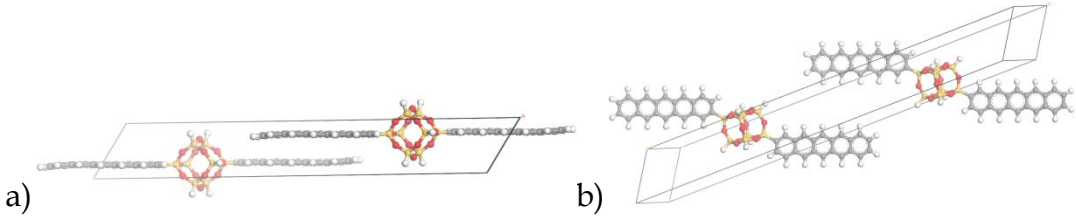

Figure 4-11 The frame #3 polymorph with $P\bar{1}$ space group of DPSQ showing excellent parallel packing of both the pentacenes and SQs in view a) and b). The feature of pentacenes alging themselves in the same plane of the body diagonal of the SQ cage resumes.

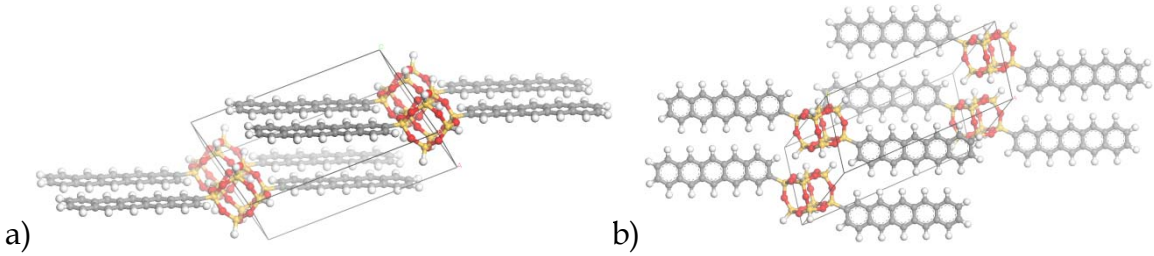

Figure 4-12 The frame #4 polymorph with $P\bar{1}$ space group of DPSQ, another excellent crystal with parallel packing of all parts of the molecules with the feature of pentacenes reside themselves in the body diagonal plane of SQ cage showing in view a) and b).

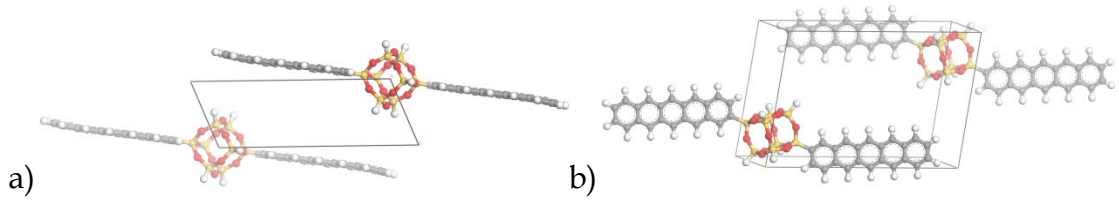

Figure 4-13 The view in a) and b) of frame #5 polymorph with $P\bar{1}$ space group of DPSQ, clearly showing the packing feathures mentioned above.

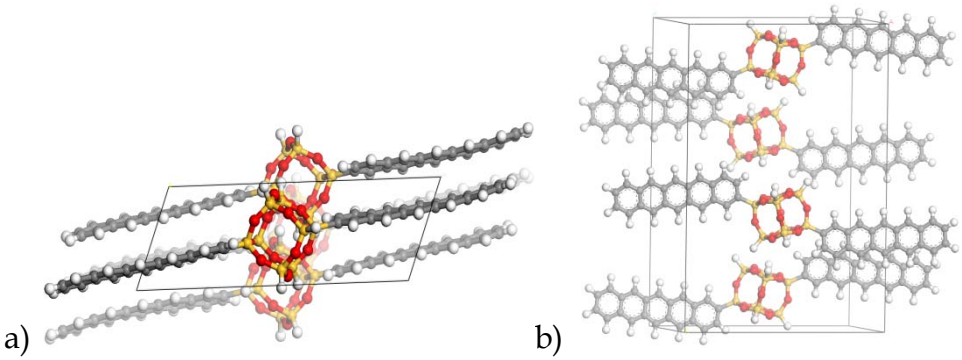

Figure 4-14 The frame #1 polymorph with $P2_1/c$ space group of DPSQ in view a) and b). This polymorph features alternating parallel packing of both pentacene groups and SQ cubes. Pentacenes are still in the same plane but pointing to different directions with a small angle. Two groups formed by the four SQ cubes. The two cubes in each group are parallel to each other. This packing fashion seems slightly increased the total energy compared to the first five frames of DPSQ in $P\bar{1}$ space group packing. The individual molecule keeps the conformation of two pentacene reside in the same plane of SQ cube body diagonal.

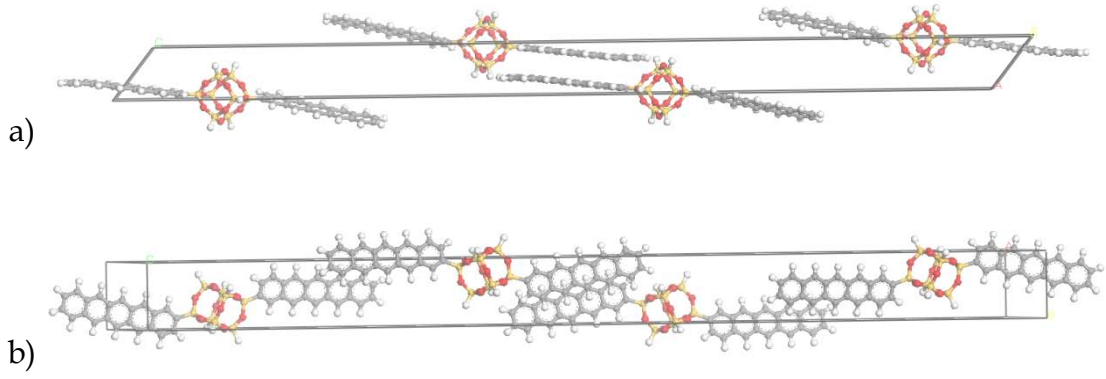

Figure 4-15 The frame #2 polymorph with $P2_1/c$ space group of DPSQ in view a) and b). This is another alternating parallel packing as mentioned above in Figure 4-14.

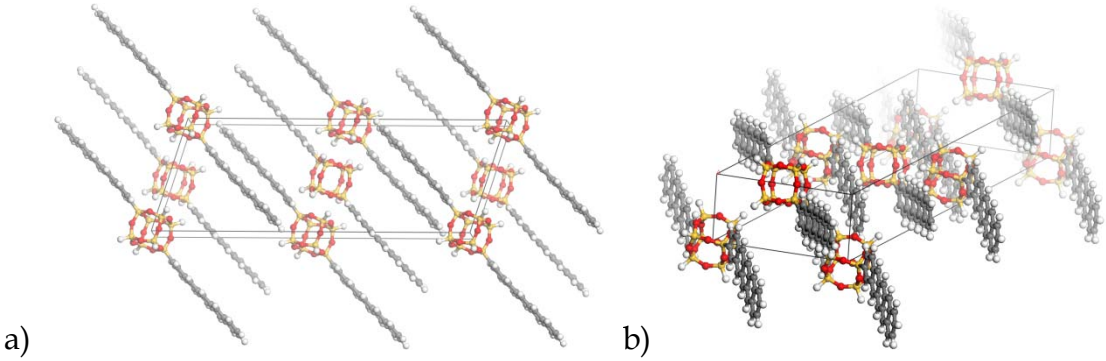

Figure 4-16 The frame #1 polymorph with *Cc* space group of DPSQ in view a) and b). The parallel packing of pentacenes and SQ cubes are similar to Figure 4-14 and Figure 4-15. This is another example of low energy crystal packing featuring alternating parallel packing of pentacenes and SQ.

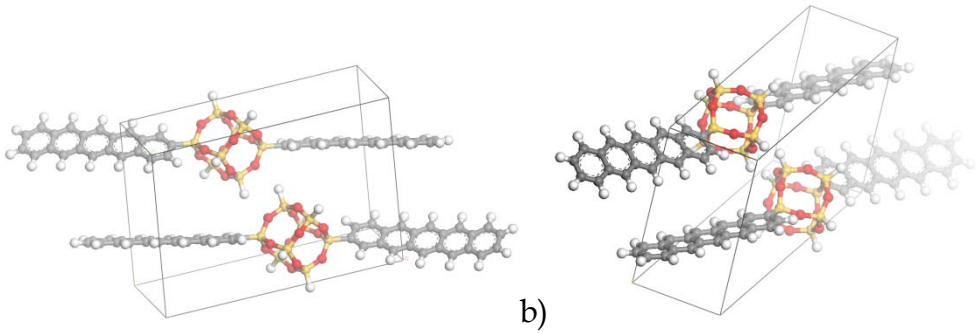

Figure 4-17 The frame #6 polymorph with $P\bar{1}$ space group of DPSQ in view a) and b). Apparently, the DPSQ molecular geometry changes to a high energy state with pentacene groups again showing herringbone packing intendency. This time, even packing in $P\bar{1}$ space group won't let this packing to have lower energy than the earlier mentioned frames. According to the polymorph procedure, the geometry of the DPSQ and crystal packing together determine the final packing energy state of the system. By introducing SQ into the system, the favorable packing of pentacenes are changed to parallel in crystalline states.

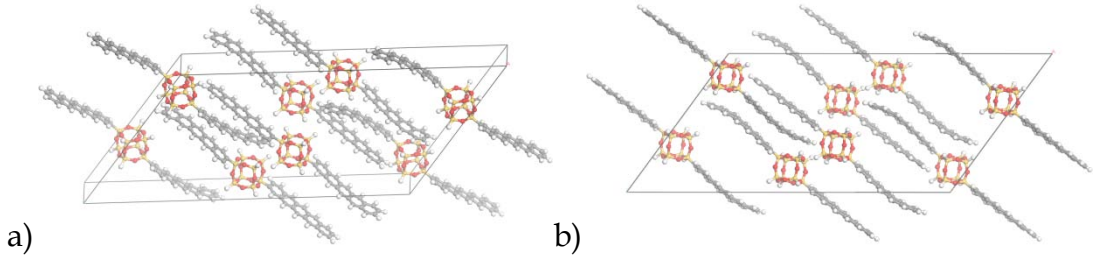

Figure 4-18 The frame #6 polymorph with $C2/c$ space group of DPSQ.

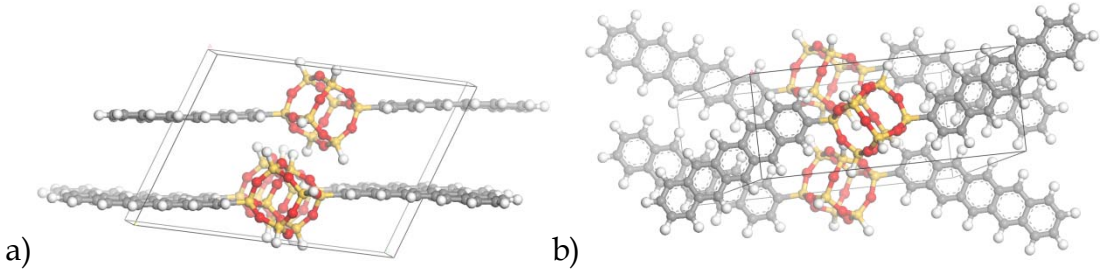

Figure 4-19 The frame #7 polymorph with $P2_1$ space group of DPSQ.

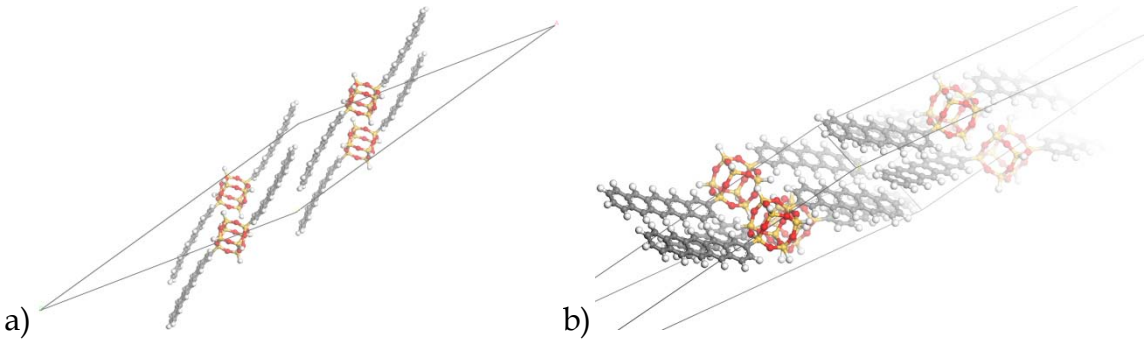

Figure 4-20 The frame #12 polymorph with *C*2 space group of DPSQ.

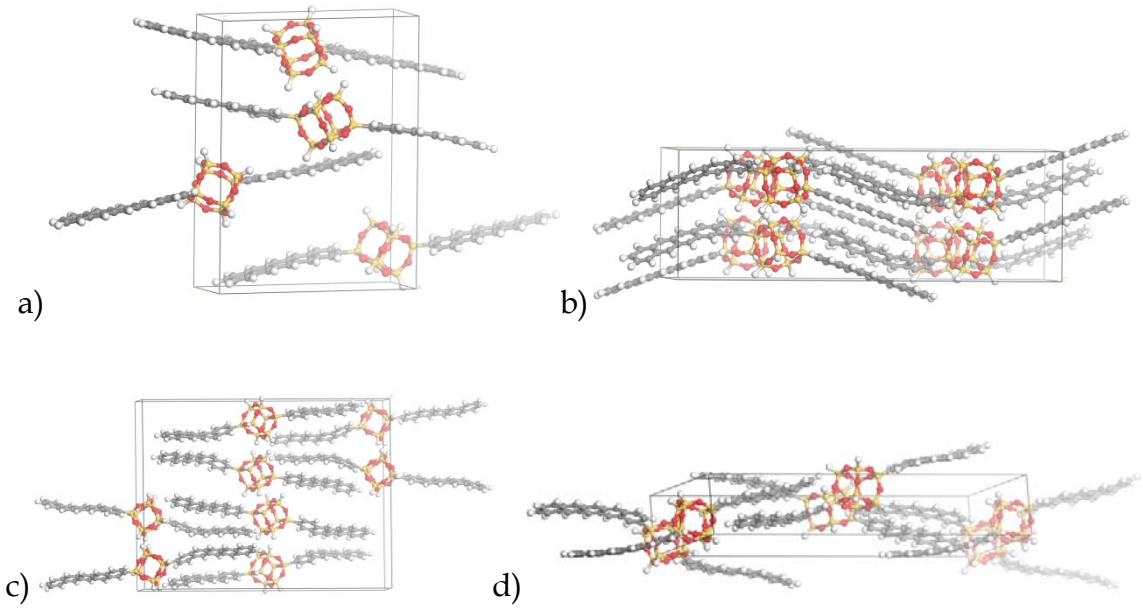

Figure 4-21 a) The frame #1 polymorph with $P2_12_12_1$ space group of DPSQ; b) frame #1 polymorph with *P*bca space group of DPSQ; c) frame #1 polymorph with Pbcn space group of DPSQ; and d) Frame #1 polymorph with $Pna2_1$ space group of DPSQ.

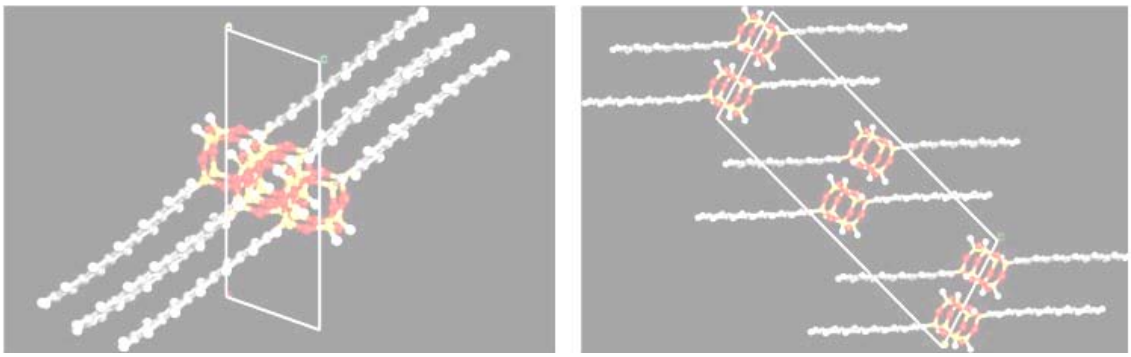

$P2_1/c$ $C2$

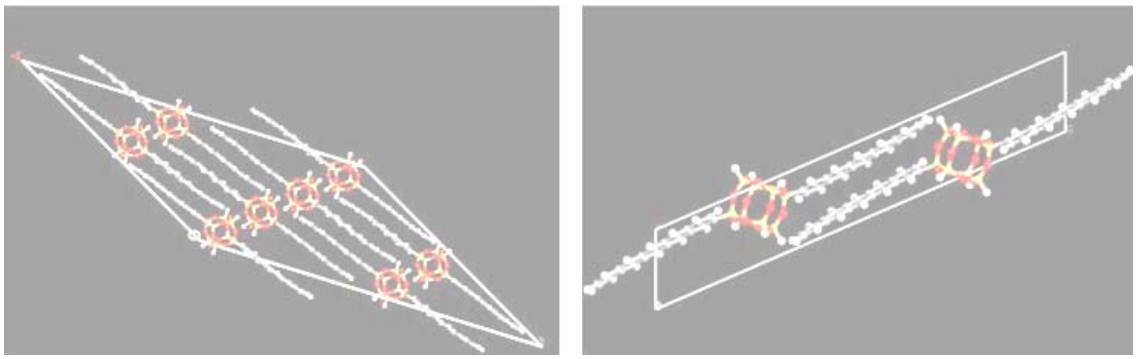

$C2/c$ $P2_1$

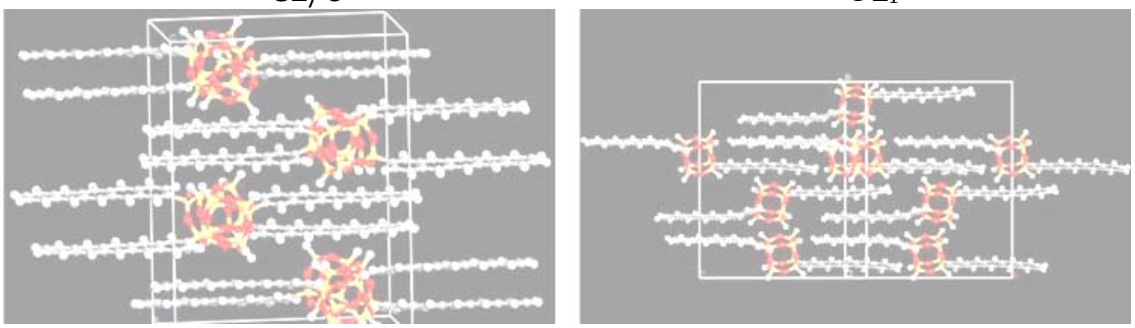

$Pbca$ Cc

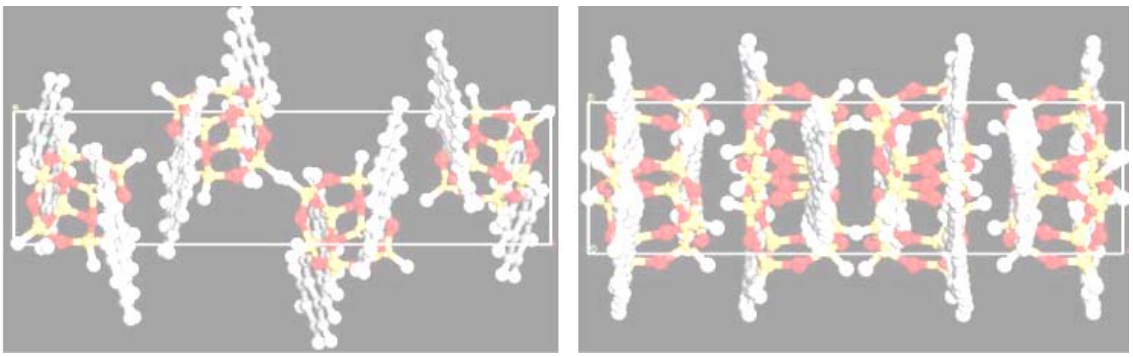

$Pna2_1$ $Pbcn$

a) Sample polymorphs of DTSQ

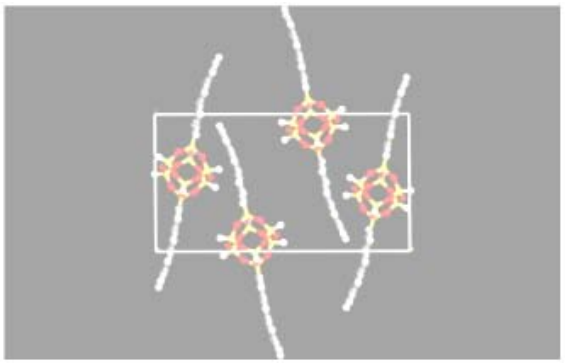

$P2_1/c$

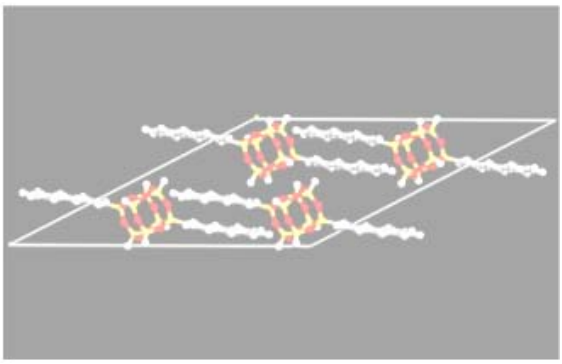

Cc

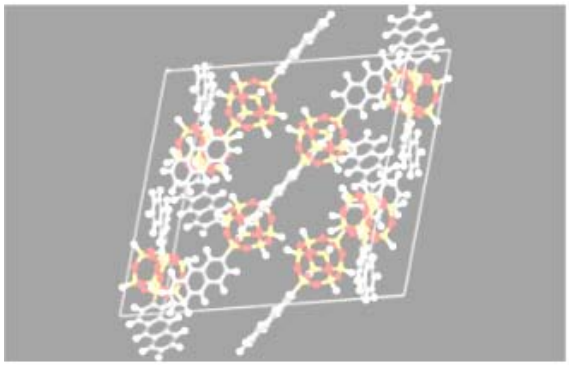

$C2/c$

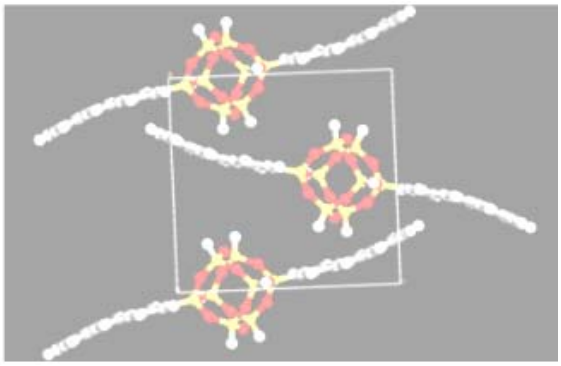

$P2_1$

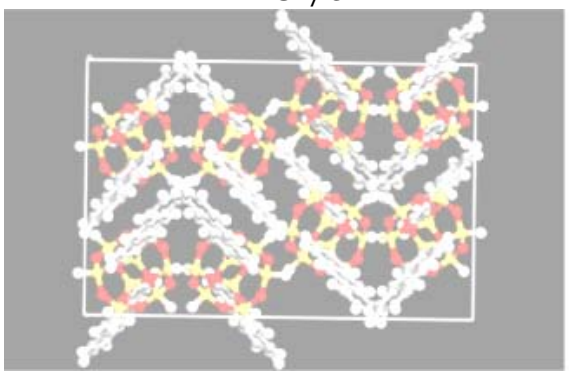

Pbca

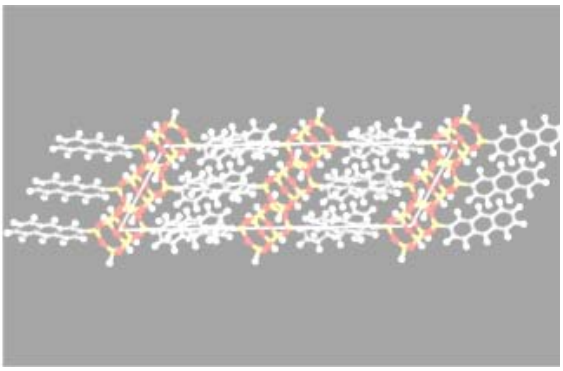

Cc

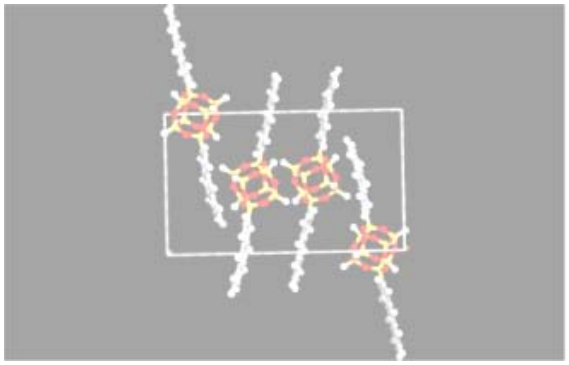

Pna2_1

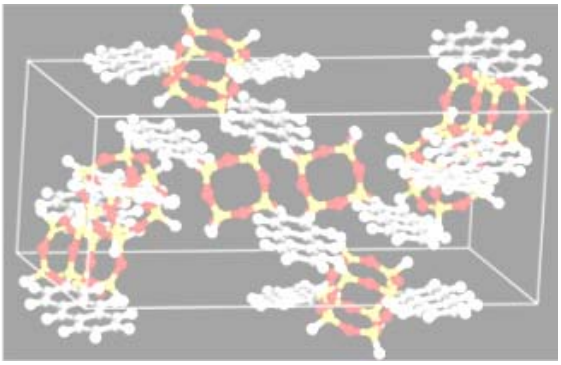

Pbcn

b) Sample polymorphs of DASQ

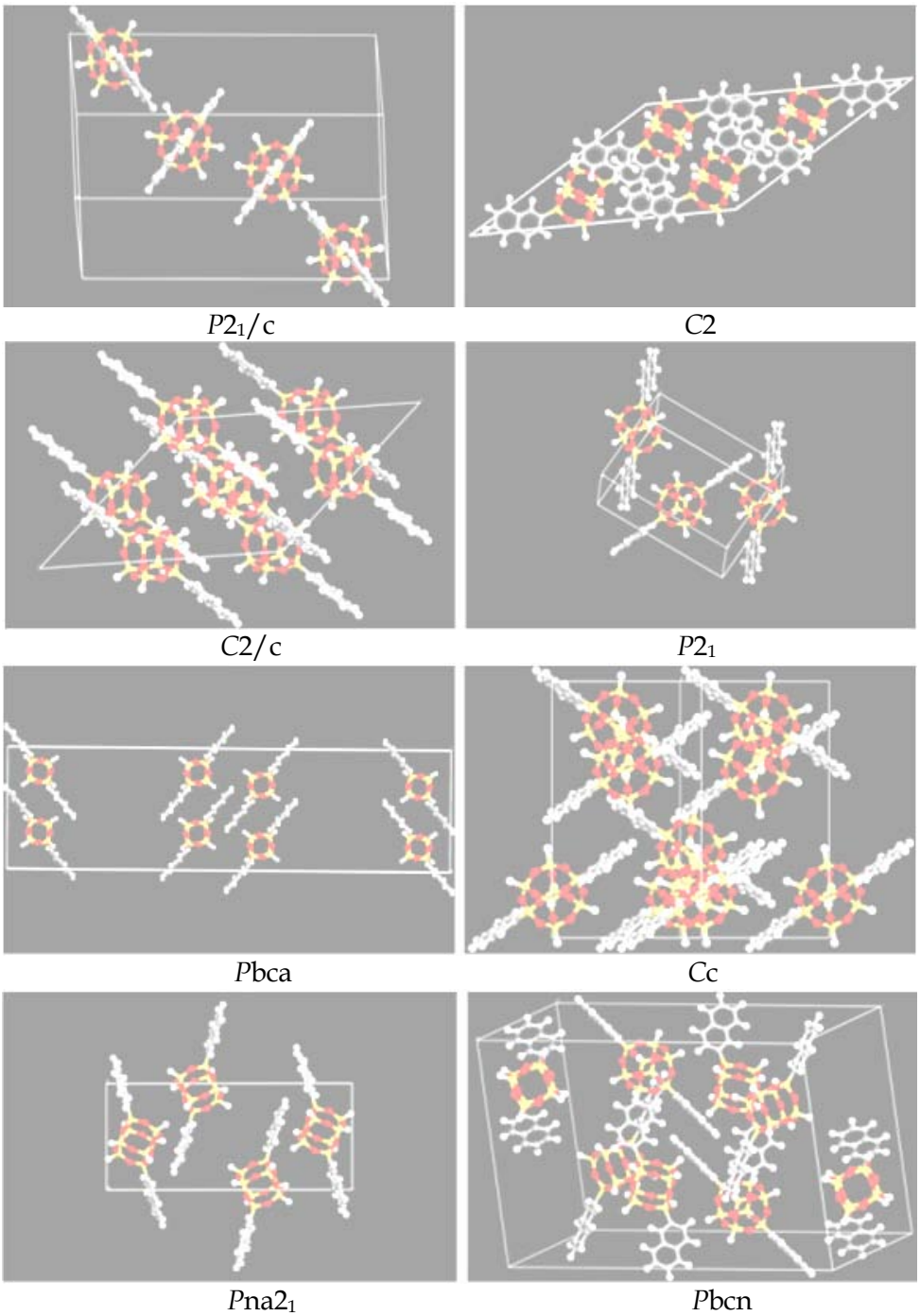

c) Sample polymorphs of DNSQ

Figure 4-22 Other polymorph predicted crystal unit cells of a) ditetracene-SQ, b) dianthracene-SQ, c) dinaphthalene-SQ

Importantly, at least two of the structures for each diacene-SQs, predicted to have the lowest energy, are characterized by paralleled packing of the acene

groups as opposed to the herringbone stacking in pure acene crystals. Seemingly, the strong packing tendency that exists between SQ cages as a result of long-range Coulomb interactions prevails even when diagonally functionalizing SQ with two acene groups. Conversely, the incorporation of SQ in between acene molecules forces these to face each other. This provides for enhanced π - π orbital overlap, and as a consequence, in these new hybrid materials one may expect higher charge carrier mobility than in pure acenes and a band-like transport mechanism between molecules, but preserved and even lowered the band gap of pure acene molecules.

4.3.3 Electronic, thermal and mechanical properties of diacene-SQs

The calculated band structures for the diacene-SQs along high symmetry direction, together with the density of states, are shown in Figure 4-23. The band gaps of the four diacene-SQ crystals are summarized in Table 4-5. As shown in the table, the band gaps of these molecular crystals are all very small. In contrast to the decrease in single molecule energy gaps, the band gaps of the DACSQ crystals are significantly lower than the corresponding acene crystals. These diacene-SQ band structures also show large band dispersion between 0.2 to 0.45 eV. The large dispersion in energy values implies the potential high mobility of charge carries along those high-symmetry directions. Apparently, the small band gap and large dispersion are both resulted by the modification of the SQ

molecule to the packing of the conjugate systems with unique molecular orbital distributions. According to the charge carrier equation we introduced in chapter 1, the small band gaps provide the molecular crystal with higher charge carrier densities, which are directly improvements to the transport properties of the molecular crystal. The highly ordered parallel packing of the acene groups give very good overlapping properties between conjugate groups and therefore promote large intermolecular transfer integrals. According to the 1D transport model, this construction of diacene-SQ molecular crystals should provide a series of very high mobility hybrid semiconductors with other potential benefits. As existing experimental evidences have shown that incorporating SQ in the semiconducting polymeric materials can bring benefits such as improved EQE, we highly expect that these series new molecular crystals will also show similar excellent electronic properties when applied these materials to electronic devices, for example, OLEDs, OPVCs and OFETs.

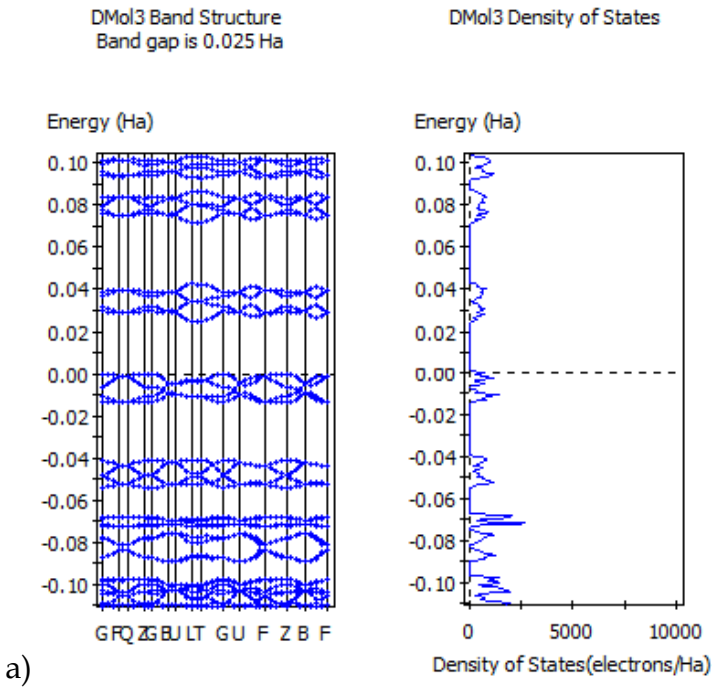
DMol3 Band Structure
Band gap is 0.025 Ha
DMol3 Density of States
Energy (Ha)
Energy (Ha)
0.10
0.08
0.06
0.04
0.02
0.00
-0.02
-0.04
-0.06
-0.08
-0.10
G F Q Z G B U L T G U F Z B F
0
5000
10000
Density of States(electrons/Ha)

a)

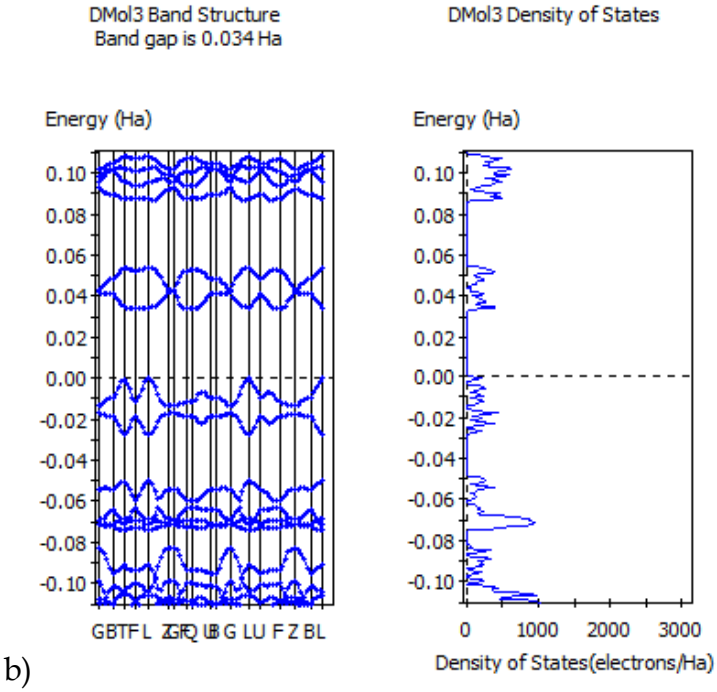
DMol3 Band Structure
Band gap is 0.034 Ha
DMol3 Density of States
Energy (Ha)
Energy (Ha)
0.10
0.08
0.06
0.04
0.02
0.00
-0.02
-0.04
-0.06
-0.08
-0.10
G B T F L Z G F Q U B G L U F Z B L
0
1000
2000
3000
Density of States(electrons/Ha)

b)

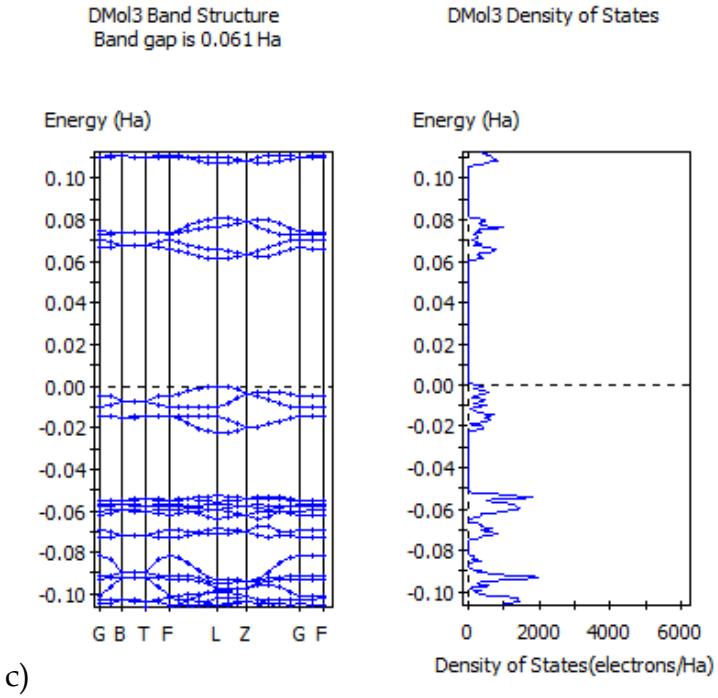

c)

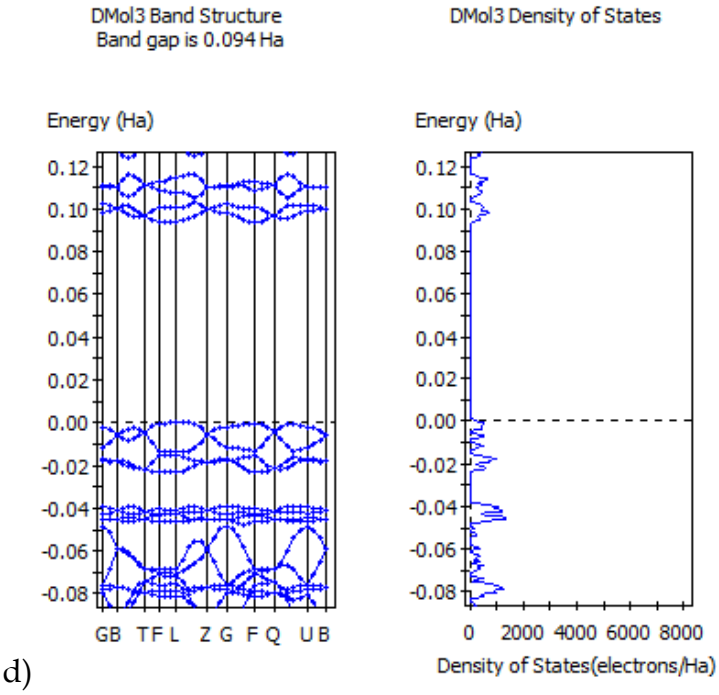

d)

Figure 4-23 The band structure and density of states of diacene-SQs: a) DPSQ; b)DTSQ; c)DASQ; d)DNSQ

In addition to the electronic band structure, we performed calculations to estimate the mechanical and thermal properties of the various predicted crystals for the diacene-SQ hybrids, and, for comparison, of the corresponding pure acenes. This was done by using MD simulations based on the aforementioned classical force field and a supercell configuration consisting of $2\times2\times2$ unit cells. Elastic moduli were determined using the static structure deformation method. In this method, each structure was subjected to incremental deformations in steps of 0.05% strain, both in uniaxial tensile and pure shear modes. After every increment the structures were relaxed to minimize potential energy, and the internal stress tensor was calculated using the virial expansion. The elastic constants and Poisson's ratio were obtained by comparing stress and strain.

Table 4-12 Effective isotropic elastic constants (GPa) of diacene-SQs with $P\bar{1}$ symmetry compared with acene crystal

	DNSQ	Naph.	%Δ	DASQ	Anth.	%Δ	DTSQ	Tetr.	%Δ	DPSQ	Pent.	%Δ
Young's Modulus	10.06	8.489	18.5	11.80	5.357	120.3	12.77	6.339	101.5	10.81	7.557	43.0
Bulk Modulus	11.03	8.254	33.6	11.31	5.987	88.9	11.86	5.279	124. 7	12.29	5.962	106.1
Shear Modulus	3.73	3.195	16.7	4.449	1.983	124.4	4.834	2.438	98.3	3.994	2.932	36.2

Table 4-12 summarizes the results for Young's, bulk and shear moduli compared to acene crystals. The Young's, bulk and shear moduli all increase by almost a factor of two for the hybrid compounds compared to pure naphthalene crystals. For other acenes, the increases are even larger. We attribute these increases to the high rigidity of the SQ cages and the strong interactions between them.

Table 4-13 Heat capacities of acene crystals and calculated diacene-SQ crystals

Molecule	T (K)	Cp($J \cdot K^{-1} \cdot g^{-1}$)	Cp_exp($J \cdot K^{-1} \cdot g^{-1}$)	Cv($J \cdot K^{-1} \cdot g^{-1}$)
DPSQ	278.1	1.633	-	1.568
Pentacene	277.4	1.469	1.033[a)]	1.463
DTSQ	277.9	1.342	-	1.122
Tetracene	274.2	0.927	1.053[a)]	0.922
DASQ	276.0	1.191	-	1.031
Anthracene	275.2	0.940	-	0.899
DNSQ	277.1	2.928	-	2.706
Naphthalene	-	-	-	-

a) Reference [34]

Table 4-13 summarizes the heat capacity of the predicted diacene-SQs and their corresponding acene crystals. The simulated systems were first relaxed under constant pressure conditions for at least 100 picoseconds, and then the statistical quantities steps were averaged over a 10 pico second time frame with a step of one femto second. The Nose-Hoover algorithm was used for thermostat and Raman-Parrinello algorithm was used for the barostat. The constant pressure heat capacity was calculated by using

$$C_p = \frac{1}{k_B T^2}\left\langle \delta(E_K + U + PV)^2 \right\rangle , \tag{4.1}$$

where k_B is the bolzmann's constant, T is the temperature, E_K is the kinectic energy, U is the potential energy, P is pressure and V is volume. And the constant volume heat capacity was calculated using

$$C_v = C_p - \frac{\langle T \rangle \langle V \rangle \alpha_p^2}{\beta_T} , \tag{4.2}$$

where α_p is thermal expansion coefficient and β_T is isothermal compressibility and they are defined by:

$$\alpha_p = \frac{1}{k_B T^2 V}\left\langle \delta V \delta (E_K + U + PV) \right\rangle , \tag{4.3}$$

and

$$\beta_T = \frac{1}{k_B T V}\left\langle \delta V^2 \right\rangle \tag{4.4}$$

The pentacene, tetracene and anthracene crystal unit cell were generated using coordinates published in literature[32, 33]. Experimental heat capacity values [34] were compared with the calculated pentacene and tetracene crystal heat capacities. The calculated pentacene and tetracene heat capacity values are very close to the experimental values[34]. According to the calculation, the diacene-SQ crystals have substantial higher heat capacity values than their corresponding acene crystals. This is an indication that they are more stable thermally than their peer acene crystals. The improved thermal property is due to the inorganic SQ core within the molecule.

4.4 Summary

Using acene and T8 H-SQ with a MD and *ad initio* DFT calculation combined method, we successfully designed a series of new small band gap semiconducting diacene-SQ organic-inorganic hybrid molecules. In our work, candidate molecular structures were first constructed by considering molecular symmetry, especially with the centrosymmetries, that are both highly predictable and promoting potential excellent electronic properties. These candidate molecular structures then were put into a refining process which involves packing and geometry optimization study using Monte Carlo simulated annealing and other optimization methods to explore thoroughly the best molecular designs. Excellent molecular designs were successfully found which show highly predictable crystal structures, which feature ideal high density parallel packing of both the conjugate acene groups and rigid SQ cubes in the crystal unit cell. Solid state DFT methods were used to examine the benchmark electronic properties of these crystal structures. Very small band gaps and large dispersion in the band lines were found for this series of diacene-SQ molecular solids. The smallest band gap derived from the design is the dipentacene-SQ. Our simulations and calculations showed the dipentacene-SQ has a band gap as low as 0.69 eV. This is a new type of semiconducting hybrid molecule with other advanced properties. The derivation of this final conformation is based on four major considerations. The first is from those trial and error experiments of

attaching different number of acene molecules from various positions at multiple corners of the SQ. With two pentacenes attached head to head to the SQ cube at body diagonal position, the relaxed molecular structure shows two pentacenes align themselves in the same plane and the system energy is at a minimum, which tells us this conformation is a stable one. Other conformations are eliminated because they either did not result in the desired packing, or exhibited higher ground state energies, indicating reduced thermodynamic stability. The second consideration is to choose molecules that have highly symmetric architectures, e.g., centrosymmetry, as these have a tendency to assemble into crystalline structures that reflect this symmetry [31].

Third, in this conformation, the SQ cube will act as a connector between the two parallel acenes that reside in the same plane. This could potentially form an even longer conjugate molecule and promote better electronic properties. The SQ cube itself may contribute to the overall conjugation in the new molecules. Compared to isolated pentacenes located at the same positions as in the dipentacene-SQ molecule, connecting them with a SQ cube increases the availability of atomic orbitals in between the two pentacene molecules, which may result in a lower HOMO-LUMO energy gap and crystal band gaps of the new molecule than pure pentacenes. This HOMO-LUMO and band gap reductions were confirmed by our quantum mechanical calculations. Fourth, the accessibility of the SQ cube in this rather open molecular architecture insures that

the electrostatic interactions between neighboring SQ molecules dominate the overall stacking in the crystalline structure and thereby control the long-range order in the pentacene packing. This is also demonstrated in the polymorph study. Molecular dynamics studies were performed examine the

4.5 References

[1] Schwab, J. J.; Lichtenhan, J. D. *Appl. Organomet. Chem.* **12**, 707 (1998)

[2] Lee, A.; Lichtenhan, J. D. *J. Appl. Polym. Sci.* **73**, 1993 (1999)

[3] Baidina, I. A.; Podberezskaya, N. V.; Alekseev, V. I.; Martynova, T. N.; Borisov, S. V.; Kanev, A. N. *J. Struct. Chem.* **20**, 550 (1979)

[4] Koellner, G.; Muller, U. *Acta Crystallogr., Sect. C* **45**, 1106 (1989)

[5] Tornroos, K. W.; Calzaferri, G.; Imhof, R. *Acta Crystallogr., Sect.C* **51**, 1732 (1995)

[6] Xu, H. Y.; Kuo, S. W.; Lee, J. S.; Chang, F. C. *Macromolecules* **35**, 8788 (2002)

[7] Rappe, A. K.; Casewit, C. J.; Colwell, K. S.; Goddard, W. A.; Skiff, W. M. *J. Am. Chem. Soc.* **114**, 10024 (1992)

[8] Marquez, A.; Sanz, J. F. *J. Am. Chem. Soc.* **114**, 10024 (1992)

[9] Martin, M. G.; Siepmann, J. I. *J. Phys. Chem. B* **102**, 2569 (1998)

[10] Baidina, I. A.; Podberezskaya, N. V.; Alekseev, V. I.; Martynova, T. N.; Borisov, S. V.; Kanev, A. N. *Journal of Structural Chemistry* **20**, 550 (1979)

[11] Accelrys Inc. http://www.accelrys.com/index.html

[12] Sun, H.; Rigby, D. Polysiloxanes: *ab initio* force field and structural, conformation and thermophysical properties. *Spectrochimica Acta Part A* **53** 1301 (1997)

[13] Sun, H.; Ren, P.; Fried, J. R. The COMMPASS force field: parameterization and validation for phosphazenes. *Computational and Theoretical Polymer Science* **8**, 229 (1998)

[14] Sun, H. COMPASS: an *ab initio* force-field optimized for condensed-phase applications-overview with details on alkane and benzene compounds. *J. Phys. Chem. B* **102**, 7338 (1998)

[15] (a) Ordejon, P.; Drabold, D. A.; Grumbach, M. P.; Martin, R. M. Unconstrained minimization approach for electronic computations that scales linearly with system size. *Phys. Rev. B* **48**, 14646 (1993) (b) Ordejon, P.; Drabold, D. A.; Martin, R. M.; Grumbach, M. P. Linear system-size methods for electronic-structure calculations. *Phys. Rev. B* **51** 1456 (1995)

[16] P. Ordejon, E. Artacho and J. M. Soler. Self-consistent order-N density-functional calculations for very large systems. *Phys. Rev. B* **53**, 10441, (1996)

[17] Sanchez-Portal, D.; Ordejon, P.; Artacho, E.; Soler, J. M. Density functional method for very large systems with LCAO basis sets. *Int. J. Quantum Chem.* **65**, 453 (1997)

[18] Artacho, E.; Sanchez-Portal, D. *et al*. *Phys. Stat. Sol. (b)* **215**, 809 (1999)

[19] Junquera, J.; Paz, O.; Sanchez-Portal, D.; Artacho, E. Numerical atomic orbitals for linear-scaling calculations. *Phys. Rev. B* **64**, 235111, (2001)

[20] Soler, J. M.; Artacho, E.; Gale, J. D.; Garca, A.; Junquera, J.; Ordejon, P.; Sanchez-Portal, D. Improved, soft-conned NAOs. The Siesta method for *ab initio* order-N materials simulation. *J. Phys.: Condens. Matter* **14**, 2745-2779 (2002)

[21] Sanchez-Portal, D.; Ordejon, P.; Canadell, E. Computing the properties of materials from first principles with Siesta. *Structure and Bonding* **113**, 103-170 (2004)

[22] Delley, B. *J. Chem. Phys.* **92**, 508 (1990)

[23] Delley, B. *J. Chem. Phys.* **113**, 7756 (2000)

[24] Delley, B. Fast Calculation of Electrostatics in Crystals and Large Molecules. *J. Phys. Chem.* **100**, 6107 (1996)

[25] Ionescu, T. C.; Qi, F.; McCabe, C.; Striolo, A.; Kieffer, J.; Cummings, P. T. Evaluation of forcefields for molecular simulation of polyhedral oligomeric silsesquioxanes. *Journal of Physical Chemistry B* **110**, 2502 (2006)

[26] Hohenberg, P.; Kohn, W. *Physical Review B* **136**, B864 (1964)

[27] Kohn, W.; Sham, L. J. *Physical Review* **140**, 1133 (1965)

[28] (a) Perdew, J. P. *Physical Review B*, **33**, 8822 (1986); (b) Becke, A. D. *Physical Review A* **38**, 3098 (**1988**); (c) Lee, C. T.; Yang, W. T.; Parr, R. G. *Physical Review B* **37**, 785 (1988); (d) Perdew, J. P.; Wang, Y. *Physical Review B* **45**, 13244 (1992); (e) Becke, A. D. *Journal of Chemical Physics* **98**, 1372 (1993); (f) Becke, A. D. *Journal of Chemical Physics* **98**, 5648 (1993)

[29] Parrinello, M.; Rahman, A. *Phys. Rev. Lett.* **45**, 1196 (1980)

[30] Parrinello, M. *Physical Review Letters* **55**, 2471 (1985)

[31] Chaka, A. M.; Zaniewski, R.; Youngs, W.; Tessier, C.; Klopman, G. Predicting the crystal structure of organic molecular materials. *Acta Cryst. B* **52**, 165 (1996)

[32] Campbell, R. B.; Robertson, J. M.; Trotter, J. *Acta Cryst.* **14**, 705 (1961)

[33] Robertson, J. M.; Sinclair, V. C.; Trotter, *J. Acta Cryst.* **14,** 697 **(**1961)

[34] Fulem, M.; Lasťovka, V.; Straka, M.; Růžička, K.; Shaw, J. M. heat capacities of tetracene and pentacene. *J. Chem. Eng. Data* **53**, 2175-2181 (2008)

Chapter 5
Computational Molecular Design and Engineering of Small Band Gap Halogen-Benzene Functionalized SQ

5.1 Introduction

5.1.1 Recently synthesized octa(halogenphenyl)-SQ crystals

Recently, the successful synthesis of a series of halogen-benzene functionalized T8 SQ molecular crystals by halogenation of octaphenylsilsesquioxane (OPS) was reported. [1-6] In contrast to diacene-SQ, which featured a pair of long acene molecules attached at the body diagonal positions, most of these halogen-benzene functionalized T8 SQ, where all the eight vertices have the same molecular group attached, retain cubic symmetry. This feature creates the possibility for three-dimensional connectivity, instead of the flat geometry for other molecular organic semiconductors. The synthesis route of this work is also attractive, as crystals are obtained from solution methods, which have much lower cost compared to other methods such as vacuum deposition. This aspect will help with industrial application of these materials.

As this point, the Laine group has been able to synthesize halogen-benzene functionalized T8 SQ molecules with up to 24 bromine atoms, averaging three bromine atoms per benzene ring. Additionally, octa(4-iodophenyl)-SQ, as shown in scheme 5-1, with one iodine atom for each benzene ring has been synthesized.

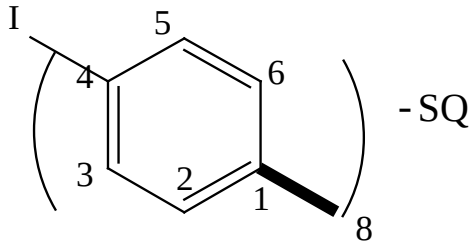

Scheme 5-1 Molecular structure of octa(4-iodophenyl)-SQ. "octa" means eight of the 4-iodophenyl groups attached to the SQ; the number 1 to 6 indicates the position of the six carbon atoms on the phenyl ring. The position 1 is defined as the carbon that bonded to the silicon atom on the SQ cage).

Unit cell coordinates of these newly synthesized crystals are reported by the inventors.[8]

5.1.2 Reported high hole mobility of 1,4-diiodobenzene

Halogenation has been shown to improve carrier mobilities in organic semiconductor materials.[9] One such material is 1,4-diiodobenzene (DIB), with experimentally determined hole mobility reported to reach ~10 $cm^2/V{\cdot}S$ at room temperature.[10,11,12] The charge transport mechanism in this material was analyzed by *ab initio* electronic structure calculations, and attributed primarily to the large size and high density of molecular orbitals in the hole band of the iodine atoms. The high atomic number of iodine results in wide conduction and

valence band widths, and a high density of sub bandlines with smaller dispersions on each sub band. Together with transfer integral calculations, the band-structure analysis confirmed the dominance of iodine interactions to the electronic coupling for both holes and electrons.[10] Further investigations indicated that incorporating iodine into benzene significantly decreases the local hole–vibration coupling.[10] The overall hole conduction bandwidth, polaron binding energy, and effective mass all indicated a band-like transport mechanism for holes in DIB.[10] Electrons, however, are localized by a very large polaron binding energy, and therefore have a low mobility in a DIB crystal.[10]

Despite the high hole mobility, several key drawbacks limit large-scale production of DIB. First, the crystalline form is not stable at room temperature, and the melting point of DIB crystal is only 404 K. Additionally, the pure crystal is hard to produce directly from solution. Therefore, it is interesting to further investigate whether functionalizing SQ with DIB molecules, to create octa(2,5-diiodophenyl)-SQ, will create a better molecular semiconductor candidate. Electronic structure analysis of this new molecule, including molecular orbitals, band structure, DOS and PDOS can be used to predict how this new molecule will perform compared to DIB.

5.1.3 Motivation and research approach

Based on these observations, halogen-benzene tethered SQ molecules merit further consideration in terms of computational molecular design. While experimental synthesis work is often expensive in both time and materials, simulations can provide a more economical and rapid way for exploring electronic properties of conceived molecular structures in advance of synthesis. As previously discussed, coordinates of experimentally realized and characterized molecular crystals are an effective starting point for exploring modified architectures. By conducting these modifications without disturbing the original space group symmetry, new molecules can be designed by atomic substitution and the systematic variation of functional end groups. For the halogen functionalized phenyl-SQ systems, the obvious modification factors are the number and type of halogen atoms attached to the phenyl rings. Although, molecules with such small modifications are expected to have geometries and symmetries similar to the starting molecules, the most likely structures of the new molecules, based on ground state energy considerations, be explored computationally. Using MD simulations based on a reliable force field the assumed initial configurations can be relaxed into stable final structures. The electronic properties of these predicted structures can then be evaluated using density functional theory calculations.

This study aims to identify new potential candidate semiconductor molecules and to identify the mechanisms by which to control their electronic and photonic properties. If small-gap SQ-based organic-inorganic hybrid materials are found by this study, the ensuing design rules may serve to guide the experimental synthesis work. Such new octa(halogenphenyl)-SQ molecular crystals have potential for use in energy and electronic applications, especially given the potential for establishing three-dimensional conduction pathways due to the cubic symmetry of the basic building blocks.

5.2 Computational Molecular Design and Engineering of Octa(halogenphenyl)-SQ

5.2.1 Verification of the simulation methods

As the previous chapter showed, using atomistic MD simulations and *ab initio* calculations, that we can successfully design SQ-based small band gap semiconductor molecules [15,16]. Results presented in this chapter are derived from density functional theory calculations using the Dmol3 software package, combined with MD simulations with the COMPASS force field. DFT calculations used the high performance double numerical polarized (DNP) basis set with PBE exchange correlation functional under GGA and pseudopotential for core electrons-nuclei interactions. Band gaps for crystal structures were calculated via the DMol3 method at the gamma point.

For a reliable molecular design, it is imperative to verify the suitability of the simulation methods in describing the targeted systems and their properties. Although the COMPASS force field was found to adequately describe the molecular structures of a number of SQ-based systems[15], a first step will still be to verify its application to the halogen-benzene-SQ system[17,18,19]. Moreover, in our approach for predicting the structure and properties of newly designed molecules, we use the crystal configurations that are known for specific molecules as starting points. We then alter the molecular architecture slightly, i.e., without perturbing the intrinsic symmetry of the original molecule, in the hopes that the crystal symmetry of the new molecule will the same as that of the original molecule as well. As a second validation step, we will therefore ascertain that this is the case. In other words, we make sure that upon relaxing the crystal structure of a newly designed molecule the system does not get stuck in a local energy minimum, but that equilibrium structure the system converges to is unique, irrespective of the starting configuration

5.2.1.1 Interaction model validation

In order to validate simulation geometry, results are compared to experimental data for bond lengths, angles, molecular conformation, crystal unit cell data and packing behaviors, to the extent that these are available. Hence, the following simulations were conducted: Starting with the known experimental atomic coordinates as input, a classical force field-based MD simulation was used for

initial geometry optimization. These partially optimized structures are then further relaxed by DFT based calculations. The DFT relaxed crystal unit cell information was then compared with the experimental values. The crystal structures and atomic coordinates of three octaphenylsilsesquioxane (OPS) derivative molecules are known from experiments and thus, are amenable for this comparison.

a) Br_{16}OPS

Synthesized Br_{16}OPS is named octa(2,5-dibromophenyl)silsesquioxane or octa(2,5-dibromophenyl)-SQ. The experimental unit cell belongs to the $P\bar{1}$ symmetry group and molecular site symmetry is *C*i (-1), which is summarized in Table 5-1. As introduced in chapter 2, the molecular site symmetry implies high probability of crystallizing in $P\bar{1}$ space group is proved in the case of Br_{16}OPS. For the other two experimental crystals, given their molecule site, the space groups of these two are falling in seldom shown space groups of *P*4/n and *I*4/m respectively.

Table 5-1 Experimental symmetry group data of Br_{16}OPS crystal

	Br_{16}OPS	OPS	8i3
Symmetry Group Name	$P\bar{1}$	*P*4/n	*I*4/m
International Tables #	2	85	87
Long Name	*P* -1	*P*4/n	*I*4/m
Schoenflies Name	*C*l -1	*C*4h-3	*C*4h-5
Crystal System	Triclinic	Tetragonal	Tetragonal
Crystal Class	-1	4/m	4/m
# of Operators	2	8	16
Molecule site symmetry	*C*i (-1)	*C*4 (4)	*C*2h (2/m)

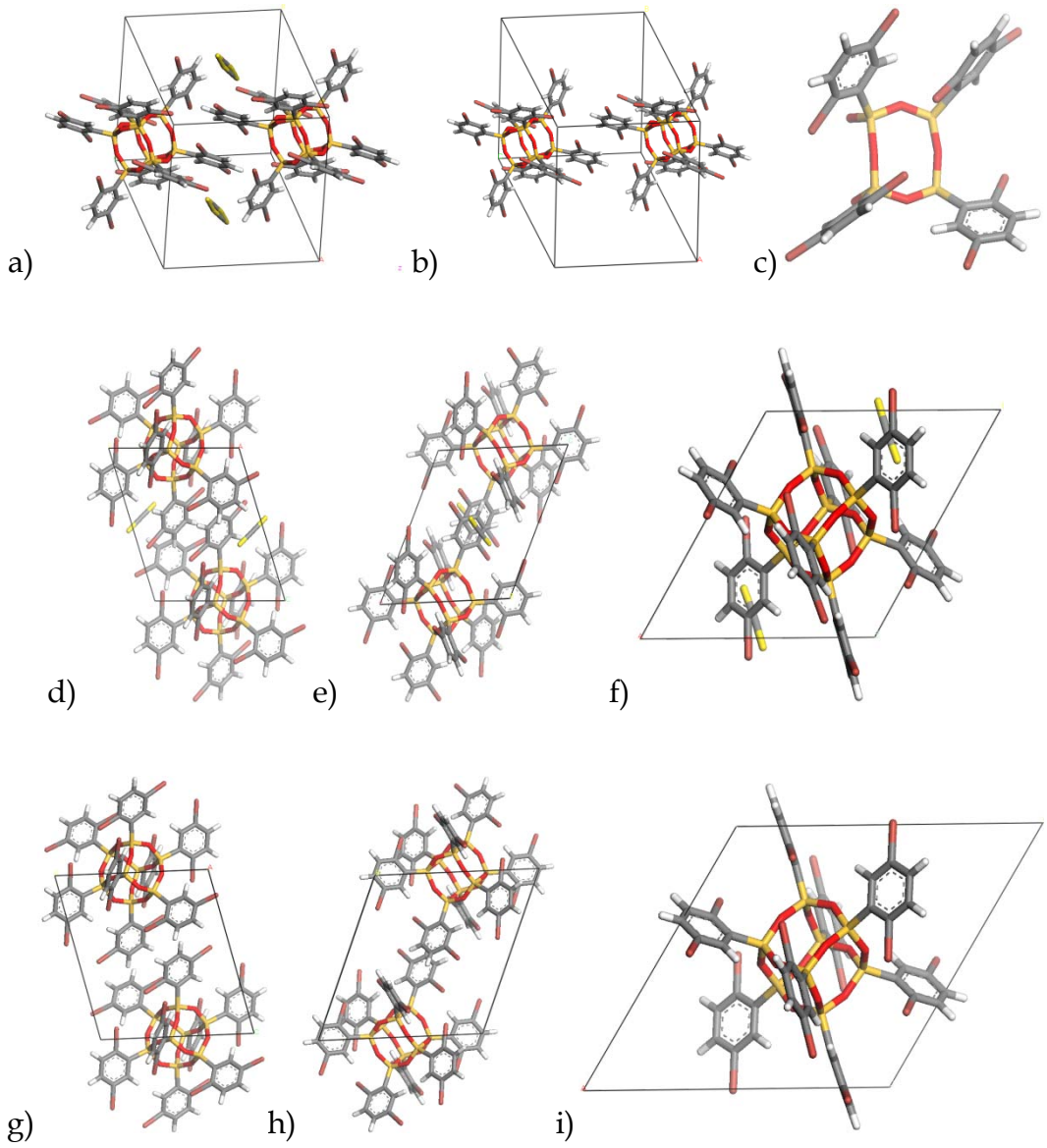

Figure 5-1 The $Br_{16}OPS$ unit cell from experimental work: a) unit cell with the CS_2 molecule; b) CS_2 was removed from the unit cell; c) the asymmetry unit;; experimental unit cell in view of d) x, e) y, and f) z direction; *ab initio* DFT refined unit cell in view of g) x, h) y and i) z direction. The DFT relaxed unit cell of $Br_{16}OPS$ has a larger cell volume and smaller density than the experimental unit cell. This discrepancy is due to the missing van der Waals interaction in current DFT method.

As shown in Figure 5-1 a), the experimental unit cell contains a CS_2 molecule. In order to test the influence of this small molecule to the crystal, two MD

relaxations are performed to test the relaxed structure with and without the CS_2 starting with the same experimental crystal unit cell coordinates. The differences of unit cell properties are summarized in Table 5-2.

Table 5-2 MD relaxation test to the Br_{16}OPS experimental coordinates

	ρ(g/cm^3)	a(Å)	b(Å)	c(Å)	α(°)	β(°)	γ(°)
With CS_2	2.23	12.35	13.88	13.32	97.49	109.81	120.68
No CS_2	2.40	12.36	12.42	13.01	95.46	112.82	114.85
% change	7.3	0.08	11.8	2.4	2.1	2.7	5.1

The comparison shows that removing the CS mainly causes one unit cell parameter (b) to change by less than 10%. The other parameters change from 0.08% to 5.1%. The average change of the six parameters is ~4%. Therefore, we consider that removal of the CS_2 molecule from the experimental unit cell will only slightly change the global energy minimum and the followed MD and DFT will overcome this optimization barrier. During the relaxation, the symmetry of the crystal is not forced to remain the same as the input. All the 6 unit cell parameters are set to be variable for the optimization method.

To further validate this result, MD and followed DFT relaxed crystal unit cell structure was compared to the experimental unit cell visually, as shown in Figure 5-1 and Figure 5-2.

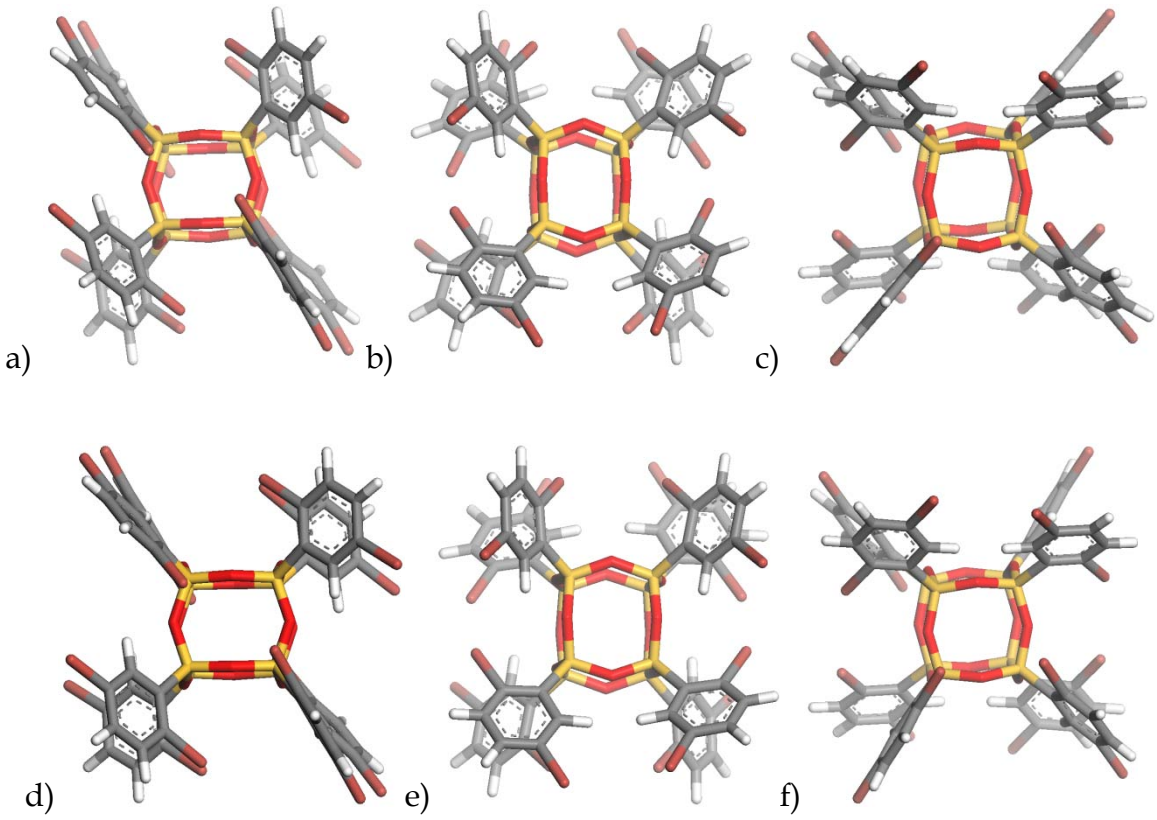

Figure 5-2 (2,5-dibromophenyl)-SQ molecule from experimental unit cell in a) x, b) y, and c) z direction; from *ab initio* DFT refined unit cell in d) x, e) y and f) z direction. DFT refined molecule keep very close geometry as experimental one.

From these plotted crystal and molecular structures, it can be concluded that both the crystal structure and molecular geometry keep very high similarity.

In Br_{16}OPS crystal, the SQ cages in neighboring unit cells are aligned parallel to each other. (Note that there is one molecule per primitive unit cell.). The structures parameters, including bond lengths and angles, relaxed in MD simulations are compared with experimental and DFT calculations with both measured smallest value and largest value. The difference between MD and experiment is from 0 to 4.88%, with an average of 1.71%. The difference between

DFT and experiment is from 0.05% to 1.8%, with an average of 0.96%. The difference between MD and DFT is from 0.16% to 5.7%, with an average of 2.09%. Overall, MD shows less than 3% difference compared to experiment and DFT calculated bond lengths and angles, which demonstrates the force field is able to effectively describe the structure of the system. The DFT calculated direct band gap is 3.48 eV, which is somewhat large to make this molecule to be considered as potential molecular semiconductors. Geometric parameters for verification of the simulation results are summarized in Tables 5-3 and 5-4.

Table 5-3 Selected geometry parameters of simulated and experimental $Br_{16}OPS$ crystals. (Bond lengths and angles vary according to the actual chemical surroundings.)

		Si-O(Å)	Si-C(Å)	Si-O-Si(°)	O-Si-O(°)	O-Si-C(°)
Exp.	Min	1.607	1.844	137.470	107.501	106.861
	Max	1.628	1.852	155.882	110.502	114.453
DFT	Min	1.636	1.869	137.392	108.329	107.251
	Max	1.651	1.872	153.406	109.906	113.782
MD	Min	1.607	1.865	139.894	106.348	105.028
	Max	1.633	1.869	162.224	109.094	120.039

Table 5-4 Selected crystallographic data of simulated and experimental $Br_{16}OPS$ crystals

	Space Group	a(Å)	b(Å)	c(Å)	α(°)	β(°)	γ(°)	ρ(g/cm^3)
Exp.	$P\bar{1}$	12.72	12.74	13.09	97.59	109.08	116.23	2.24
DFT	$P\bar{1}$	13.19	13.29	13.58	97.46	109.05	117.08	2.02
MD	$P\bar{1}$	12.36	12.42	13.01	95.46	112.82	114.85	2.40

b) Octaphenylsilsesquioxane (OPS)

The OPS crystal unit cell has two molecules per unit cell. SQ cage faces are again parallel, as shown in Figure 5-3. The isolated OPS molecule itself has *C*4

symmetry, while the crystal unit cell has a *P*4/n symmetry group, which is summarized in Table 5-1.

The unit cell of the OPS crystal is shown is Figure 5-3.

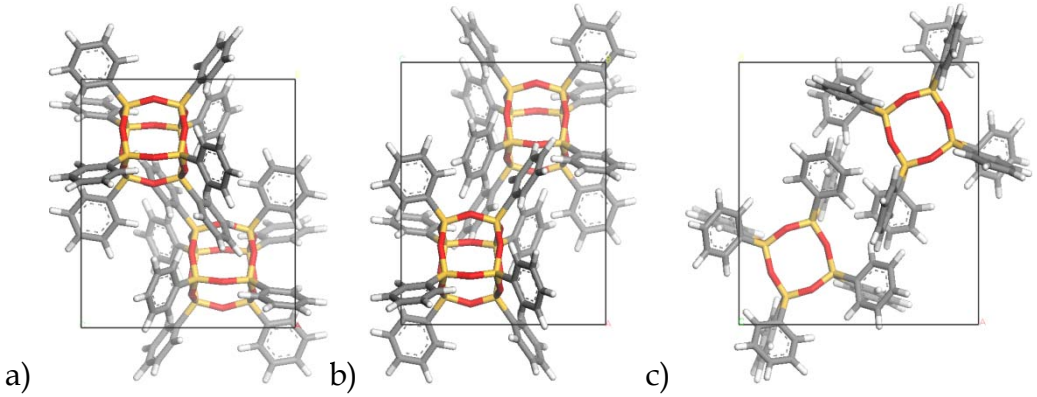

Figure 5-3 OPS crystal unit cell view in a) x, b) y and c) z direction

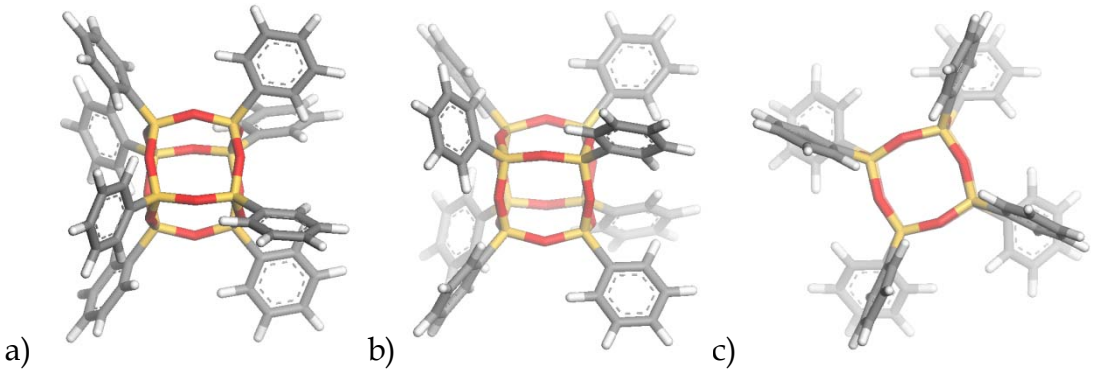

Figure 5-4 Views of OPS molecule at a)x, b)y, and c)z direction

To illustrate the conformation of the OPS molecule, one molecule inside the unit cell is isolated in 3-D view. As shown in Figure 5-4, the OPS molecule features an "upper" four phenyl rings, which have roughly a 45 degree angle with respect to the plane containing the four silicon atoms they are connected to, and a "lower" four phenyl rings oriented at roughly a 90 degree with respect to the

corresponding silicon plane. MD energy minimization and then DFT relaxations to the same crystal structure were also carried out to check consistency. The overall differences for measured bond lengths and angles between MD, DFT and experiment are also within 3% range. The DFT calculated direct band gap of this crystal structure is 4.36 eV, which is much larger than the threshold benchmark value of 3 eV to be considered small band gap molecular crystal. Selected structural characteristics are summarized in Table 5-5 and 5-6.

Table 5-5 Selected geometry parameters of simulated and experimental OPS crystals

		Si-O(Å)	Si-C(Å)	Si-O-Si(°)	O-Si-O(°)	O-Si-C(°)
Exp.	Min	1.607-	1.829-	144.629-	107.992-	108.254-
	Max	1.617	1.838	151.531	109.952	111.674
DFT	Min	1.621-	1.846-	148.482-	107.309-	108.049-
	Max	1.624	1.857	151.882	109.167	113.289
MD	Min	1.621-	1.866-	148.433-	107.315-	108.084-
	Max	1.624	1.867	151.945	109.142	113.212

Table 5-6 Selected crystallographic data of simulated and experimental OPS crystals

	Space Group	*a*(Å)	*b*(Å)	*c*(Å)	*α*(°)	*β*(°)	*γ*(°)	*ρ*(g/cm^3)
Exp.	*P* 4/n	14.608	14.608	12.918	90	90	90	1.245
DFT	*P* 4/n	14.556	14.556	12.519	90	90	90	1.294
MD	*P* 4/n	14.573	14.573	12.557	90	90	90	1.287

c) Para-octaiodophenylsilsesquioxane (8i3), [p-IC$_6$H$_4$SiO$_{1.5}$]$_8$

The experimentally synthesized para-octaiodophenylsilsesquioxane (4-iodophenyl-SQ) molecule [1] unit cell belongs to the *I*4/m symmetry group,

which is summarized in Table 5-1. It contains one iodine atom at the para-position of the benzene, which is attached to the SQ cage. The molecule site symmetry is *C*2h. The crystal unit cell has four molecules, as shown in Figure 5-5.

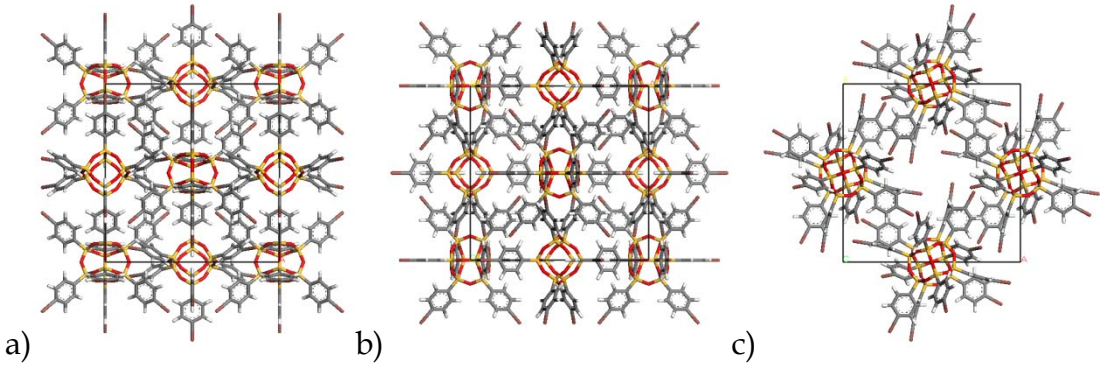

Figure 5-5 Para-octaiodophenylsilsesquioxane crystal unit cell with a) x direction view; b) y direction view; and c) z direction view. 4 molecules per unit cell, not all SQ cages are paralleled facing each other

In this crystal, the SQ cages are not directly parallel to each other. There is instead a 45 degree angle between adjacent cages. This forms a corner to face packing pattern for SQ molecules instead of the parallel packing seen for other molecules, as shown in Figure 5-5. The *I*4/m symmetry of the crystal is mostly due to the high symmetry of the octa(iodophenyl)-SQ molecule itself, which has a *C*2h(2/m) symmetry, as shown in Figure 5-6.

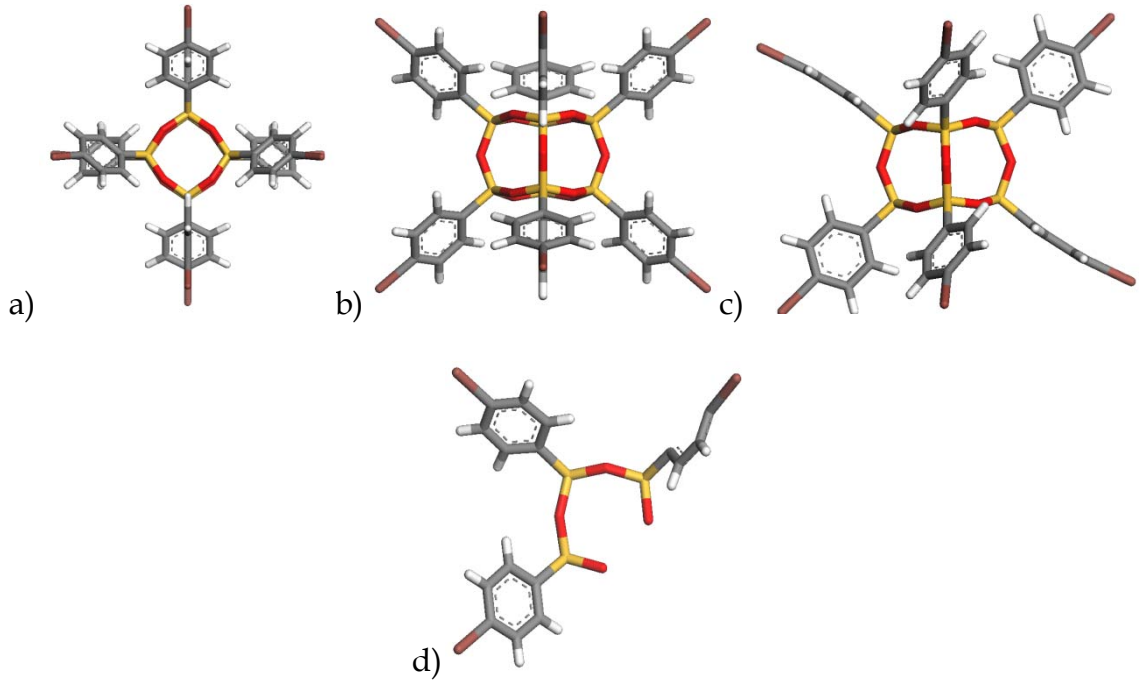

Figure 5-6 isolated para-octaiodophenylsilsesquioxane molecule with a) x direction view; b) y direction view; and c) z direction view, and d) the asymmetry unit.

The calculated direct (gap between CB and VB at gamma point) band gap of this molecule is 3.04 eV, which is only slightly larger than 3 eV, bringing it very close to the threshold value for being considered a semiconductor small molecule. The simulation results are summarized in Table 5-7 and 5-8. The overall differences for measured bond lengths and angles between MD, DFT and experiment are again within 3% change range.

Table 5-7 Selected geometry parameters of simulated and experimental [p-$IC_6H_4SiO_{1.5}]_8$ crystals

		Si-O(Å)	Si-C(Å)	Si-O-Si(°)	O-Si-O(°)	O-Si-C(°)
Exp.	Min	1.590	1.804	144.761	108.000	108.469
	Max	1.616	1.828	152.015	110.292	112.124
DFT	Min	1.63	1.848	139.759	107.906	107.457
	Max	1.647	1.857	152.373	111.483	110.608
MD	Min	1.62-	1.865	148.203	107.831	109.782
	Max	1.627	1.874	152.172	108.838	112.333

Table 5-8 Selected crystallographic data of simulated and experimental [p-$IC_6H_4SiO_{1.5}]_8$ crystals

	Space Group	*a*(Å)	*b*(Å)	*c*(Å)	*α*(°)	*β*(°)	*γ*(°)	*ρ*(g/cm^3)
Exp.	*I*4/m	20.04	20.04	21.46	90	90	90	1.573
DFT	*I*4/m	20.916	20.916	20.439	90	90	90	1.516
MD	*I*4/m	20.956	20.956	21.828	90	90	90	1.414

5.2.1.2 Validation of the model system symmetry and space group

We conducted a series of simulations to ascertain that the structural relaxation procedure we subjected our modified molecules to indeed reach a truly representative minimum-energy configuration as opposed to getting stuck in a local energy minimum because the MD and DFT-based energy minimization algorithms do not allow for crossing between symmetry groups. To this end, we purposely start our structure optimization in the "wrong" symmetry group, i.e., a different symmetry group than that found experimentally for unmodified molecule, and compare the result with the one we obtained when using the "correct" experimental structure of the original molecule. MD geometry optimization is performed using COMPASS force field and a smart minimization

algorithm, which combines the steepest descent, conjugate gradient, and Newton-Raphson algorithms in searching the energy minimums [35-37]. DFT calculations are performed using Dmol3 with exchange correlation functional by PBE and core electron treated with semi-core pseudopotentials

Table 5-9 Experimental molecular crystal unit cells with symmetry information

Molecule	8i3	Br3ops	Brops	Obr8a	OPS
Symmetry Space Group	*I*4/m	$P\bar{1}$	$P\bar{1}$	*I*4(1)/a	*P* 4/n
Molecule site symmetry	*C*2h	*C*i	*C*i	-	*C*4
Symmetry Cell Setting	Tetragonal	Triclinic	Triclinic	Tetragonal	Tetragonal

Based on available experimental molecular site symmetry and crystal space group information, summarized in Table 5-9, the following two typical molecular crystal systems are selected as the starting configurations for unmodified molecules.

1) Octa(2,5-bromophenyl)-SQ with experimental $P\bar{1}$ crystal symmetry, containing 1 molecule per unit cell (the small solvent molecule CS_2 was removed from the unit cell)
2) Octa(4-iodophenyl)-SQ with experimental *I* 4/m crystal symmetry, containing 4 molecules per unit cell

For the MD simulations, the initial coordinates are based on the modified experimental coordinates of Br_{16}OPS and octa(4-iodophenyl)-SQ. Initial bond

lengths and angles were set by performing one step energy minimization to accommodate elemental changes.

The results are shown in Table 5-10. For the Br16OPS crystal both simulation methods yield lower system energy when the crystal is in the structure with $P\bar{1}$ packing symmetry as opposed to the structure with $I4/m$ symmetry. In the case of the octa(4-iodophenyl)-SQ molecular crystal, MD simulations predict that again that the $P\bar{1}$ space group SQ has the lower ground state energy, while DFT calculations predict the $I4/m$ symmetry is more stable, although, the two calculated energy values are too close to be considered a criterion for which structure is more stable. One possible explanation for this discrepancy between experiment and simulation is that experiments probe structures at room temperature, whereas the calculated ground state energies reveal the structures that are stable at zero Kelvin. The true indicator for thermodynamic stability is the free energy, which includes the product of temperature and entropy. It is therefore possible that the octa(4-iodophenyl)-SQ molecular crystal would assume a structure with $P\bar{1}$ symmetry at zero Kelvin and $I4/m$ at room temperature. Free energy calculations of these systems were beyond the scope of this investigation. Since we are evaluating the modified structure of the above molecules also at zero Kelvin, we decided to carry out calculations for all differently functionalized molecules using the Br_{16}OPS.molecule in space group $P\bar{1}$ as the starting configuration. For the iodo-complexes this is justified,

considering the small difference in the ground state energy between $P\bar{1}$ and $I4/m$ symmetries. Also, as shown in our chapter 2, many molecules with site symmetry other than *C*i, *C*1, *C*2 and *C*s will be very hard to predict their crystal space group. Therefore, in this study we focus on using Br_{16}OPS as the model to modify molecules and keep their site symmetry and crystal space group as the same as Br_{16}OPS for the most probable prediction.

Table 5-10 Total system energy of minimized octa(2,5-dibromophenyl)-SQ and octa(4-iodophenyl)-SQ under $P\bar{1}$ and $I4/m$ symmetry

	Octa(2,5-dibromophenyl)- SQ (Br_{16}OPS)		Octa(4-iodophenyl)-SQ (8i3)	
Relaxation Method	MD (kcal/mol)	*Ab initio* (Ha)	MD (kcal/mol)	A*b initio* (Ha)
P -1	-851.30	-10562.28	-692.89	-6575.33
I 4/m	-811.70	-10560.69	-670.62	-6575.45
Stable Symmetry	$P\bar{1}$	$P\bar{1}$	$P\bar{1}$	$I4/m$
Exp. Symmetry	$P\bar{1}$	$P\bar{1}$	$I4/m$	$I4/m$

5.2.2 Computational molecular engineering strategy for octa(halogenphenyl)-SQ

5.2.2.1 Methods, strategy and procedures

The next step is to construct molecular derivatives based on the experimental molecular systems. The designed molecular systems were optimized by classical force field [17-19] and further optimized by *ab initio* methods [20-23]. The optimization algorithms used in these simulations include steepest descents, conjugate gradient and Newton-Raphson methods. After geometric validation, a series of octa(halogenphenyl)-SQ molecules was constructed using Br_{16}OPS

experimental unit cell information. To maintain the cubic molecular symmetry, all eight phenyl groups were kept identical for the novel systems. These molecular systems, including unit cell parameters, were relaxed by system energy minimization using previously described methods. Electronic properties were measured for each successfully relaxed molecular crystal. Among the properties, we calculated the band gap of the molecular crystal at the gamma point. Since the experimentally synthesized octa(4-iodophenyl)-SQ shows a small band gap, it may be possible to find other functionalized molecules with even smaller band gaps, which are expected to be within 0.5 to 3 eV.

The Br_{16}OPS unit cell provides a starting point, and the modifications we performed consisted of replacing the hydrogen atoms on the benzene ring with halogen atoms in a systematically varied order. There are five available positions for the halogen atoms and four candidate halogen atoms: F, Br, Cl and I. These designed molecules were modified from the experimental crystal coordinates and adapted to the same space group crystal symmetry [1].

By substituting bromine atoms for hydrogen on the benzene ring, the total number of bromine atoms increases from one to five for each benzene ring attached to the SQ cage. All eight benzene rings on the SQ cage are identical. At the start of the structure optimization, bromine atoms have the same coordinates as the original H atoms attached to the phenyl ring. These initial structures are then relaxed. Since there are four halogen species considered, the design process

explores a two-dimensional parameter space. First, all possible combinations of replacing hydrogen with between 1 and 5 halogens are considered. Given 5 possible sites per benzene, and constraining all benzene rings to identical configurations, 30 possible molecules are considered, including the experimental Br16-OPS structure. Second, for each of these geometric configurations, a different halogen species was used, while each system contains only one halogen species. We did not consider mixing halogen species because the shear number of possibilities would exceed the scope of this project. It did also not seem indicated based on the results we obtained for single-species systems. In fact, considering the rather weak and similar trends observed when substituting from 1 to 5 hydrogens with bromine or fluorine, we only examined the octa(2,3,4,5,6-pentachlorophenyl)-SQ and octa(2,3,4,5,6-pentaiodophenyl)-SQ in the end. Ultimately, 45 total molecular systems were constructed and studied.

For each system, valance band (VB) edge, conduction band (CB) edge and the band gap are calculated at the gamma point (direct band gap), and compared to illustrate the trend of band gaps changing with different atomic species and functionalization locations. After band gap trends have been identified, the detailed electronic property analysis was conducted. The distribution of frontier orbitals for select molecules was further examined to understand how the SQ cage contributes to the HOMO, LUMO and energy gap changes. In order to compare with reported high mobility diiodobenzene reports [10], the HOMO and

LUMO are calculated for 1,4-diiodobenzene for comparison with octa(2,5-diiodophenyl)-SQ. Band structures, DOS, and PDOS were also calculated for the octa(2,5-diiodophenyl)-SQ to evaluate the possible carrier mobility in this molecular crystal. Since a full characterization of the mobility mechanism in molecular semiconductor is not the focus of this thesis, higher level calculation and analysis methods, such as transfer integral, polaron binding energies, and electron and hole coupling with the lattice vibrational phonon, are not explicitly studied. A more complete characterization of carrier mobility study can be found in the original reference [10].

5.3 Results and Discussion

5.3.1 Structure and electronic properties of octa(halogenphenyl)-SQ

The calculated VB, CB and band gaps from the relaxed unit cell of the modified molecular systems are summarized from Table 5-11 to Table 5-18. All systems are optimized using a combination of classical force field and *ab initio* methods.

Octa(bromophenyl)-SQ

There are five possible configurations for a single bromine atom on the phenyl ring of the octa(bromophenyl)-SQ molecular system. The calculated VB, CB and band gaps are summarized in Table 5-12 and Figure 5-7. A relaxed unit cell of octa(2-bromophenyl)-SQ is shown in Figure 5-8.

Table 5-11 VB, CB, band gaps and total energy of octa(bromophenyl)-SQ $(C_6BrH_4(SiO_{1.5}))_8$

	VB (eV)	CB (eV)	Band Gap (eV)	E_{tot} (Ha)
Octa(2-bromophenyl)-SQ	-6.35	-2.60	3.75	-7816.146625
Octa(3-bromophenyl)–SQ	-6.43	-2.50	3.93	-7816.147735
Octa(4-bromophenyl)–SQ	-6.58	-2.54	4.04	-7816.166537
Octa(5-bromophenyl)–SQ	-6.32	-2.60	3.72	-7816.16146
Octa(6-bromophenyl)-SQ	-6.28	-2.64	3.63	-7816.100829

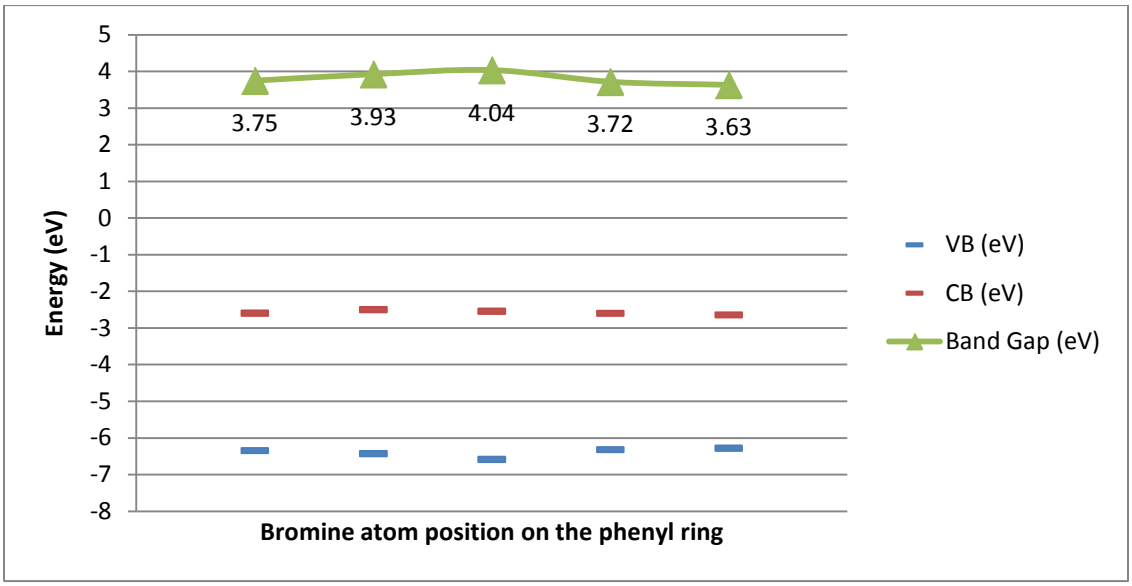

Figure 5-7 VB, CB and band gaps for one bromine octa(bromophenyl)-SQ

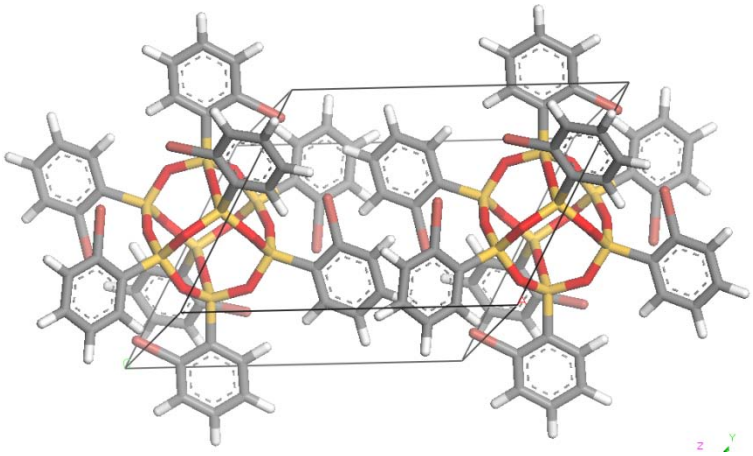

Figure 5-8 The unit cell of one bromine octa(6-bromophenyl)-SQ

Depending on the location of the single bromine substitution, the octa(bromophenyl)-SQ molecule has a band gap from 3.63 to 4.03 eV, with the smallest band gap achieved with octa(6-bromophenyl)-SQ. Hence, varying the position of the bromine atom on the phenyl ring changes the band gap by 10% or less.

Octa(dibromophenyl)-SQ

There are ten possible configurations of two bromine atoms on each of the phenyl ring in the octa(dibromophenyl)-SQ molecular system. As previously mentioned, we keep the eight phenyl ring identical in the design. The calculated VB, CB and band gaps are summarized in Table 5-12 and Figure 5-9. An example of the unit cell is shown in Figure 5-10.

Table 5-12 Band gaps of octa(dibromophenyl)-SQ, $(C_6Br_2H_3(SiO_{1.5}))_8$

	VB (eV)	CB (eV)	Band Gap (eV)	E_{tot} (Ha)
Octa(2,3-dibromophenyl)-SQ	-6.27	-2.88	3.40	-10562.34072
Octa(2,4-dibromophenyl)-SQ	-6.37	-2.70	3.67	-10562.39751
Octa(2,5-dibromophenyl)-SQ	-6.21	-2.72	3.48	-10562.42334
Octa(2,6-dibromophenyl)-SQ	-6.10	-2.87	3.23	-10562.31978
Octa(3,4-dibromophenyl)-SQ	-6.26	-2.66	3.60	-10562.38383
Octa(3,5-dibromophenyl)-SQ	-6.17	-2.68	3.49	-10562.41809
Octa(3,6-dibromophenyl)-SQ	-6.18	-2.74	3.44	-10562.35566
Octa(4,5-dibromophenyl)-SQ	-6.26	-2.74	3.52	-10562.38418
Octa(4,6-dibromophenyl)-SQ	-6.41	-2.74	3.67	-10562.38782
Octa(5,6-dibromophenyl)-SQ	-6.22	-2.88	3.34	-10562.32325

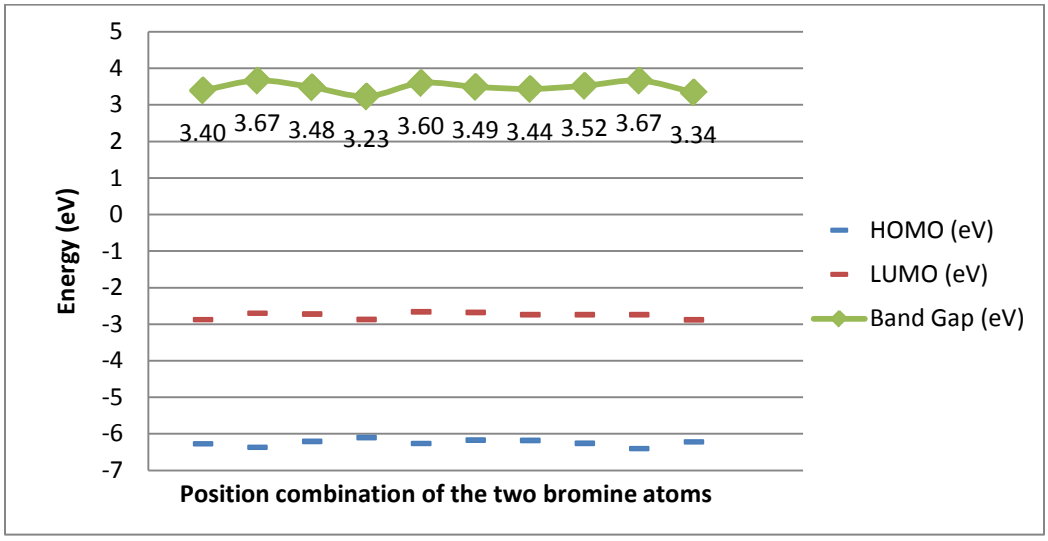

Figure 5-9 VB, CB and band gaps for two bromine octa(dibromophenyl)- SQ. Starting from the left, the first column is octa(2,3-dibromophenyl)-SQ then goes as the sequence in the table 5-12 to octa(5,6-dibromophenyl)-SQ.

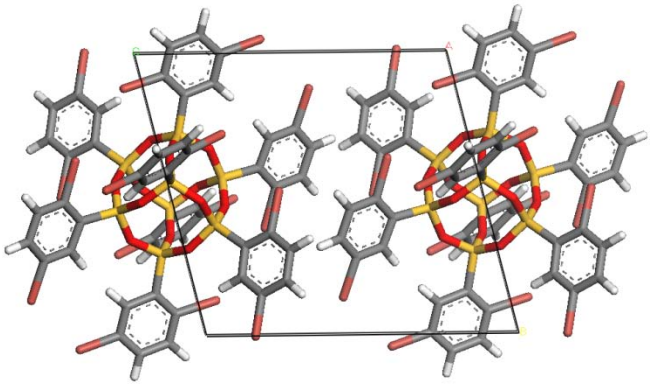

Figure 5-10 Unit cell structure of octa(2,5-dibromophenyl)-SQ

These octa(dibromophenyl)-SQ configuration have band gaps ranging from 3.23 to 3.67 eV, with the octa(2,6-dibromophenyl)-SQ configuration having the smallest band gap and octa(2,4-dibromophenyl)-SQ has the largest. Varying the positions of the two bromine atoms on the phenyl ring can a effect changes in the band gap of up to 11.9%. Compared to single bromine systems, the band gaps of octa(dibromophenyl)-SQ molecular systems are on average smaller by about 0.4 eV.

Octa(tribromophenyl)-SQ

There are 10 combinations by placing three bromine atoms on the phenyl ring of octa(tribromophenyl)-SQ molecular system. Calculated VB, CB levels and band gaps are summarized in Table 5-13 and Figure 5-11. An example of the unit cell is shown in Figure 5-12.

Table 5-13 HOMO, LUMO and band gaps of octa(tribromophenyl)-SQ $(C_6Br_3H_2(SiO_{1.5}))_8$

	VB (eV)	CB (eV)	Band Gap (eV)	E_{tot} (Ha)
Octa(2,3,4-tribromophenyl)–SQ	-6.24	-3.00	3.25	-13308.56718
Octa(2,3,5-tribromophenyl)–SQ	-6.22	-2.79	3.43	-13308.61394
Octa(2,3,6-tribromophenyl)–SQ	-6.13	-3.01	3.12	-13308.53501
Octa(2,4,5-tribromophenyl)–SQ	-6.16	-2.82	3.34	-13308.61901
Octa(2,4,6-tribromophenyl)–SQ	-6.21	-2.94	3.27	-13308.5438
Octa(2,5,6-tribromophenyl)–SQ	-6.17	-3.13	3.04	-13308.53287
Octa(3,4,5-tribromophenyl)–SQ	-6.24	-2.87	3.37	-13308.60098
Octa(3,4,6-tribromophenyl)–SQ	-6.21	-2.76	3.46	-13308.61716
Octa(3,5,6-tribromophenyl)–SQ	-6.15	-2.92	3.22	-13308.59819
Octa(4,5,6-tribromophenyl)-SQ	-6.32	-3.09	3.24	-13308.58254

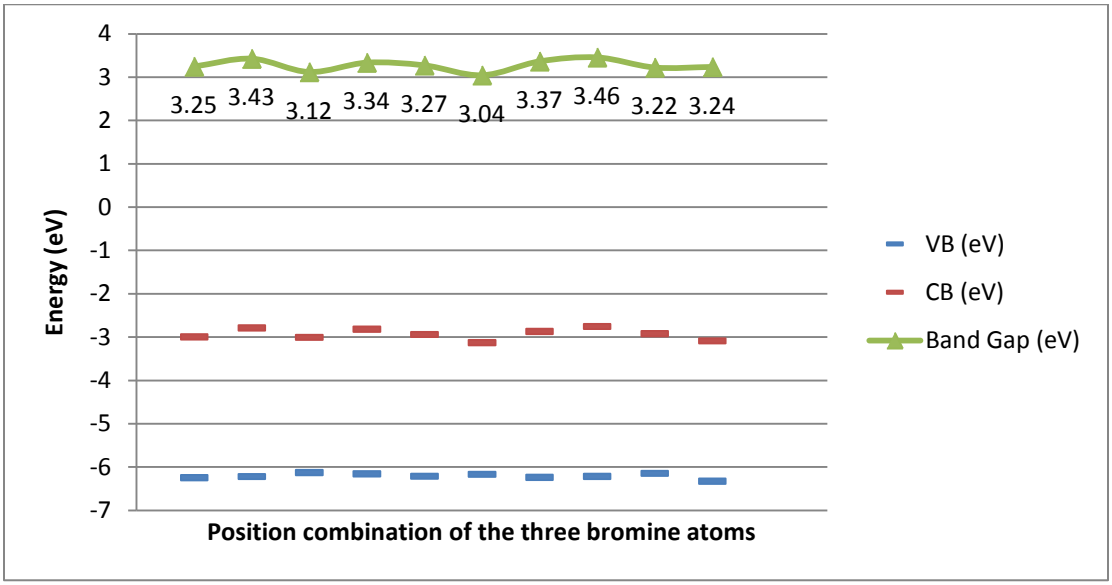

Figure 5-11 HOMO, LUMO and band gaps of octa(tribromophenyl)-SQ. Starting from the left, the first column is octa(2,3,4-tribromophenyl)-SQ then goes as the sequence in the table 5-13 to octa(4,5,6-tribromophenyl)-SQ.

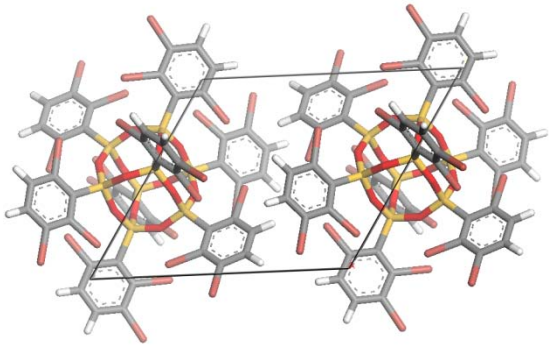

Figure 5-12 Unit cell structure of octa(2,5,6-tribromophenyl)-SQ

These octa(tribromophenyl)-SQ systems have band gaps ranging from 3.04 to 3.46 eV. The addition of a third bromine atom results in a further band gap decrease of approximately 0.2 eV. The molecule with the smallest band gap given three bromine atoms is octa(2,5,6-tribromophenyl)-SQ, and the one with the largest gap is octa(3,4,6-tribromophenyl)–SQ. Variations in the band gap are of the order of 12.1%.

Octa(tetrabromophenyl)-SQ and octa(pentabromophenyl)-SQ

There are four combinations of four bromine atoms on each of the phenyl rings. Each molecular system was optimized by the classical force field method. Three of the molecular crystals were further optimized by *ab initio* DFT geometry optimization method, but one structure was unable to be optimized. This system did not converge during the self-consistent field (SCF) solution. Various force and energy tolerances have been tried to further continue the relaxation, but it continued to fail to converge. At this point, this molecule is considered not chemically stable, and henceforth rejected from consideration.

Among the three optimized structures, the octa(tetrabromophenyl)-SQ crystals have band gaps of 2.90, 2.94 and 3.02 eV. As previously, the precise position has a limited effect on the overall band gap. Compared to octa(tribromophenyl)-SQ systems with three bromines, the band gaps of octa(tetrabromophenyl)-SQ further drop by 0.1 eV on average. The molecule with the smallest band gap of 2.90 eV is the octa(2,3,4,5-tetrabromophenyl)-SQ. All the three molecules are now falling into the small band gap semiconductor molecule range.

The system with all hydrogen atoms replaced by bromine atoms on the phenyl ring, the octa(pentabromophenyl)-SQ, was effectively optimized by both the classical force field and DFT methods. The band gap of octa(pentabromophenyl)-SQ further decreases to 2.72 eV. Compared to the octa(tetrabromophenyl)-SQ molecules, this is a relatively large change. The VB, CB and band gaps of four- and five- bromine octa(halogenphenyl)-SQ systems are summarized in Table 5-15 and Figure 5-13. The example unit cell of octa(tetrabromophenyl)-SQ is shown in Figure 5-14 and octa(pentabromophenyl)-SQ unit cell is shown in Figure 5-15.

Table 5-14 HOMO, LUMO and band gaps of octa(tetrabromophenyl)-SQ $(C_6Br_4H_1(SiO_{1.5}))_8$ and octa(pentabromophenyl)-SQ $(C_6Br_5(SiO_{1.5}))_8$

	VB (eV)	CB (eV)	Band Gap (eV)	E_{tot} (Ha)
Octa(2,3,4,5-tetrabromophenyl)-SQ	-6.18	-3.28	2.90	-16054.80144
Octa(2,3,4,6-tetrabromophenyl)-SQ	-6.23	-3.21	3.02	-16054.74101
Octa(2,3,5,6-tetrabromophenyl)-SQ	-	-	-	-
Octa(3,4,5,6-tetrabromophenyl)-SQ	-6.18	-3.25	2.94	-16054.75515
Octa(pentabromophenyl)-SQ	-6.19	-3.48	2.72	-18800.9101

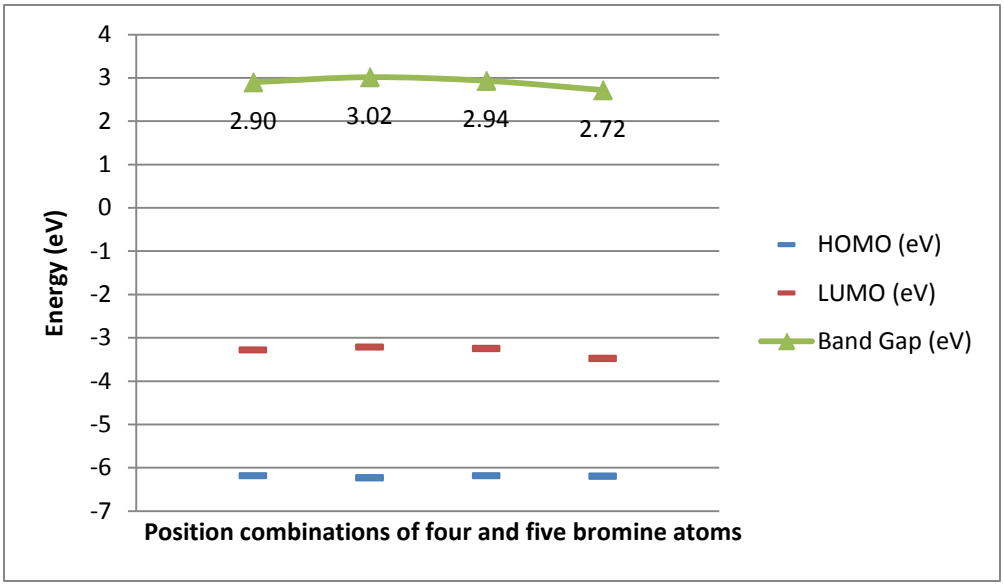

Figure 5-13 VB, CB and band baps of four and five bromine octa(bromophenyl)-SQ. Starting from left, the first is octa(2,3,4,5-tetrabromophenyl)-SQ, then octa(2,3,4,6-terabromophenyl)-SQ, octa(3,4,5,6)-tetrabromophenyl)-SQ and octa(pentabromophenyl)-SQ

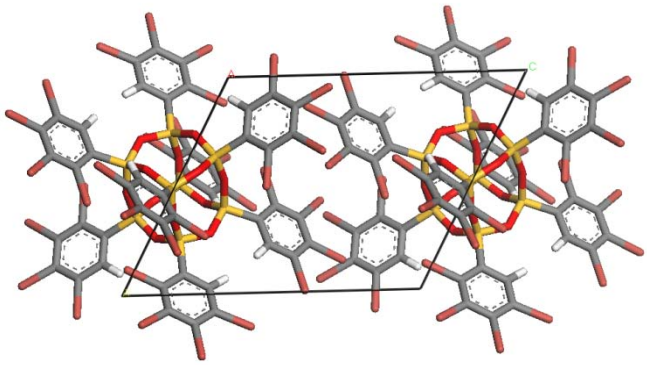

Figure 5-14 Crystal unit cell of octa(tetrabromophenyl)-SQ

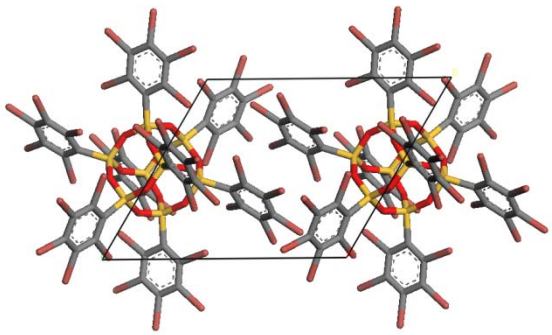

Figure 5-15 Unit cell of octa(pentabromophenyl)-SQ

Octa(bromophenyl)-SQ band gaps summary

The lowest band gap values for different numbers of bromine atom substitutions on the phenyl ring are summarized in Table 5-15 and Figure 5-16. The band gap decreases with the number of bromine atoms replacing hydrogen on the phenyl ring. With more than four bromine atoms, the band gaps are lower than 3.0 eV, which making octa(tetrabromophenyl)-SQ and octa(pentabromophenyl)-SQ potential new small band gap semiconductor molecules.

Table 5-15 HOMO, LUMO and band gaps of octa(bromophenyl)-SQ

	VB (eV)	CB (eV)	Band Gap(eV)
octa(6-bromophenyl)–SQ	-6.28	-2.64	3.63
octa(2,6-dibromophenyl)–SQ	-6.10	-2.87	3.23
octa(2,5,6-tribromophenyl)–SQ	-6.17	-3.13	3.04
octa(2,3,4,5-tetrabromophenyl)–SQ	-6.18	-3.28	2.90
octa(2,3,4,5,6-pentabromophenyl)-SQ	-6.19	-3.48	2.72

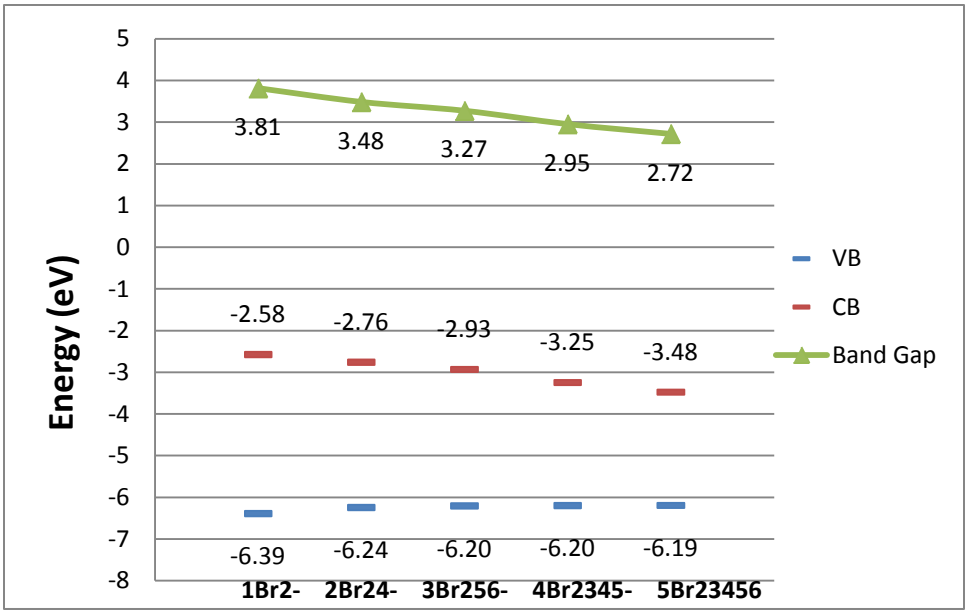

Figure 5-16 HOMO, LUMO and band gaps of octa(bromophenyl)-SQ with 1 to 5 bromine atoms on each phenyl ring.

5.3.2 Octa(fluorophenyl)-SQ

As shown in the previous section, the position of halogen atoms on the phenyl ring will have very limited influence on the band gap of the crystal. Therefore, it is justified to limit the tested molecules with only one configuration. There selection rule is based on potential of interest. Five octa(fluorophenyl)-SQ molecular systems were constructed and studied by using one to five fluorine atoms on the phenyl ring at previously identified configurations of interest. The selection rule is based on first to avoiding the high symmetry molecular structure and to include the 1,4-dihalogenbenzene to further compare the results with existing literature. The five molecular systems are octa(2-fluorophenyl)-SQ, octa(2,5-difluorophenyl)-SQ, octa(2,5,6-trifluorophenyl)-SQ, octa(3,4,5,6-

tetrafluorophenyl)-SQ, and octa(pentafluorophenyl)-SQ. These five systems then were optimized by classical force field and *ab initio* DFT methods in sequence. The calculated VB, CB and band gaps of the selected systems, with between one to five fluorine atoms on the phenyl ring of the octa(fluorophenyl)-SQ, are shown in Table 5-16 and Figure 5-17. Two of the optimized unit cell structures are illustrated in Figure 5-18.

Table 5-16 VB, CB and band gaps of octa(fluorophenyl)-SQ

	VB(eV)	CB(eV)	Band Gap(eV)	E_{tot} (Ha)
octa(2-fluorophenyl)-SQ	-6.56	-2.49	4.07	-5863.507516
octa(2,5-difluorophenyl)-SQ	-6.39	-2.65	3.74	-6657.088635
octa(2,5,6-trifluorophenyl)-SQ	-6.44	-2.67	3.77	-7450.624165
octa(3,4,5,6-tetrafluorophenyl)-SQ	-6.36	-2.54	3.82	-19771.94391
octa(2,3,4,5,6-pentafluorophenyl)-SQ	-6.49	-2.60	3.89	-23447.41287

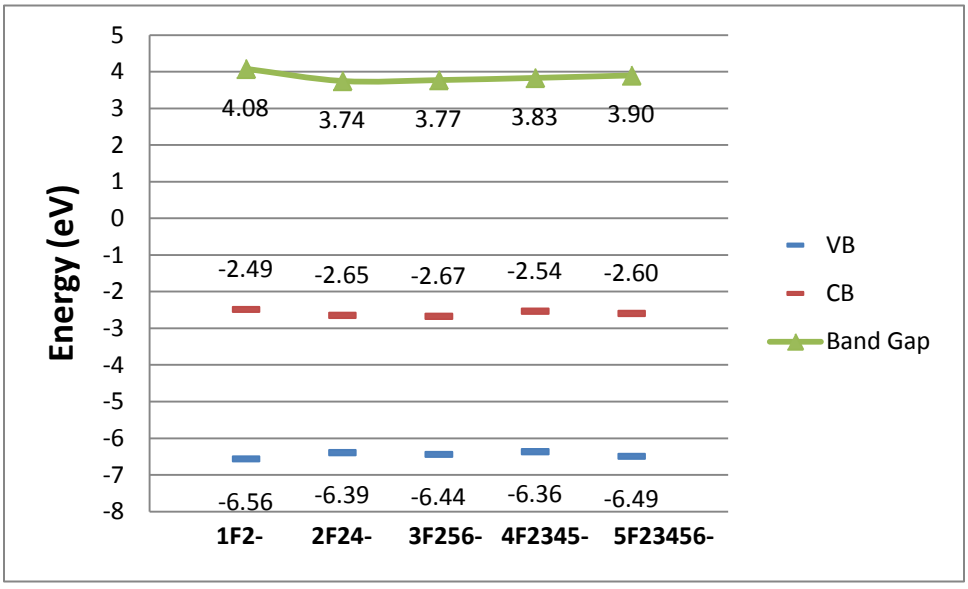

Figure 5-17 VB, CB and band gaps of octa(fluorophenyl)-SQ with 1 to 5 fluorine atoms on each phenyl ring. The molecule is labeled with number of fluorine atoms on the phenyl ring.

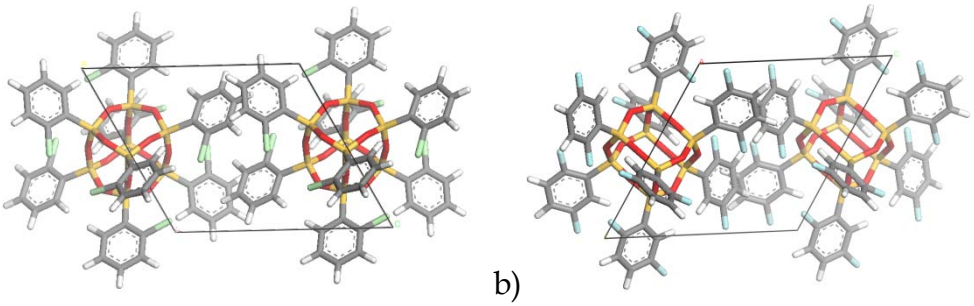

Figure 5-18 Unit cell of octa(fluorophenyl)-SQ: a) octa(2-fluorophenyl)-SQ; b) octa(2,5-difluorophenyl)-SQ

The results show that the five octa(fluorophenyl)-SQ systems will not generate molecules with band gap smaller than 3 eV. According to the previously studied bromophenyl-SQ system, varying the positions of these fluorine atoms on the phenyl ring should not significantly alter the band gap. Therefore, it is unlikely that octa(fluorophenyl)-SQ molecules will have band gaps smaller than 3 eV.

According to Figure 5-16, increasing number of fluorine atoms on the phenyl ring does not consistently decrease the band gap. When number of fluorine atoms increased from one to two, the gap significantly decreased from 4.08 to 3.74 eV. Beyond two fluorine atoms the band gap increases again. The smallest calculated band gap is 3.74 eV for the octa(2,5-difluorophenyl)-SQ, and is the only crystal that has a lower band gap than any of the octa(bromophenyl)-SQ molecules.

5.3.3 Octa(chlorophenyl)-SQ

The same strategy was applied to chlorophenyl-SQ molecular designs as was used for fluorophenyl-SQ. Using chlorine atoms to replace fluorine on the phenyl ring of octa(fluorophenyl)-SQ, the five octa(chlorophenyl)-SQ molecular systems were generated and analyzed. The five molecular systems are octa(2-chlorophenyl)-SQ, octa(2,5-dichlorophenyl)-SQ, octa(2,5,6-trichlorophenyl)-SQ, octa(3,4,5,6-tetrachlorophenyl)-SQ, and octa(pentachlorophenyl)-SQ. The calculated VB, CB and band gaps of the five systems are presented in Table 5-17 and Figure 5-19. Two of the optimized unit cell structures are illustrated in Figure 5-20. The results show that for the five calculated octa(chlorophenyl)-SQ systems, band gap initially decreases with increasing number of chlorine atoms but increases very slightly for four and five chlorine atoms. The band gap energy curve shows a shallow minimum at octa(2,5,6-trichlorophenyl)-SQ.

Table 5-17 VB, CB and band gaps of octa(chlorophenyl)-SQ

	VB(eV)	CB(eV)	Band Gap(eV)	E_{tot} (Ha)
octa(2-chlorophenyl)-SQ	-6.47	-2.59	3.89	-8745.439161
octa(2,5-dichlorophenyl)-SQ	-6.32	-2.72	3.60	-12420.99872
octa(2,5,6-trichlorophenyl)-SQ	-6.27	-2.89	3.38	-16096.42813
octa(3,4,5,6-tetrachlorophenyl)-SQ	-6.26	-2.84	3.42	-19771.94391
octa(2,3,4,5,6-pentachlorophenyl)-SQ	-6.34	-2.97	3.37	-12597.34314

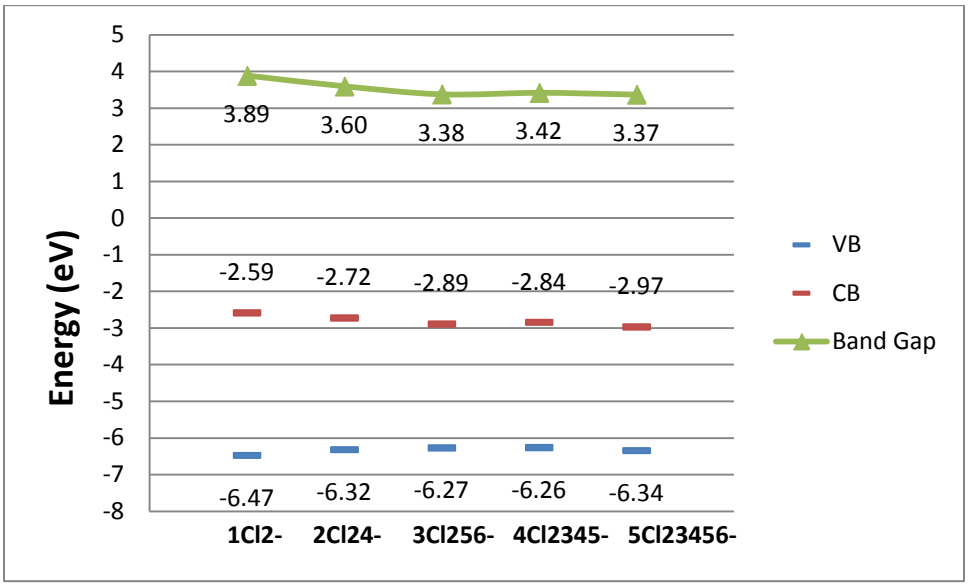

Figure 5-19 VB, CB and band gaps of octa(chlorophenyl)-SQ with 1 to 5 chlorine atoms on each phenyl ring.

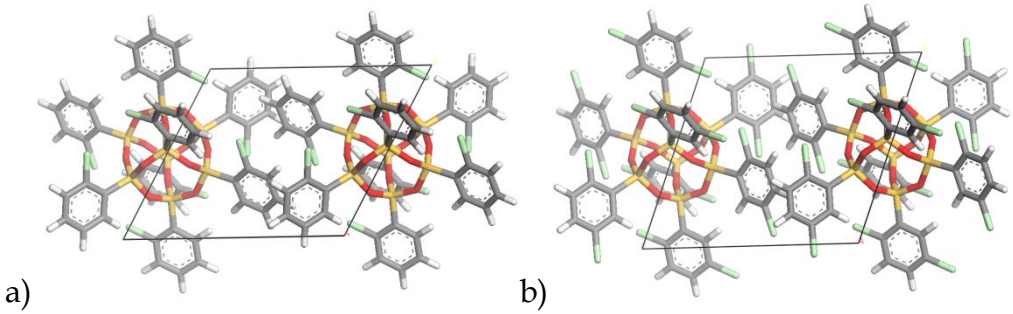

a) b)

Figure 5-20 Unit cell of octa(chlorophenyl)-SQ: a) octa(2,5-dichlorophenyl)-SQ; b) octa(pentachlorophenyl)-SQ

5.3.4 Octa(iodophenyl)-SQ

The previous procedures were repeated for iodine. The five molecular systems are octa(2-iodorophenyl)-SQ, octa(2,5-diiodorophenyl)-SQ, octa(2,5,6-iodophenyl)-SQ, octa(3,4,5,6-tetraiodorophenyl)-SQ, and octa(pentaiodophenyl)-

SQ. The calculated VB, CB and band gap of the five systems are shown in Table 5-18 and Figure 5-21. These results show that replacing hydrogen with two to five iodine atoms on the phenyl ring in the octa(iodophenyl)-SQ systems will generate small band gap molecules. The band gap decreases approximately linearly with the increasing number of iodine atoms present on the phenyl ring. The unit cell structure of octa(pentaiodophenyl)-SQ, is shown in Figure 5-22.

Table 5-18 VB, CB and band gaps of octa(iodophenyl)-SQ

	VB(eV)	CB(eV)	Band Gap (eV)	E_{tot} (Ha)
octa(2-iodophenyl)-SQ	-6.11	-2.77	3.34	-6575.428101
octa(2,5-diiodophenyl)-SQ	-5.84	-3.00	2.84	-8080.997297
octa(2,5,6-triiodophenyl)-SQ	-5.90	-3.77	2.13	-9586.402809
octa(3,4,5,6-tetraiodophenyl)-SQ	-5.59	-3.69	1.90	-11091.98106
octa(2,3,4,5,6-pentaiodophenyl)-SQ	-5.28	-4.11	1.17	-12597.34314

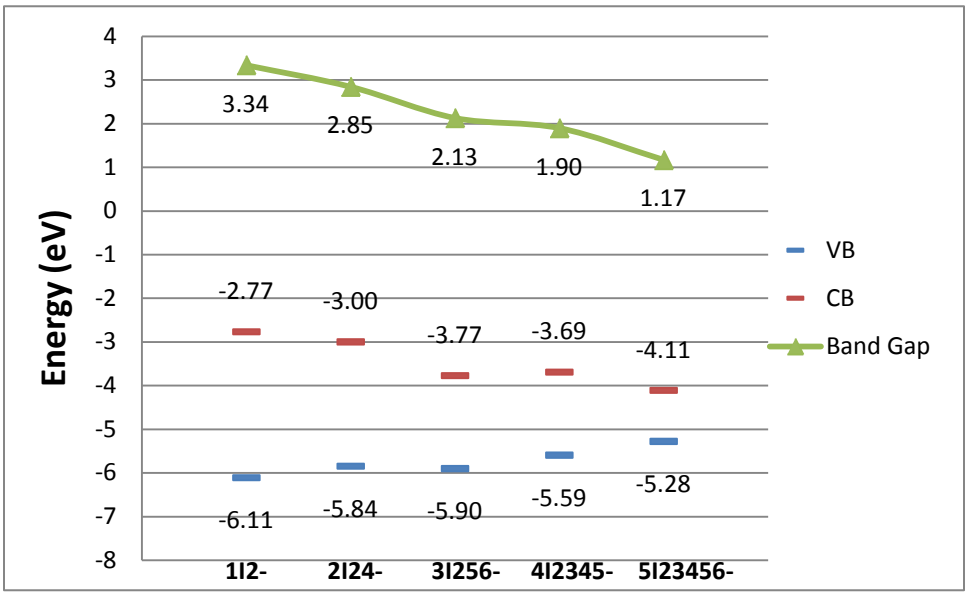

Figure 5-21 VB, CB and band gaps of octa(iodophenyl)-SQ with 1 to 5 iodine atoms on each phenyl ring.

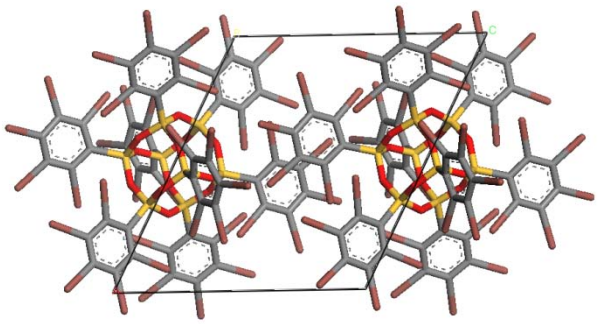

Figure 5-22 Unit cell of octa(pentaiodophenyl)-SQ with five iodine atoms on each phenyl ring

5.3.5 Octa(halogenphenyl)-SQ summary

The band gap energies of the simulated octa(*n*-halogenphenyl)-SQ crystals, where *n*- refers to mono, di, tri, tetra, and penta, are summarized in figures 5-23 through 5-27. Of the octa(halogenphenyl)-SQ molecules with a single halogen substitution on the phenyl ring, octa(iodophenyl)-SQ has the lowest band gap. Similarly, among the octa(dihalogenphenyl)-SQ crystals the octa(dihalogenphenyl)-SQ has the lowest band gap, which is 2.84 eV, making it a potential small band gap semiconductor molecule. Compared to the high mobility of 1,4-diiodobenzene, which is reported to have a band gap of 3.7 eV by DOS analysis[10-12], in this new molecule the band gap is further decreased by about 1 eV. In order to compare the current results with these existing reported discoveries, detailed electronic structure calculations to this molecule about single molecule HOMO, LUMO and crystal band structure and DOS are necessary, and are reported in the later section of this chapter.

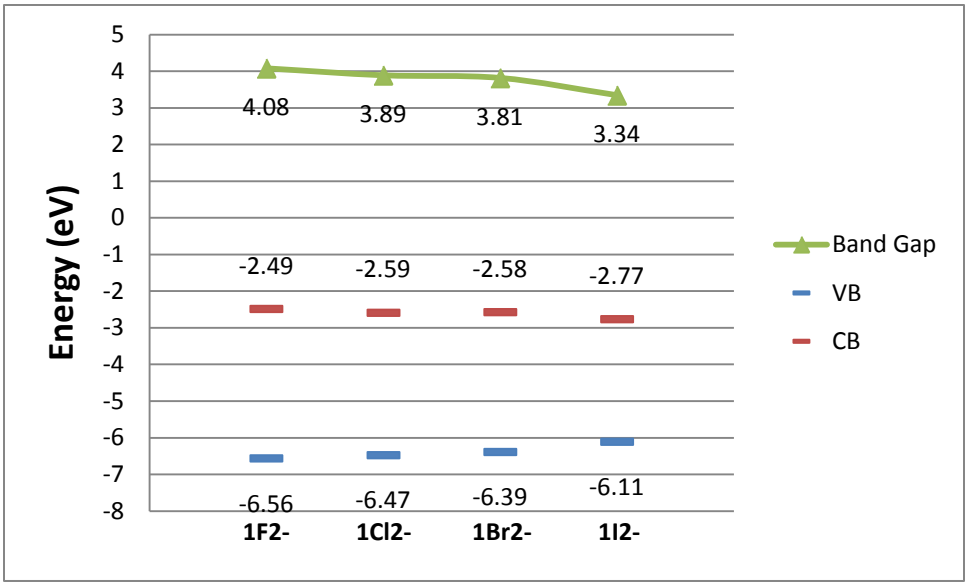

Figure 5-23 VB, CB and band gaps with one halogen atom on the phenyl ring of octa(halogenphenyl)-SQ

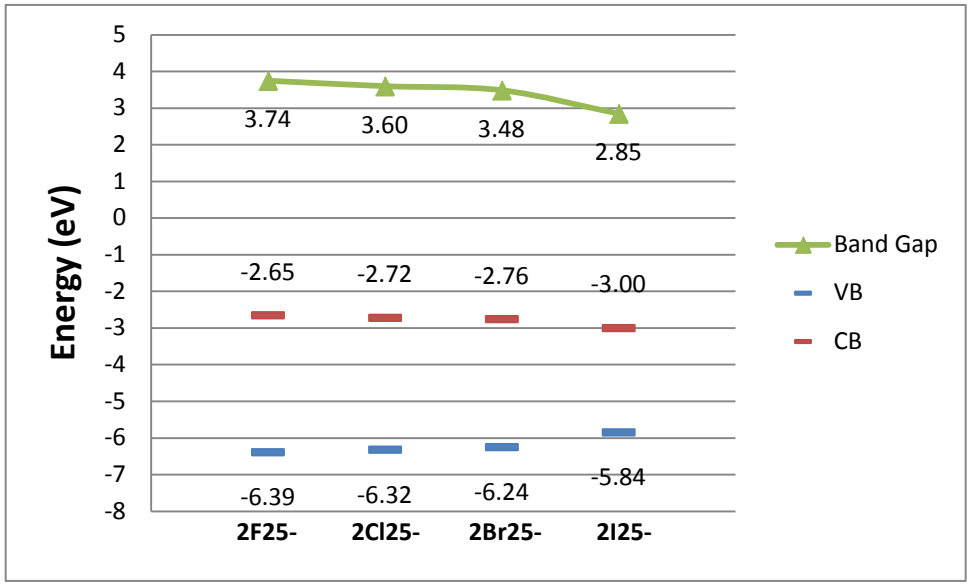

Figure 5-24 VB, CB and band gaps with two halogen atoms on the phenyl ring of octa(dihalogenphenyl)-SQ

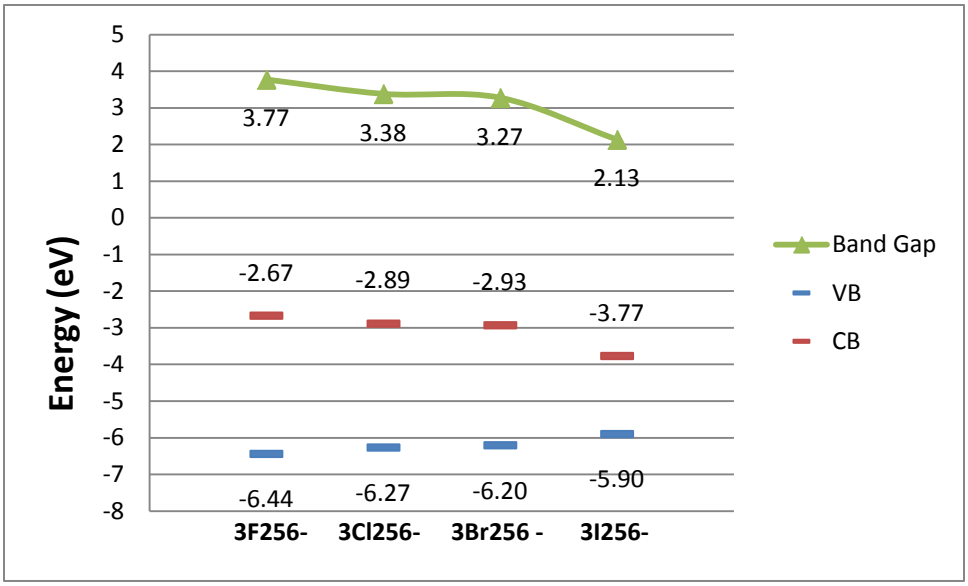

Figure 5-25 VB, CB and band gaps with three halogen atoms on the phenyl ring of octa(trihalogenphenyl)-SQ

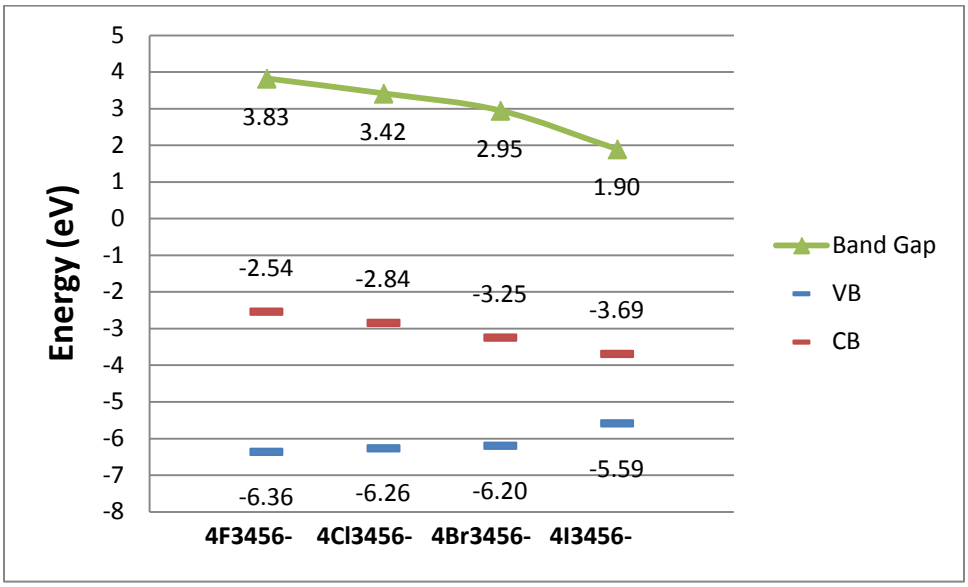

Figure 5-26 VB, CB and band gaps with four halogen atoms on the phenyl ring of octa(tetrahalogenphenyl)-SQ

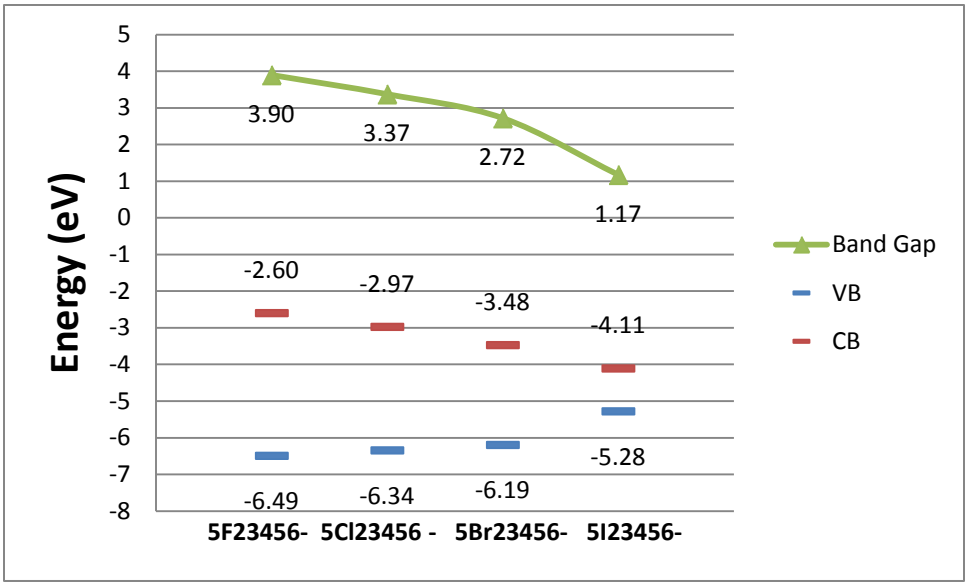

Figure 5-27 VB, CB and band gaps with five halogen atoms on the phenyl ring.

The trend continues for the tri, tetra, and penta substituted octa(halogenphenyl)-SQ molecular crystals. The band gap decreases steadily with the mass of the halogen species in each subgroup. If we consider potential small band gap semiconductors those with a band gap of less than 3 eV, these include octa(2,5-diiodophenyl)-SQ (Eg = 2.85 eV), octa(2,5,6-triiodophenyl)-SQ (Eg = 2.13 eV), octa(3,4,5,6-tetraiodophenyl)-SQ (Eg = 1.90 eV), octa(3,4,5,6-tetrabromophenyl)-SQ (Eg = 2.95 eV), octa(pentaiodophenyl)-SQ (Eg = 1.17 eV), and octa(pentabromophenyl)-SQ (Eg = 2.72 eV).

5.3.6 Frontier orbitals of selected octa(halogenphenyl)-SQ

In this study, frontier orbitals were calculated for select halogen-benzene-SQ molecules, using their ground state optimized crystal structures. This is different

somewhat from the conventional method of using geometries optimized for individual molecules. The motivation for choosing crystal packing geometry instead of individual optimized geometry is because being packed into a three-dimensional continuous structure causes subtle changes in the molecular conformations. We want to understand the effect of these small deformations, and thus the influence of the molecular surroundings on the spatial location of frontier orbitals. Therefore, in this study, the geometries of the molecules in the optimized crystal structure were used instead of the geometries of isolated molecules in vacuum. This will give better understanding of the bulk electronic properties of these predicted molecular crystals. For comparison purpose, the frontier orbitals of several small molecules, such as 1,4-diiodobenzene and hexaiodobenzene , are obtained from their optimized conformation.

As previously shown in Chapter 4, it is interesting to explore partially hexaiodobenzene functionalized SQ, especially those body diagonal functioned SQ. Geometry optimization is performed with Dmol3 for (pentaiodophenyl)-SQ, di(pentaiodophenyl)-SQ and tetra(pentaiodophenyl)-SQ single molecules, as shown in Figure 5-28. Frontier orbitals are then calculated to the three optimized molecules.

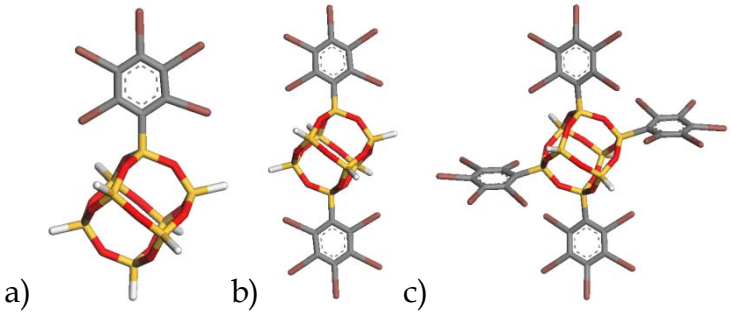

Figure 5-28 Three hexaiodobenzene functionalized SQ. A) pentaiodophenyl-SQ (I_5Ph)-SQ; b) Di(pentaiodophenyl)-SQ or $(I_5Ph)_2$-SQ; c) Tetra(pentaiodophenyl)-SQ or $(I_5Ph)_4$-SQ

Orthogonal grouping of HOMO and LUMO in cubic halogenphenyl-SQ

The calculated HOMO and LUMO orbitals for these selected molecules are viewed at an iso value level of 0.03 e/ $Å^3$ in Figure 5-29 to Figure 5-37.

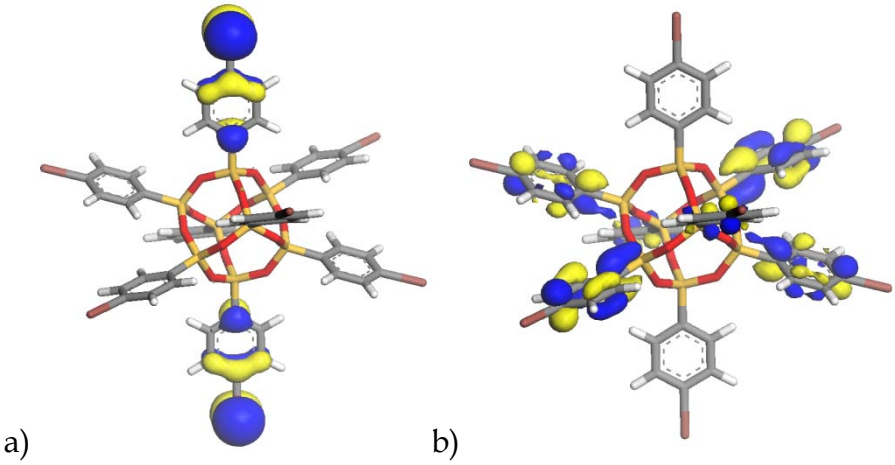

Figure 5-29 Frontier orbitals of octa(4-iodophenyl)-SQ: for a) HOMO and b)LUMO

As seen in Figure 5-29a) the HOMO is mainly located at the two iodophenyl group at body diagonal. The two groups are parallel and appear to be in the exactly same plane. Figure 5-29b) shows the LUMO distributed over the other 6

iodophenyl groups and the two Si atoms of the SQ connected to the two most participating iodophenyl groups positioned at the body diagonal of SQ. The strong Si and C bond is σ type and conjugated with the π orbital on the connecting phenyl ring. The 6 groups seem to keep a certain directional relevance, although they are not completely parallel to each other. At this electron density observation level, no portion of the HOMO or LUMO is seen located at the SQ.

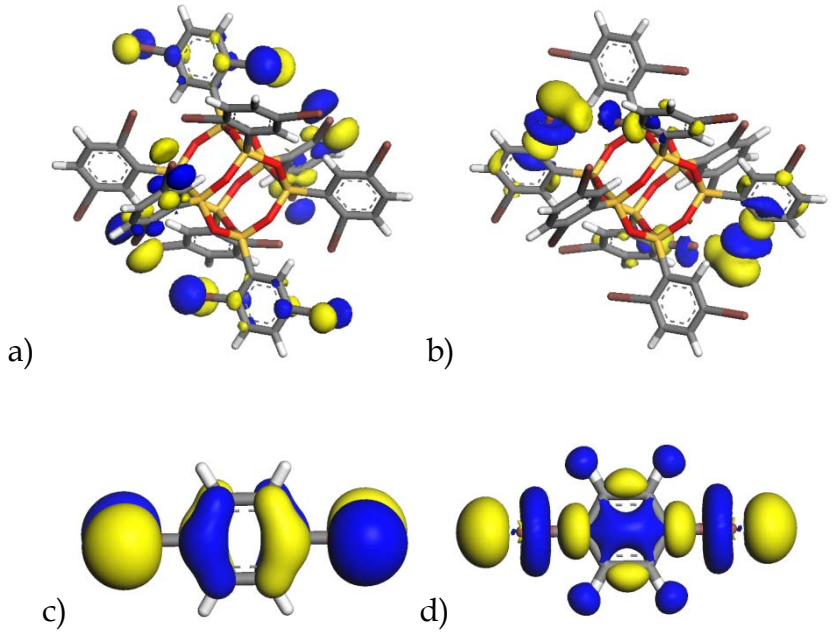

Figure 5-30 Frontier orbitals of octa(2,5-diiodophenyl)-SQ: a)HOMO and b) LUMO and 1,4-diiodobenzene: c)HOMO and d)LUMO

The HOMO is shown in Figure 5-30a) to be distributed at four of the eight iodophenyl groups. Compared with 1,4-diiodobenzene, we can see that by attaching to the Si atom on the SQ, the HOMO of diiodophenyl group roughly maintains its shape, with less delocalization contribution on the π conjugation

orbital of the phenyl ring . In Figure 5-30b) the LUMO orbitals are distributed at the other four diiodophenyl groups. There are extra conjugated molecular orbitals between neighboring iodine atoms. The conjugation on the phenyl ring is reduced. For reference, frontier orbital of 1,4-diiodobenzene is shown in Figure 5-30c-d), for the HOMO and LUMO, respectively. The 1,4-diiodobenzene is geometry optimized with by Dmol3. The calculated HOMO-LUMO energy gap is 3.68 eV, which is large than the direct gamma point band gap of 2.84 eV. According to a) and b), frontier orbital is again grouped into two seemingly orthogonal molecular groups.

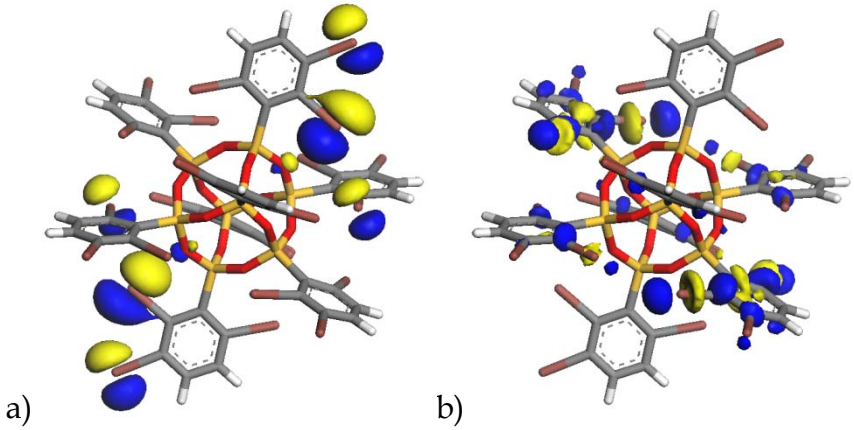

Figure 5-31 Frontier orbitals of octa(2,3,6-triiodophenyl)-SQ with a) HOMO and b)LUMO.

These orbitals continue showing two groups distribution among the eight iodophenyl groups, with the four iodophenyl molecules of each groups are approximately located in the same plane, which almost perpendicular to the approximate plane containing the other four iodophenyl groups. Compared with

the frontier orbitals of previous described molecules, this molecule has poorly conjugated molecular orbitals on iodophenyl groups. There is a small part of the HOMO is located at the two oxygen atoms showing in Figure 5-31a), which means these two oxygen atoms of SQ are together exposed in the HOMO to outside electronic environment.

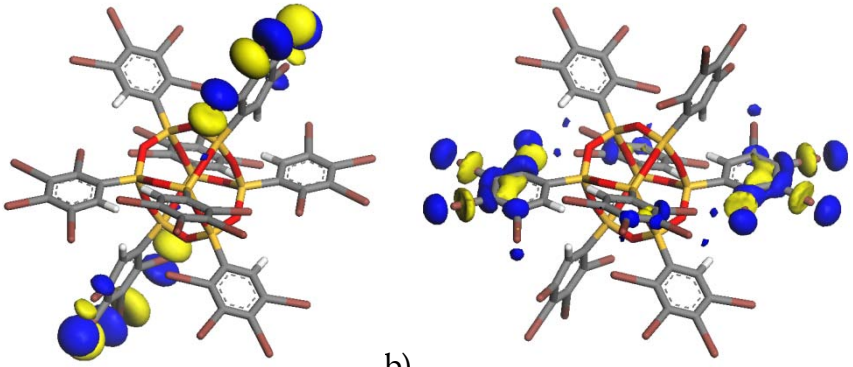

a) b)

Figure 5-32 Frontier orbitals of octa(2,3,4,5-tetraiodophenyl)-SQ with a) HOMO and b)LUMO.

There are only 6 out of the 8 iodophenyl groups sharing the HOMO and LUMO, again they are divided into two groups in Figure 5-32. The HOMO is located on the two iodophenyl groups that are almost exactly in the same plane and located at the body diagonal of the SQ. LUMO is distributed among the four iodophenyl groups, with major portion located at the two body diagonal groups, which are parallel and in the same plane. The remaining small portion of LUMO is shared between the other two phenyl groups located at body diagonal positions of SQ. At this iso value, there are two iodophenyl groups out of the eight of the SQ are

not covered by HOMO or LUMO at all. SQ itself is also not covered by the frontier orbital.

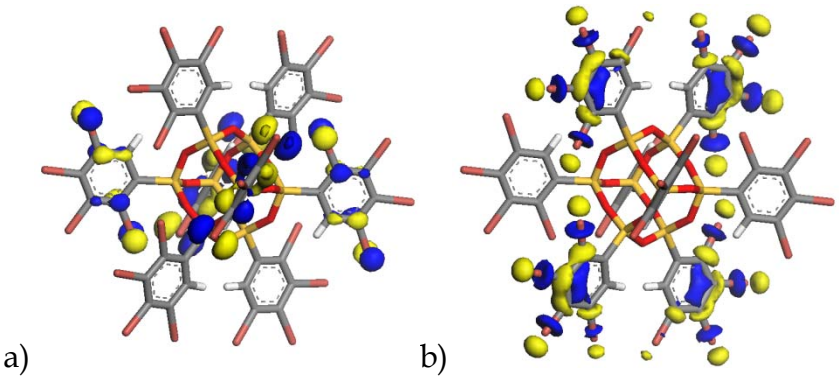

Figure 5-33 Frontier orbitals of octa(2,3,4,5-tetrabromophenyl)-SQ with a) HOMO and b)LUMO.

The HOMO is distributed among four tetraiodophenyl groups and LUMO is distributed to the other four tetrabromophenyl groups, shown in Figure 5-33. The two groups of molecular tetrabromophenyl molecules have good conjugations. The directions of the plane that contain the two groups show certain perpendicular relationship according to the figure, which is similar to the previous described features in iodophenyl-SQ.

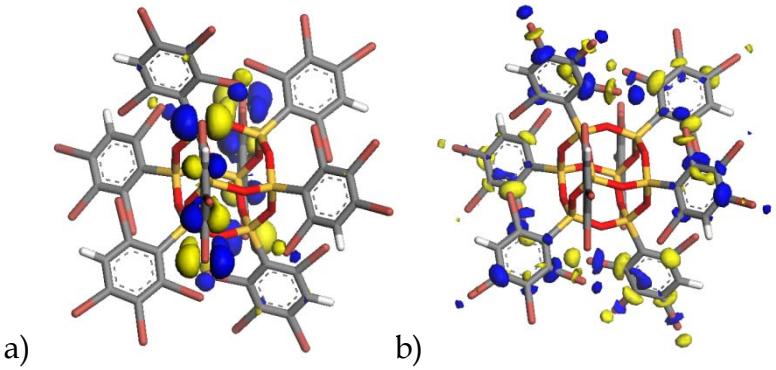

Figure 5-34 Frontier orbitals of octa(2,3,4,6-tetrabromophenyl)-SQ with a) HOMO and b) LUMO

As presented in Figure 5-34, the HOMO is again distributed among four out of 8 of the tetrabromophenyl on the SQ with the LUMO on the other four tetrabromophenyl. Orbital shape and overall distribution is similar to that of Figure 5-33.

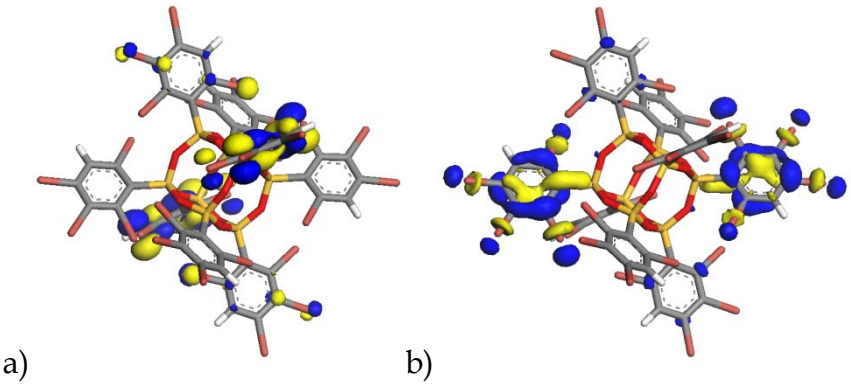

a) b)

Figure 5-35 Frontier orbitals of octa(2,4,5,6-tetrabromophenyl)-SQ with a) HOMO and b)LUMO

In Figure 5-35a), HOMO is distributed to four out of the eight phenyl rings and is mostly distributed on the body diagonal functionalized two phenyl rings, Figure 5-35b) shows the LUMO is distributed to the other four phenyl rings, though it is primarily distributed to the two body diagonal phenyl rings sharing a common plane. In the two phenyl ring, Si atoms are involved in the molecular orbital and formed a sigma pi conjugation along the Si-C bond.

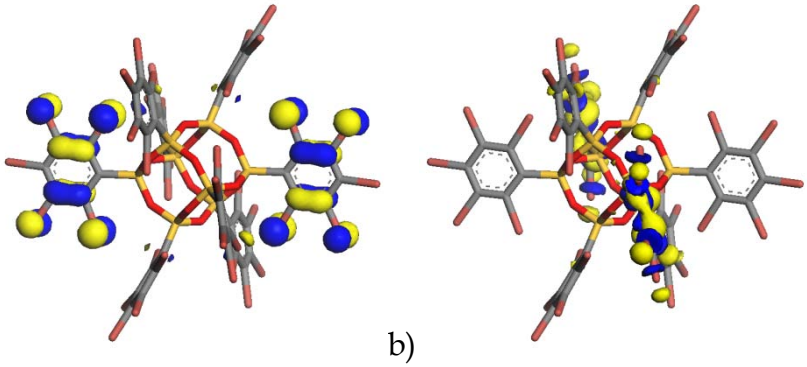

a) b)

Figure 5-36 Frontier orbitals of octa(2,3,4,5,6-pentabromophenyl)-SQ with a) HOMO and b) LUMO

The HOMO shown in Figure 5-36a) is mainly distributed to the two pentabromophenyl while in Figure 5-36b), LUMO is mainly distributed to a different two pentabromophenyl. The two sets of molecular groups are roughly perpendicular in space. The HOMO is in different shape compared with hexabromobenzene.

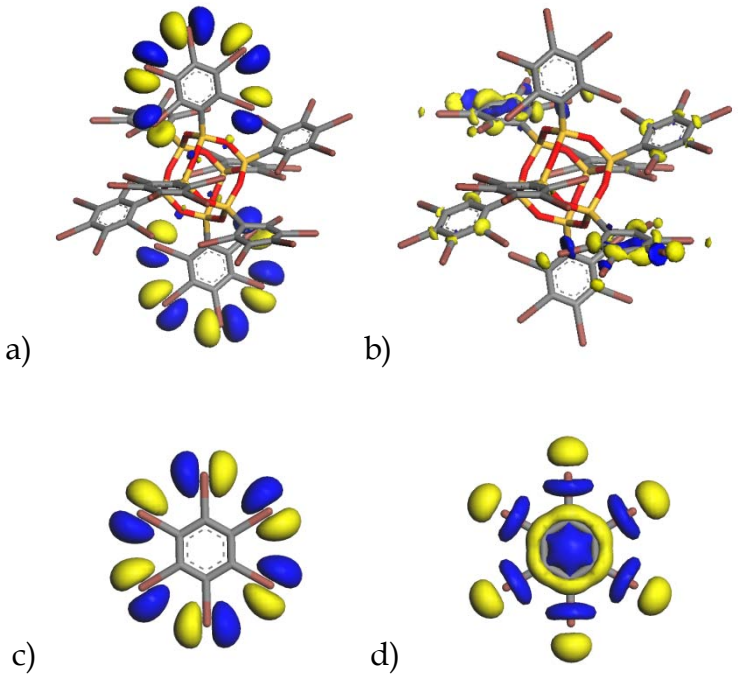

Figure 5-37 Frontier orbitals of octa(2,3,4,5,6-pentaiodophenyl)-SQ with a) HOMO, b) LUMO, , and isolated hexaiodobenzene e)HOMO and f)LUMO

The HOMO of octa(2,3,4,5,6-pentadiodophenyl)-SQ seen in Figure 5-37a)is mainly distributed to the body diagonal pentaiodophenyl. LUMO is distributed to the four phenyl groups in the middle plane. The perpendicular HOMO and LUMO can be seen by comparing a) and b). In reference, the frontier orbitals of isolated hexaiodobenzene obtained from DFT geometry optimization is shown in c) for HOM and d) for LUMO, respectively.

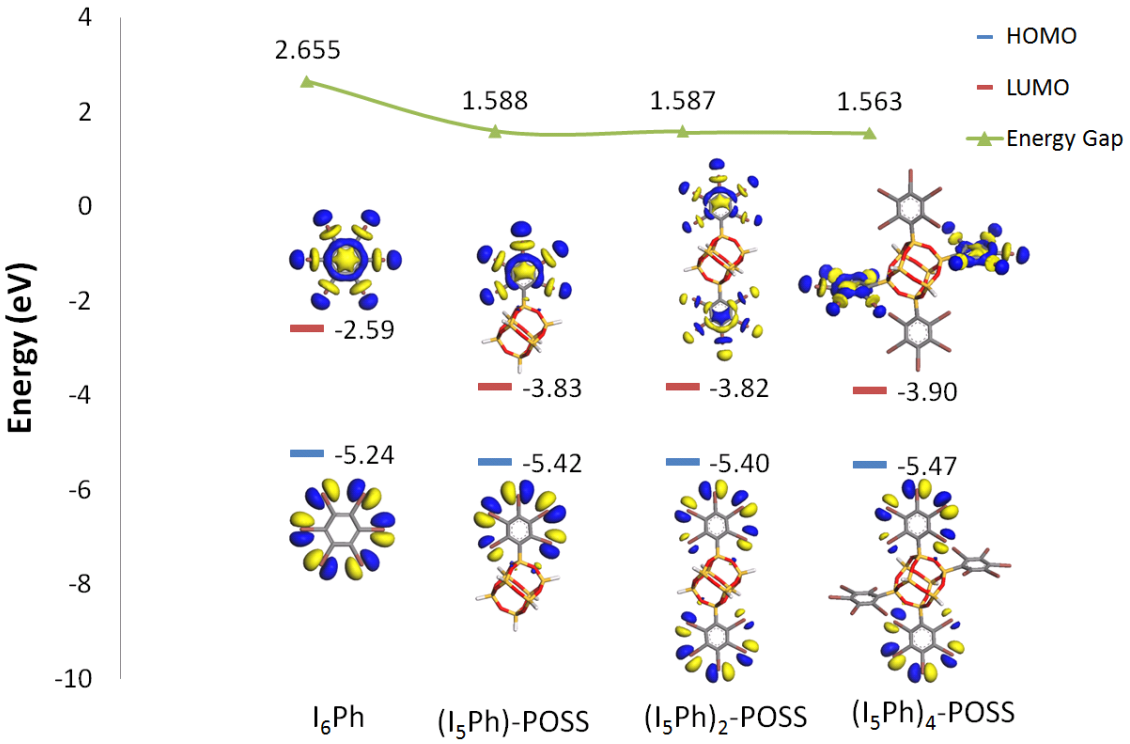

Figure 5-38 HOMO, LUMO and HOMO-LUMO energy gaps of hexaiodobenzene, pentaiodophenyl-SQ or (I_5Ph)-SQ, di(pentaiodophenyl)-SQ or ($I_5Ph)_2$-SQ, tetra(pentaiodophenyl)-SQ or ($I_5Ph)_4$-SQ.

Similar to the findings in Chapter 4, Figure 5-38 shows that attaching I_6Ph with SQ will reduce further the HOMO, LUMO gap of I_6Ph, resulting in a new molecule with HOMO-LUMO energy gap of 1.5-1.6 eV. Attaching more than one hexaiodobenzene to SQ does not significantly further reduce the HOMO-LUMO energy gap. The decrease of HOMO-LUMO gap is mainly from the lower LUMO level for the new molecules. Both HOMO and LUMO are mainly located at the iodophenyl molecular groups. SQ is only very slightly involved in the Frontier orbitals.

According to the ground state calculation of the frontier orbitals, the typical scenario is that HOMO and LUMO are not evenly distributed to the eight corner benzene molecules on the SQ, but possess certain directional related distribution according to selection rules among the eight attached phenyl rings. In some cases, only 6 out the 8 phenyl rings are covered. An across the board comparison can show that the HOMO and LUMO have roughly orthogonal relationship. Figure 5-37 b) and d) demonstrate this relationship. This is further proved in Figure 5-38, where for (I_5Ph)-SQ and $(I_5Ph)_2$-SQ case, when only one planar group existing, the HOMO and LUMO are at the same plane, while in $(I_6Ph)_2$-SQ the HOMO and LUMO distribute to the two perpendicular body diagonal groups respectively. However, since these molecules all have three-dimensional symmetry, the selection criterion seems dependent on the nuclei coordination fluctuation caused by thermal vibration.

In a parallel packing molecular crystal solid of these cubic molecules, although the HOMO-LUMO gap is further reduced due to the lattice periodicity and crystal symmetry, it can be expected that a large fraction of the highest occupied and lowest unoccupied molecular orbitals will be aligned in common directions. Given that the HOMO and LUMO can be approximately considered as linear combination of plane waves of electrons and holes, the transport property will be more uniform in three dimensions for a band-like transport mechanism, and even with thermally induced vibration dominating hopping-like transport, due

to the layout of orbitals, it can also be also 3D in nature. The benefits come from the cubic shape of SQ, which orients these orbitals in 3D perpendicular directions.

Since the optical levels may possess the same direction selection features, the experimentally observed 3-D photoluminescence may be related and determined from the local distribution of these unevenly allocated molecular orbitals. It must be noted that this analysis is only a conceptual estimation and limited by the missing interpretation of electron and hole coupling to the vibrational optical modes, etc. More detailed optical property studies to these molecular systems are needed, which is beyond the scope of this thesis.

According to all studied systems, the center LUMO orbital within the SQ was not found in all calculated octa(halogenphenyl)-SQ molecular systems. Only small contributions from oxygen and silicon can be seen from these frontier orbital displays. Among the calculated HOMO and LUMO structures, by comparing the HOMO LUMO energy levels to the OPS, it was found that introducing bromine and iodine atoms to the phenyl ring of the SQ causes the new molecules to have halogen associated conjugate molecular orbitals and lowered band gaps. The HOMO of the whole molecule will be higher and LUMO will be lower than in OPS.

By attaching one hexaiodobenzene to T8 H-SQ, HOMO-LUMO gaps can be decreased from 2.655 to 1.588 eV for hexaiodobenzene and pentaiodophenyl-SQ.

Increasing the number of iodobenzene groups on the SQ does not further decrease HOMO-LUMO gap significantly. This suggests, instead of halogenation, direct reaction of hexaiodobenzene and hexabromobenzene with T8 SQ is another way to directly synthesize this new type of small band gap 3D shaped semiconductor molecules. Crystal gamma point band gaps can be as low as 1.17 eV for octa(pentaiodophenyl)-SQ, as calculated in the previous section.

5.3.7 Band structure, DOS and PDOS of octa(2,5-diiodophenyl)-SQ

As previously mentioned, 1,4-diiodobenzene (DIB) has been studied by *ab initio* methods.[10-12] These results show that electronic structure calculations can be used to elucidate the mechanisms governing the transport properties of carriers in the DIB molecular crystal. Therefore, it is of interest to investigate some of the typical electronic properties of DIB-functionalized SQ. The band structure, DOS and PDOS for the new octa(2,5-diiodophenyl)-SQ (ODIPS) are calculated with the geometry optimized crystal unit cell at selected high symmetry k points within the first Brillouin Zone. The calculated band structure and total DOS of predicted ODIPS crystal is shown in Figure 5-39. According to our calculation, the band gap of ODIPS is 2.829 eV, which is about 1 eV smaller than the reported band gap of the DIB. [10] Secondly, the conduction band and valance band both show a large bandwidth with many sub-band energy levels and small dispersion on each of the sub energy levels, which is very similar to the DIB band structure

described in references. [10-12] This indicates that a similar iodine-dominating effect to the carrier transport exists in the ODIPS. Therefore, a high hole mobility is expected with this predicted ODIPS molecular crystal.

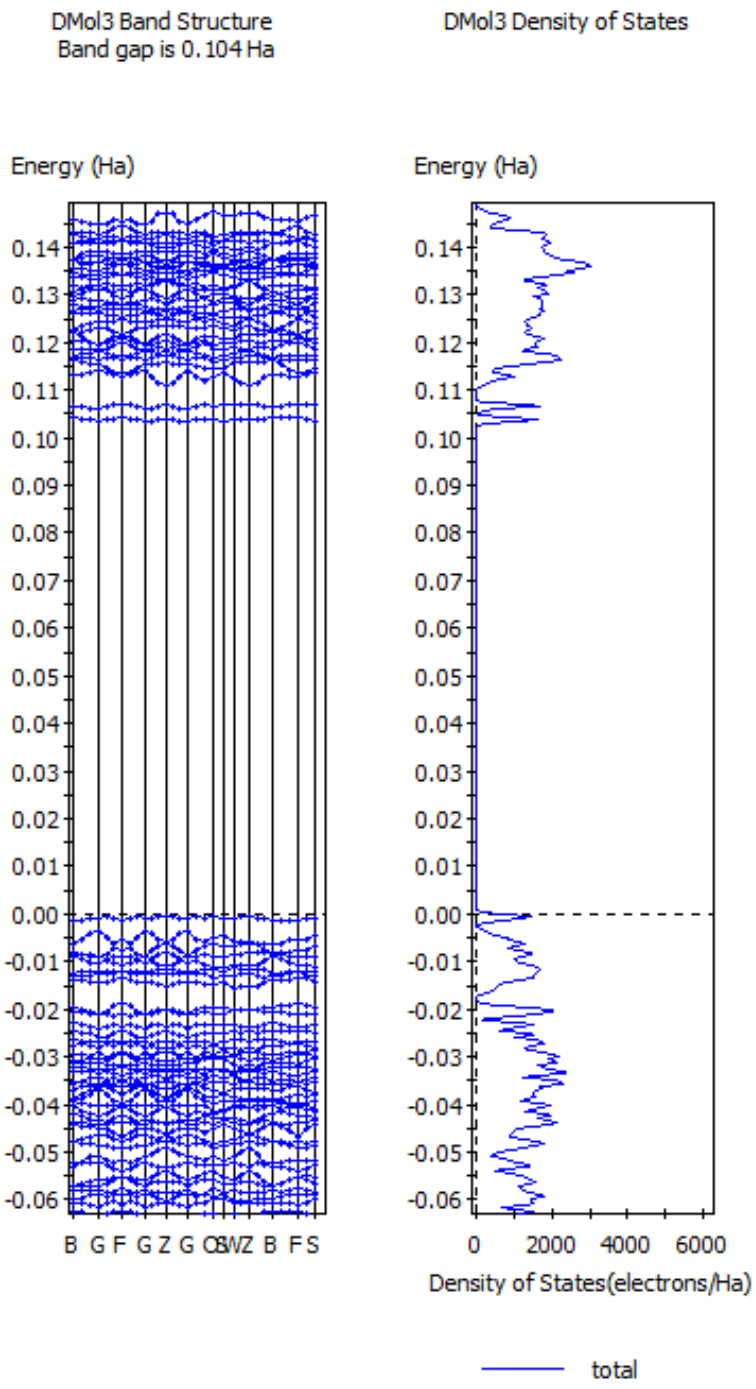

Figure 5-39 Band structure and total DOS of octa(2,5-diiodophenyl)-SQ crystal at selected high symmetry points.

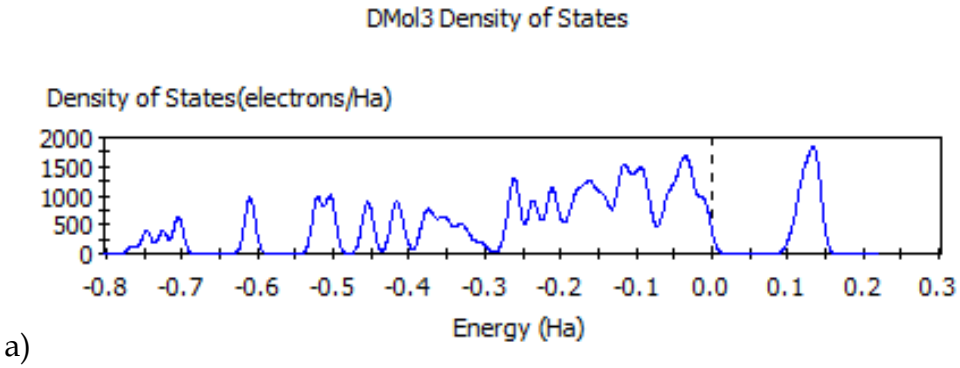
DMol3 Density of States
Density of States(electrons/Ha)
2000
1500
1000
500
0
-0.8 -0.7 -0.6 -0.5 -0.4 -0.3 -0.2 -0.1 0.0 0.1 0.2 0.3
Energy (Ha)

a)

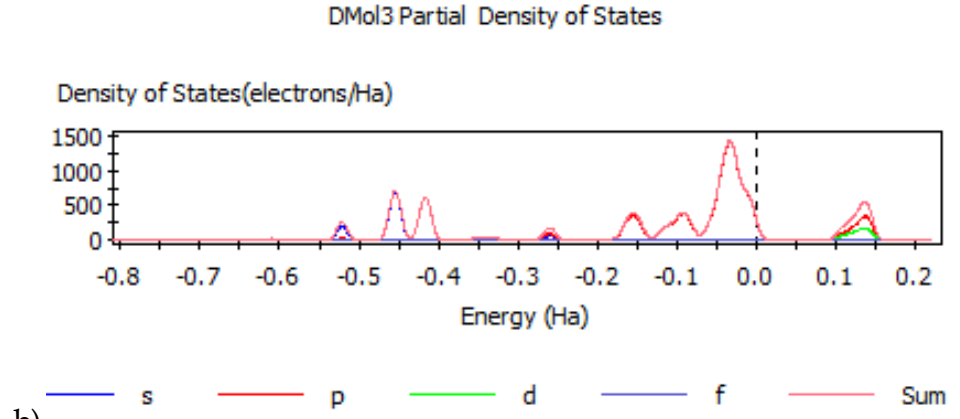
DMol3 Partial Density of States
Density of States(electrons/Ha)
1500
1000
500
0
-0.8 -0.7 -0.6 -0.5 -0.4 -0.3 -0.2 -0.1 0.0 0.1 0.2
Energy (Ha)
s
p
d
f
Sum

b)

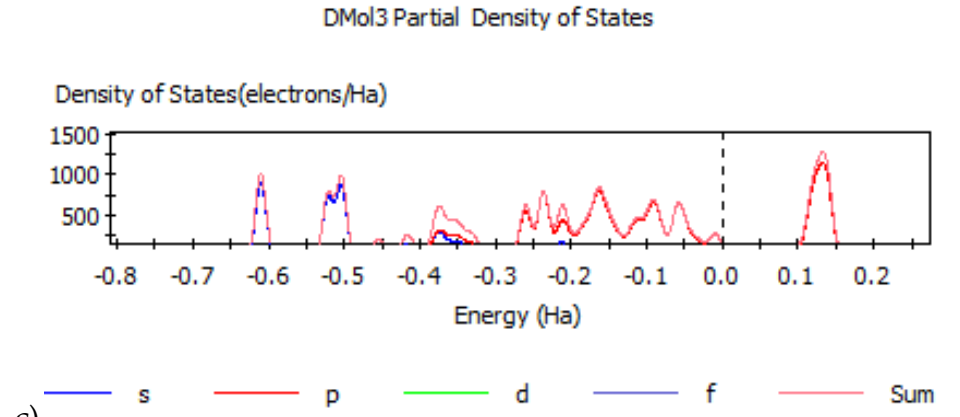
DMol3 Partial Density of States
Density of States(electrons/Ha)
1500
1000
500
-0.8 -0.7 -0.6 -0.5 -0.4 -0.3 -0.2 -0.1 0.0 0.1 0.2
Energy (Ha)
s
p
d
f
Sum

c)

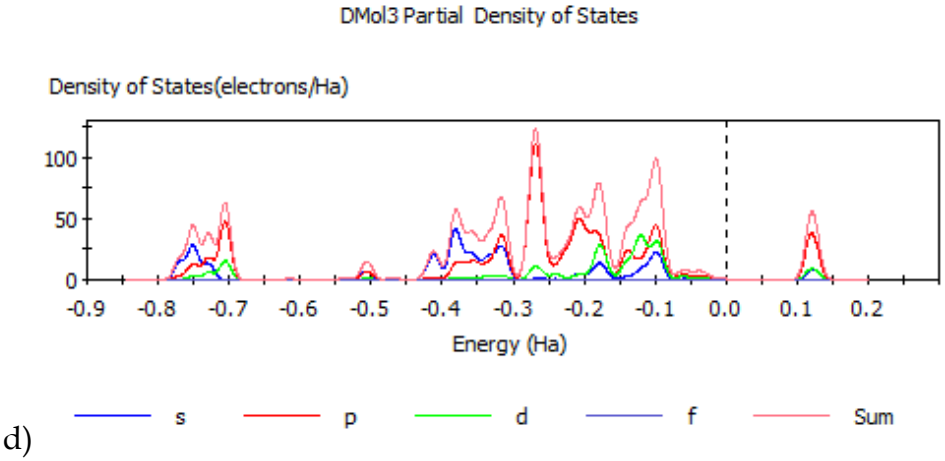

d)

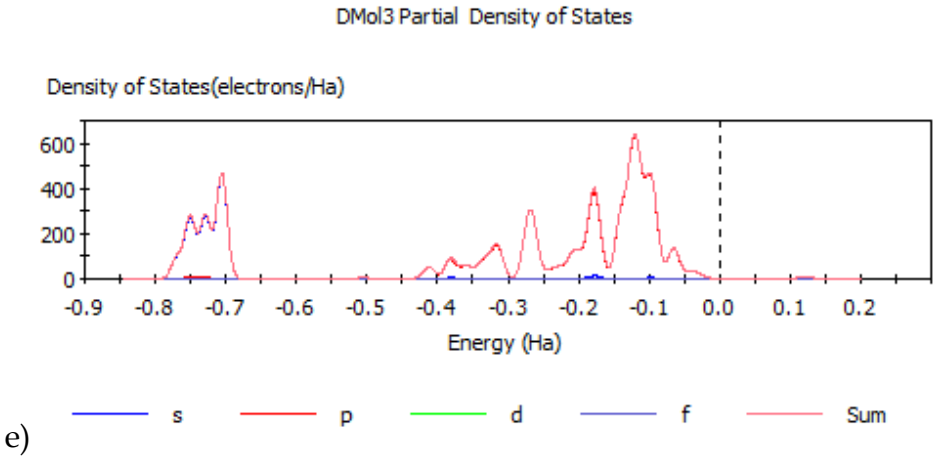

e)

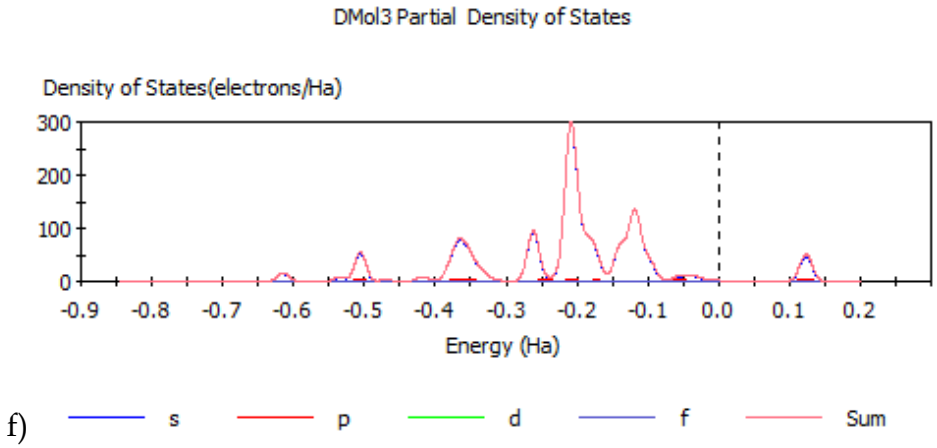

f)

Figure 5-40 Total DOS a) and PDOS of I b), C c), O d), Si e), H f) for ODIPS. Note the different scales of the various sub-plots.

Total DOS and PDOS of the predicted ODIPS molecular crystal are shown in Figure 5-40. Different sub-plots are shown at different scales for clarity. The total density of states shows a higher density on the hole band than on the electron band. The partial density of states plots show that the most significant hole band contribution comes from iodine atomic orbitals. Carbon atoms are the species contributing the second most electronic states in the hole band. This confirms that the hole band is dominated by iodine atomic orbitals. There are also very limited Si, O and H contributions in the hole band. This may indicate the SQ cage itself is only slightly involved in hole transportation.

As for the electron band, the most strongly contributing species is carbon, followed by iodine. It is interesting to see that silicon atoms are also contributing to the electron band, though still to a lesser degree. This indicates that the involvement of the SQ cage in the electron transport of the ODIPS molecular crystal is more significant than to the hole transport, but overall the contribution is still very small.

A normalized total DOS and PDOS is shown in Figure 5-41 in order to compare contributions of different species. Silicon is shown to contribute a small percentage of conduction band states. Although the contribution of atomic orbitals for silicon atoms in the conduction band is small, a better electron carrier mobility and electroluminescent property can be expected than DIP alone. More theoretical studies would need to be performed to further explore the mechanism

and evaluate the ODIPS molecular crystal. Those works are beyond the scope of this thesis and are not treated here. Experimental work to the ODIPS will also be required for evaluation.

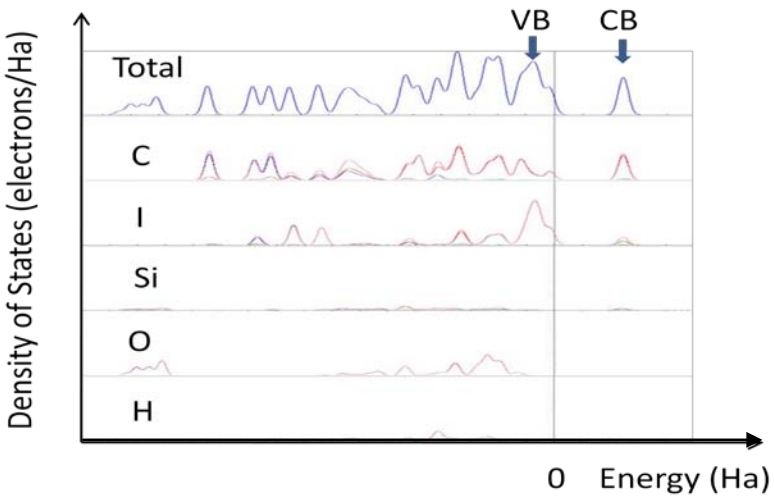

Figure 5-41 Normalized total DOS and PDOS of I, C, Si, O and H

5.4 Summary

In this chapter, a family of new molecules and crystals based on halogens, benzene and SQ building blocks are created and studied by computational molecular design. Using existing experimental halogen-benzene-SQ crystal unit cell information, a series of new small band gap semiconductor SQ based organic-inorganic hybrid molecules have been evaluated. The smallest band gap derived from the systematic study is octa(pentaiodophenyl)-SQ. These simulations and calculations show the pentaiodo-benzene functionalized T8 SQ has a band gap as small as 1.17 eV. Pentabromo-benzene functionalized T8 SQ,

the Br_{48}OPS, also has a small band gap of 2.72 eV. Another molecule of interest is octa(2,5-diiodophenyl)SQ, which has a band gap of 2.829 eV, which is approximately 1 eV smaller than the band gap of 1,4-diiodobenzene. Experimental synthesis and further theoretical study of this molecule would be a very interesting topic and could reveal more of the underlying mechanism for halogenated semiconductor materials.

The experimental crystal of octa(4-iodophenyl)-SQ has a calculated band gap of 3.04 eV, which is already within the semiconductor band gap range. More experimental measurements are also highly desired from this existing material. Although the iodine concentration is not as high as other more iodine functionalized molecules, the small band gap may play a role in high carrier mobilities in this material. Molecular orbital studies to some of the interested halogen-benzene-SQ molecules show that the frontier orbitals are formed mostly by the contributions from the large quantities of iodine or bromine atomic orbitals.

Electronic structures of octa(2,5-diiodophenyl)-SQ (ODIPS) were studied by using *ab initio* methods, including band structure, DOS and PDOS calculations and analysis. The band structure shows similar transport mechanism in the ODIPS crystal as in DIB. The PDOS analysis shows potential SQ cage involvement in the hole and electron transport process and may indicating better performance of the ODIPS crystal.

Overall, the work in this chapter serves to elucidate the electronic structures of halogen-benzene functionalized T8 SQ, and supports computational design and experimental synthesis efforts to identify potential semiconductor hybrid molecular molecules. Computational methods can also be used to further study their electronic properties, such as conductivity and photoluminescence, in the molecular crystal solid state.

5.5 References

[1] Roll, M. F.; Sulaiman, S.; Mathur, P.; Takahashi, K.; Brick, C.; Tamaki, R.; Laine, R. M. $[PhSiO_{1.5}]_8$ autocatalytically brominates to produce $[o\text{-}BrPhSiO_{1.5}]_8$. Further bromination gives crystalline $[2,5\text{-}Br_2PhSiO_{1.5}]_8$ with a density of 2.38 g/cc and calculated refractive index of 1.7 (RI of sapphire is 1.76) or the tetraisocosa-bromo compound $[Br_3PhSiO_{1.5}]_8$. Submitted to *Organometallics*.

[2] Roll, M. F.; Kampf, J. W.; Laine, R. M. Crystalline polyphenylene macromolecular clusters from octaalkynylsilsesquioxanes, their crystal structures and a potential route to 3-d graphenes. *Macromolecules*, in press.

[3] Laine, R. M.; Roll, M. F. Polyhedral phenylsilsesquioxanes. *Macromolecules* **43**, 6995-7000 (2010)

[4] Roll, M. F.; Kim, Y.; Yi, E.; Kampf, J. W.; Laine, R. M. Nano building blocks via iodination of $[PhSiO_{1.5}]_n$, forming $[p\text{-}i\text{-}C_6H_4SiO_{1.5}]_n$ (n = 8, 10, 12), and a new route to high-surface-area, thermally stable, microporous materials via thermal elimination of I2. *J. Am. Chem. Soc.* **132**, 10171–83 (2010).

[5] Roll, M. F.; Asuncion, M. Z.; Kampf, J. W.; Laine, R. M. Para-octaiodophenylsilsesquioxane $[p\text{-}IC_6H_4SiO_{1.5}]_8$, a nearly perfect nano-building block. *ACS Nano* **2**, 320-326 (2008)

[6] Brick, C. M.; Tamaki, R.; Kim, S. G.; Asuncion, M. Z.; Roll, M. F.; Nemoto, T.; Ouchi, Y.; Chujo, Y.; Lane, R. M. Spherical, polyfunctional molecules using poly(bromophenylsilsesquioxane)s as nanoconstruction sites. *Macromolecules* **38**, 4655-4660 (2005)

[7] Laine, R. M.; Roll, M. F.; Asuncion, M.; Sulaiman, S.; Popova, V.; Bartz, D.; Krug, D.J.; Mutin, P.H. Perfect and nearly perfect silsesquioxane (SQs) nanoconstruction sites and Janus SQs. *J Sol-Gel Sci Technol* **46**, 335–347 (2008)

[8] Roll, M. F. *Symmetric Functionalization of Polyhedral Phenylsilsesquioxanes as a Route to Nano-Building Blocks* University of Michigan (2010)

[9] Tang, M.; Bao, Z. Halogenated materials as organic semiconductors. *Chem. Mater.* **23**, 446–455 (2011)

[10] Sanchez-Carrera, R. S.; Coropceanu, V.; Kim, E.-G.; Bredas, J.-L. Charge-transport properties of the 1,4-diiodobenzene crystal: a quantum-mechanical study. *Chem. Mater.* **20**, 5832–5838 (2008)

[11] Ellman, B.; Nene, S.; Semyonov, A. N.; Twieg, R. J. High mobility, low dispersion hole transport in 1,4-diiodobenzene. *Adv. Mater.* **18**, 2284–2288 (2006)

[12] Ellman, B. A*b initio* study of the electronic structure of the crystalline high-mobility organic semiconductor 1,4-diiodobenzene. *THE JOURNAL OF CHEMICAL PHYSICS* **125**, 074702 (2006)

[13] Laine, R. M.; Sulaiman, S.; Brick, C.; Roll, M. F.; Tamaki, R.; Asuncion, M. Z.; Neurock, M.; Filhol, J.-S.; Lee, C.-Y.; Zhang, J.; Goodson III, T.; Ronchi, M.; Pizzotti, M.; Rand S. C.; Li., Y. Synthesis and photophysical properties of stilbeneoctasilsesquioxanes. Emission behavior coupled with theoretical modeling studies suggest a 3-d excited state involving the silica core. *J. Am. Chem. Soc.* **132**, (11), 3708–3722 (2010)

[14] Sulaiman, S.; Bhaskar, A.; Zhang, J.; Guda, R.; Goodson III, T.; Laine, R. M. *Chem. Mater.* **20**, 5563 (2008)

[15] Ionescu, T. C.; Qi, F.; McCabe, C.; Striolo, A.; Kieffer, J.; Cummings, P. T. Evaluation of forcefields for molecular simulation of polyhedral oligomeric silsesquioxanes. *Journal of Physical Chemistry B* **110**, 2502 (2006)

[16] Qi, F.; Durandurdu, M.; Kieffer, J. Computational molecular design of organic semiconductors using T8 SQ and acene, unpublished work

[17] Sun, H.; Rigby, D. Polysiloxanes: *ab initio* force field and structural, conformation and thermophysical properties. *Spectrochimica Acta Part A* **53** 1301 (1997)

[18] Sun, H.; Ren, P.; Fried, J. R. The COMMPASS force field: parameterization and validation for phosphazenes. *Computational and Theoretical Polymer Science* **8**, 229 (1998)

[19] Sun, H. COMPASS: an *ab initio* force-field optimized for condensed-phase applications-overview with details on alkane and benzene compounds. *J. Phys. Chem. B.* **102**, 7338 (1998)

[20] Neurock, M.; Filhol, J.-S.; Lee, C.-Y. Unpublished work.

[21] Bassindale, A. R.; Pourny, M.; Taylor, P. G.; Hursthouse, M. B.; Light, M. E. Angew. *Chem., Int. Ed.* **42**, 3488 (2003)

[22] Bassindale, A. R.; Parker, D. J.; Pourny, M.; Taylor, P. G.; Horton, P. N.; Hursthouse, M. B. *Organometallics* **23**, 4400 (2004)

[23] Pach, M.; Stosser, R. *J. Phys. Chem. A* **101**, 8360 (1997)

[24] Ganesan, P.; Yang, X.; Loos, J.; Savenije, T. J.; Abellon, R. D.; Zuilhof, H.; Sudholter, E. R. R. *J. Am. Chem. Soc.* **127**, 14530 (2005)

[25] Oldham, W. J., Jr.; Lachicotte, R. J.; Bazan, G. C. *J. Am. Chem. Soc.* **120**, 2987 (1998)

[26] Robello, D. R.; Andre, A.; McCovick, T. A.; Kraus, A.; Mourey, T. H. *Macromolecules* **35**, 9334 (2002)

[27] Wang, S.; Oldham, W. J., Jr.; Hudack, R. A., Jr.; Bazan, G. C. *J. Am. Chem. Soc.* **122**, 5695 (2000)

[28] Brown, J. F., Jr.; Vogt, L. H.; Prescott, P. I. Preparation and characterization of the lower equilibrated phenylsilsesquioxanes. *Journal of the American Chemical Society* **86**, 1120-5 (1964)

[29] Delley, B. *J. Chem. Phys.* **92**, 508 (1990)

[30] Delley, B. *J. Chem. Phys.* **113**, 7756 (2000)

[31] (a) Perdew, J. P. *Physical Review B*, **33**, 8822 (1986); (b) Becke, A. D. *Physical Review A* **38**, 3098 (**1988**); (c) Lee, C. T.; Yang, W. T.; Parr, R. G. *Physical Review B* **37**, 785 (1988); (d) Perdew, J. P.; Wang, Y. *Physical Review B* **45**, 13244 (1992); (e) Becke, A. D. *Journal of Chemical Physics* **98**, 1372 (1993); (f) Becke, A. D. *Journal of Chemical Physics* **98**, 5648 (1993)

[32] Delley, B. Hardness conserving semilocal pseudopotentials. *Phys. Rev. B* **66**, 155125 (2002)

[33] Delley, B. Fast calculation of electrostatics in crystals and large molecules. *J. Phys. Chem.* **100**, 6107 (1996)

[34] Schwartz, L. M.; Hornig, J. F. *Mol. Cryst.* **2**, 379 (1967)

[35] Debye, P. J. W. Näherungsformeln für die zylinderfunktionen für große werte des arguments und unbeschränkt veränderliche werte des index. *Mathematische Annalen* **67,** (4), 535–558, (1954)

[36] Hestenes, M. R.; Stiefel, E. Methods of conjugate gradients for solving linear systems. *Journal of Research of the National Bureau of Standards* **49**, (6), 409-436 (1952)

[37] Press, W. H.; Flannery, B. P.; Teukolsky, S. A.; Vetterling, W. T. *Numerical recipes in C: the art of scientific computing* Cambridge University Press (1992)

Chapter 6
Conclusions and Future Directions

6.1 Contributions

This dissertation has focused on the molecular simulation and computational molecular design of SQ-based low band gap organic-inorganic hybrid semiconductors using atomistic MD simulations and *ab initio* DFT methods. A first attempt was made to evaluate the existing force fields to simulate cubic functionalized SQ systems. Force field parameters were developed for FLX force field. MD simulations carried out using the FLX and COMPASS force fields both showed thermal and dynamic properties of the simulated system are in good agreement with existing experimental results.

Diacene-SQ molecules and crystal structures were designed and studied with the two atomistic simulation methods and a polymorph method involving Monte Carlo and symmetry group operations. These newly designed diacene-SQ molecules and predicted crystal structures were determined by density functional theory to be molecular semiconductors with improved electronic, thermal and mechanical properties. This work shows that using a atomistic simulation and quantum computational scheme including *ab initio* calculations,

MD simulations, symmetry-based polymorph predictions, Monte Carlo, and energy minimization algorithms, a series of semiconductor diacene-SQ hybrid small molecule materials can be successfully designed. These newly designed molecules have beneficial properties of both the rigid inorganic core and parallel packed acene groups. More specifically, the new molecules have potential capability of self-assembling into ordered structures, including hard molecular crystals, increasing potential compatibility with Si or other inorganic surfaces, electrodes, etc. It also preserves the potential of cross linking with other cage corners to remain functionalizable.

It can be expected that these new materials will achieve better electronic properties. These properties include band gaps that are tunable by varying the attached acene groups and an inorganic rigid core that makes the molecule more stable to promote higher photo-luminescent efficiency. Additionally, a higher density improves the mechanical properties. The larger molecule also has a lower band gap, and the parallel packing enhances the π-π conjugation with the rigid T8 SQ involved in the bond hybridization, which makes the new molecule a longer conjugated conformation.

The new octa(halogenphenyl)-SQ systems were designed and studied from a series of recent experimentally synthesized SQ molecules. By modifying experimental coordinates, a new molecule a series of low band gap halogen-benzene SQ molecular systems were designed. The Br_{16}OPS experimental crystal

unit cell was chosen as the design frame to initiate the searching process. In the octa(halogenphenyl)-SQ molecular systems, variations come from the number and species of halogen atoms attached to the benzene ring that attached to the SQ cage. Using MD and *ab initio* DFT combined methods, more than 50 molecular systems are constructed, optimized and band gaps are calculated. It was found that this kind of molecular crystals is very interesting because they are hybrid in nature, with cubic symmetry and band gaps can be tuned to as small as 1.2 eV. Among these new molecules, there are more than eight different molecules having a band gap smaller than 3 eV, indicating they are potential small band gap molecular semiconductor crystals. The frontier molecular orbital calculations of selected systems showed the halogen atoms, the phenyl ring and SQ cage are forming delocalized orbitals jointly. It is highly possible that with these new crystal systems, not only new materials can be synthesized but more interesting molecular physics models may be studied. The octa(2,5-diiodophenyl)-SQ (ODIPS) molecule shows similar electronic properties to 1,4-diiodobenzene (DIB). High hole mobilities are also possible for ODIPS. DOS and PDOS indicated that the SQ cages are contributing in the electronic transport process and may promote a whole molecule with better electronic properties.

6.2 Future Directions

A number of potential future directions are possible. Further refinement of the atomic force field of organic molecules could lead to improved atomistic

predictions. The polymorph method also has room for further improvement. It would also be of interest to apply the polymorph method to additionally systems, particularly the halogenphenyl-SQ molecules. Inclusion of electronic transport properties during the design process could more rapidly direct the engineering of new molecules. Finally, the addition of synthesis experiments could help direct the design process and validate results.